# OPTIMAL RESERVOIR MANAGEMENT AND WELL PLACEMENT UNDER GEOLOGIC UNCERTAINTY

A Dissertation

by

SATYAJIT VIJAY TAWARE

Submitted to the Office of Graduate Studies of
Texas A&M University
in partial fulfillment of the requirements for the degree of

DOCTOR OF PHILOSOPHY

August 2012

Major Subject: Petroleum Engineering

Optimal Reservoir Management and Well Placement

Under Geologic Uncertainty

# OPTIMAL RESERVOIR MANAGEMENT AND WELL PLACEMENT UNDER GEOLOGIC UNCERTAINTY

A Dissertation

by

SATYAJIT VIJAY TAWARE

Submitted to the Office of Graduate Studies of
Texas A&M University
in partial fulfillment of the requirements for the degree of

DOCTOR OF PHILOSOPHY

Approved by:

| | |
|---|---|
| Co-Chairs of Committee, | Akhil Datta-Gupta |
| | Michael King |
| Committee Members, | Ding Zhu |
| | Wolfgang Bangerth |
| Head of Department, | Dan Hill |

August 2012

Major Subject: Petroleum Engineering

# ABSTRACT

Optimal Reservoir Management and Well Placement
Under Geologic Uncertainty. (August 2012)
Satyajit Vijay Taware, B.E., Pune University, India;
M.E., Pune University, India.
Co-Chairs of Advisory Committee: Dr. Akhil Datta-Gupta
Dr. Michael King

Reservoir management, sometimes referred to as asset management in the context of petroleum reservoirs, has become recognized as an important facet of petroleum reservoir development and production operations.

In the first stage of planning field development, the simulation model is calibrated to dynamic data (history matching). One of the aims of the research is to extend the streamline based generalized travel time inversion method for full field models with multi-million cells through the use of grid coarsening. This makes the streamline based inversion suitable for high resolution simulation models with decades long production history and numerous wells by significantly reducing the computational effort. In addition, a novel workflow is proposed to integrate well bottom-hole pressure data during model calibration and the approach is illustrated via application to the $CO_2$ sequestration.

In the second stage, field development strategies are optimized. The strategies are primarily focused on rate optimization followed by infill well drilling. A method is proposed to modify the streamline-based rate optimization approach which previously focused on maximizing sweep efficiency by equalizing arrival time of the waterfront to producers, to account for accelerated production for improving the net present value (NPV). Optimum compromise between maximizing sweep efficiency and maximizing

NPV can be selected based on a ‘trade-off curve’. The proposed method is demonstrated on field scale application considering geological uncertainty.

Finally, a novel method for well placement optimization is proposed that relies on streamlines and time of flight to first locate the potential regions of poorly swept and drained oil. Specifically, the proposed approach utilizes a dynamic measure based on the total streamline time of flight combined with static and dynamic parameters to identify “Sweet-Spots” for infill drilling. The ‘Sweet-Spots’ can be either used directly as potential well-placement locations or as starting points during application of a formal optimization technique. The main advantage of the proposed method is its computational efficiency in calculating dynamic measure map. The complete workflow was also demonstrated on a multi-million cell reservoir model of a mature carbonate field with notable success. The infill locations based on dynamic measure map have been verified by subsequent drilling.

# DEDICATION

To God for all his blessings.

To my parents and sister for their love, care and support

## ACKNOWLEDGEMENTS

I would like to thank my committee co-chairs, Dr. Akhil Datta-Gupta and Dr. Michael King for their valuable guidance and financial support throughout the course of this research. Also I want to thank my committee members, Dr. Ding Zhu and Dr. Wolfgang Bangerth for their valuable feedback and questions that have shaped the work in this research. Special thanks to Dr. Shrikanta Mishra of Battelle for valuable support in $CO_2$ sequestration research and to Dr. Torsten Friedel of Schlumberger for valuable support in streamline based history matching.

Thanks to my colleagues in the MCERI research group for the constructive discussions and their friendship. Especially, I want to acknowledge Eric, Alvaro, Mohan, Anish, Kaushik, Akshay, Nimish, Yonnie, Park, Shingo, Ahmed, Suksang, Jichao and Xie for all the valuable inputs and support through the different stages of my work.

# TABLE OF CONTENTS

CHAPTER Page

CHAPTER Page

# LIST OF FIGURES

FIGURE Page

FIGURE Page

FIGURE Page

FIGURE Page

FIGURE Page

FIGURE Page

FIGURE Page

FIGURE Page

FIGURE Page

FIGURE Page

FIGURE Page

FIGURE Page

# CHAPTER I

# INTRODUCTION

## 1.1 Introduction to the Problem

Reservoir management, sometimes referred to as asset management in the context of petroleum reservoirs, has become recognized as an important facet of petroleum production operations in recent years (Fowler et al., 1996). Reservoir management takes an interdisciplinary (Geology, Geophysics and Petroleum Engineering) approach to managing oil and gas fields. Reservoir simulation integrates all of these disciplines in optimizing field development. Reservoir simulation is used in two stages: In the first stage the simulation model is calibrated to dynamic data (history matching) to improve its predictive capability and in the second stage field development strategies are planned and optimized.

History matching primarily involves the characterization of subsurface heterogeneities for example – permeability, porosity etc. In addition, the assimilation of production data into high-resolution geologic models poses an underdetermined inverse problem (Gavalas et al., 1976; Yeh et al., 1986; Moore and Doherty, 2005; Oliver et al., 2008). This is due to the fact that updated properties (permeability, porosity) are defined at individual grid cells are more numerous than measured data. Therefore multiple solutions exist in history matching. These multiple solutions should reasonably encompass all the perceived uncertainties in spatial properties like permeability, porosity, structure etc.

The calibration problem becomes more complicated for multi-million grid cell simulation models with significant number of wells and decades long production history as they pose the problem of long simulation run times. The complexity of such models result in a large number of model parameters which is not only related to the problem of non-uniqueness but also to the significant computational expense of deriving sensitivities of model parameters to production response which is a prerequisite in any

optimization technique (Stenerud et al., 2008). Reservoir calibration of model(s) is carried with the objective of utilizing them for planning and optimizing field development strategies. Geological storage of $CO_2$ (Carbon sequestration) has been carried out in several locations around the world (Benson, 2006) as a method to avoid atmospheric emission of $CO_2$. Model calibration is quite challenging for $CO_2$ sequestration as normally only bottom-hole pressure data is available at injection and observation wells. This makes the model calibration problem more non-unique and ill-posed than regular history matching problem. In addition, pressure data is diffusive making it difficult to resolve heterogeneities.

In second stage of planning field development strategies are optimized. The strategies are primarily focused on rate optimization followed by infill well drilling. One of the major challenges is to incorporate geologic uncertainty in field planning decision so that the planners have greater degree of confidence in their decisions. This issue becomes challenging for high resolution simulation models due to computational intensity.

Field scale rate optimization problems often involves highly complex reservoir model, production and facility related constraints and geological uncertainty. All these make optimal reservoir management via rate and flood front control difficult without efficient optimization tools. More recently, the increasing deployments of the smart well technology have led to the development of efficient algorithms to optimize production/injection along the intervals of smart wells, and thereby improved sweep efficiency via flood front management. Two main types of optimization algorithms have been developed, namely gradient-based algorithms and stochastic algorithms (Brouwer and Jansen 2004; Tavakkolian et al., 2004). The gradient-based algorithms require an efficient estimation of the gradient of the objective function with respect to the control variables. In contrast, the stochastic algorithms such as the genetic algorithm do not require estimation of the gradient but typically require multiple forward simulations for evaluations of the objective function or an appropriately defined fitness function. The advantage of stochastic optimization is the ability to search for a global solution while

the gradient-based optimizations typically search for a local solution. The disadvantage of the stochastic optimization is the extensive computational power requirement, especially when the number of control variables is large.

The placement of infill producers and injectors is another important aspect in the overall development strategy of any field and is particularly challenging for large mature fields with high levels of water-cut. Previous screening approaches based upon static reservoir quality maps (da Cruz et al., 2004) have limited applicability as these do not account for the drainage and swept volumes from existing wells. In contrast, direct application of formal optimization methods such as evolutionary algorithms (Bittencourt et al.,1997) and adjoint-based methods (Sarma et al.,2008) to high resolution geologic models may better represent reservoir dynamics but can be complex to implement and/or computationally prohibitive for large simulation models. The challenge is to develop a method for infill well placement which is suitable for large-scale field application along with uncertainty assessment through examination of multiple geologic realizations.

## 1.2 Literature Review and Present Status

### 1.2.1 Model Calibration for Multi-million Gridcell Models

The first stage of field planning consists of model calibration. There are many different approaches for model calibration available in the literature, for example, gradient based methods (Bissel et al., 1994, Brun et al., 2001), stochastic approaches based on simulated annealing and genetic algorithms (Quenes et al., 1994), Ensemble Kalman filter based stochastic approach (Devegowda et al., 2007; Liu et al., 2005), parameterization using signal processing methods (Bhark et al., 2009; Jaffarpour et al., 2009), dual scale (coarsened and non-coarsened) approach (Jong et al., 2010), hierarchical assisted history matching approach (Yin et al., 2010) to name a few.

Multimillion grid cell models are frequently used in reservoir simulation. But these models, which very often have a significant number of wells and decades long production history, pose the problem of long simulation run times. Grid coarsening during simulation is a practical solution for large runtimes whereby there is no need of further upgridding so as to preserve original resolution. Although such coarsened models

might show differences in its numerical production response compared to non-coarsened simulation model, its global nature, i.e., the field or group wise production response, is close to its non-coarsened input model. Coarsening is typically implemented quite flexibly in modern commercial simulation packages and can be adjusted for different regions of the field or changed as the history matching progresses.

To evaluate sensitivities of global parameters, coarsened or upscaled simulation models can be useful as they can significantly reduce simulation runtimes which is vital for deriving efficient parameter sensitivities (Mamanov et al., 2007; Jong et al., 2010). They are also more suitable than proxy response surfaces constructed using experimental design techniques as they are directly derived from the non-coarsened or non upscaled simulation input models. In our convention, simulation model running with grid coarsening will be referred to as coarsened models and normal simulation model will be referred to as non-coarsened model. Coarsening is typically implemented quite flexibly in modern commercial simulation packages and can be adjusted for different regions of the field or changed as the history matching progresses. The comparable results of coarsened models are acceptable during initial stages of history matching where it is more important to obtain satisfactory global or large scale features like structure, contacts, PVT behavior, relative permeability and capillary pressure behavior, porosity-permeability transformations and fault sealing capacity.

After satisfactory matching at the global scale, a well by well water-cut and gas oil ratio match can be attempted, this is termed as local match (Yin et al., 2010). Often this is accompanied by a revisit of some of the global match assumptions to justify geological discrepancies created during the local match. This process is iterative and often time consuming. To accelerate it, various assisted history matching techniques are regularly deployed in the process.

Grid coarsening has been previously used for model calibration. Mamonov et al., (2007) applied a finite-volume optimal grid approach with an aim of preserving an aggregate objective value. Their aim was not to generate most accurate representation of flow parameters like pressure, saturations etc. but to preserve a predetermined objective

function like cumulative oil production. Jong et al., (2009) used a combination of non-coarsened and upscaled models to achieve better convergence with a streamline based inversion technique called as Generalized travel time inversion (GTTI) (He et al., 2002). They non-uniformly upscaled the properties like permeability and porosity in the fine model to preserve its essential features. They optimized the layer scheme for upscaling by means of bias-variance tradeoff (King et al., 2005). This helped them in reducing the number of parameters during inversion thus making it converge faster as there are few local minima at a larger scale. However, it should be noted that authors did not upgrid the model during simulation so as to make it run faster.

Krogstad et al., (2009) utilized a multi-scale pressure and saturation solver with flow based coarsening to simulate fine grids. A multi-scale pressure technique solved for pressure on coarse grid while preserving fine details in the velocity field. The fine grid effects are incorporated using numerically computed basis functions. Adjoint sensitivities from this multi-scale simulator helped in water-flood optimization which gave results comparable to an equivalent fine grid optimization. Stenerud et al., (2008) used the Generalized Travel Time Inversion (He et al., 2002) together with streamline based analytical sensitivities and a multi-scale pressure solver for inversion of high resolution geological models. Thus, the fine scale velocity field was the basis for streamline tracing. The authors have shown that appropriate coarsening based results are comparable to fine scale models, resulting in a speedup up to an order of magnitude.

### 1.2.2 Bottom-hole Pressure Data Integration for $CO_2$ Sequestration

Geological storage of $CO_2$ (carbon sequestration) has been carried out in several locations around the world (Benson, 2006) as a method to avoid atmospheric emission of $CO_2$. The International Government Panel on Climate Change (Hollaway et al., 2001) recommended "modeling the injection of $CO_2$ into storage reservoir and future behavior, monitoring the storage system and using the monitoring results to validate and update the model". Carbon sequestration in brine aquifers faces many different challenges in both engineering and economical aspects. There is considerable uncertainty associated

with the injection of $CO_2$ in deep aquifers. Engineering problems such as the leakage of $CO_2$ can compromise the integrity of fresh waters, ecosystems and the health of populations exposed to high concentration of $CO_2$ (Ha-Duong, 2003; Gasda et al., 2004). There are also economic liabilities associated with legal disputes and fines imposed by regulatory agencies. These challenges have spurred considerable research and development efforts in $CO_2$ capture and storage technologies along with monitoring, verification and accounting of $CO_2$ sequestration.

An overview of currently ongoing $CO_2$ sequestration projects has been given by Wright et al., (2009). The authors have discussed four projects Sleipner (Norway), Salah (Algeria), Weyburn-Midale (Canada) and Snohvit (Norway). Reasonable success has been accomplished for all these projects. Monitoring, verification and accounting (MVA) are the activities directed to determine the location of the injected $CO_2$ and the presence of possible leaks in order to provide public assurance. MVA is crucial to ensure that the $CO_2$ sequestration is safe and will be safe in the future. Many techniques have been developed for monitoring the performance of $CO_2$ injection projects and the migration of the $CO_2$ in the geologic formations (Benson, 2006).

Most of the studies surveyed were found to be related to prediction and planning of $CO_2$ sequestration projects based on simulation models. Better predictive capability demands better simulation models and relatively little study has been done in methods for calibration of these simulation models to the dynamic data like injection and observation well bottom-hole pressure and time lapse seismic data. Even less study is done for actual fields or aquifers undergoing $CO_2$ sequestration.

Various methods have been reported in the literature for monitoring $CO_2$ sequestration. Benson (2006) has given a summary of these methods. The author has also pointed out the advantages and limitations of each method. Inversion of the time-lapse seismic responses have been used for quantitative interpretation of the movement of the $CO_2$ plume in the subsurface, specifically in saline aquifers (Chadwick et al, 2005, Chadwick et al, 2009; Delépine et al., 2009). A combination of 2-D and 3-D seismic data is being used to track $CO_2$ migration in Sleipner reservoir in Norway (Nooner et al.,

2007). In Weyburn field a comprehensive program consisting of time lapse 3-D seismic for monitoring migration and geochemical analysis for ensuring containment is being used (Wilson et al., 2004). Rey et al. (2010) presented a novel streamline based approach to integrate time lapse seismic data for improving characterization of the aquifer during $CO_2$ sequestration. A crucial element in their work is accounting for the gravity segregation of the injected $CO_2$ and the resulting implications on the quantitative interpretation of the time-lapse seismic response. All the researchers have showed potential benefits of integrating seismic data in forecasting the performance of $CO_2$ sequestration.

In addition to the seismic methods pressure transient analysis using bottom-hole pressure data from injection and observation wells is the most widely used monitoring method. Utilizing pressure data either by conducting pressure transient test or using well bottom-hole pressure data is an inexpensive way to monitor $CO_2$ sequestration. Bottom hole pressure data along with rate data is normally acquired as a routine procedure during $CO_2$ injection. Spatial data like porosity and permeability influences pressure behavior in the reservoir. So pressure transients as well as injection / observation well pressure data can be used to infer porosity and permeability. Pressure data can also be used to validate and calibrate geological and simulation models used for planning and forecasting of $CO_2$ sequestration projects. Many researchers and companies have used pressure transient data and bottom hole pressure data for validating and calibrating single or multiple simulation models.

One of the examples of using pressure transient tests for reservoir characterization has been presented by Mishra et al., (2011). They have developed a systematic approach for deriving permeability-thickness product (*kh*) and porosity-compressibility product (*phi-ct*) from falloff test by using a radial composite model due to presence of two different mobility zones during $CO_2$ injection. The study of influence of permeability barriers and faults on pressure buildup, $CO_2$ injectivity and risk of leakage was done by Oruganti et al., (2009). They concluded that reservoir and structural heterogeneities do affect $CO_2$ injectivity and storage capacity.

Mantilla et al., (2009) used probabilistic history matching for generating multiple realizations calibrated to injection and observation well bottom-hole pressures for inferring $CO_2$ plume behavior. They found out that the pressure data at inactive / observation wells are very useful in detecting features which influence $CO_2$ plume location. Bhowmik et al., (2011) also used probabilistic history matching for calibrating simulation models to bottom hole pressure data. They used a two-step approach for integrating high permeability streaks / fractures. In the first stage they constrained the model to permeability histogram based on well log data and injection data from horizontal injectors. In the second stage they improved the match by introducing high permeability streaks constrained only by injection data.

Along with porosity and permeability, uncertainty also exists in $CO_2$ desorption control mechanism, typically modeled by Langmuir isotherm. This uncertainty was evaluated in predicting $CO_2$ storage capacity in a coalbed methane reservoir (Calderon et al., 2010). Reservoir model was history matched to methane production data by changing porosity and permeability. Then this history matched model was used to predict uncertainty in $CO_2$ storage using three Langmuir isotherms derived from experimental data.

ChevronTexaco conducted a sensitivity study of geological, rock and fluid properties along with rock / fluid interactions and gas-water hysteresis effects for $CO_2$ sequestration in deep saline formation (Flett et al., 2007). After conducting numerous experimental design studies for different parameters discussed earlier, on a reservoir simulation model the authors came to conclusion that gas trapping due to gas-water relative permeability hysteresis has a large effect on the volumes of mobile $CO_2$. In addition, the geological heterogeneities influence amount of mobile and trapped $CO_2$.

### 1.2.3 Rate Optimization Under Geological Uncertainty

In field planning model calibration is generally followed by rate optimization. In rate optimization the well rates of existing well rates are modified to achieve a particular objective like maximizing net present value, sweep efficiency or minimizing water production.

Field scale rate optimization problems often involve highly complex reservoir model, production and facility related constraints and geological uncertainty. All these make optimal reservoir management via rate and flood front control difficult without efficient optimization tools. More recently, the increasing deployments of the smart well technology have led to the development of efficient algorithms to optimize production/injection along the intervals of smart wells, and thereby improved sweep efficiency via flood front management. Two main types of optimization algorithms have been developed, namely gradient-based algorithms and stochastic algorithms (Brouwer and Jansen 2004; Tavakkolian et al. 2004). The gradient-based algorithms require an efficient estimation of the gradient of the objective function with respect to the control variables. In contrast, the stochastic algorithms such as the genetic algorithm do not require estimation of the gradient but typically require multiple forward simulations for evaluations of the objective function or an appropriately defined fitness function. The advantage of stochastic optimization is the ability to search for a global solution while the gradient-based optimizations typically search for a local solution. The disadvantage of the stochastic optimization is the extensive computational power requirement, especially when the number of control variables is large.

In previous works, the gradient-based optimization of waterflooding was implemented mainly using the optimal control theory to maximize the net present value (NPV) or the displacement efficiency at water breakthrough (Sudaryanto and Yortsos 2001; Brouwer and Jansen 2004). Alhuthali et al., (2007; 2008; 2010) proposed a different approach that relies on a streamline-based method to maximize the waterflood sweep efficiency. The main principle behind this optimization scheme is to equalize the arrival time of the waterfront at all producers within selected sub-regions of a waterflood

project. A major advantage of the streamline-based approach is the efficient and analytical computations of the sensitivities of the waterfront arrival times at the producers to well injection/production rates.

To address geological uncertainty one needs to consider multiple geologic realizations during optimization. Van Essen et al., (2006) extended the work done by Brouwer et al., (2004) and used an objective function in terms of the expected value of NPV obtained from multiple realizations. An adjoint method is used to compute the gradient of the objective function and the steepest ascent algorithm to maximize it. Their results showed that their optimization approach improved the expected NPV and resulted in smaller variance of possible NPV outcomes.

Naevdal et al., (2006) utilized a closed-loop control approach based on a combination of an optimal control for waterflood optimization and ensemble Kalman filter for reservoir model updating. The measurements from smart wells are used to continuously update an ensemble of reservoir models. An optimal control strategy is then used to allocate rates based on the most recently updated reservoir models. A similar closed-loop approach was adopted by Sarma et al., (2005) where they used Karhunen-Loeve (K-L) expansion for model parameterization and Bayesian inversion for history matching and model updating. Wang et al., (2007) also used the ensemble Kalman filter for history matching and model updating. For rate control optimization, they compared the performance of three different methods: steepest ascent, simultaneous perturbation stochastic approximation (SPSA) and ensemble Kalman filter and found the steepest ascent algorithm to be the most efficient.

The streamline-based approach proposed by Alhuthali et al., (2007; 2008; 2010) focused on equalizing arrival time of the waterfront to producers for a group of injectors. This resulted in delayed water breakthrough and reduced field water cut after water breakthrough. The work also took into account geological uncertainty using multiple geological realizations and an expected value of the objective function with an associated risk coefficient. The optimization was performed under operational and facility constraints using a sequential quadratic programming approach. A major

advantage of the streamline-based approach is the analytical computation of the gradient and Hessian of the objective function which makes it computationally efficient and suitable for large field cases. However, one potential drawback of this approach is that it solely focuses on maximizing sweep efficiency, and not necessarily the net present value (NPV). In other words, no credit was given to accelerated production.

### 1.2.4 Optimal Well Placement Under Geological Uncertainty

Generally rate optimization is not enough to achieve field planning objectives like maximizing net present value or cumulative oil production. Infill well drilling has to be undertaken in addition to rate optimization to achieve this objective. Placement of infill producers and injectors is an important aspect of the overall development strategy of any field. Well placement optimization becomes particularly important in mature fields where new infill wells have to be drilled based on an improved understanding of the reservoir description and performance. There could be a large number of possible candidate locations for new infill wells. To search through and evaluate all the possible locations is not practically feasible, particularly for high resolution geologic models consisting of multimillion cells. In addition, we must account for geologic uncertainty using multiple plausible realizations while deciding on optimal well placement locations. For large-scale field applications, a practical method is needed to mitigate the computational burden associated with the large number of search locations to minimize the number of simulation runs.

Previous applications of well placement optimization have utilized derivative-free optimization methods such as genetic algorithm or simulated annealing which are typically computationally expensive and thus, may not be well-suited for large-scale field applications (Centilmen et al., 1999). More efficient gradient based optimization algorithms that compute the gradient by solving adjoint equations have also been used. However, the adjoint methods are difficult to implement and typically require access to the simulator source code. The gradient-based methods can require a large number of iterations to converge and are very sensitive to the starting point for the optimization.

Because of these difficulties, large-scale field applications of well placement optimization have been relatively few and far between. Many of the field applications have used upscaled models which tend to homogenize the reservoir and are unable to properly characterize the bypassed oil location which is closely tied to the well placement optimization problem.

Much of the prior work in the literature related to well placement optimization can be classified into two broad categories: reservoir quality maps and formal optimization methods. The reservoir quality maps are typically based on static properties (permeability, porosity, structure, net thickness) and dynamic properties (remaining oil, pressure, well productivity and cumulative oil production) of the reservoir. The high value regions on these maps are targeted for infill well locations. The formal optimization methods attempt to maximize a particular objective function, for example, cumulative oil or NPV. The optimization solution techniques have utilized heuristic algorithms, for example genetic and evolutionary algorithms and also adjoint formulations to calculate gradient of a related objective function such as maximization of cumulative oil production or net present value.

*Quality Maps*

Da Cruz et al., (2004) proposed quality maps which are 2D representations of reservoir responses like cumulative oil production and calculated their uncertainty over multiple realizations. They used single well perforated through all layers. 3D models were converted into 2D maps showing cumulative oil production if the well was perforated through all the layers. As it is computationally expensive to simulate cumulative oil production by each well in the each grid cell of 2D map, authors simulated only a fraction of grid cells. For non-simulated grid cells they used kriging for interpolation between simulated grid cells. After kriging authors found a set of wells, which minimizes a loss function (i.e. maximizes net present value). For multiple wells an optimization method was developed to locate wells based on maximization of the cumulative oil production. Uncertainty was taken into account using multiple

realizations and maximizing cumulative oil production for each realization and each set of wells. Ranking of realizations was based on sum of cumulative oil production for each 2D map, which gave low side, expected and high side realizations. Drawback of this approach is it is difficult to predetermine number of grid cells in which vertical well is to be simulated to get 2D map of cumulative oil production. Authors argue that fraction of grid cells to be simulated is based on geological heterogeneities. This can be cumbersome and computationally intensive for high-resolution heterogeneous geological models.

Kharghoria et al., (2003) used heuristic methods to find out well trajectory based on productivity potential map. The productivity potential map is combination of petrophysical (porosity, permeability), dynamic attributes (oil saturation) and geometric parameter (distance form well boundaries).

Nakajima et al., (2003) used Babu and Odeh's analytical solution for horizontal well's productivity to calculate well productivity index for all the layers. They fixed the drainage volume for a fixed length of a horizontal well. The horizontal and vertical permeabilities were the average permeabilities in the drainage box. Based on this they calculated productivity index for that well and attributed this value to the center of the drainage box. They did this for all the grid cells and created a 3D quality map which can be quickly used for decision making.

Liu et al., (2006) proposed using maps of production potential for screening favorable regions for well placement. Authors took into consideration time invariant properties (permeability, porosity) and time variant properties like (saturation, pressure). The parameter for production potential contained the following parameters: oil saturation, oil phase pressure, natural log permeability and natural log of distance from closest boundary which was based on Kharghoria et al., (2003). Liu et al., (2006) modified their definition of productivity potential to include mobile oil saturation and effective pore pressure. Moving average method (4x4) was used to compute average productivity potential at each grid block. The automatic well placement algorithm then

scanned the productivity potential map at a particular time step and selected optimum well location based on the grid block, which maximized the production potential.

Guerra et al., (2006) used multiple realizations of high resolution geological model to construct productivity potential map. Productivity potential proxy was based on analytical calculation of well productivity of each grid block along with relative oil mobility and oil phase pressure.

*Shortcomings of quality maps :* Although quality maps take static and dynamic properties into account they don't take into consideration structure of the reservoir, reservoir drive mechanisms, existing wells and existing drainage and sweep areas. These factors influence field production.

*Formal Optimization Methods*

Bittencourt et al., (1997) optimized number of vertical and horizontal wells using a hybrid optimization scheme consisting of genetic algorithm (GA), polytype and TABU search. Centilmen et al., (1999) were first to use Artificial Neural Network (ANN) to mimic reservoir simulator. They used number of well scenarios to train an ANN and then used trained ANN model to predict optimized well patterns based on it. Guyaguler et.al (2002, 2004) used hybrid optimization technique comprising of a genetic algorithm (GA), polytype algorithm, kriging and ANN to optimize infill drilling in waterflooding project in Gulf of Mexico. Their study found that using these helper methods with GA reduced number of required simulations and made this workflow applicable to real field cases. They also evaluated uncertainty in decision making through multiple realizations.

Yeten et al., (2003) used genetic algorithms with hill climbing and near well upscaling method for optimizing well type (monobore, tri and quad lateral) and used ANN as a proxy for reservoir simulation. For dealing with large number of GA runs they used hill climbing algorithm which helped them in minimizing the objective function near minima & near well upscaling helped them to reduce simulation time. Ozdogan et al., (2005) used updated geological realizations at fixed time intervals to take into account new wells being drilled and new production information being available. They

used pseudo-history defined as probable (future) responses of the reservoir that is generated by a probabilistic future model. This forecasted response till a particular time acted as a history till that time. This forecasted history was used in history matching. They used Hybrid Genetic Algorithm (HGA) along with risk decision framework for optimization of net present value (NPV). HGA used GA as main search engine for global search and a polytype algorithm (hill climbing algorithm) to refine a local search. It also used a proxy model based on kriging to reduce the number of simulations. They showed that the subsequent well placement results were improved using this new workflow. Further work was done again by Ozdogan et al., (2006) using HGA to find optimum well placement restricted to a fixed pattern such as line drive or spot patterns. This combined reservoir engineering principles of drilling wells within a GA framework. Authors showed that by using this fixed pattern approach not only reduces number of simulations but the final solution was also practical. They also took uncertainty of property distributions like porosity and permeability and uncertainty in reservoir structure into consideration using multiple realizations. These realizations were selected by an experimental design approach.

Artus et al., (2006) used genetic algorithm to optimize well locations for a monobore and dual lateral well placement. They used multiple realizations to incorporate geological uncertainty. They also used proxies to reproduce the reservoir performance. These proxies were based on an ANN model. These proxies helped them in reducing the number of required simulations by 80%.

Bangerth et al., (2005) evaluated different optimization algorithms and analyzed their effectiveness. They compared and analyzed the efficiency, effectiveness and reliability of several optimization algorithms for the well placement problem. In particular, they considered the simultaneous perturbation stochastic approximation (SPSA) developed by Spall (1992), finite difference gradient (FDG) and very fast simulated annealing (VFSA) algorithms. None of these algorithms is guaranteed to find the optimal solution, but they showed that both SPSA and VFSA were very efficient in finding nearly optimal solutions with a high probability. They illustrated this with a set

of numerical experiments based on real data for single and multiple well placement problems.

Zandvliet et al., (2008) studied the effect of production constraints on the optimal well placement problem. Authors also developed a gradient based optimization using adjoint method for well placement. Authors surrounded the well at initial location with 8 pseudo wells in 8 surrounding grid blocks. These wells were produced at a low negligible rates and the gradient of objective function (NPV) was calculated at all the time steps. Their method proceeded with a calculated step length in the direction of pseudo well with maximum positive sum of gradients. Advantage of this method was that it requires one forward and backward simulation. In addition authors compared their results with exhaustive search on a 2D synthetic field. No field example was shown in their paper.

Sarma et al., (2008) used a continuous approximation of the discrete spatial parameter (x,y) for finding optimized well location. The authors calculated the gradient of an objective function (NPV) with respect to x, y locations of wells using adjoint formulation. This method gave the exact position of optimal well location for simple synthetic cases but authors warned that their method can get caught in local minima. Also their method requires access to source code.

Vlemmix et al., (2009) used adjoint based well trajectory optimization. Their method consisted of using pseudo side tracks to all adjacent gridblocks that produce very small amount of fluid so that they don't influence the overall production. The authors calculated the gradient of NPV with respect to positions of these sidetracks. The average of these gradients gave new coordinates on which new trajectory was constructed. The curvature of trajectory was restricted by dog leg severity and other drilling constraints. This helped them in achieving realistic trajectories. They demonstrated this technique on a 3D synthetic field with a single well drilled at the crest. Its kick off point was fixed and trajectory was optimized for maximizing NPV.

Emerick et al., (2009) used genetic algorithm for numerical optimization of constrained problems to optimize field development scenarios having hundreds of

decision variables. The decision variables they used were number of horizontal wells, type of wells and their locations. The constraints they used were maximum length of wells, minimum distance between wells, inactive grid cells and user defined regions. Their objective function was NPV and they applied this for a real field models in campos basin in Brazil. For a particular strategy they used engineer's judgment to select 50% of initial members of the population. They found out that judgment based population selection gave better result for NPV optimization. But this strategy took more simulations than normal GA.

Some recent applications in the area of formal optimization method are use of particle swarm optimization (Onwunalu et al., 2010) for determining well location and type and use of covariance matrix adaptation evolution strategy for determining optimal well locations and trajectories along with meta-models for reducing number of simulations (Bouzarkouna et al., 2011).

*Shortcomings of formal optimization methods:* Adjoint based well placement optimization methods are complex to apply in commercial simulators because access to source code is required. Both gradient (like adjoints, SPSA) and global optimization methods (like GA) require considerable reservoir simulations to converge if the starting points for well placement are far away from good solution. So good starting points should be known in advance in order to minimize the number of simulations. Gradient based convex optimization methods have problem of converging to local minimas. There have been limited applications to real field cases due to requirement of large number of simulations along with long runtimes. It is difficult to incorporate uncertainties in static properties like structure, permeability and dynamic properties like remaining oil etc as it requires using multiple realizations which is computationally expensive.

### 1.3 Research Objectives and Dissertation Contributions

The motive of this research is to further the advancement of history matching of high resolution simulation models and field rate optimization. A novel method will be proposed using streamline based quality maps for infill well placement in high resolution simulation models. The four primary objectives of this research are as follows:

a) Extend the generalized travel time streamline based inversion method to cater for usage of grid coarsening. This will help in streamline based inversion of high resolution simulation models with decades long production history and numerous wells by reducing computational effort. This will help in practically extending generalized travel time inversion for water-cut history matching to large simulation models by reducing inversion time. The proposed method will be tested on multimillion gird cell simulation model with decades long production history and hundreds of wells. This research objective along with methodology and supporting examples will be discussed thoroughly in the **chapter II.**

b) Develop a novel workflow to integrate well bottom-hole pressure data during $CO_2$ sequestration for simulation model calibration. Pressure data from injection well as well as observation wells is utilized for the model calibration. An approach is proposed to integrate the available pressure data into the simulation model thus improving forecasting capability of the simulation model. In the proposed approach, the first step consists of volume calibration using information from pseudo-steady state flow regime of the injection well. This is followed by bottom-hole pressure inversion of zeroth-order frequency (mean) of the bottom-hole pressure at the injection well. This approach is based on the asymptotic expression for transient pressure variations which is valid at the low frequencies, presented by Vasco et al., (2006). This is followed by transient pressure peak arrival time inversion of

bottom-hole pressure at the observation wells (Vasco et al., 2000). This inversion is based on sensitivities derived using the high frequency asymptotic solution for the transient flow. As a last step, a gradient optimization technique is used to modify global multiplier of permeability. This proposed methodology will be illustrated on 2D and 3D examples and is discussed thoroughly in the **chapter III**. The calibrated model can be further utilized in optimizing $CO_2$ sequestration and drilling of the injection wells.

c) Modify the streamline-based rate optimization approach proposed by Alhuthali et al., (2007; 2008; 2010) which focused on equalizing arrival time of the waterfront to producers, to account for accelerated production in addition to maximizing sweep efficiency. New modification will help in improving Net Present Value (NPV). Optimum compromise between maximizing sweep efficiency and maximizing NPV can be selected based on the 'trade-off curve'. In addition the existence of multiple local minimas and dependence of optimal rates on starting rates due to multiple local minimas will also be investigated. The proposed approach will be illustrated using high resolution simulation model. Geologic uncertainty will also be considered using multiple realizations. This research objective along with methodology and supporting examples will be discussed thoroughly in **chapter IV.**

d) Propose a novel method for well placement optimization that relies on streamlines and time of flight to locate the potential regions of poorly swept and drained oil. Specifically, the proposed approach utilizes a dynamic measure based on the total streamline time of flight, combined with static and dynamic parameters to identify "Sweet-spots" for infill drilling. Sweet-spots thus obtained can be used directly as new infill locations or can act as starting points for a formal optimization method. If used with formal optimization

method optimum infill locations will be achieved with relatively few iterations because of the reduced search space. The main advantage of the proposed method is its computational efficiency. This will make the approach suitable for large-scale field applications and also enable uncertainty assessment through examination of multiple geologic realizations. The complete workflow will be demonstrated on a multi-million cell reservoir models. First simulation model is of a conventional carbonate oil field under waterflood and second simulation model is a heavy oil reservoir under aquifer drive. This research objective along with methodology and supporting examples will be discussed thoroughly in **chapter V.**

**Chapter VI** concludes this dissertation with a summary of the key results of the research developments and applications in the chapter II to chapter V. Recommendations and proposals for future research for all of the four chapters are also presented in the **chapter VI**.

# CHAPTER II

# ASSISTED HISTORY MATCHING USING GRID COARSENING AND STREAMLINE-BASED INVERSION*

## 2.1 Summary

Flow simulation of multimillion grid cell models with hundreds of wells and decades long production history can be extremely time-consuming. This often limits the applicability of assisted history matching techniques. A pragmatic solution to this problem is grid coarsening which is now embedded in many commercial reservoir simulators.

Instead of up-scaling geological models in external packages, grid cells are automatically amalgamated within the simulator while preserving flux distribution and reducing the total number of active cells. The resulting speedup can be significant, often only at small loss of accuracy. Both characteristics are essential elements of any inversion technique in a multimillion grid cell environment. For water-flood history matching, a commercial finite-volume simulator is utilized and the streamline-based generalized travel time inversion whereby water-cut behavior is matched by adjusting inter-well permeabilities.

To apply the assisted history matching technique on high resolution models, a flux reconstruction method is devised which makes full use of the benefits of automatic grid coarsening. It approximates fluxes in the original geological grid by recalculating transmissibility at the fine scale and redistributing coarse scale fluxes accordingly. The

*Part of this chapter is reprinted with permission from "A Practical Approach For Assisted History Matching Using Grid Coarsening And Streamline-Based Inversion: Experiences in a Giant Carbonate Reservoir" by Taware, S., Friedel, T. and Datta-Gupta, A. 2011. Paper SPE 141606-MS presented at the 2011 SPE Reservoir Simulation Symposium, 21-23 February 2011, The Woodlands, Texas, USA. Copyright 2011 by the Society of Petroleum Engineers.

inversion is thus conducted on the fine scale grid, while the forward simulation model uses the coarse grid. A streamline based inversion technique called Generalized Travel Time method (Wu et al., 2002; He et.al, 2002) is used for well by well water-cut match. This inversion technique is briefly explained in the following section. The global match is conducted manually as there are considerable uncertainties in well completions and trajectories, structure and contacts in the fields under consideration. Instead of upscaling simulation models externally coarsening feature in the commercial simulator is used both for the manual global match and for the streamline based well by well match. While solving for an inexpensive coarse model, the calibration takes into account fine grid resolution. Upscaling is not required and the degree of coarsening can be adjusted during the matching process.

The proposed method was successfully tested on a supergiant carbonate oilfield with about hundred wells and large-scale water injection. The history match improved dramatically at relatively low numerical cost, which also allowed for investigating multiple sensitivities. The results were verified against non-coarsened model. The significant increase in efficiency makes this a potential method of choice for cases, where previously assisted history matching techniques could not be deployed due to excessive run times.

The organization of this chapter is as follows. First, the problem of using streamline based inversion for multimillion grid cell models with decades long production history is briefly introduced. Then the major steps of the proposed method are outlined. After that the proposed flux reconstruction method is illustrated. This is followed by demonstration of approach to a synthetic field. Results are compared for case with grid coarsening during simulation and non-coarsened simulation. Finally, the proposed approach is successfully applied to a supergiant carbonate oilfield with about hundred wells, large-scale water injection and decades' long production history.

## 2.2 Streamline Based Inversion for Assisted History Matching using Grid Coarsening

Streamline based travel time inversion for well by well water-cut history matching uses a direct analogy between the streamline methods and the seismic waveform inversion (Vasco et al., 1999; Datta-Gupta et al., 2002). This travel time inversion approach was extended to cater for realistic field conditions with changing production conditions like infill drilling, work-overs and rate changes by a method called as Generalized travel time inversion (GTTI) (He et al., 2002). In GTTI an analogy with the travel time tomography is exploited to preserve the quasi-linear behavior of travel time inversion (Cheng et al. 2005). Quasi-linear behavior helps in rapid convergence of data misfit between observed and simulated production responses. Instead to trying to match production response at a particular time, GTTI introduces an optimal shift calculation to maximize the coefficient of correlation between observed and simulated production response (water-cut). The corresponding sensitivities for the optimal time shift are calculated analytically. They are sensitivities of production responses (water-cut) to reservoir parameters, mainly permeability. This technique has been successfully applied to many field cases (Jong et al., 2010; Oyerinde et al., 2009; Rey et al., 2009, Cheng et al. 2006).

### 2.2.1 New Approach Using Grid Coarsening

The streamline based inversion method explained above is extended to cater for usage of grid coarsening. Grid coarsening has been previously used for model calibration. Mamonov et al., (2007) applied a finite-volume optimal grid approach with an aim of preserving an aggregate objective value. Their aim was not to generate most accurate representation of flow parameters like pressure, saturations etc. but to preserve a predetermined objective function like cumulative oil production. Jong et al., (2009) used a combination of non-coarsened and upscaled models to achieve better convergence with a streamline based inversion technique. They non-uniformly upscaled the properties like permeability and porosity in the fine model to preserve its essential features. They optimized the layer scheme for upscaling by means of bias-variance tradeoff (King et al., 2004). This helped them in reducing the number of parameters during inversion thus

making it converge faster as there are few local minima at a larger scale. However, it should be noted that authors did not upgrid the model during simulation so as to make it run faster.

Krogstad et al., (2009) utilized a multi-scale pressure and saturation solver with flow based coarsening to simulate fine grids. A multi-scale pressure technique solved for pressure on coarse grid while preserving fine details in the velocity field. The fine grid effects are incorporated using numerically computed basis functions. Adjoint sensitivities from this multi-scale simulator helped in water-flood optimization which gave results comparable to an equivalent fine grid optimization. Stenerud et al., (2008) used the Generalized Travel Time Inversion together with streamline based analytical sensitivities and a multi-scale pressure solver for inversion of high resolution geological models. Thus, the fine scale velocity field was the basis for streamline tracing. The authors have shown that appropriate coarsening based results are comparable to fine scale models, resulting in a speedup up to an order of magnitude.

The proposed approach here is different from previous approaches. History matching of multimillion grid cell models with hundreds of wells and decades long production history can be extremely time-consuming. Development of the proposed approach originated from the need for a pragmatic solution to investigate multiple sensitivities like oil water contacts, relative permeability along with absolute permeability modification to production responses. Coarsening is utilized to avoid the need for property upscaling with upgridding and in particular to avoid areal property upscaling which can be considered most complicated. Instead, the geomodel's areal resolution is conserved and only vertical upscaling is conducted which is significantly less sensitive and complex. The aim is to retain the highest possible resolution which later will benefit the well placement while, on the other hand, have a model at hand which allows for running sophisticated workflows such as experimental design or assisted streamline based history matching described before. The amalgamation of grid-cells reduces the runtime significantly at a relatively small loss of accuracy as shown in **Fig. 2.1** and **Fig. 2.2**. This allows utilizing the proposed streamline based inversion

technique on a fast coarsened model during history matching. After reasonable history match, the coarsening can be deactivated and the original high resolution model can be used, for example, for more thorough investigation of specific sectors or for conducting highly detailed well placement planning in the dynamic model.

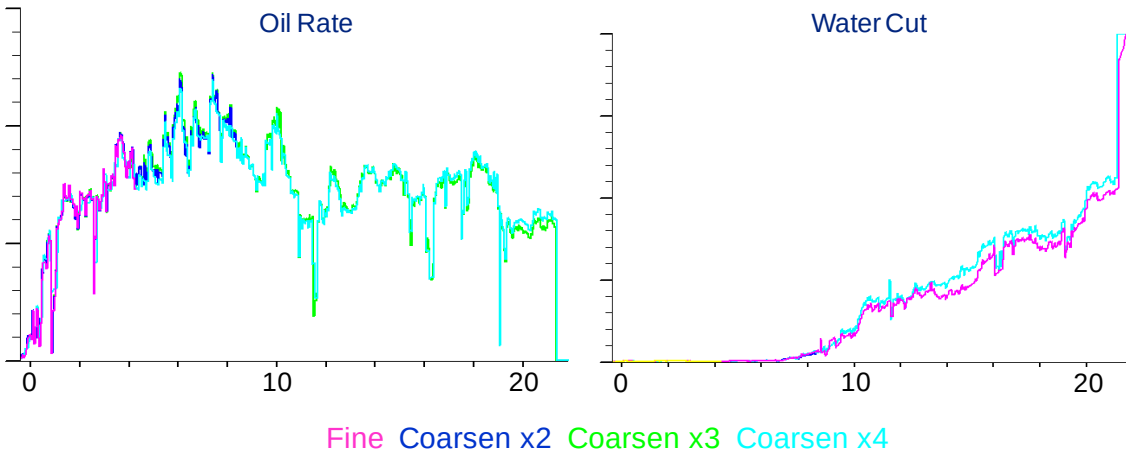


**Fig. 2.1 - Field oil production rate and field water-cut comparison for different coarsening levels (X axis is in years).**

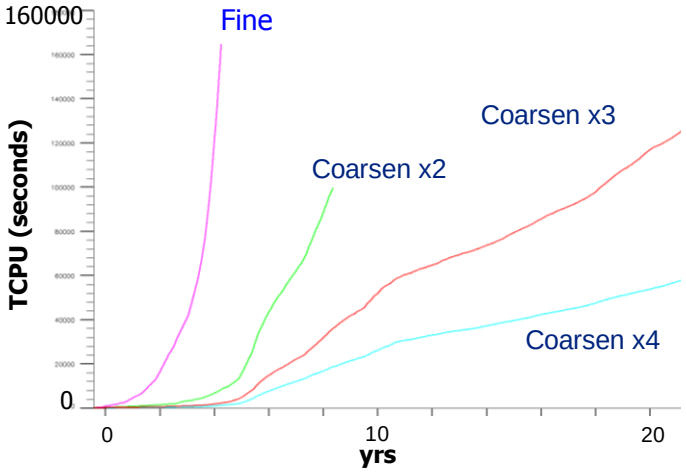


**Fig. 2.2 - Runtime comparison for different coarsening levels (X axis is in years, Y axis is in seconds).**

### 2.2.2 Proposed Workflow

A commercial finite-volume simulator is deployed for full field simulation of a multimillion grid-cell carbonate reservoir with decades of production history. That implies taking into account full physics of hydrocarbon production as well as active reservoir management involving work-over, infill drilling, rate changes and well type changes from producer to injector. The phase fluxes from this finite-volume simulator are used for tracing streamlines. The proposed workflow is as follows:

1. **Vertical upscaling of geomodel properties and simulation model construction.** Starting point for the simulation is always the vertically upscaled and upgridded high resolution geomodel. An 'optimal' upgridding strategy based on bias-variance trade-off criterion (King et al., 2004) is used.
2. **History matching simulation using simulator embedded coarsened dynamic model**. During simulation grid coarsening is applied resulting in significant speedup of simulation runs. The simulator automatically determines coarsened static properties (pore-volume, permeability etc.) and dynamic properties

(transmissibility). Areal coarsening, i.e., reduction in cells along X and Y direction leads to quadratic reduction in active cells compared to linear reduction in vertical coarsening. Details about the simulator implementation are given in **Appendix A**.

3. **Coarse scale fluxes.** Oil and water fluxes obtained for the coarsened cell are saved for non-coarsened, fine scale flux reconstruction and streamline tracing.
4. **Conducting phase flux reconstruction on non-coarsened, fine scale**. This step is conducted to 'back-allocate' coarse scale fluxes to the underlying non-coarsened, fine scale grid based on recalculated non-coarsened transmissibilities. This is explained in detail in section **2.2.3**.
5. **Streamlines tracing and time of flight computations on non-coarsened grid** using these newly reconstructed 'fine scale' phase fluxes.
6. **Quantification of mismatch** between observed and computed well water-cut in terms of generalized travel time (Wu et al., 2002) for all wells or preselected wells.
7. **Calculation of an augmented objective function (section 2.2.6)** to minimize the changes to the prior geological model and to allow for smooth and large changes because production data has low resolution (Cheng et al., 2004).
8. **Computation of streamline based analytical sensitivities** of production response (water-cut) to reservoir parameter (permeability) described by He et al., (2002).
9. **Inversion** is carried out using these sensitivities on the non-coarsened permeability and the new updated non-coarsened permeability is used for next iteration. Until a prescribed convergence criteria is met, the loop restarts at item 2 of this list.

The inversion is thus conducted on the non-coarsened grid, while the forward simulation model uses the coarsened grid. While solving for a relatively inexpensive coarse model, the calibration takes into account the full non-coarsened resolution.

Upscaling is not required and the degree of coarsening can be adjusted during the matching process. No vertical coarsening is conducted as models were already upgridded and upscaled vertically. This could be a potential additional step for future workflows.

The initial areal resolution of geomodel was kept unchanged during history matching. Model was only coarsened areally to get a quadratic reduction in number of active cells which is shown for the example in **Fig. 2.3**. After satisfactory production match the updated non-coarsened permeability field can be used for forecasting and production optimization. As inversion is conducted at non-coarsened scale updated permeability field is obtained at non-coarsened scale. This is presumed to aid in infill well planning and EOR studies since the coarsening can be deactivated once the history matching has been completed.

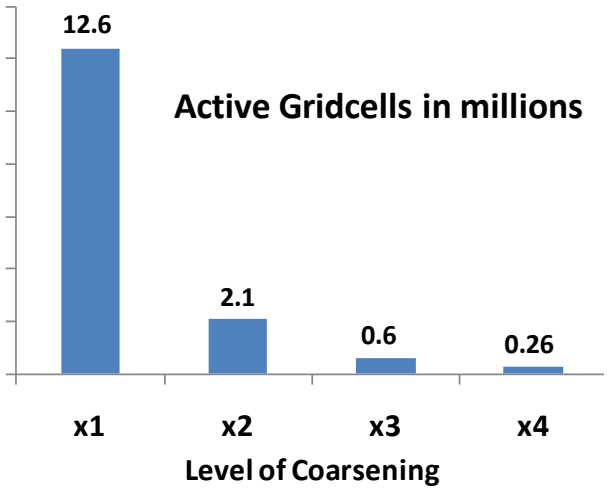


**Fig. 2.3 - Number of active grid cells in millions for different level of coarsening.**

### 2.2.3 Flux Reconstruction

Streamline tracing requires phase fluxes for each grid block whereby oil and water phase fluxes are particularly required for the proposed application. The phase flux reconstruction at non-coarsened scale uses coarsened phase fluxes and the reconstruction of the coarse fluxes to the original fine grid is thus an important component of the workflow.

Flux reconstruction during downscaling has been studied previously by several authors. Mahani et al., (2007) used weighted transmissibility of non coarsened cells to distribute fluxes in the coarsened cell. They have used these fluxes to calculate pressure and saturation in non-coarsened cells based on coarsened fluxes obtained during coarse grid simulation. This weighted transmissibility approach is consistent with upscaling transmissibilities. Transmissibilities are upscaled by taking harmonic average of fine scale transmissibilities (Durlofsky, L.J, 1996). When downscaling the coarsened fluxes there is a need to redistribute these fluxes by inverting the upscaled transmissibility. This approach is followed which is consistent with the coarsening technique implemented in the commercial simulator.

Consider a simple diagram having two cells (A & B) in **Fig. 2.4.** These two cells are amalgamated into a coarse cell. The idea is to split the coarse flux into cell A and B based on transmissibilities in cell A & B. The coarse flux is divided based on the ratio of transmissibilities of cell A & B assuming no cross-flow between cells A & B. No-flow boundary is assumed to be surrounding the amalgamation.

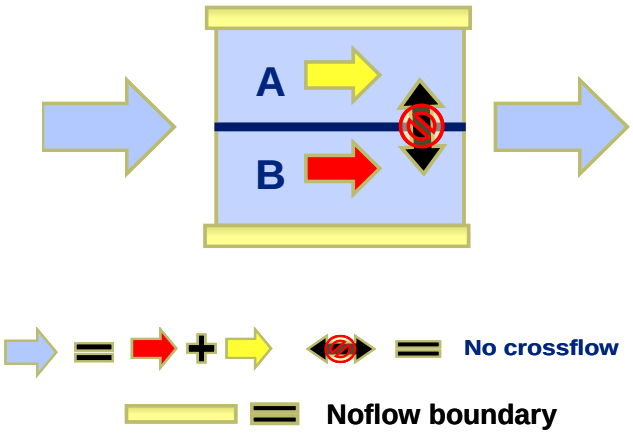


**Fig. 2.4 - Schematic for explanation of non-coarsened flux reconstruction (red and yellow) using coarsened flux (light blue) for an amalgamation C, consisting of cells A & B.**

The coarse flux or amalgamated cell flux (shown by light blue arrow) is termed a $Flux_C$. Transmissibilities of cell A & B are termed as $Trans_A$ and $Trans_B$. Flux in cell A (shown by yellow arrow) is termed as $Flux_A$ and flux in cell B (shown by red arrow) is termed as $Flux_B$. The fluxes are individual phase fluxes. Following the Darcy's law for a constant pressure gradient $\Delta P / \Delta L$ and constant phase viscosity $\mu$, the fluxes for cells A and B can be written as follows,

$$Flux_A = Trans_A \cdot \frac{\Delta P}{\mu \cdot \Delta L} \quad \text{.....(2.1)}$$

$$Flux_B = Trans_B \cdot \frac{\Delta P}{\mu \cdot \Delta L} \quad \text{.....(2.2)}$$

Considering the conservation of fluxes,

$$Flux_C = Flux_A + Flux_B \quad \text{.....(2.3)}$$

Combining the three equations yields the flux for the coarse cell,

$$Flux_C = \left(Trans_A + Trans_B\right) \cdot \frac{\Delta P}{\mu \cdot \Delta L} \quad \text{.....} \quad (2.4)$$

Similarly $Flux_A$ and $Flux_B$ can be defined in terms of $Flux_C$ assuming constant $\Delta P / \mu \cdot \Delta L$ as follows,

$$Flux_A = \frac{Trans_A}{Trans_A + Trans_B} \cdot Flux_C \quad \text{.....} \quad (2.5)$$

$$Flux_B = \frac{Trans_B}{Trans_A + Trans_B} \cdot Flux_C \quad \text{.....} \quad (2.6)$$

### 2.2.4 Flux Reconstruction at Non-Coarsened Scale from Coarsened Scale in X Direction

Based on the above formulation oil and water phase fluxes are reconstructed at non-coarsened scale from coarsened scale. The schematic for flux reconstruction, i.e., conversion of coarsened flux in amalgamation to non-coarsened fluxes in X direction is shown in **Fig. 2.5**. The assumptions for flux reconstruction are as follows:

- Same flux in non-coarsened cells with same direction index (*J1*, *J2* etc), along direction of coarsened flux (X direction) considered for reconstruction as shown in **Fig. 2.5**,
- No cross-flow of flux in other directions different from direction of coarsened flux (X direction) considered for reconstruction as shown in **Fig. 2.5**,
- No flow boundary at boundary of amalgamated cell in coarsened flux direction (X direction) considered for reconstruction,
- Constant phase viscosity in the amalgamated cell so that it is same in the non-coarsened cells.

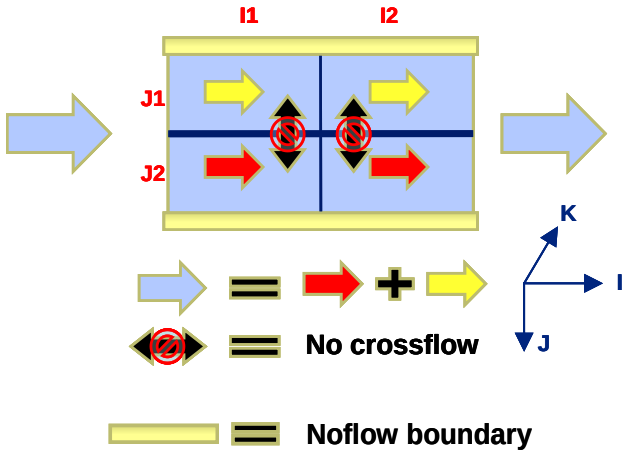


**Fig. 2.5 - Schematic of non-coarsened flux reconstruction (red and yellow) using coarsened flux (light blue) for 2x2 coarsening in X direction.**

The coarsened cell transmissibility can be derived by taking harmonic average of *TransX* along X direction for a particular J index *J1* and particular K index *K1*, at non-coarsened scale (*n*):

$$TransX_{K1,J1} = \frac{I2 - I1 + 1}{\sum_{I}\left(\frac{1}{TransX_n}\right)} \quad \text{.....(2.7)}$$

This harmonic average transmissibility $TransX_{K1,J1}$ along the X direction is used to redistribute phase fluxes in X direction in the non-coarsened grid. X direction phase fluxes for non-coarsened cells along a particular J index *J1* and K index *K1* are calculated as follows,

$$FLOOILI_{K1,J1} = \frac{TransX_{K1,J1}}{\sum_{K}\sum_{J} TransX_{K,J}} \bullet FLOOILI_C \quad \text{.....(2.8)}$$

$$FLOWATI_{K1,J1} = \frac{TransX_{K1,J1}}{\sum_{K}\sum_{J} TransX_{K,J}} \bullet FLOWATI_C \quad \text{.....(2.9)}$$

$$FLOGASI_{K1,J1} = \frac{TransX_{K1,J1}}{\sum_K \sum_J TransX_{K,J}} \bullet FLOGASI_C \quad \text{.....(2.10)}$$

Similarly for other cells with $n^{th}$ J Index and $n^{th}$ K Index are calculated as follows,

$$FLOOILI_{Kn,Jn} = \frac{TransX_{Kn,Jn}}{\sum_K \sum_J TransX_{K,J}} \bullet FLOOILI_C \quad \text{..... (2.11)}$$

$$FLOWATI_{Kn,Jn} = \frac{TransX_{Kn,Jn}}{\sum_K \sum_J TransX_{K,J}} \bullet FLOWATI_C \quad \text{..... (2.12)}$$

$$FLOGASI_{Kn,Jn} = \frac{TransX_{Kn,Jn}}{\sum_K \sum_J TransX_{K,J}} \bullet FLOGASI_C \quad \text{..... (2.13)}$$

The details for flux reconstruction in Y and Z direction are given in **Appendix A**. The three combined represent the basis for the streamline tracing and inversion using grid coarsening.

### 2.2.5 Workflow Implementation

The new streamline based permeability inversion workflow with grid coarsening is illustrated in **Fig. 2.6**. The components of the workflow shown in the red boxes are the new components added to the previous streamline based GTTI inversion workflow (Cheng et al., 2004). This previous GTTI inversion workflow can be found in publications by Cheng et al., (2004); Oyerinde et al., (2009) and Rey et al., (2009).

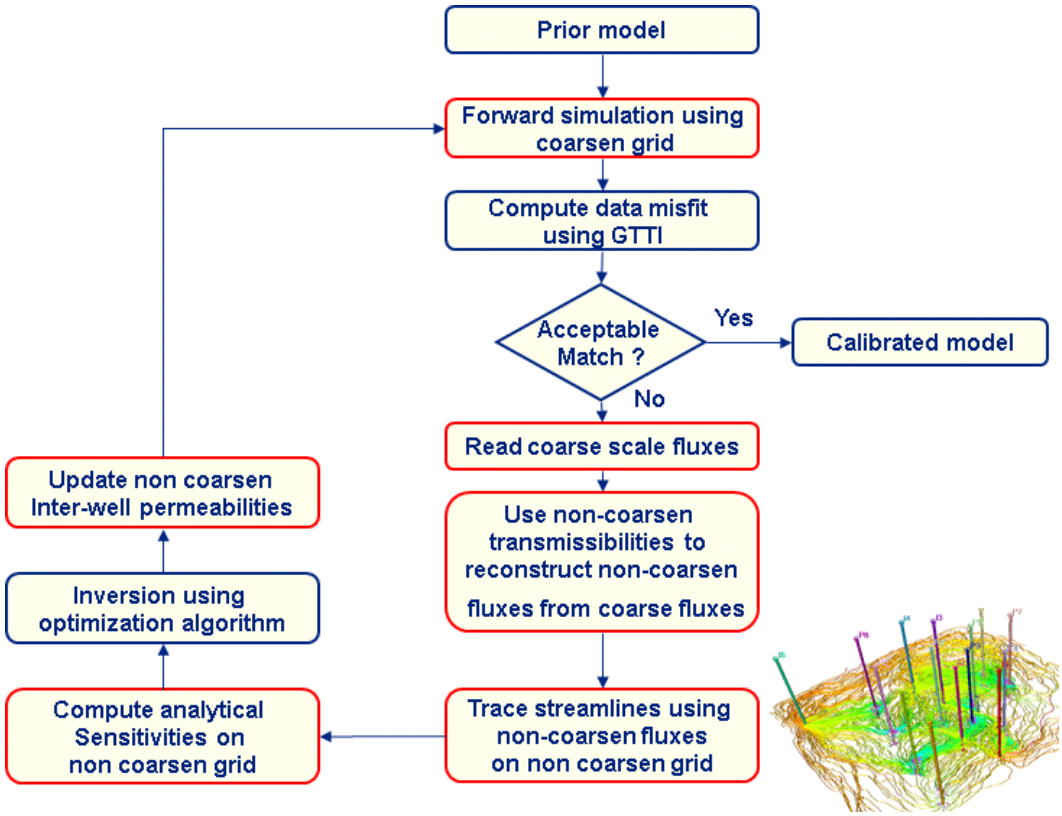


**Fig. 2.6 - Schematic of streamline based permeability inversion workflow using grid coarsening during simulation. Red box highlights proposed things added to original workflow.**

The individual steps required for the new streamline based inversion with grid coarsening during simulation are as follows:

1. Prior or starting model is simulated using grid coarsening which gives drastic reduction in runtime for multi-million grid cells with hundreds of well and decades long production history.
2. Well by well water-cut data misfit is calculated using Generalized Travel Time (GTTI), (Wu et al., 2002). An augmented objective function (**section 2.2.6**) is also calculated.

3. Coarsened phase (Oil and water) fluxes are read from commercial simulator's restart files. Non-coarsened porosity, permeability and transmissibilities are read from commercial simulator's property file.
4. Non-coarsened phase fluxes are reconstructed from coarsened fluxes using non-coarsened transmissibilities. The flux reconstruction is explained in detail in **sections 2.2.3** and **2.2.4**. It should be noted that only water and oil phases are reconstructed for the illustrated applications (**section 2.3**).
5. Streamlines are traced and time of flight computed on non-coarsened grid using non-coarsened summed oil and water phase flux. This is necessary as the well by well water-cut inversion has to carried out on non-coarsened grid.
6. Computation of streamline based analytical sensitivities of well production responses (water-cut) to fine-scale reservoir parameters (permeability) described by He et al., (2002).
7. Permeability inversion is carried out on a non-coarsened grid using a conjugate gradient minimization algorithm to minimize the augmented objective function (Cheng et al., 2004).
8. The new updated non-coarsened permeability is used for next iteration. As the inversion is iterative the entire process described above is repeated until an acceptable well by well water-cut match is obtained. The entire workflow is fully automated and requires little user intervention.

### 2.2.6 Production Data Integration Philosophy

The production data philosophy followed in the proposed approach is as follows,

1) Given a geologic model, match the production history within specified tolerance
2) Keep changes to the geologic model to a minimum
3) Allow for smooth and large-scale changes because production data has low resolution

This philosophy is implemented using an augmented objective function described in the **Eq. 2.14,**

$$\|\delta\mathbf{d} - \mathbf{S}\delta\mathbf{R}\| + \beta_1\|\delta\mathbf{R}\| + \beta_2\|\mathbf{L}\delta\mathbf{R}\| \quad \text{.....(2.14)}$$

In the **Eq. 2.14**, ***δR*** correspond to the change in the reservoir property, ***δd*** correspond to the GTTI water-cut misfit calculated over all the producers and ***L*** is a second spatial difference operator that is a measure of roughness and is analogous to imposing a prior variogram or covariance constraint. The first term in the **Eq. 2.14** ensures that the difference between the observed and calculated production response is minimized. The second term, called a "norm constraint", penalizes deviations of updated model from the initial model. This helps in preserving geologic realism because the initial or prior model already incorporates available geologic and static information related to the reservoir. Finally, the third term, a roughness penalty, simply recognizes the fact that production data are an integrated response and are thus, best suited to resolve large-scale structures rather than small-scale property variations. $\boldsymbol{\beta_1}$ and $\boldsymbol{\beta_2}$ are weights on the norm term (second term) and roughness term (third term) respectively. The influence of these terms can be controlled by using these weights.

## 2.3 Applications

The workflow will be first demonstrated on coarsened model of the Brugge field and is compared with results from non-coarsened model, in **section 2.3.1**. This field is discussed in detail in **section 3.5.2.1** (Chapter-3). In addition the proposed workflow was also applied to a supergiant offshore oilfield in **section 2.3.2**.

### 2.3.1 Demonstrative Example: Brugge Field

The comparison is done for the non-coarsened GTTI inversion with 2x2 areal coarsen GTTI inversion. The 2x2 coarsen inversion will be using the new proposed flux reconstruction method for streamline tracing. The field oil rate and field total oil production are plotted for non-coarsen (blue line) and coarsen 2x2 case (pink dot) in **Fig.**

**2.7**. A very little difference is observed between the two cases. But there is considerable difference in runtime between two cases. Non-coarsen case took 55 seconds while 2x2 coarsen case took 18 seconds. This extra savings in runtime results in large savings in entire GTTI inversion if large number of iterations is required.

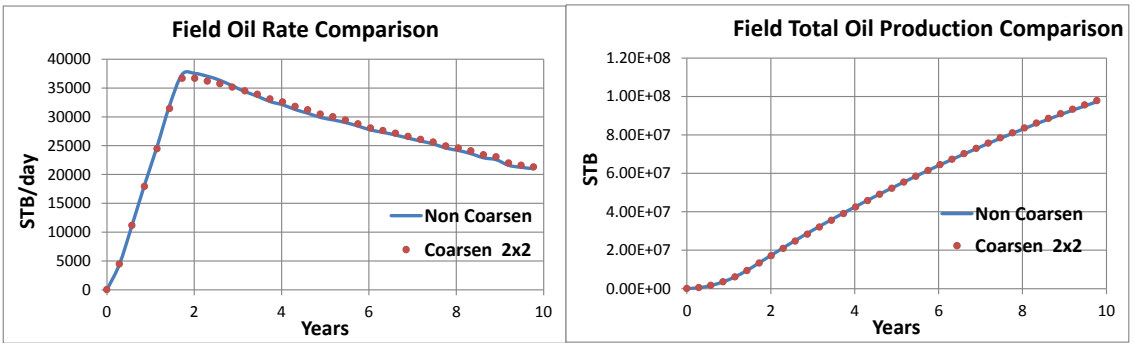


**Fig. 2.7 - Comparison of field oil rate (left) and field total oil production (right) for non-coarsen and coarsen 2x2 Brugge field case.**

**Fig. 2.8** shows streamlines traced from producer plotted for 2x2 coarsened grid (left) using the proposed flux reconstruction method for streamline tracing. This can be compared to streamlines traced for non-coarsened grid (right) using conventional streamline tracing (Jimenez et al., 2010). Considerable similarity is observed between spatial distribution of streamlines and time of flight for both cases.

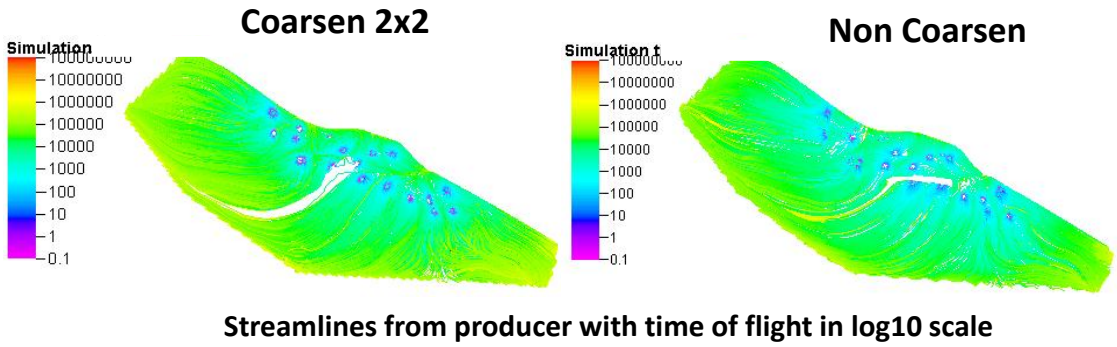


**Fig. 2.8 - Streamlines from producer are plotted for coarsened grid 2x2 (left) and non-coarsened grid (right). Time of flight (log10 days) measured from producers is also plotted on streamlines.**

**Fig. 2.9** shows plot of GTTI sensitivities for 2x2 coarsening (left) and non-coarsening (right) for the Brugge field.

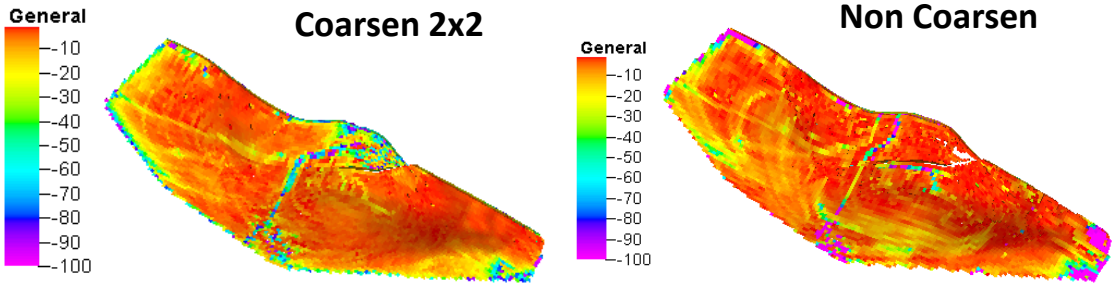


**Fig. 2.9 - GTTI sensitivities plotted for coarsened grid 2x2 (left) and non-coarsened grid (right).**

**Fig. 2.10** illustrates comparison of histogram of GTTI sensitivities for 2x2 coarsening and non-coarsening for same grid. Overall distribution is comparable but there are some differences for higher values of sensitivities.

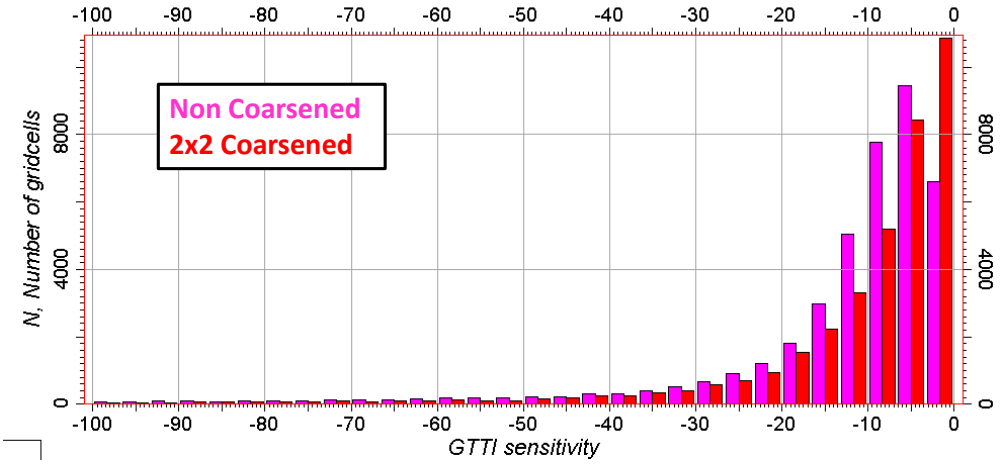


**Fig. 2.10 - Comparison of histogram of GTTI sensitivities for coarsened grid 2x2 (red) and non-coarsened grid (pink).**

The effect of this difference can be observed in the travel time misfit performance for both cases as illustrated in **Fig. 2.11**. Although reasonable reduction in travel time misfit is seen for 2x2 coarsen case as compared to non-coarsen case, there is slower convergence compared to non-coarsen case.

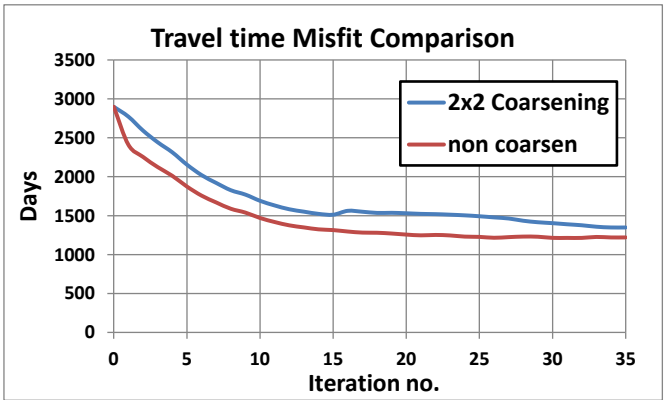


**Fig. 2.11 - Comparison of travel time misfit reduction for coarsened grid 2x2 (blue) and non-coarsened grid (pink).**

In addition comparison of distribution of final (after convergence) inverted permeabilities using non-coarsened and coarsened inversion for Brugge is illustrated in **Fig. 2.12**. Overall the distributions are quite similar. Sensitivities reconstructed based on the coarse scale simulation are approximate but the results show that they are adequate for obtaining downward direction during optimization. Coarsening case might require more iterations but this will be compensated by reduction in simulation runtimes because of coarsening.

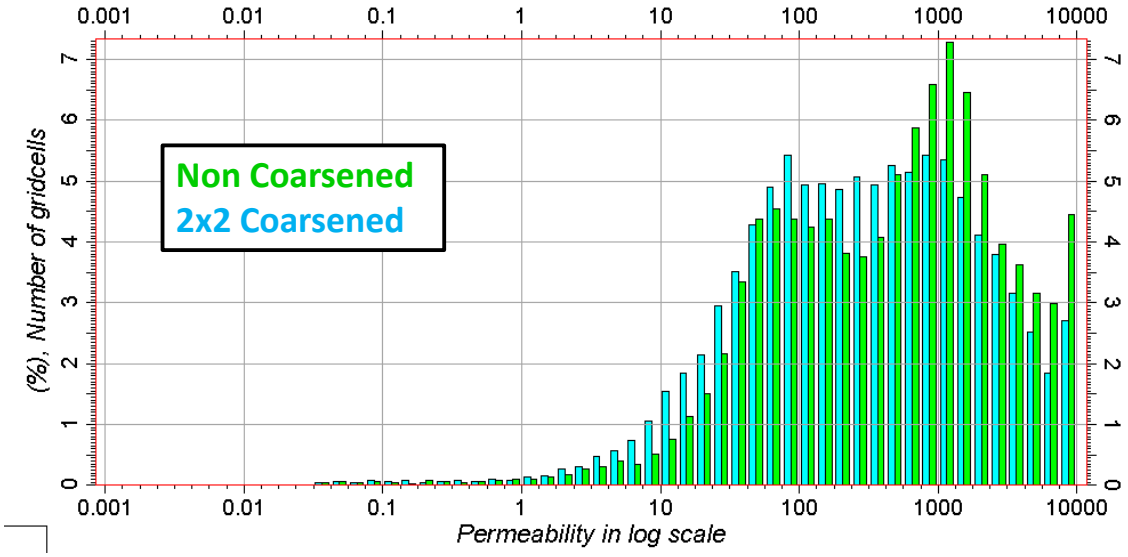


**Fig. 2.12 - Comparison of histogram of final inverted permeability for coarsened grid 2x2 (blue) and non-coarsened grid (green).**

In addition the watercut history match for two sample wells P15 and P17 is illustrated in **Fig. 2.13**. It can be observed that watercut match for 2x2 coarsened inversion is comparable to that of non-coarsen inversion.

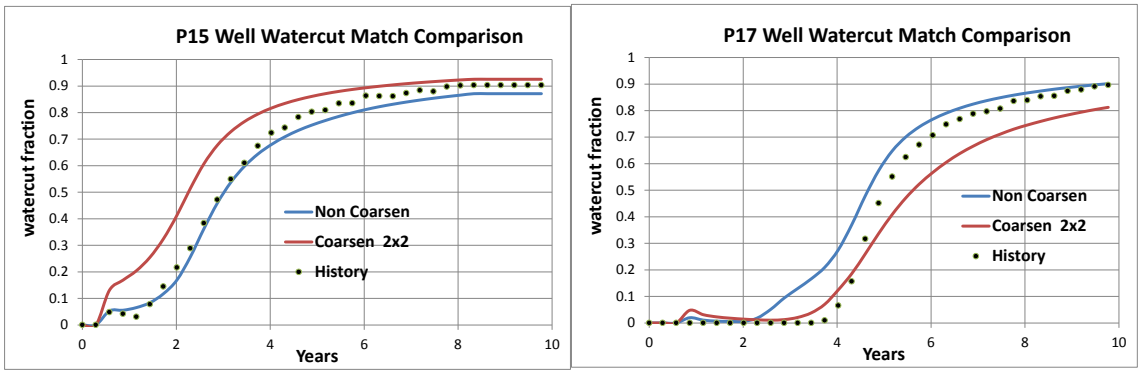


**Fig. 2.13 - Comparison of well watercut history match for non-coarsen and coarsen 2x2 Brugge field case for wells P15 (left) and P17 (right).**

### 2.3.2 Large Offshore Carbonate Field Application

The proposed GTTI using flux reconstruction is applied to the multi-million grid-cell field application. This field is a large and heterogeneous multilayered offshore carbonate reservoir with 30 years of production history. The field was developed by a very large number of wells, including horizontal and multi-lateral wells. A large scale field wide water injection program is ongoing.

Highly detailed static models were constructed for the field, with the ultimate aim to support both effective reservoir management but also to allow for better well placement in order to target remaining oil pockets. Due to the model size and the resulting runtimes, it became clear that certain workflows are not practical in a field of that size, for example experimental design or any assisted history matching techniques. In the fine scale areal grid resolution, initial models had significant convergence problems in the linear solver (and to a lesser degree in the nonlinear solver), partially caused by a significant amount of areal heterogeneity in the reservoir. **Fig. 2.2** shows the nonlinear behavior with exponentially increasing runtimes. This challenge could be effectively overcome by introducing areal coarsening.

With the significant uncertainties in permeabilities in mind, streamline inversion offers a sensible tool to adjust permeabilities according to the observed water production behavior field wide.

The streamline plots for a selected section with and without grid coarsening are shown in **Fig. 2.14.** Time of flight from the producer is plotted on the streamlines. Low (violet) values of time of flight indicate well locations. It can be seen that streamline patterns for coarsened grid are reasonably similar to non-coarsened grid. The little differences arises due to difference in non-neighbor connection (NNC) fluxes as some of the original NNC's are deleted and new NNC's are created during grid coarsening in commercial reservoir simulator. A smoothing of well water-cut using equal intervals of cumulative oil production for that well is also used. This smoothing method for streamline based inversion has shown to be effective for a field case having active reservoir management (Rey et al., 2009).

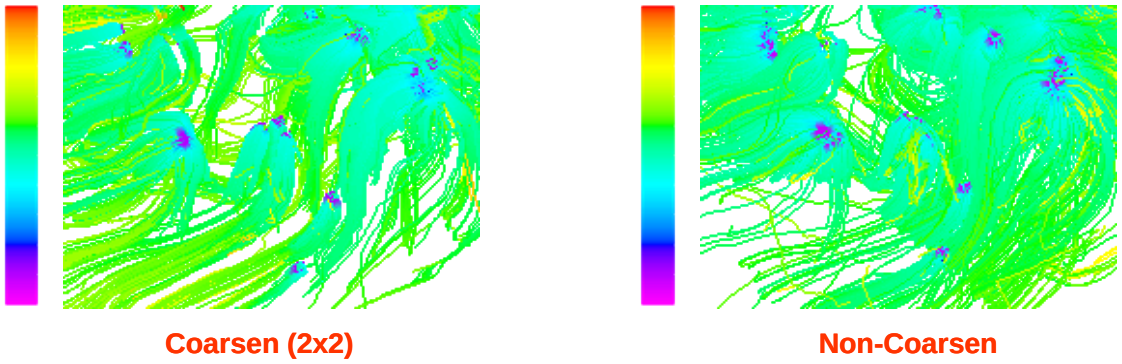


**Fig. 2.14 – Comparison of streamlines for coarsened grid 2x2 (left) and non-coarsened grid (right). Time of flight from producers is plotted. Low values (violet) indicate wells.**

The travel time misfit performance, i.e., sum of misfit between observed and simulated water break through for all wells is shown in **Fig. 2.15**. The misfit has been normalized between 0 and 1. A considerable reduction is seen in travel time misfit at end of 10 iterations.

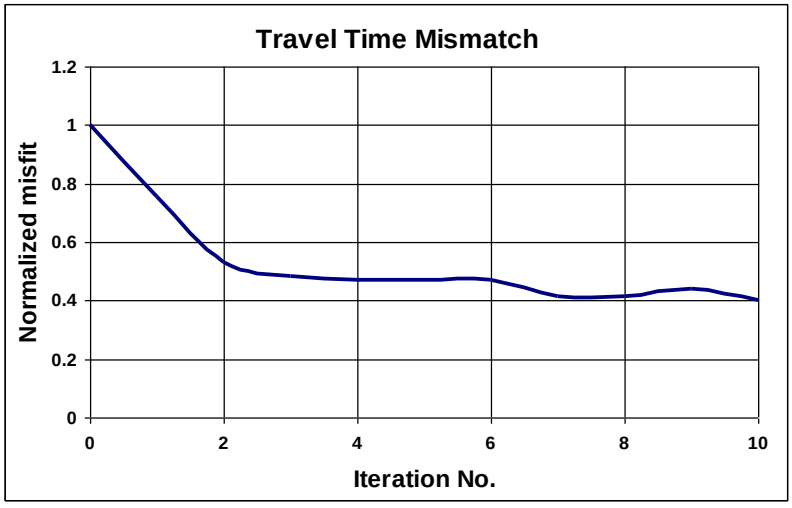


**Fig. 2.15 - Travel time misfit performance combined for all the wells.**

Similarly normalized amplitude misfit performance, i.e., sum of misfit between observed and simulated water cut, is shown in **Fig. 2.16**. A considerable reduction in amplitude misfit is also achieved at end of 10 iterations. The computational effort for running such numbers of iterations is manageable, even for the largest models which took 24 hours on a high performance cluster for the entire history matching.

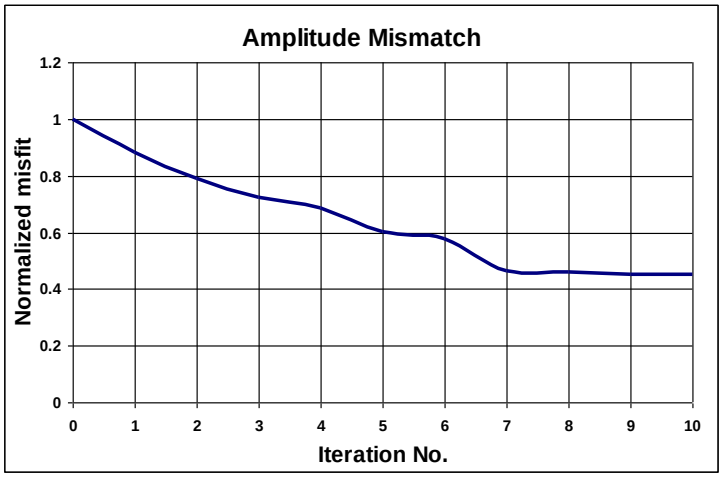


**Fig. 2.16 - Amplitude misfit performance combined for all the wells.**

**Fig. 2.17** shows the field production results. Black dots are historical production data. Orange is the starting model and blue is the model using streamline based permeability inversion with grid coarsening. Although wells were on historical liquid rate control it was initially difficult to match field liquid rate due to lower connectivity in the field. After the streamline inversion, the field liquid rate matches satisfactorily. Also, field oil rates and field water cut improved considerably after the inversion.

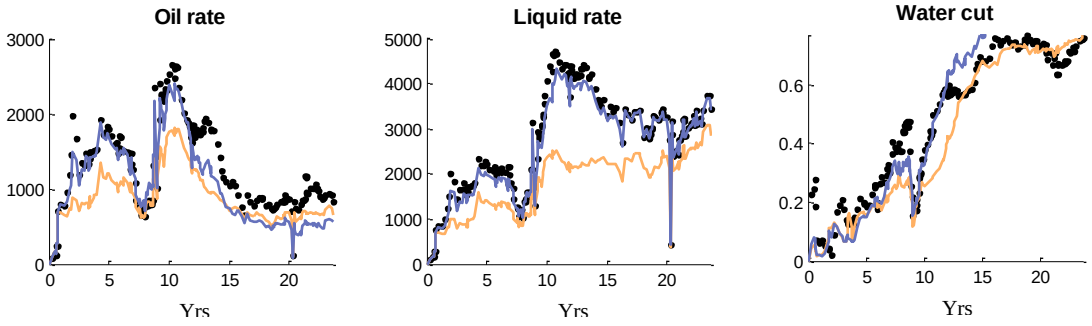


**Fig. 2.17 - Impact on field level (black... history, orange...initial model, blue...after streamline inversion).**

**Fig. 2.18** shows the results for one of the production platforms. Remarkable improvement in platform water-cut can be observed. A better match for platform liquid and oil rate is also observed.

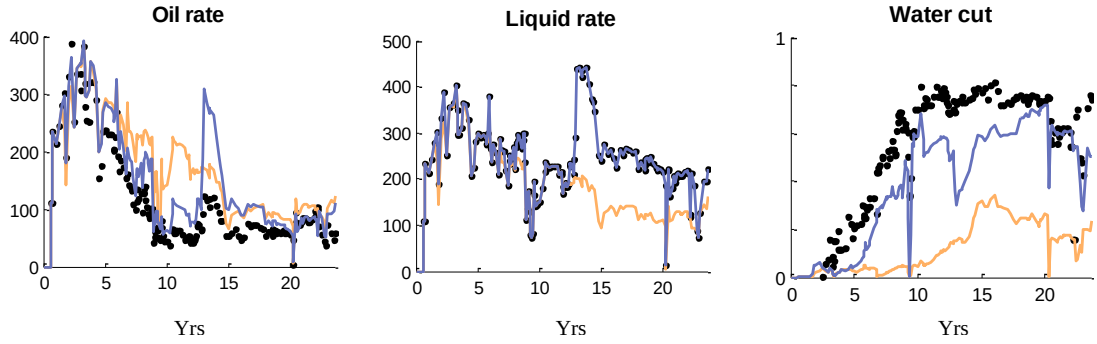


**Fig. 2.18 - Impact on platform level (black... history, orange...initial model, blue...after streamline inversion).**

**Fig. 2.19** repeats the same plots for one of the wells. Again good improvements in well water-cut and oil rate are achieved. While not all platforms or wells experience

such dramatic improvement in match quality, none of them showed deterioration when compared to the initial model.

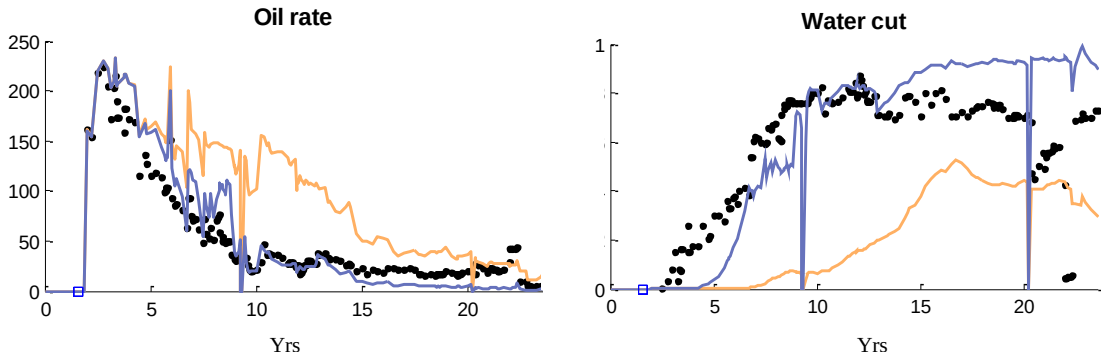


**Fig. 2.19 - Impact on well level (black... history, orange...initial model, blue...after streamline inversion).**

For individual well matched, the changes were solely achieved by changing interwell permeabilities. As mentioned earlier, a manual history matching was carried out for matching at the regional scale, for example pressure. **Fig. 2.20** compares the initial permeability field (left) and the calibrated permeability field (right). Changes are naturally found by and large between the wells where most of the information for the inversion is originating. There are overall minimum changes in the field, major changes are predominantly occurring in the best reservoir facies which also have the highest uncertainty in spatial distribution of permeability.

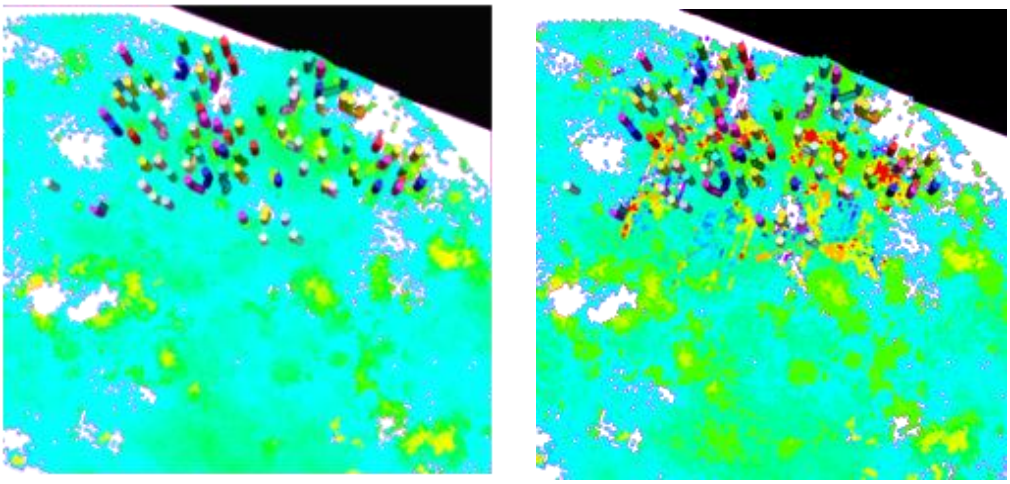

**Fig. 2.20 - Initial permeability distribution (left) and inverted permeability (right). Red color implies high values.**

**Fig. 2.21** contrasts connectivity between water injection platform A and production platform B in the initial model with the one in the inverted model. Enhanced connectivity was expected by production engineers between these platforms based on their experience in the field and from field surveillance data. This improved connectivity can be found in the inverted model as well.

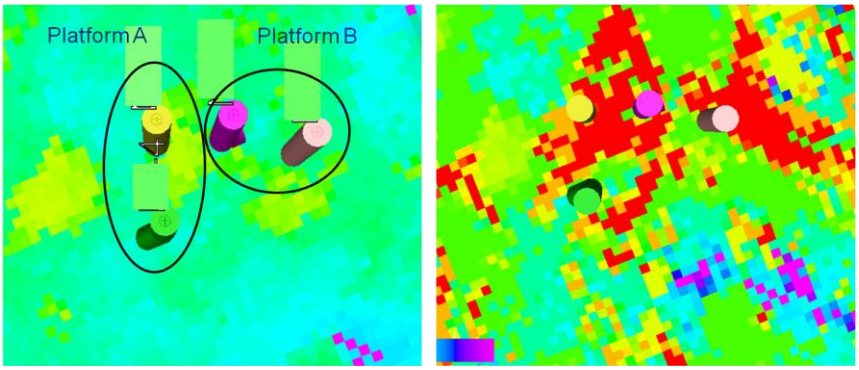


**Fig. 2.21 - Comparison of connectivity between water injection platform A and production platform B in initial model (left) and inverted model (right). Expected improved connectivity is seen in the inverted model.**

The impact of this improved connectivity is shown on one of the wells in production platform B in **Fig. 2.22**. Although the well is on historical liquid rate control the initial model could not match it due to lack of support from water injection platform A. Similarly historical oil rate has been poorly matched in the initial model. But after inversion there is sufficient support from water injection platform A. This can be verified by satisfactorily matched liquid and oil rate in that well in the inverted model. A better match for well water-cut breakthrough is also observed in the inverted model. The high value of water-cut was considered to be the result of erroneous completion intervals.

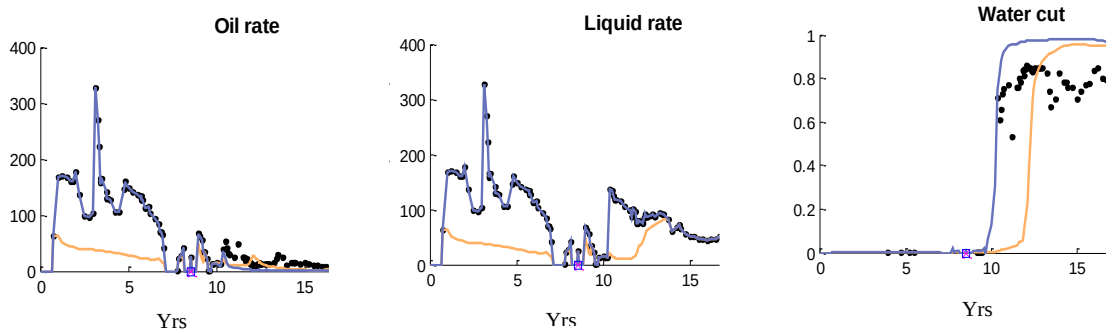


**Fig. 2.22 - Impact of improved connectivity on a well in platform B (black... history, orange...initial model, blue...after streamline inversion).**

## 2.4 Summary and Conclusions

In this chapter a pragmatic application of streamline based generalized travel time inversion is presented using grid coarsening during simulation. Streamlines traced by reconstructing fluxes from the grid coarsened simulation model of this field give

comparable results when compared to a non-coarsened simulation model. The proposed approach has been demonstrated on a synthetic field. Generalized travel time inversion (GTTI) using grid coarsening on the coarsened model was compared with non-coarsened model. The distribution of GTTI sensitivities is comparable for coarsened model using flux reconstruction with non-coarsened model. The history matched watercut results were quite comparable although coarsened inversion using the proposed method might take more iterations (considerably less time than non-coarsened models) than non-coarsened inversion.

The proposed approach was successfully applied to streamline based watercut inversion of a multimillion cell carbonate field with hundreds of wells and decades of production history. Remarkable improvement is seen in the history match of production responses like liquid rate, oil rate and water-cut at the field, platform and well level. It should be noted that there were minimum changes done in the model during inversion. Expected improved connectivity between platforms was seen in the inverted model which was not present in the initial model. This improved connectivity was verified by matched production history of one of the wells.

Future research can be conducted, on using the coarsened fluxes obtained during coarsened simulation directly for streamline tracing leading to better streamline tracing than the proposed approach. Also a dual scale approach can be easily be implemented whereby inversion is carried out using the proposed approach till a considerable reduction in well by well watercut mismatch is obtained and then for further reduction in mismatch original workflow can be applied with non-coarsened model. This will lead to considerable savings in computational time for large simulation models with long runtimes.

# CHAPTER III

# BOTTOM-HOLE PRESSURE DATA INTEGRATION FOR $CO_2$ SEQUESTRATION IN DEEP SALINE AQUIFERS

## 3.1 Introduction

Geological storage of $CO_2$ (carbon sequestration) has been carried out in several locations around the world (Benson, 2006) as a method to avoid atmospheric emission of $CO_2$. The International Government Panel on Climate Change (Hollaway et al., 2001) recommended "modeling the injection of $CO_2$ into storage reservoir and future behavior, monitoring the storage system and using the monitoring results to validate and update the model". Carbon sequestration in brine aquifers faces many different challenges in both engineering and economical aspects. There is considerable uncertainty associated with the injection of $CO_2$ in deep aquifers. Engineering problems such as the leakage of $CO_2$ can compromise the integrity of fresh waters, ecosystems and the health of populations exposed to high concentration of $CO_2$ (Ha-Duong, 2003; Gasda et al., 2004). There are also economic liabilities associated with legal disputes and fines imposed by regulatory agencies. These challenges have spurred considerable research and development efforts in $CO_2$ capture and storage technologies along with monitoring, verification and accounting of $CO_2$ sequestration.

Various methods have been reported in the literature for monitoring $CO_2$ sequestration. Benson (2006) has given a summary of these methods. The author has also pointed out the advantages and limitations of each method. Inversion of the seismic responses have been used for quantitative interpretation of the movement of the $CO_2$ plume in the subsurface, specifically in saline aquifers (Chadwick et al., 2005, Chadwick et al., 2009; Delépine et al., 2009). All the researchers have showed potential benefits of integrating seismic data in forecasting the performance of $CO_2$ sequestration.

In addition to the seismic methods pressure transient analysis using bottom-hole pressure data from injection and observation wells is the most widely used monitoring

method. Utilizing pressure data either by conducting pressure transient test or using well bottom-hole pressure data is an inexpensive way to monitor $CO_2$ sequestration. Bottom hole pressure data along with rate data is normally acquired as a routine procedure during $CO_2$ injection. Spatial data like porosity and permeability influences pressure behavior in the reservoir. So pressure transients as well as injection / observation well pressure data can be used to infer porosity and permeability. Pressure data can also be used to validate and calibrate geological and simulation models used for planning and forecasting of $CO_2$ sequestration projects. Many researchers and companies have used pressure transient data and bottom hole pressure data for validating and calibrating single or multiple simulation models.

In this chapter use of well bottom-hole pressure data for calibration of high resolution compositional simulation model during $CO_2$ sequestration is illustrated. Pressure data from injection well as well as observation wells is utilized for model calibration. A novel approach is presented to integrate the available pressure data into the simulation model, thus improving forecasting capability of the simulation model. The first step consists of volume calibration using information from pseudo-steady state flow regime of the injection well. This is followed by the bottom-hole pressure inversion of zeroth-order (mean) frequency of the pressure of the injection well. This approach is based on a low-frequency asymptotic solution to the equation governing transient head variations (Vasco et al., 2006). This is followed by transient pressure arrival time inversion of bottom-hole pressure at the observation wells (Vasco et al., 2000, Kulkarni et al., 2001). This inversion is based on sensitivities derived using the high frequency asymptotic solution (sharp pressure front) for the transient flow. It can be noted that both the methods are complimentary to each other. As a last step, a gradient based optimization technique is used to modify global multiplier of permeability (X direction). This optimization uses Levenberg-Marquardt algorithm.

The organization of this chapter is as follows. First, a novel approach is proposed for integrating bottom-hole pressure data of injection and observation wells in the simulation model. This is followed by the motivation for the proposed approach. Then the proposed approach is discussed in the detail. This is followed by demonstrating the utility of the proposed approach on 2-D and 3-D example applications. The bottom-hole pressure data used for history matching is generated using a reference 2-D and 3-D model respectively. These reference models are based on well log data.

### 3.2 Proposed Approach and Motivation

Goal of this study is to contribute to the development of bottom-hole pressure history matching workflow for $CO_2$ sequestration. Brief outline of the study is as follows,

1. A simulation model (2-D and 3-D) is setup with known properties using hard well data, for example, well logs. This model acts as a true\reference model.
2. Synthetic pressure data is generated at the injection well and observation wells following $CO_2$ injection for 11 months followed by shutoff for 1 month. This pressure data generated using reference model is used for history matching.
3. Model inversion is carried out using a prior model (2-D and 3-D), generated using limited information from the reference model. A novel approach is proposed which consists of volumetric calibration based on pseudo-steady state analysis followed by the bottom-hole pressure inversion of injection well. This step is followed by the peak pressure arrival time inversion of bottom-hole pressure at the observation wells. As a last step, a gradient optimization technique is used to modify global multiplier of permeability (X direction) and/or global anisotropy multiplier (PermX / PermY).

The proposed workflow for integration of bottom-hole pressure data during $CO_2$ sequestration is outlined in **Fig. 3.1.**

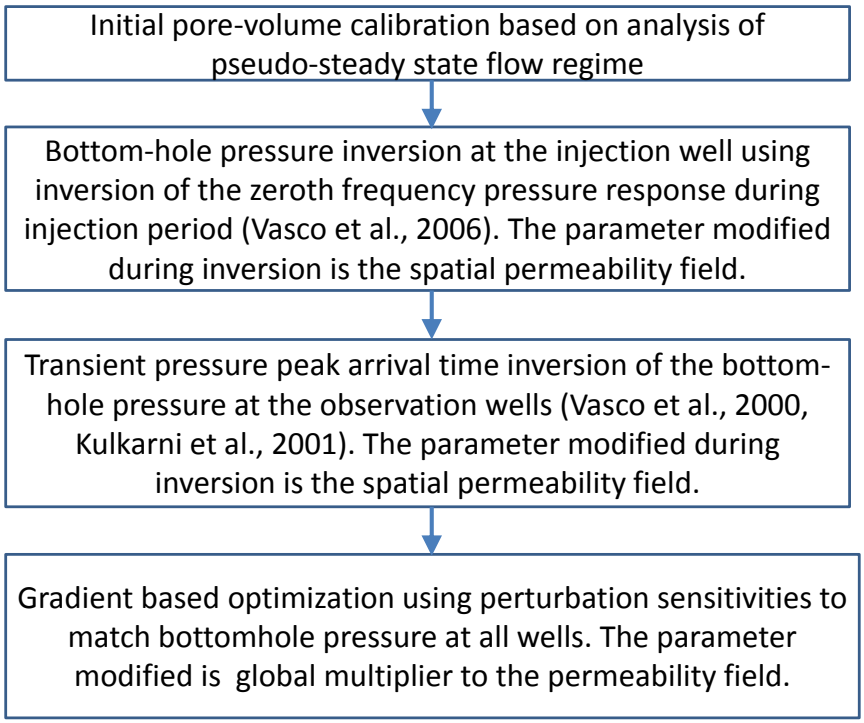


**Fig. 3.1 – Workflow for integration of bottom-hole pressure data during $CO_2$ sequestration.**

The pore-volume calibration is based on a pseudo-steady state analysis of injection well bottom-hole pressure. This is an elementary analysis helping to match the reservoir pressure due to storage effect. In addition, the injection well bottom-hole pressure also contains information pertaining to movement of the $CO_2$ plume. This information can be used to resolve permeability of the region covered by the $CO_2$ plume. The bottom-hole pressure data at the observation wells contains information related to the inter-well heterogeneities. The proposed workflow consists of first integrating bottom-hole pressure data of the injection well followed by integrating bottom-hole pressure data at the observations wells. The last step regarding gradient optimization is

used for fine tuning the bottom-hole pressure match by appropriately shifting the magnitude of the entire permeability field.

The elements of the proposed workflow (**Fig. 3.1**) are described in detail from **section 3.2.1 to 3.2.4**.

### 3.2.1 Pore-volume Calibration Based on Pseudo-steady State Analysis

The pseudo-steady regime denoted by a constant slope in the bottom-hole pressure of an injection well can be used to calculate pore-volume connected to the injection well. The connected pore-volume is calculated as follows,

$$V_P = \frac{-qB}{c_t\left(\frac{\partial P_{wf}}{\partial t}\right)} \quad \text{..... (3.1)}$$

Where $V_p$ is the connected pore-volume in reservoir barrels, $q$ is the injection rate in Stock Tank Barrel (STB) per day, $B$ is the formation volume factor of injected fluid, $c_t$ is the total compressibility ($psi^{-1}$) and $\frac{\partial P_{wf}}{\partial t}$ is the constant slope of the bottom-hole pressure in the pseudo-steady regime (straight line) in a pressure vs. time plot. This calculation is performed for reference and simulation bottom-hole pressure data of the injection well. Pore-volume of the simulation model is calibrated using the ratio of calculated pore-volumes for reference and simulation pressure data. This step is used to match the slope of the pseudo-steady state flow regime of the bottom-hole pressure of the injection well which is governed by the storage of the reservoir. The amplitude of the bottom-hole pressure will be governed by the permeability which will be modified in the subsequent steps (**section 3.2.2** to **section 3.2.4**).

### 3.2.2 Bottom-hole Pressure Inversion of $CO_2$ Injector

The low frequency asymptotic expansion for transient pressure variations, presented by Vasco et al., (2006) is used for the bottom-hole pressure (BHP) inversion of an injection well. This approach is based on a low-frequency asymptotic solution to the equation governing transient variation (**Eq. 3.2**). This approach is selected for BHP inversion because it is computationally efficient as the inverse modeling only requires the solution of two problems which are equivalent to the steady state equation (Vasco et al., 2006).

The transient pressure response in a heterogeneous medium as a function of space (**x**) and time (*t*) is described by the diffusivity equation, given as follows,

$$\phi(\mathbf{x})\mu c_t \frac{\partial P(\mathbf{x},t)}{\partial t} - \nabla \cdot \left(k(\mathbf{x})\nabla P(\mathbf{x},t)\right) = 0 \quad \text{..}\ldots\ldots\ldots\ldots\ldots\ldots\ldots\ldots\ldots\ldots\ldots\ldots\ldots\ldots\ldots \quad (3.2)$$

Where $\phi(\mathbf{x})$ is porosity, $k(\mathbf{x})$ is permeability, $\mu$ is total fluid viscosity and $c_t$ is total compressibility. The Fourier transform of **Eq. 3.2** in the frequency domain is given as follows,

$$\frac{\phi(\mathbf{x})\mu c_t}{k(\mathbf{x})}(-i\omega)\hat{P}(\mathbf{x},\omega) = \nabla^2\hat{P}(\mathbf{x},\omega) + \frac{\nabla k(\mathbf{x})}{k(\mathbf{x})}\cdot\nabla^2\hat{P}(\mathbf{x},\omega) \ldots\ldots\ldots\ldots\ldots\ldots\ldots\ldots\ldots\ldots \quad (3.3)$$

Where $\hat{P}$ is the Fourier transform of the pressure variation (Arsac, 1966) as a function of space (**x**) and time (*t*) is given as follows,

$$\hat{P}(x,\omega) = \int_{-\infty}^{\infty} e^{-i\omega t} P(x,t)dt \quad \ldots\ldots\ldots\ldots\ldots\ldots\ldots\ldots\ldots\ldots\ldots\ldots\ldots\ldots\ldots \quad (3.4)$$

A low frequency power series representation of the pressure in the frequency domain is given by,

$$\hat{P}(x,\omega) = \frac{e^{-\sqrt{i\omega}\sigma(x)}}{\sqrt{\omega}} \sum_{n=0}^{\infty} P_n(x)\omega^n \quad \text{..... (3.5)}$$

Where ***σ(x)*** is the phase of the propagating pressure front. The expansion of $\hat{P}(\mathbf{x},\omega)$ (**Eq. 3.5**) is dominated by the first few terms of the summation, when ω is small. As the interest is in low-frequency asymptotic solution of the **Eq. 3.2**, for zeroth frequency (i.e. mean of the pressure series) the **Eq. 3.5** is reduced to,

$$\hat{P}(x,\omega) = \frac{e^{-\sqrt{i\omega}\sigma(x)}}{\sqrt{\omega}} P_o(x) \quad \text{..... (3.6)}$$

Vasco et al., (2004) derived the pressure sensitivity, i.e. the partial derivative of the pressure at the observation point *x* due to a perturbation of the permeability at *y***,** which is given by the integrand,

$$\frac{\delta P(x,\omega)}{\delta K(y)} = \prod(x_s, x, \omega) e^{-\sqrt{i\omega}\Sigma(x_s,x)} \quad \text{..... (3.7)}$$

$$\prod(x_s, x, \omega) = -2\nabla P_o(y,x) \cdot \nabla P_o(x_s, y)\psi^2(\omega) \quad \text{..... (3.8)}$$

$\psi(\omega)$ in the **Eq. 3.8** accounts for windowing of the observations (taking observations discontinuously). The term $P_o(y,x)$ represents zeroth-order representation of the pressure *P*, at point *x* due to the source (or sink) at *y*. Practically it is difficult to evaluate $P_o(y,x)$ as the source (or sink) has to be placed at every gridblock location

whose sensitivity has to be evaluated. It is easy to reciprocate this by keeping the source at original *x* location and evaluate $P_o(x, y)$. While $P_o(x_s, y)$ represents the zeroth-order representation of the pressure *P*, at point *y* due to a source at $\boldsymbol{x_s}$. This term is evaluated for all the sources and sinks simultaneously by running the simulation model at the operating conditions. For details refer to the Vasco et al., (2004; 2006).

For the case of only injection well, $x_s$ and *y* coincide and only the laplacian $P_o(x_s, y)$ needs to be evaluated required just one steady state solution. As presented above, the pressure inversion for the zeroth-order frequency and several other frequencies is possible. In this work however, only the zeroth-frequency (mean) component is inverted which results in simplification of the **Eq. 3.7**. For instance for $\omega = 0$ and $\psi(\omega) = 1$, the sensitivity term (Vasco et al., 2004) reduces to,

$$\frac{\delta P(x, \omega = 0)}{\delta K(y)} = -2\nabla P_o(x_s, y) \cdot \nabla P_o(x_s, y) \quad \text{.....} \quad (3.9)$$

The inversion of the zeroth-frequency component follows an approach with the augmented objective function as described in the **Eq. 3.10** (Yoon et al., 2001),

$$\left\| \delta P_o - S\delta R \right\| + \beta_1 \left\| \delta R \right\| + \beta_2 \left\| L\delta R \right\| \quad \text{.....} \quad (3.10)$$

where in the **Eq. 3.10**, *S* represents the sensitivity matrix, $\delta R$, correspond to the change in the reservoir property (permeability), and $\delta P_o$, the misfit in the zeroth-frequency component of the Fourier transformed pressure. In addition $\boldsymbol{L}$ is a second spatial difference operator that is a measure of roughness and is analogous to imposing a prior variogram or covariance constraint. The first term in **Eq. 3.10** ensures that the difference between the observed and calculated mean bottom-hole pressure response is minimized. The second term, called a "norm constraint", penalizes deviations of updated model from the initial model. This helps in preserving geologic realism because starting or

prior model already incorporates available geologic and static information related to the reservoir. Finally, the third term, a roughness penalty, simply recognizes the fact that production data are an integrated response and are thus, best suited to resolve large-scale structures rather than small-scale property variations. $\boldsymbol{\beta_1}$ and $\boldsymbol{\beta_2}$ are weights on the norm term (second term) and roughness term (third term) respectively. The influence of these parameters can be controlled by using them. This augmented function is minimized using a conjugate gradient minimization algorithm.

The proposed approach is computationally efficient as solution of the **Eq. 3.9** requires ($N_{well}$ + 1) steady state simulations, where $N_{well}$ is no. of wells. So the time required for inverse modeling scales with number of wells not number of gridcells. This is particularly helpful in BHP inversion for $CO_2$ sequestration models where the simulation models are large with low number of active wells. The BHP inversion sensitivity is derived using steady state solution described in the **Eq. 3.9**.

### 3.2.3 Pressure Peak Arrival Time Inversion of Observation Wells

In this section pressure peak arrival time inversion based on a high frequency asymptotic solution for the transient flow is discussed. A high frequency asymptotic solution of the diffusivity equation leads to the Eikonal equation which governs the propagation of the pressure front (Vasco et al., 2000). The pressure front is defined as the propogation of the peak response corresponding to an impulse source or sink (Lee J, 1982).

A high frequency asymptotic solution for a transient pressure response (**Eq. 3.2**) assumes the following form (Fatemi et al., 1995; Vasco et al., 2000; Datta-Gupta et al., 2002),

$$\hat{P}(\mathbf{x},\omega) = e^{-\sqrt{-i\omega}\sigma(\mathbf{x})}\sum_{k=0}^{\infty}\frac{A_k(\mathbf{x})}{\left(\sqrt{-i\omega}\right)^k}. \quad \text{..... (3.11)}$$

where ***σ(x)*** is the phase of the propagating pressure front. The motivation for using expansion of $\hat{P}(\mathbf{x},\omega)$ (**Eq. 3.11**) in terms of inverse powers of $\omega$ is that initial terms of

the series represent rapidly varying (high frequency i.e. sharp pressure front) components and successive terms are associated with the lower frequency behavior (Vasco and Datta-Gupta, 1999). The asymptotic solution, the **Eq. 3.11**, is the summation of an infinite number of terms with coefficients $A_n(\mathbf{x})$. Only the first few terms which correspond to high frequency (large $\omega$) in the series are considered. They describe the physical propagation of a 'sharp pressure front' (Vasco et al., 2000; Datta-Gupta et al., 2002). Considering the first term only,

$$\hat{P}(\mathbf{x},\omega) = e^{-\sqrt{-i\omega}\sigma(\mathbf{x})} A_0(\mathbf{x}) \quad \text{....} \qquad (3.12)$$

After inserting the **Eq. 3.12** into the **Eq. 3.3** and collecting terms with the highest order of $\sqrt{-i\omega}$, the equation for the front propagation in an isotropic permeable media is given as follows,

$$\nabla\sigma(\mathbf{x}) \cdot \nabla\sigma(\mathbf{x}) = \frac{1}{\alpha(\mathbf{x})} \qquad (3.13)$$

Where $\alpha(\mathbf{x})$ is the diffusivity given by,

$$\alpha(\mathbf{x}) = \frac{k(\mathbf{x})}{\phi(\mathbf{x})\mu c_t} \qquad (3.14)$$

**Eq. 3.13** is the Eikonal equation widely used to explain a variety of propagation behavior (Kline and Kay, 1965; Kravtsov and Orlov, 1990). In addition the **Eq. 3.13** has the similar form of the streamline time of flight equation which describes the propagation of a neutral tracer (Datta-Gupta and King, 2007). Using analogy of the time of flight formulation, diffusive time of flight ($\tau$) for propagation of a pressure front is defined as follows (Datta-Gupta et al., 2002),

$$\tau(\mathbf{x}) = \int_{\psi} \frac{d\zeta}{\sqrt{\alpha(\mathbf{x})}} \quad \text{...} \qquad (3.15)$$

Diffusive time of flight is defined along the trajectory of a 'pressure front' $\psi$, and these trajectories are not necessarily the streamlines (Vasco and Finsterle, 2004). But Kim et al., (2009) showed that by exploiting the analogy between tracer and pressure trajectories, one can approximate the pressure front trajectory with streamlines especially when the pressure propagation is transient such as in case of $CO_2$ sequestration in large aquifers.

The relationship between $\tau(x)$ and the physical time ($t$) when the pressure response (drawdown or build up) reaches a maximum at position **x,** is given by (Vasco et al., 2000),

$$t_{\max} = \frac{\tau^2(\mathbf{x})}{6} \quad \text{...} \qquad (3.16)$$

The **Eq. 3.16** refers to the arrival time of the peak pressure response corresponding to an impulse source and sink. In practice, there is a step change in rate at the injector. Noting that the derivative of the step function is an impulse function, the arrival time of the pressure front at a location can be interpreted as the time when time derivative of the pressure reaches maximum (or minimum) at that point.

For data inversion, one needs to quantify parameter sensitivity, i.e. the relationship between changes in model parameters (permeability, porosity) and variations in the predicted pressure peak arrival time $\tau$. From the **Eq. 3.14** and the **Eq. 3.15**, sensitivity coefficient of diffusive time of flight $\tau$ with respect to permeability $k$ can be obtained analytically as follows (Vasco et al., 2000),

$$\frac{\partial \tau(\mathbf{x})}{\partial k(\mathbf{x})} = -\frac{1}{2} \int_{\psi} \frac{\sqrt{\phi(\mathbf{x}) \mu c_t}}{k(\mathbf{x}) \sqrt{k(\mathbf{x})}} d\zeta \quad \text{...} \qquad (3.17)$$

Integration in the **Eq. 3.17** is evaluated along the streamlines (Kim et al., 2009) which can be efficiently computed using fluxes derived from a full physics compositional finite volume simulation (Rey et al., 2010). In this work, fluxes derived from the compositional simulation of $CO_2$ sequestration are used to trace streamlines from each grid-cell to the injector. For inversion only the streamlines passing nearby the observation wells are considered as they are representing pressure trajectories passing through them. The details of compositional streamline tracing are given in **Appendix B.1**.

### 3.2.4 Gradient Based Optimization

In the last step of the proposed approach, a gradient based optimization technique using sensitivities derived using numerical perturbation via finite difference are used to modify global parameters for example permeability and Ky/Kx multiplier. The Levenberg–Marquardt algorithm is used for calibrating global multiplier on the permeability field to improve the match for bottom-hole pressure data for observation wells.

## 3.3 Compositional Flow Simulation of $CO_2$ Sequestration

There are a variety of physical and chemical mechanisms interacting together when modeling the $CO_2$ sequestration process. The $CO_2$ is normally injected under supercritical conditions but depending on the pressure, temperature and salinity of brine, it can exist either as a gas or liquid phase. The injected $CO_2$ can also initiate a variety of chemical reactions resulting from the acidification of the aquifer brine and eventually precipitate in a solid form of carbonate mineral. Eventually over a long period of time, mineral precipitation can induce changes in the formation modifying transport properties like porosity and permeability (Kumar et al., 2008). Although $CO_2$ mineralization is the most effective method of $CO_2$ sequestration, it occurs over very long time scales. Other mechanisms by which $CO_2$ is sequestered in the reservoir are structural trapping, residual trapping and dissolution in reservoir brine. Structural trapping of $CO_2$ is dependent on the quality and integrity of the structural seal. This is one of the major

uncertainties of CCS projects. Residual trapping is related to immobile phase trapping of $CO_2$ as $CO_2$ rises up because of buoyancy and travels through the water phase. This residual trapping is dependent on rock-fluid properties such as permeability, relative permeabilities and also the phase behavior of the reservoir fluids and the injected $CO_2$. Dissolution of $CO_2$ in reservoir brine is typically small (about 3–7% by mass) and depends on salinity of the reservoir brine and reservoir pressure and temperature (Leonenko, 2008)).

### 3.4 Applications

In this section, the proposed approach in **section 3.2** is illustrated by using two 2-D examples in **section 3.4.1** and a 3-D example in **section 3.4.2**. In the first 2-D example the prior (starting) model is conditioned to the well data and is selected to be visually similar to the reference model. In the second 2-D example the prior (starting) model is selected to be significantly different from the reference model, to demonstrate the robustness of the approach. In all the cases (2-D and 3-D) the inversion results at each step are compared to the reference model.

#### 3.4.1 2-D Synthetic Examples

A 2-D synthetic model of dimension 8000 feet by 8000 feet is used for the illustration. The thickness of the model is 50 feet. Number of grid cells in X and Y direction are 40 each, having dimension of 200 feet x 200 feet. The reference permeability field is shown in **Fig. 3.2**. The reference permeability is $49^{th}$ layer of the 3-D model generated using well log data from Weaber Horn well in the Illinois basin (Finley, 2005). The generation of the 3-D model is discussed in detail in **section 3.4.2**. There is an injection well I1 in the center (20, 20) with three observations wells O1, O2 and O3. The distance of O1 from I1 is approximately 1200 feet, O2 from I1 is approximately 2400 feet and O3 from I1 is approximately 3600 feet. The location of the wells along with their relative distances is illustrated in **Fig. 3.2**. The injection rate is 2500 Reservoir Barrels per day.

The injection is carried out for 11 months and after that injection well is shut-in for 1 month.

Permeability in X direction and Y direction are assumed to be the same (No Anisotropy). Permeability in Z direction is $1/10^{th}$ that of permeability in X direction. Constant porosity of 0.2 is used. A commercial compositional simulator (Eclipse™ Compositional Simulator) is used with the $CO_2$ sequestration option that allows modeling all the three $CO_2$ sequestration mechanisms (**section 3.3**). The $CO_2$ storage model includes three phases: a $CO_2$ rich phase, a $H_2O$ rich phase and a solid phase. The $CO_2$ rich phase is mostly in gas state while $H_2O$-rich phase is mostly in liquid state. The solid state consists of salts, for example, $CaCl_2$ and NaCl . Phase splitting between $CO_2$ and $H_2O$ is modeled after Spycher and Preuss (Spycher et al., 2003). Salts are present in the liquid as well as the solid phase and the relevant geochemical reactions arising from the acidification of brine from the injected $CO_2$ and salt precipitation are also modeled. In addition, mobility reduction due to solid precipitation is also accounted. In this work, four components are used in the compositional simulation, which are $CO_2$, $H_2O$, NaCl and $CaCl_2$.

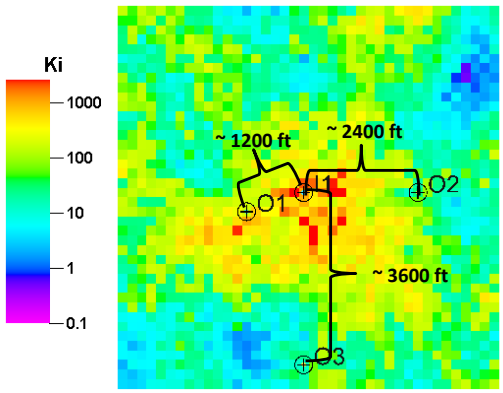


**Fig. 3.2 – Well locations and their relative distances are shown on the reference permeability (md) map.**

The described proposed workflow (**section 3.2**) is used for integration pressure data obtained during $CO_2$ sequestration. $CO_2$ is injected in the reference model for 11 months and after that the well is shut-in for 1 month. The pressure data thus generated by the injection and observation wells is considered as the historical data for history matching.

Two cases are discussed for the 2-D synthetic application. In the first 2-D case the prior (starting) model is constructed using the same variogram for sequential Gaussian simulation, as the reference model using same well data. The starting model is geo-statistically similar to the reference model. In the second 2-D case the prior (starting) model is not conditioned to the well data used in the reference model and is different or geo-statistically dissimilar from the reference model.

#### 3.4.1.1 Starting (Prior) Model Is Conditioned to the Well Data

The starting (initial) permeability field which is geostatistically similar to the reference model is shown in **Fig. 3.3**. On comparison with **Fig. 3.2** a significant differences in the details of the permeability fields is observed.

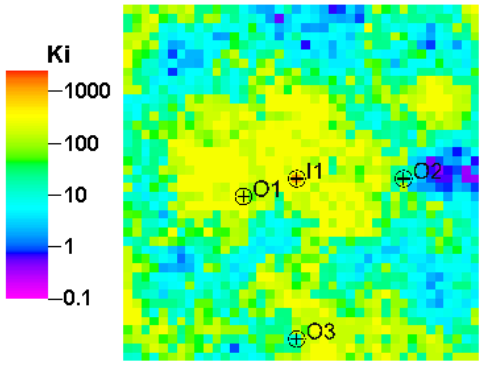


**Fig. 3.3 – Starting 2-D permeability field (md) which is conditioned to the well data used for the reference model and is geo-statistically similar to the reference model.**

#### 3.4.1.1.1 Pore-volume Calibration Based on Pseudo-steady State Analysis

The connected pore-volume calculation is performed for reference and simulation bottom-hole pressure data of the injection well I1 as described in **section 3.2.1**. This analysis is shown in **Fig. 3.4**. A constant pore-volume multiplier of 1.13 is applied to the starting simulation model.

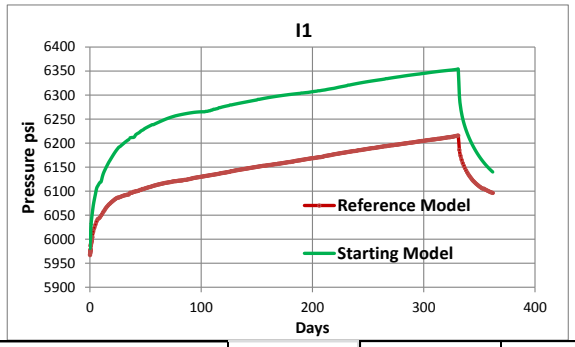


| | Porevolume RB | | |
|---|---|---|---|
| | Reference | Starting | Multiplier |
| Injector | 9.58E+07 | 8.47E+07 | 1.13 |

| | Reference | Starting |
|---|---|---|
| Psuedosteady State flow Slope psi/day | 0.3536 | 0.4 |

**Fig. 3.4 – Pseudo-steady state analysis of bottom-hole pressure of reference and starting models for volumetric comparison.**

The difference in slope is due to difference in permeability between reference and starting models which can be compensated to some degree by modifying pore-volume. As a result there is a small improvement in the bottom-hole pressure match of wells after pore-volume multiplier of 1.13 as shown in **Fig. 3.5**.

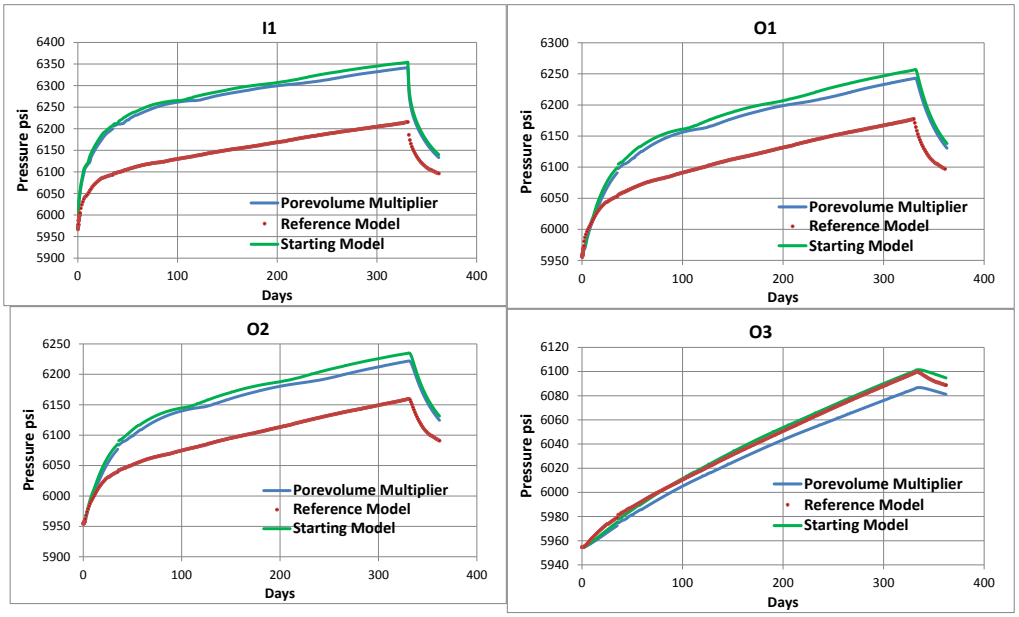


**Fig. 3.5 – Bottom-hole pressure match for injection well I1, observation wells O1, O2 and O3 after pore-volume multiplier of 1.13 based on pseudo-steady state analysis (blue) compared to bottom-hole pressure of the starting model (green).**

### 3.4.1.1.2 Bottom-hole Pressure Inversion

Bottom-hole pressure (BHP) inversion is carried out using method described in **section 3.2.2.** The improved pressure match for injector I1 after BHP inversion is shown in **Fig. 3.6**. A considerable improvement in the pressure match is observed.

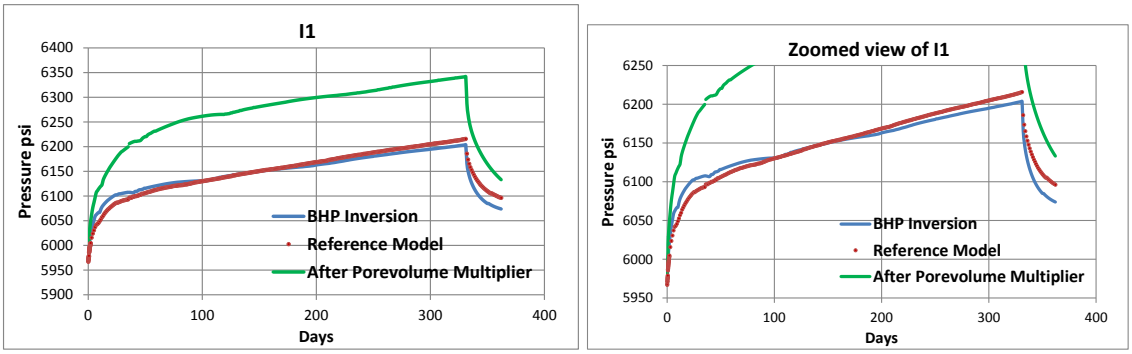


**Fig. 3.6 – Bottom-hole pressure match for well I1 after BHP inversion (left). Zoomed view is shown on right.**

A significant improvement in bottom-hole pressure match for observation wells O1 and O3 after BHP inversion is observed in **Fig. 3.7**. Although match for well O3 has worsened slightly.

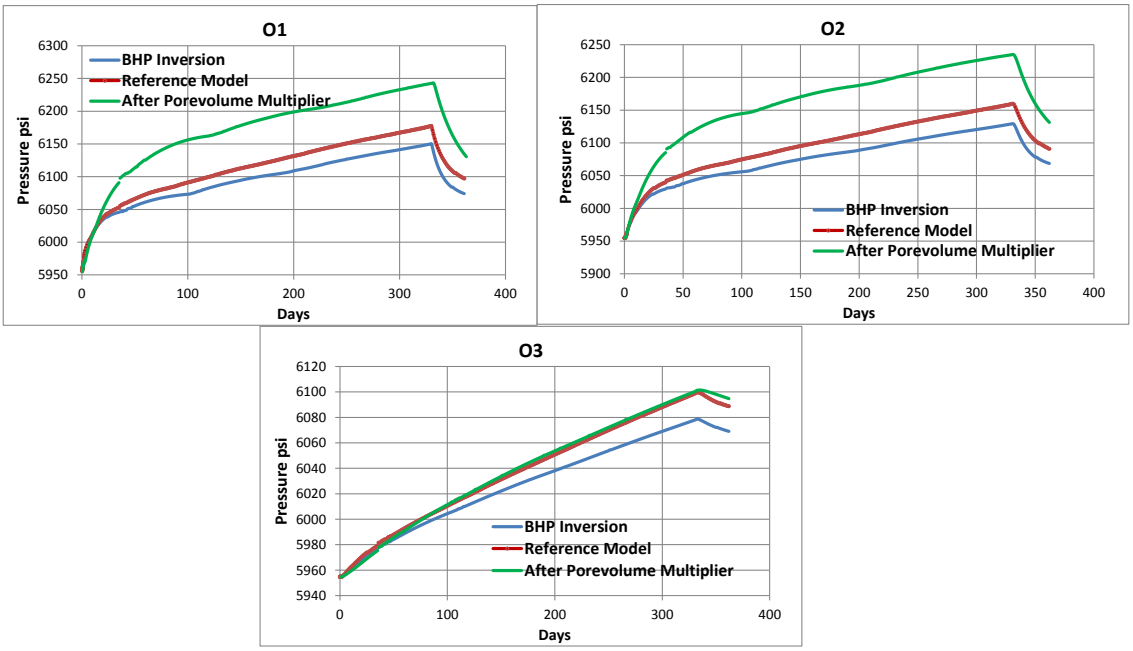


**Fig. 3.7 – Bottom-hole pressure match (in psi) for observation wells O1, O2 and O3 after BHP inversion.**

The 2-D permeability field after BHP inversion is compared to the reference and starting (initial) permeability field in **Fig. 3.8**.

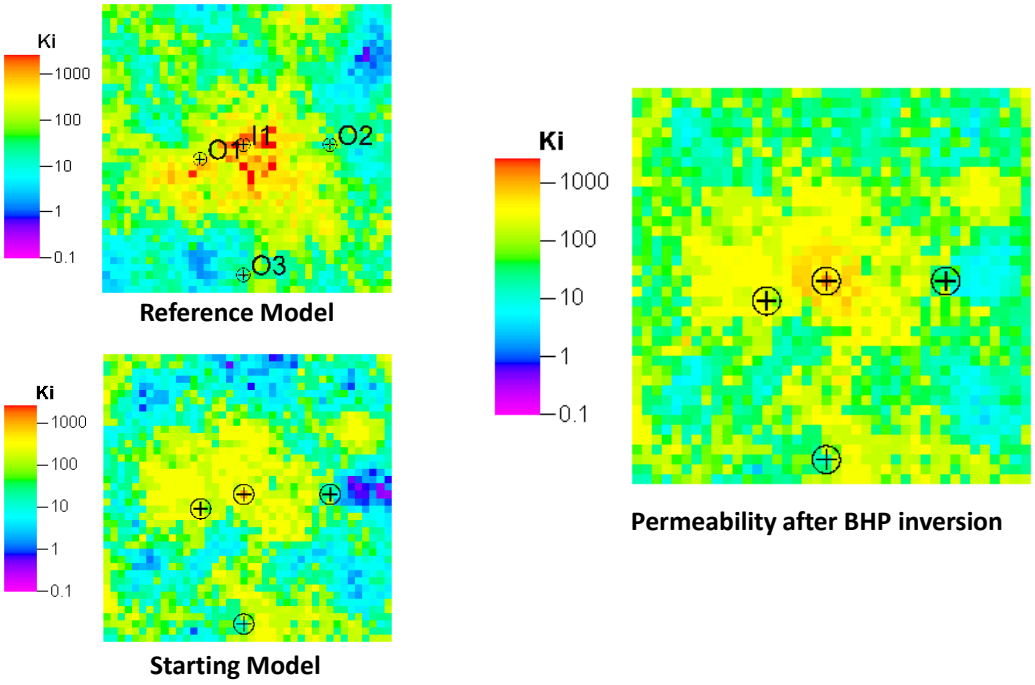


**Fig. 3.8 – 2-D permeability fields (md) after BHP inversion.**

For further understanding, the changes in permeability made after BHP inversion are compared to permeability changes required in **Fig. 3.9**. Permeability changes required are derived by subtracting the starting (initial) permeability field from the reference permeability field. The changes made are quite comparable to changes required, especially for the high permeability areas.

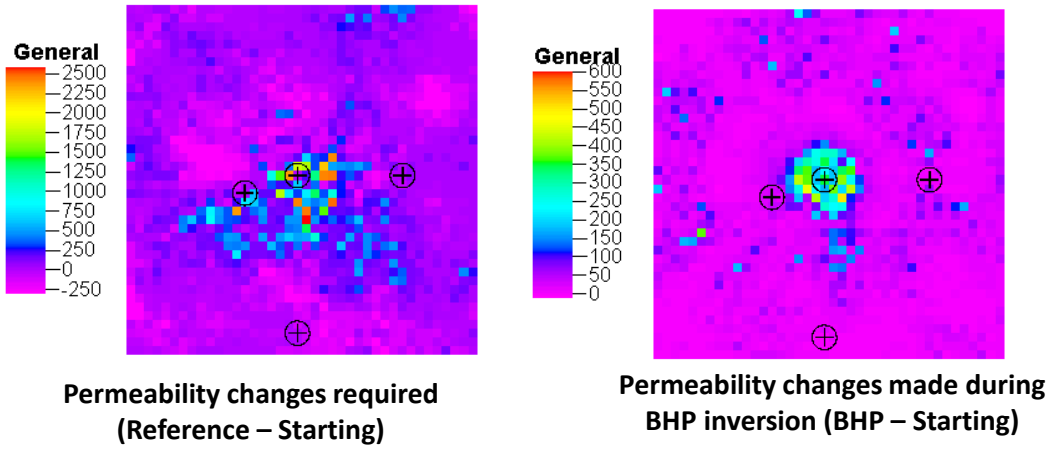


**Fig. 3.9 – Permeability changes required (md) are compared with changes made after BHP inversion.**

### 3.4.1.1.3 Pressure Peak Arrival-time Inversion

After BHP inversion, pressure peak arrival time inversion for observations wells O1, O2 and O3 is carried out using compositional streamline tracing as described in **Appendix B.1**. The peak arrival time match improvement after pressure peak arrival–time inversion is shown in **Fig. 3.10**. The peak arrival time after arrival time inversion (X axis) is compared to reference model peak arrival time (Y axis). It can be observed that only observation well O3 has shown improvement compared to the peak arrival time after BHP inversion.

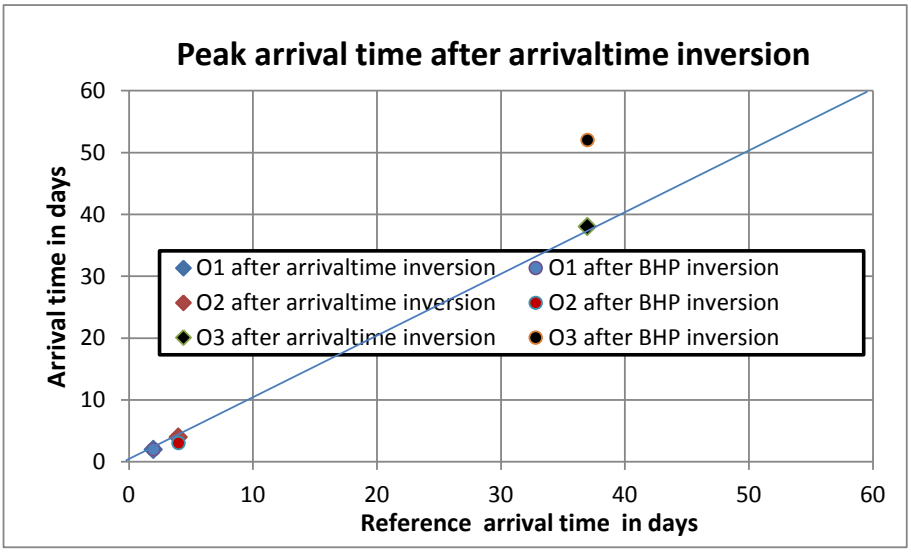


**Fig. 3.10 – Peak arrival time comparison between pressure peak arrival time inversion and BHP inversion.**

The slightly worsened pressure match for injector I1 after arrival time inversion is shown in **Fig. 3.11**.

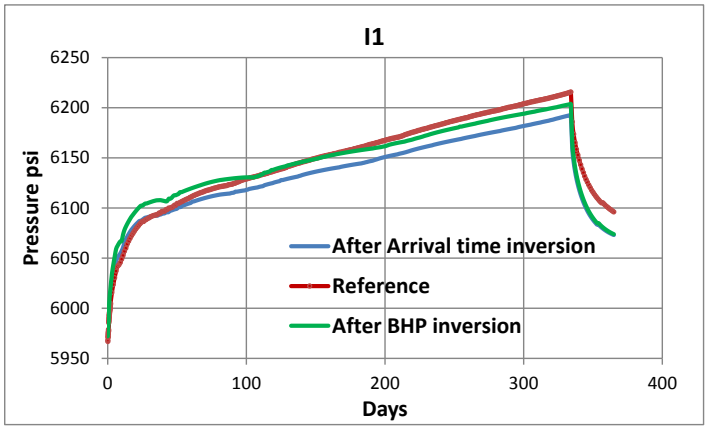


**Fig. 3.11 – Bottom-hole pressure match for well I1 after pressure peak arrival time inversion (blue) compared to bottom-hole pressure after BHP inversion (green).**

The bottom-hole pressures for observation wells O1, O2 and O3 after the pressure peak arrival time inversion are shown in **Fig. 3.12**. Very little change is observed compared to the BHP inversion as the peak arrival time inversion pertains to improvement in the arrival time of the pressure front no the magnitude of the pressure.

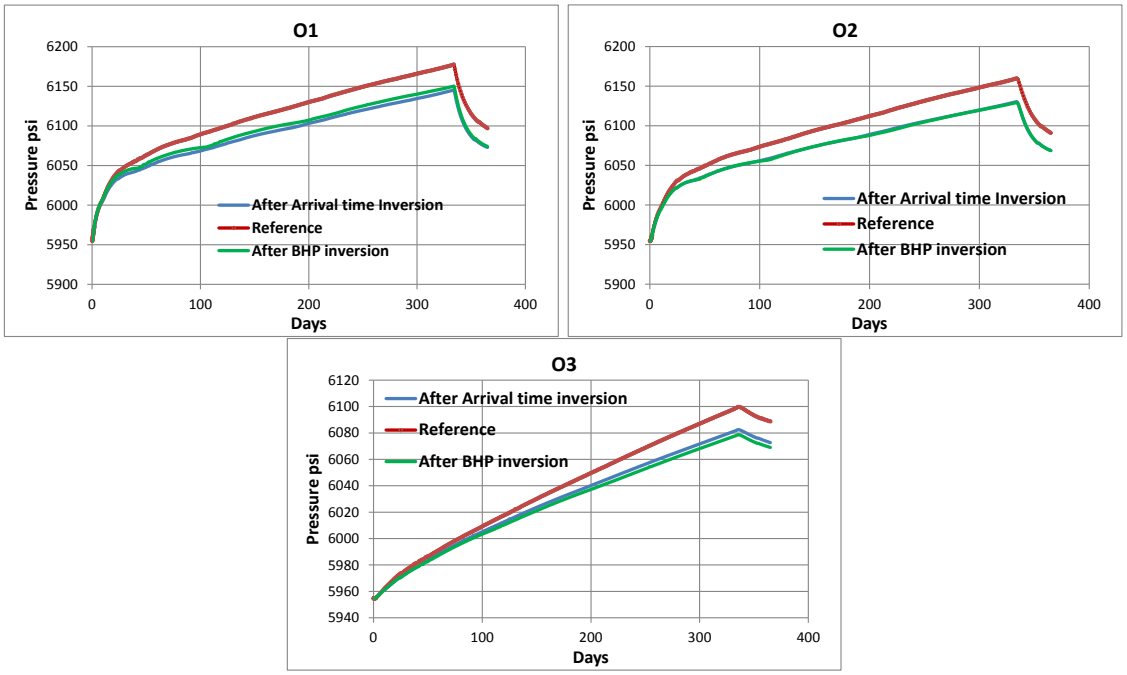


**Fig. 3.12 – Bottom-hole pressure match for observation wells O1, O2 and O3 after pressure peak arrival time inversion (blue) compared to bottom-hole pressure after BHP inversion (green).**

The 2-D permeability field after pressure peak arrival time inversion is compared to the reference, starting (initial) permeability field and permeability after BHP inversion in **Fig. 3.13**.

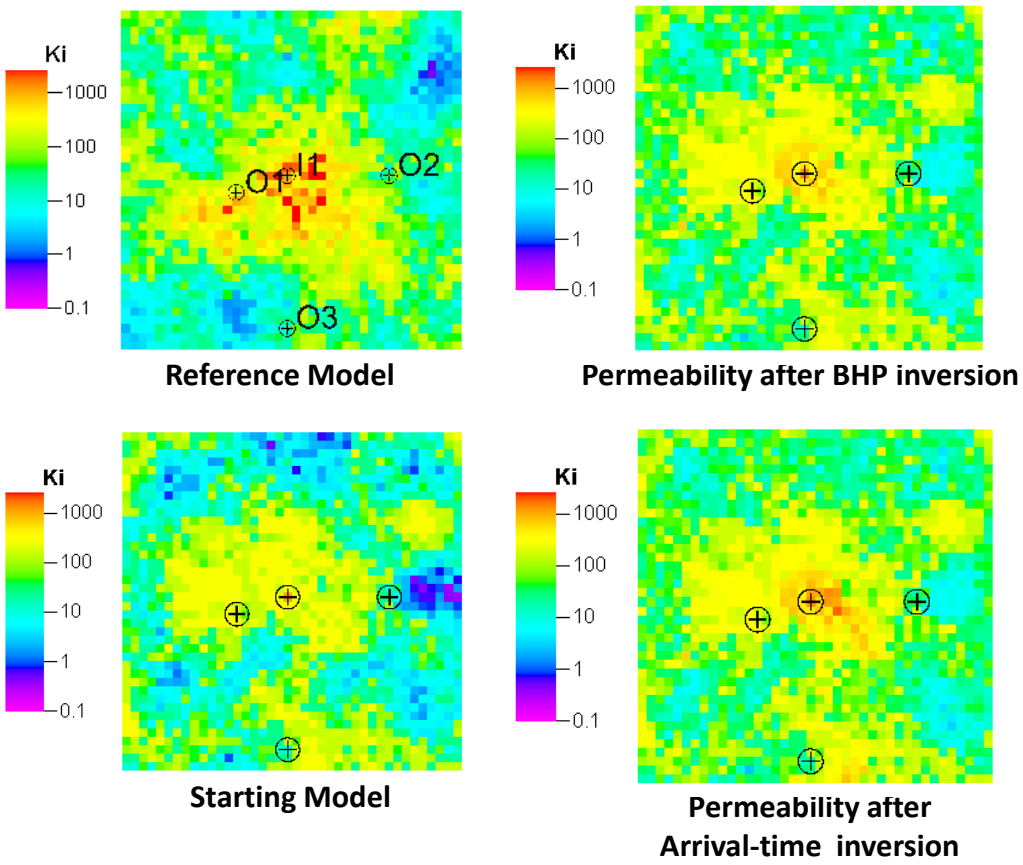


**Fig. 3.13 – 2-D permeability field (md) after pressure peak arrival time inversion compared to permeability field after BHP inversion**

For further understanding of the permeability changes made after the pressure peak arrival time inversion, they are compared to the permeability changes made after the BHP inversion and permeability changes required in the starting (initial) model in **Fig. 3.14**. It can be observed that high permeability is generated around well O3 after the

arrival time inversion. This change has resulted in a lowering of the peak arrival time for the well O3 similar to that observed in the reference model. The traced compositional streamlines from every grid cell are also plotted in the lower right corner of **Fig. 3.14**.

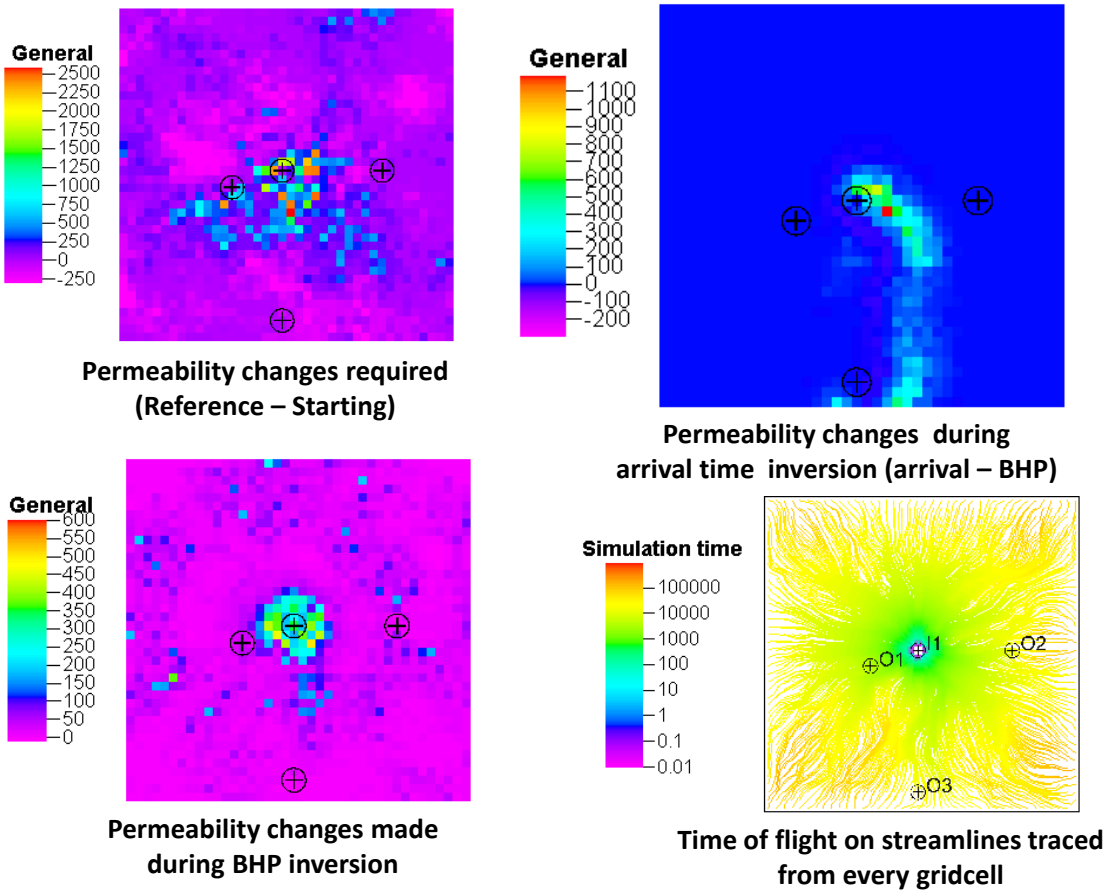


**Fig. 3.14 –Permeability changes required (md) are compared with changes made after arrival time inversion.**

### 3.4.1.1.4 Gradient Based Constant Permeability Multiplier Inversion

In the final stage of the proposed approach a gradient based optimization technique using perturbation sensitivities is used to modify a global multiplier on the permeability in X direction. The final multiplier obtained on permeability after arrival time inversion is 0.7. The bottom-hole pressure results using this multiplier for injector I1 is shown in **Fig.**

**3.15**. A very good match to the reference pressure is observed for well I1. Also significant improvement in the bottom-hole pressure after arrival time inversion is observed.

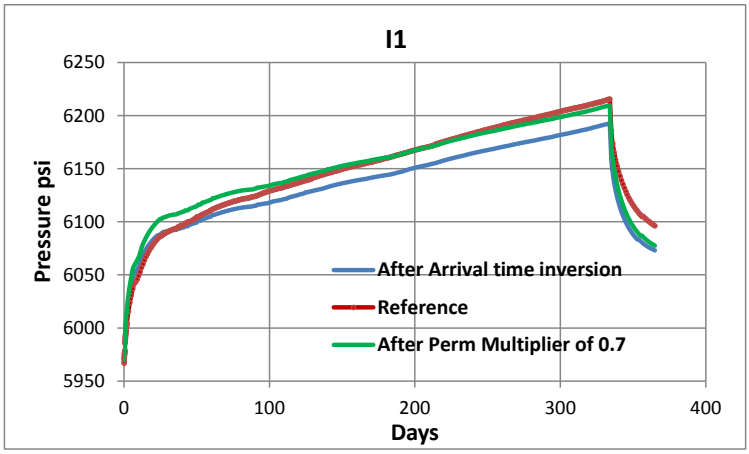


**Fig. 3.15 – Bottom-hole pressure match for well I1 after global permeability multiplier (green) compared to bottom-hole pressure after arrival time inversion (blue).**

Similarly a good bottom-hole pressure match after global permeability multiplier is observed for three observation wells O1, O2 and O3 in **Fig. 3.16**. There is considerable improvement compared to bottom-hole pressure result from arrival time inversion.

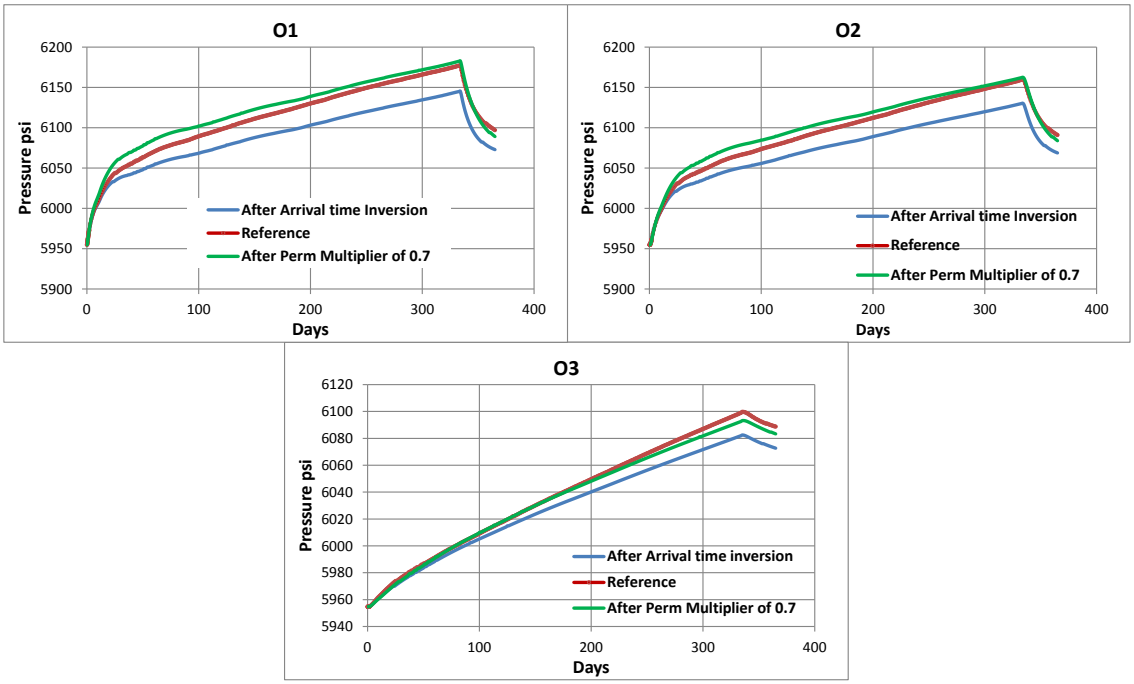


**Fig. 3.16 – Bottom-hole pressure match for observation wells O1, O2 and O3 after global permeability multiplier (green) compared to bottom-hole pressure after arrival time inversion (blue).**

The 2-D permeability field after global permeability multiplier is compared to the reference permeability field, starting (initial) permeability field and permeability after arrival time inversion in **Fig. 3.17**. An overall lower shift in permeability is observed over permeability field derived after arrival time inversion.

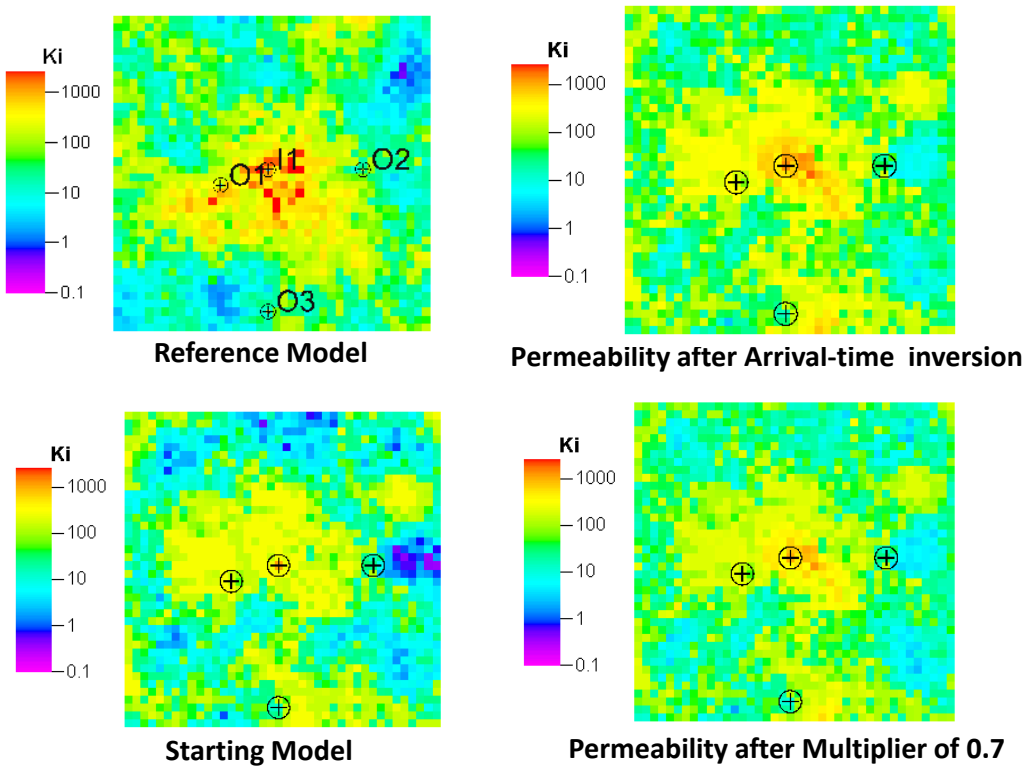


**Fig. 3.17 – 2-D permeability field (md) after global permeability multiplier is compared to permeability field after arrival time inversion.**

Although the final permeability field after proposed approach may not look like reference permeability field the bottom-hole pressure matches are very good. This is expected because of the high non-uniqueness of the fine-scale inversion. Also, the pressure propagation is very diffusive and is better suited to resolve large scale trends as opposite to the small scale variation.

The pressure field (in psi) after 4 months for the final model after proposed approach is compared using same scale to the pressure field after 4 months for the reference model, and starting (initial) model in **Fig. 3.18**. The pressure field looks reasonably similar to that of the reference model. Significant improvement is observed for the pressure field as compared to the starting (initial) model.

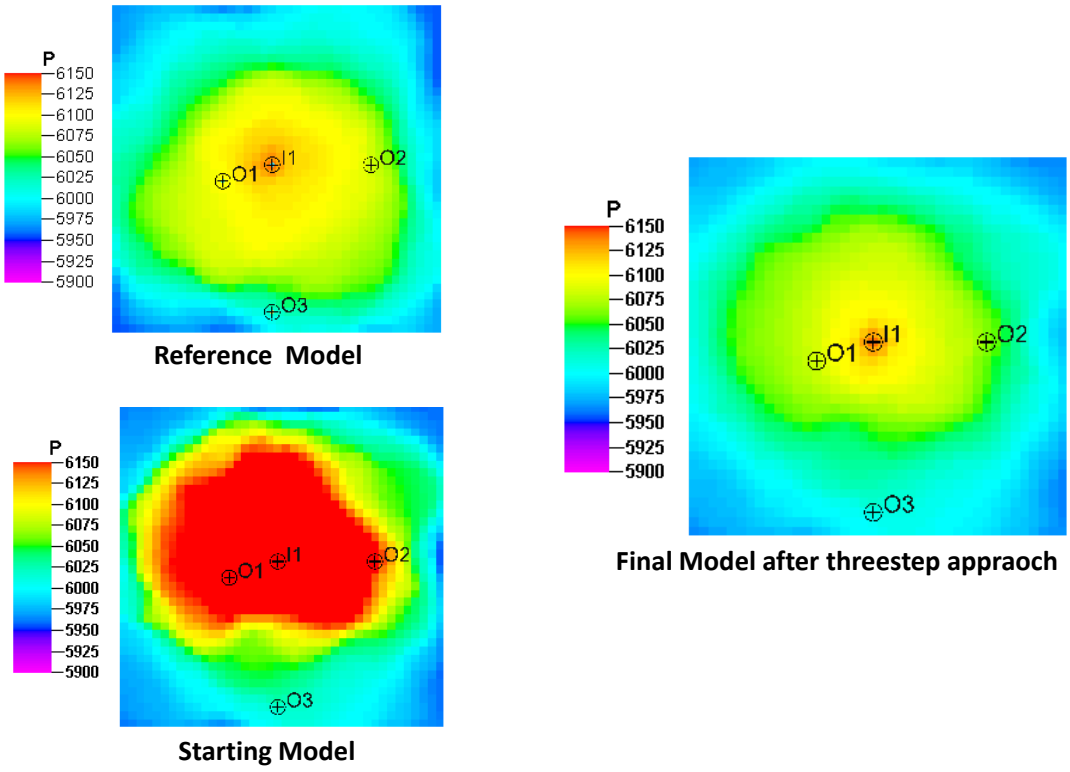


**Fig. 3.18 – Pressure field (in psi) after 4 months after proposed approach.**

### 3.4.1.1.5 Validation of History Matching

History matched model is validated by forecasting the bottom-hole pressure performance of the history matched model after proposed approach and comparing it with reference and starting (initial) model. The forecast period is for two years after 11 months of $CO_2$ injection at the rate of 2500 reservoir barrels per day, followed by 1 month of shut-in. The result for injection well I1 is shown in **Fig. 3.19**. On the right, a zoomed view is shown. Excellent agreement is observed for the bottom-hole pressure for reference and history matched model in the forecast period after proposed approach.

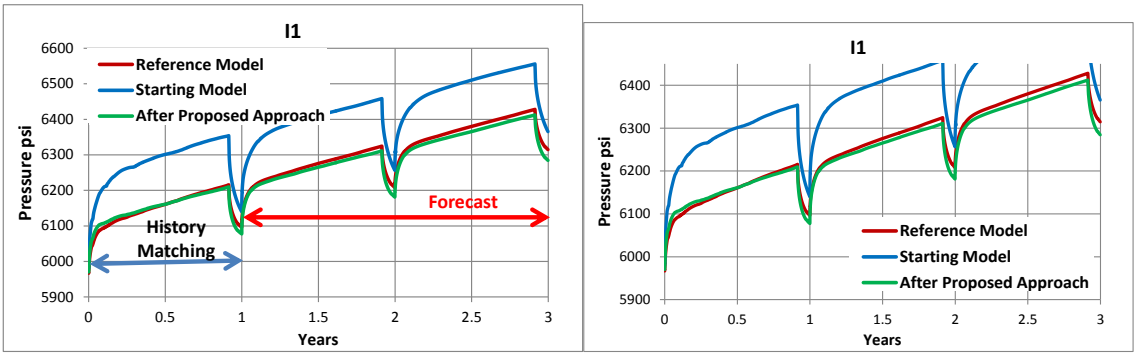


**Fig. 3.19 – Comparison of forecast of bottom-hole pressure for injection well I1 for history matched, reference and starting model. Zoomed view is shown on right. History matching is performed for 1 year followed by 2 years of forecasting.**

Similarly the results for observation wells O1, O2 and O3 are illustrated in **Fig. 3.20**. Barring well O3 a good agreement is observed for reference and history matched model in the forecast period after the proposed approach.

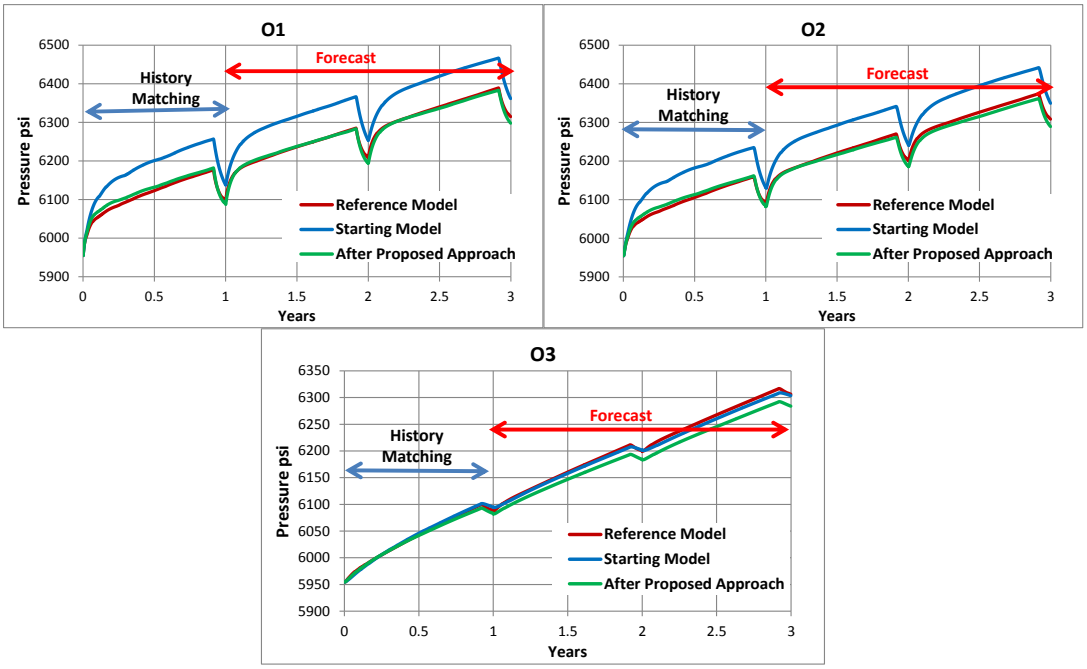


**Fig. 3.20 – Comparison of forecast of bottom-hole pressure for observation wells O1, O2 and O3 for history matched, reference and starting model. History matching is performed for 1 year followed by 2 years of forecasting.**

The gas saturation difference map between gas saturation at the end of the 3rd year (end of two year forecasting) and 1st year (end of history matching period) for starting, reference and final (after proposed approach) models is illustrated in **Fig. 3.21**. The impact of pressure history matching on the gas saturation difference map seems to be relatively small, although some improvement in the saturation trend can be observed.

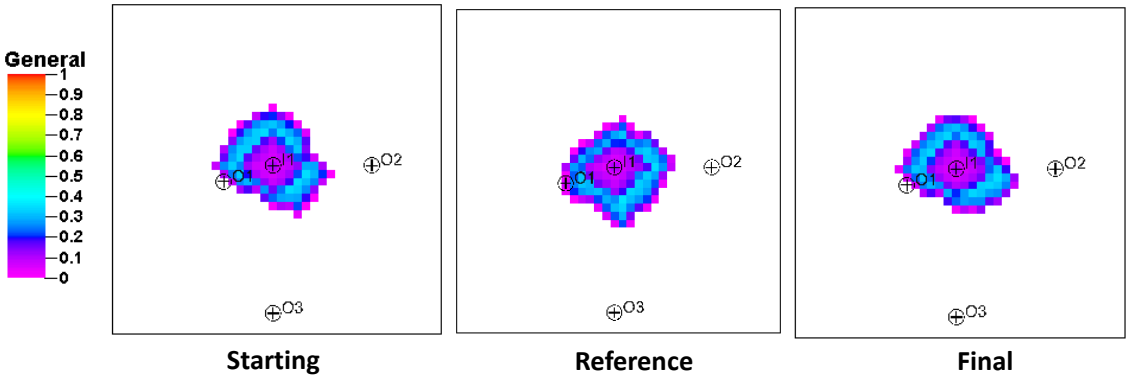


**Fig. 3.21 – Gas saturation difference between gas saturation at the end of the 3rd year (end of two year forecasting) and 1st year (end of history matching period) for starting, reference and final (after proposed approach) models**

For better understanding of the improvement in the spatial distribution of the gas saturation difference at the end of the 3rd year and 1st year for the final model, a cross-plot of comparison of gas saturation difference (**Fig. 3.21**) for the reference and final model (after proposed approach) along with reference and starting model is illustrated in **Fig. 3.22**. It can be observed that the coefficient of correlation has improved from 0.78 to 0.8 after the proposed approach.

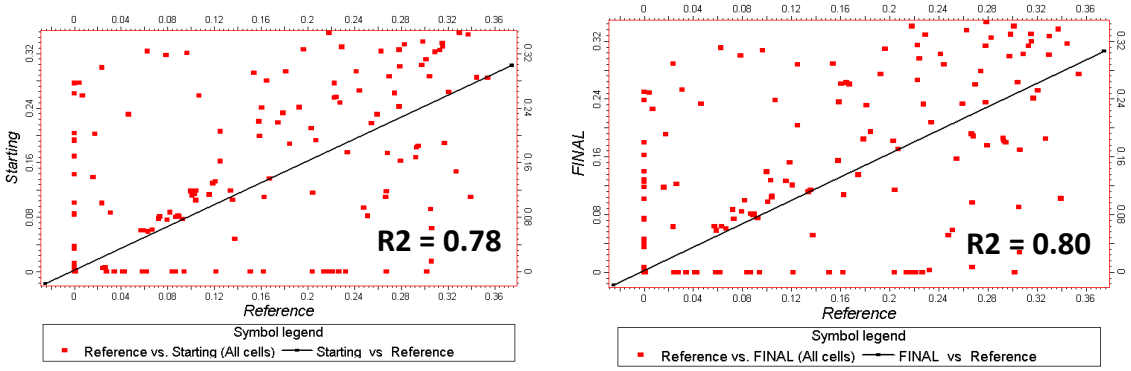


**Fig. 3.22 – Cross-plot comparison of gas saturation difference at the end of 3rd year and 1st year for the reference and final models (right), reference and starting models (left).**

### 3.4.1.2 Starting (Prior) Model Is Not Conditioned to the Well Data

The starting (initial) permeability field is not conditioned to the well data used for the reference model and is geo-statistically dissimilar to the reference model is shown in **Fig. 3.23**. On comparison with **Fig. 3.2,** it can be seen that the prior model is significantly different from the reference model.

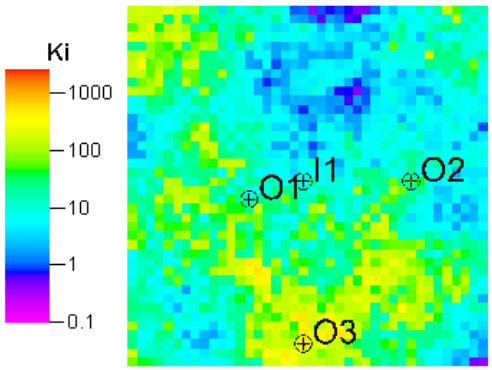


**Fig. 3.23– Starting 2-D permeability field (md) which is not conditioned to the well data used for the reference model and is geo-statistically dissimilar to the reference model.**

There is a small improvement in bottom-hole pressure matches of all wells using pore-volume calibration based on pseudo-steady state analysis as presented in **section 3.4.1.2.1.** Therefore, pore-volume calibration based on the pseudo-steady state analysis will not be performed for this 2-D case.

### 3.4.1.2.1 Bottom-hole Pressure Inversion

Bottom-hole pressure (BHP) inversion is carried out using the method described in **section 3.2.2.** The improved pressure match for injector I1 after BHP inversion is shown in **Fig. 3.24**. A considerable improvement in the pressure match is observed.

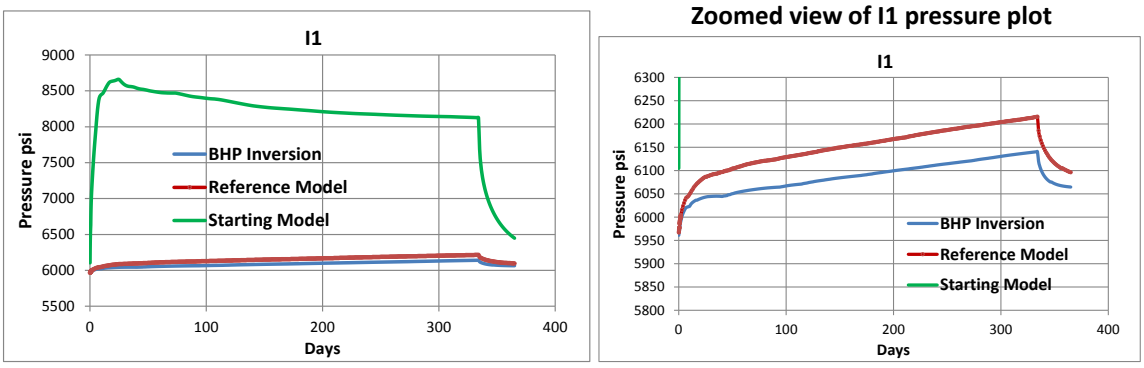


**Fig. 3.24 – Bottom-hole pressure match for well I1 after BHP inversion (left). Zoomed view is shown on right.**

A significant improvement in bottom-hole pressure match for observation wells after BHP inversion is observed in **Fig. 3.25**.

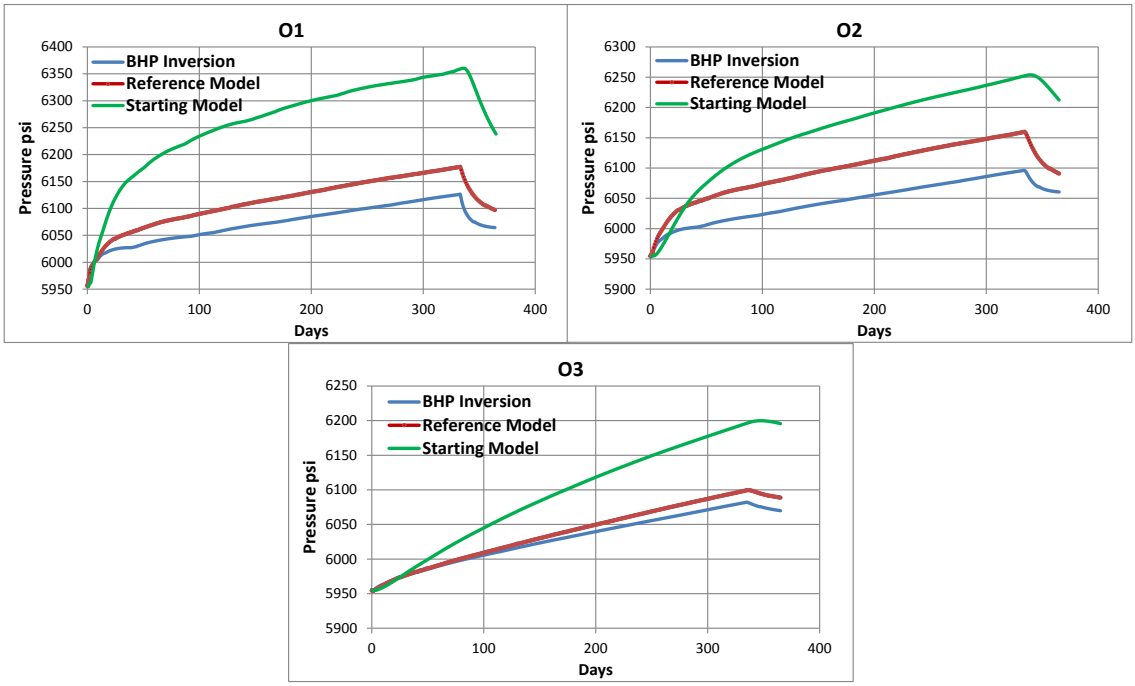


**Fig. 3.25 – Bottom-hole pressure match (in psi) for observation wells O1, O2 and O3 after BHP inversion.**

The 2-D permeability field after BHP inversion is compared to the reference and starting (initial) permeability field in **Fig. 3.25**. A remarkable improvement is seen in the BHP inverted permeability field compared to the starting (initial) permeability.

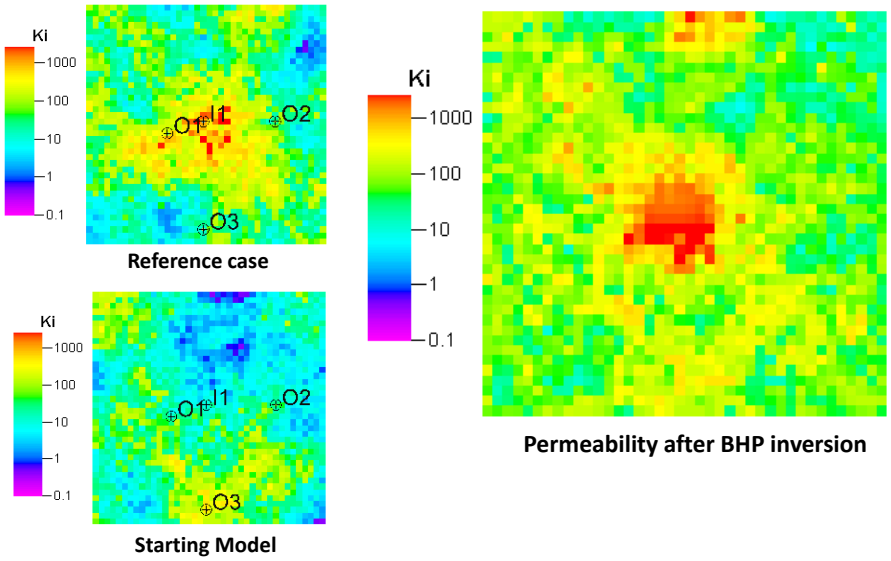


**Fig. 3.26 – 2-D permeability field (md) after BHP inversion.**

For further understanding, the changes in permeability made after BHP inversion are compared to permeability changes required in **Fig. 3.27**. Permeability changes required are derived by subtracting the starting (initial) permeability field from the reference permeability field. The changes made are quite comparable to changes required, especially the high permeability areas.

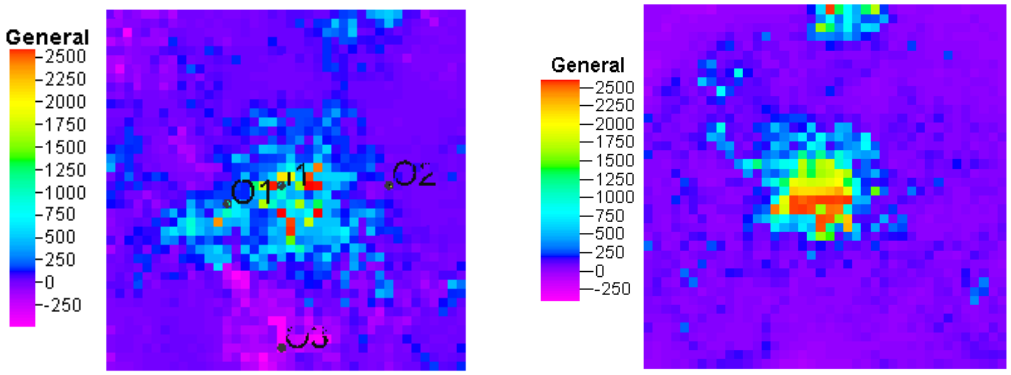


**Fig. 3.27 –Permeability changes required (md) are compared with changes made after BHP inversion.**

#### 3.4.1.2.2 Pressure Peak Arrival-time Inversion

After BHP inversion, pressure peak arrival time inversion for observations wells O1, O2 and O3 is carried out using compositional streamline tracing as described in **Appendix B.1**. The peak arrival time improvement after pressure peak arrival–time inversion is shown in **Fig. 3.28**. The peak arrival time after arrival time inversion (X axis) is compared to reference model peak arrival time (Y axis). It can be observed that the observation well O3 has shown significant improvements with regards to peak arrival time after BHP inversion.

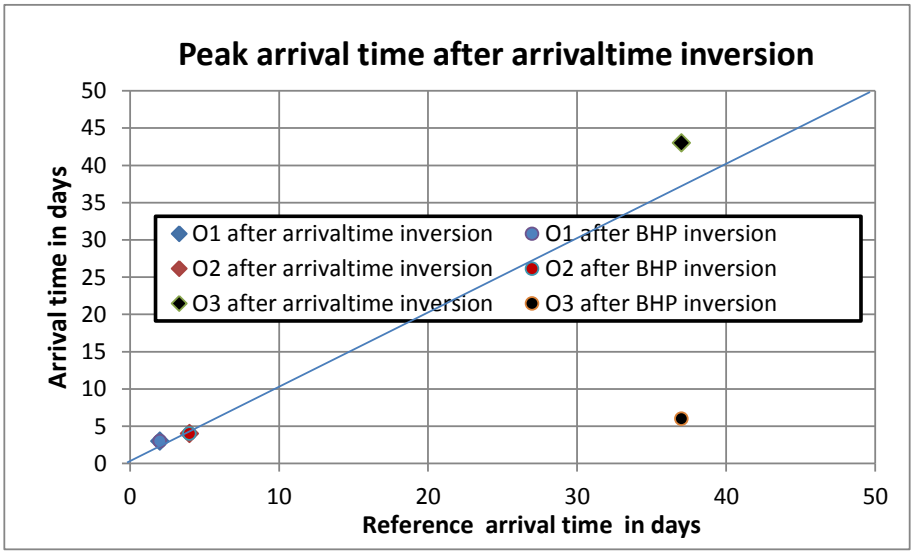


**Fig. 3.28 – Peak arrival time comparison between pressure peak arrival time inversion and BHP inversion.**

The little improved pressure match for injector I1 after arrival time inversion is shown in **Fig. 3.29**.

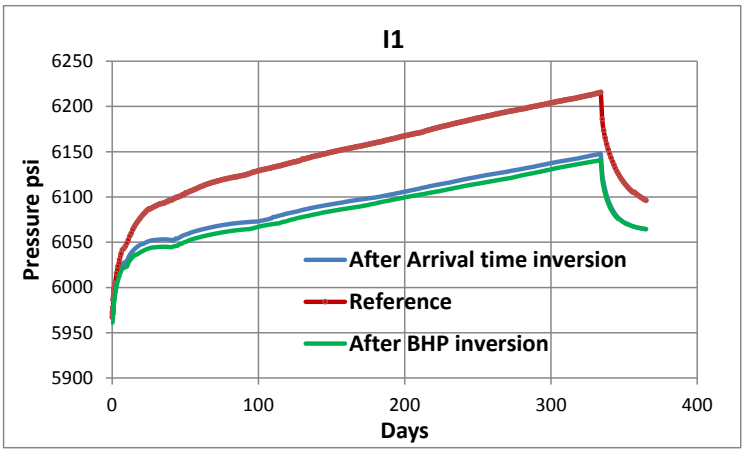


**Fig. 3.29 – Bottom-hole pressure match for well I1 after pressure peak arrival time inversion (blue) compared to bottom-hole pressure after BHP inversion (green).**

The bottom-hole pressures for observation wells O1, O2 and O3 after the arrival time inversion are shown in **Fig. 3.30**.

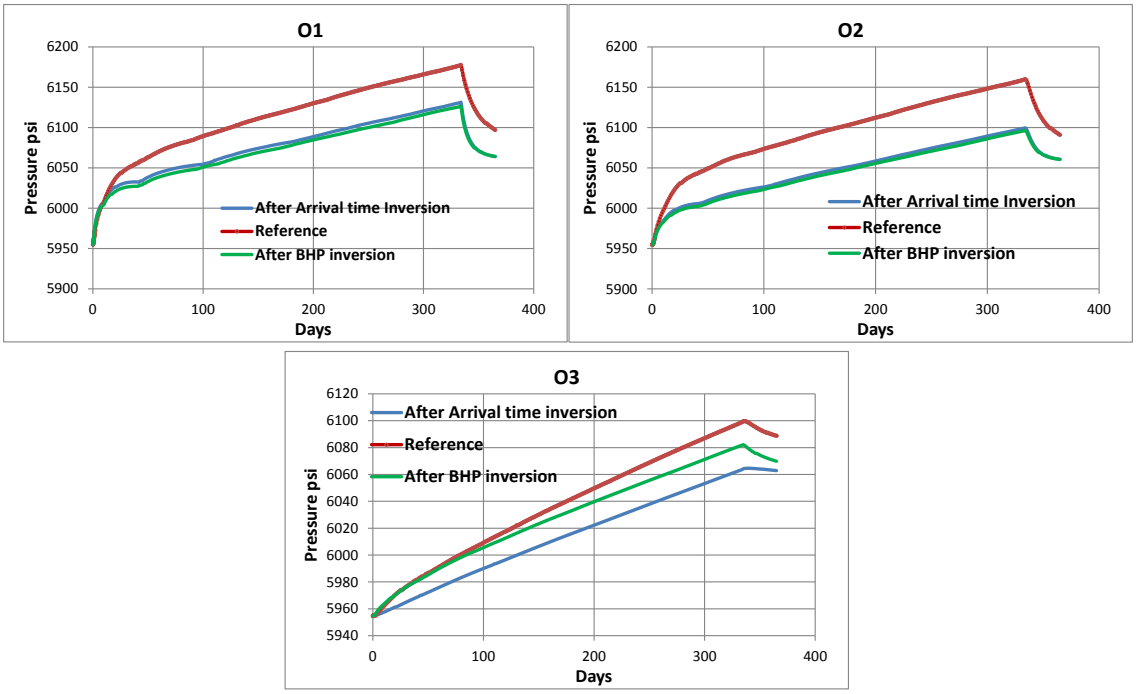


**Fig. 3.30 – Bottom-hole pressure match for observation wells O1, O2 and O3 after arrival time inversion (blue) compared to bottom-hole pressure after BHP inversion (green).**

The 2-D permeability field after pressure peak arrival time inversion is compared to the reference, starting (initial) permeability field and permeability after BHP inversion in **Fig. 3.31**. Considerable improvement is observed in the area consisting of well O3 and I1 over the permeability field derived after BHP inversion. This new improvement after the arrival time inversion corresponds to the low permeability region around well O3 in the reference model. This permeability improvement around well O3 is the result of the arrival time match improvement for well O3 in **Fig. 3.28**.

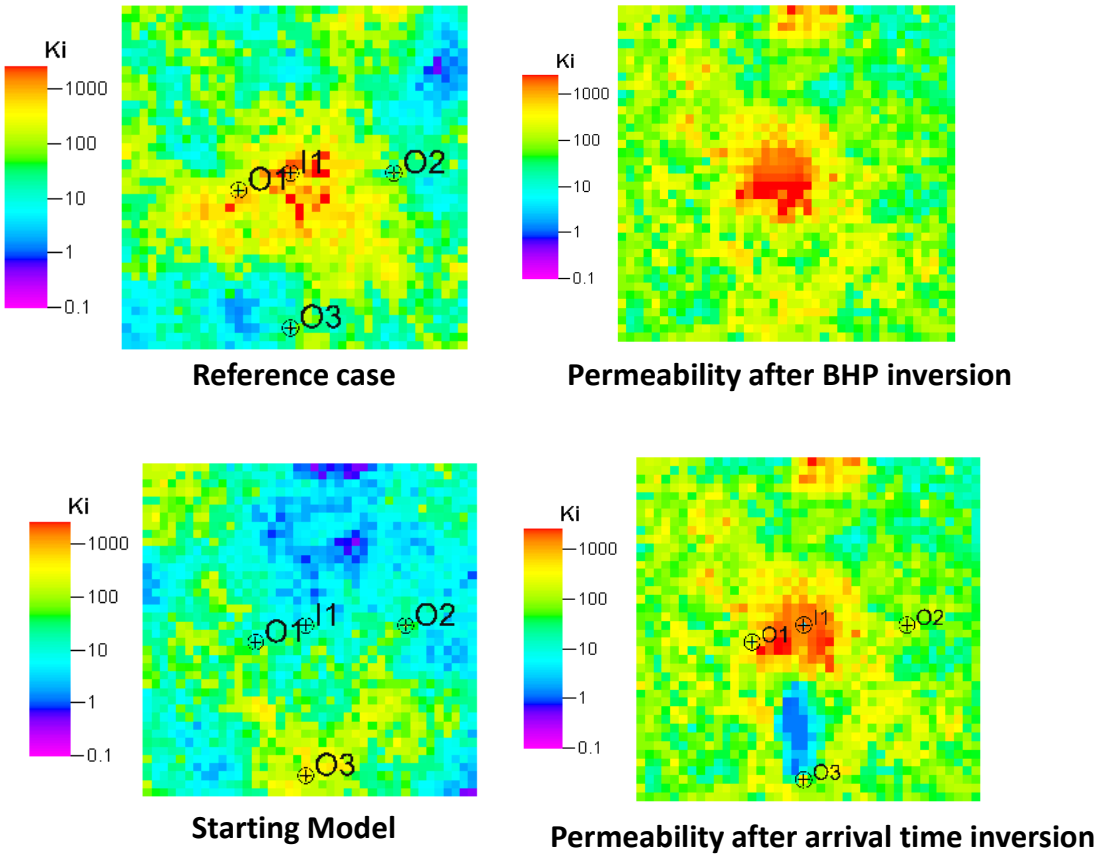


**Fig. 3.31 – 2-D permeability field (md) after pressure peak arrival time inversion compared to permeability field after BHP inversion.**

The permeability changes made after the pressure peak arrival time inversion are compared to the permeability changes made after the BHP inversion and permeability changes required in the starting (initial) model in **Fig. 3.32**. The traced compositional streamlines from every grid cell are also plotted in the lower right corner of **Fig. 3.32**. It can be observed that high permeability generated around well O3 after BHP inversion is lowered after the arrival time inversion. This change has resulted in a lower permeability area around well O3 similar to that observed in the reference model.

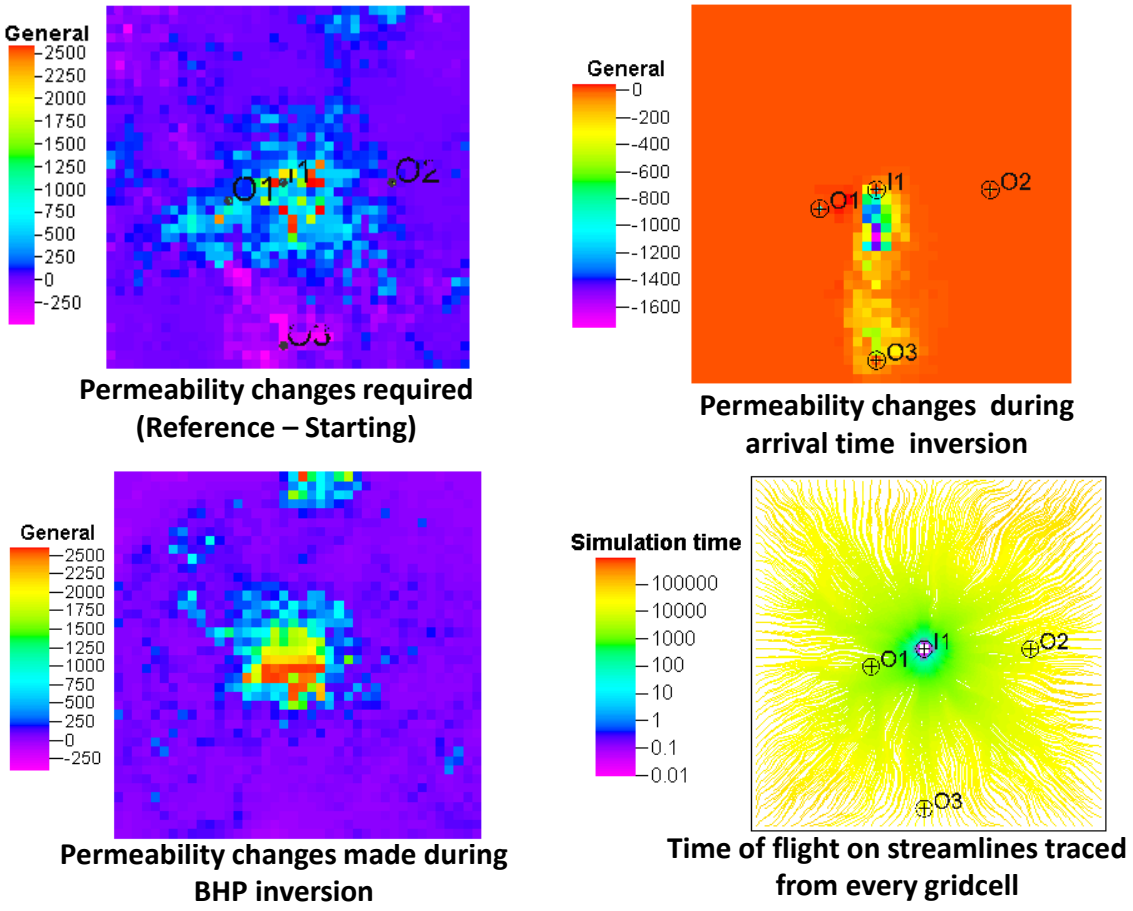


**Fig. 3.32 –Permeability changes required (md) are compared with changes made after arrival time inversion along with compositional streamlines traced from every gridcell.**

### 3.4.1.2.3 Gradient Based Constant Permeability Multiplier Inversion

In the final stage of the proposed approach a gradient based optimization technique using perturbation sensitivities is used to modify global multiplier on permeability in X direction. The final multiplier obtained on permeability after arrival time inversion is 0.535. The bottom-hole pressure results using this multiplier for injector I1 is shown in **Fig. 3.33**. A very good match to the reference pressure is observed for well I1. Also significant improvement in the bottom-hole pressure after arrival time inversion is observed.

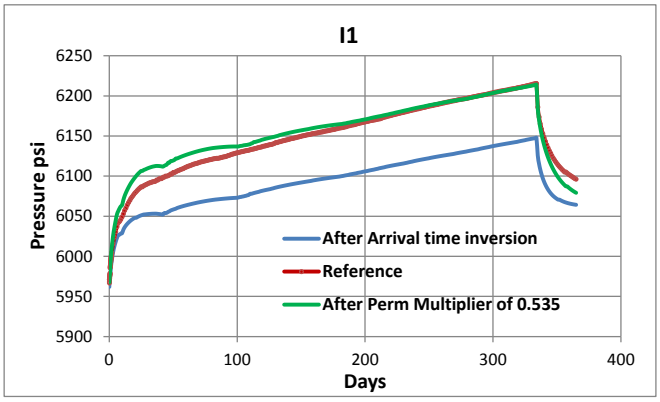


**Fig. 3.33 – Bottom-hole pressure match for well I1 after global permeability multiplier (green) compared to bottom-hole pressure after arrival time inversion (blue).**

Similarly a good bottom-hole pressure match after global permeability multiplier is observed for three observation wells O1, O2 and O3 in **Fig. 3.34**. There is considerable improvement compared to bottom-hole pressure result from arrival time inversion.

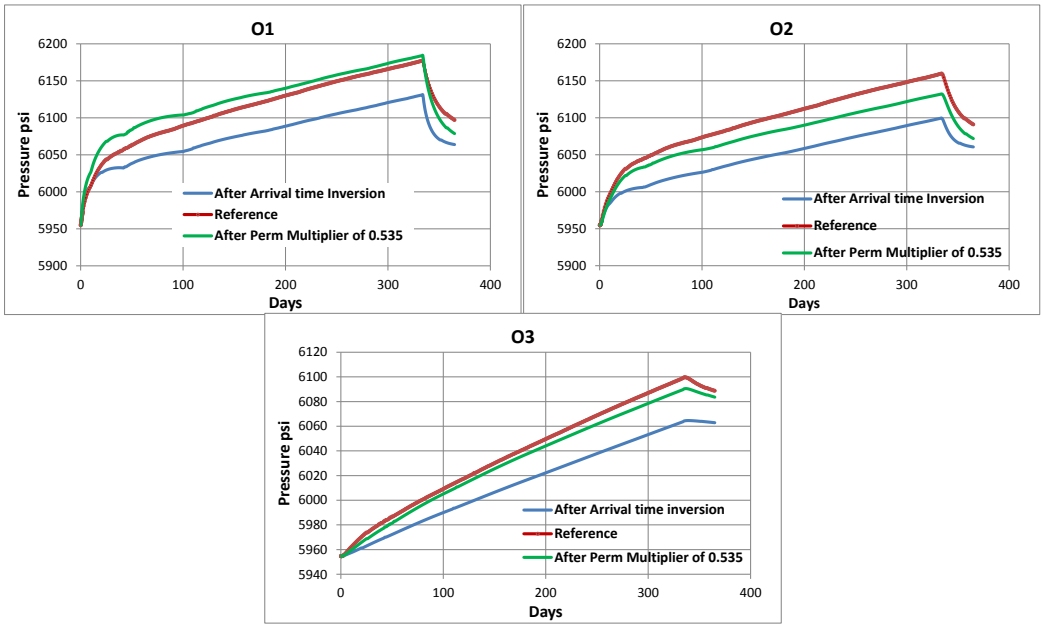


**Fig. 3.34 – Bottom-hole pressure match for observation wells O1, O2 and O3 after global permeability multiplier (green) compared to bottom-hole pressure after arrival time inversion (blue).**

The 2-D permeability field after global permeability multiplier is compared to the reference permeability field, starting (initial) permeability field and permeability after arrival time inversion in **Fig. 3.35**. An overall lower shift in permeability is observed over permeability field derived after arrival time inversion.

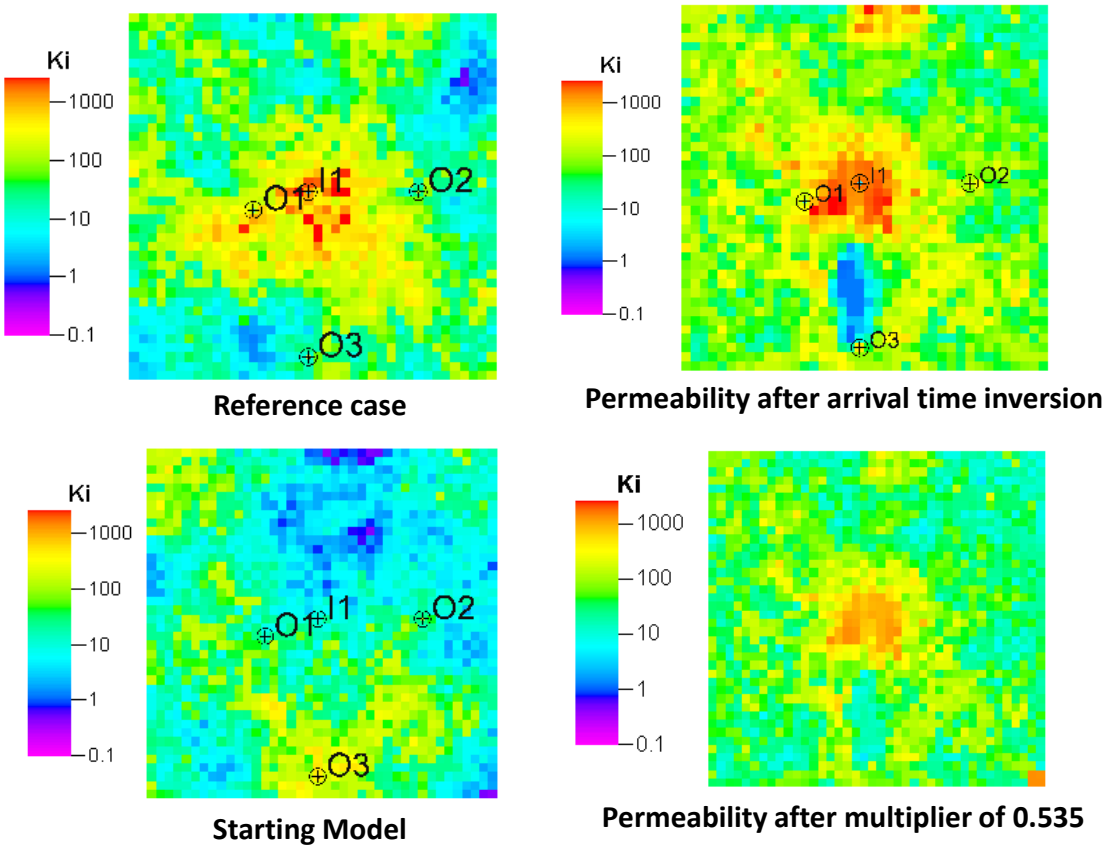


**Fig. 3.35 – 2-D permeability field (md) after global permeability multiplier is compared to permeability field after arrival time inversion.**

The pressure field (in psi) after 4 months for the final model after proposed approach is compared using same scale to the pressure field after 4 months for the reference model, and starting (initial) model in **Fig. 3.36**. The pressure field looks quite similar to that of the reference model. Significant improvement is observed for the pressure field as compared to the starting (initial) model.

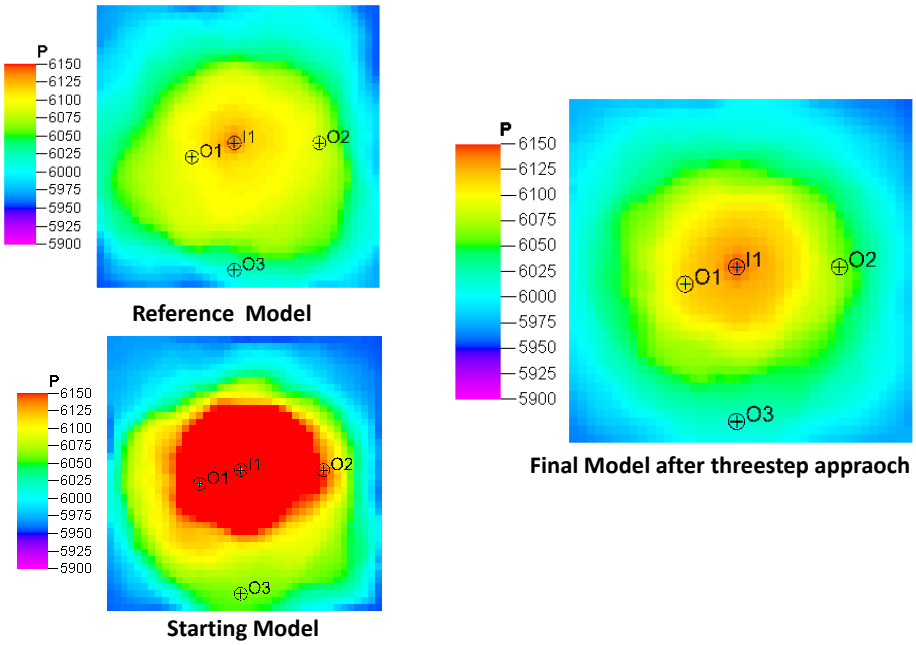


**Fig. 3.36 – Pressure field (in psi) after 4 months after proposed approach.**

### 3.4.1.4 Validation of History Matching

History matched model is validated by forecasting the bottom-hole pressure performance of the history matched model after proposed approach and comparing it with reference and starting (initial) model. The forecast period is for two years after 11 months of $CO_2$ injection at the rate of 2500 reservoir barrels per day, followed by 1 month of shut-in. The result for injection well I1 is illustrated in **Fig. 3.37**. On the right, a zoomed view is

shown. Excellent agreement is observed for the bottom-hole pressure for reference and history matched model in the forecast period after proposed approach.

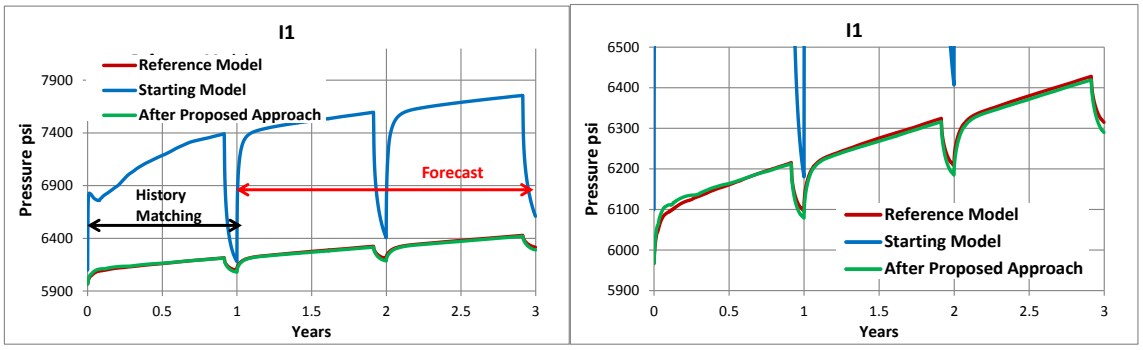


**Fig. 3.37 – Comparison of forecast of bottom-hole pressure for injection well I1 for history matched, reference and starting model. Zoomed view is shown on right. History matching is performed for 1 year followed by 2 years of forecasting.**

Similarly the results for observation wells O1, O2 and O3 are illustrated in **Fig. 3.38**. Barring well O2 a good agreement is observed for reference and history matched model in the forecast period after the proposed approach.

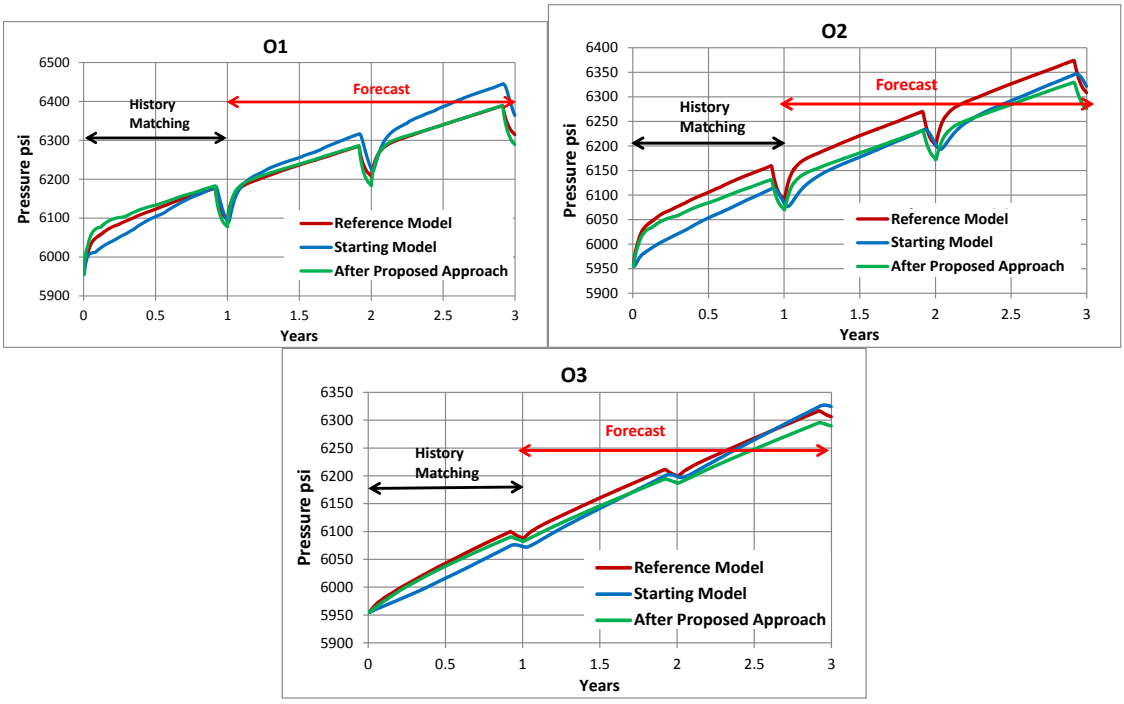


**Fig. 3.38 – Comparison of forecast of bottom-hole pressure for observation wells O1, O2 and O3 for history matched, reference and starting model. History matching is performed for 1 year followed by 2 years of forecasting.**

The gas saturation difference map between gas saturation at the end of the 3rd year (end of two year forecasting) and 1st year (end of history matching period) for starting, reference and final (after proposed) models is illustrated in **Fig. 3.39**. There is a substantial improvement in the gas saturation difference map for the final model. In particular, the front has propagated further compared to the starting model. The saturation from location is consistent with the reference model.

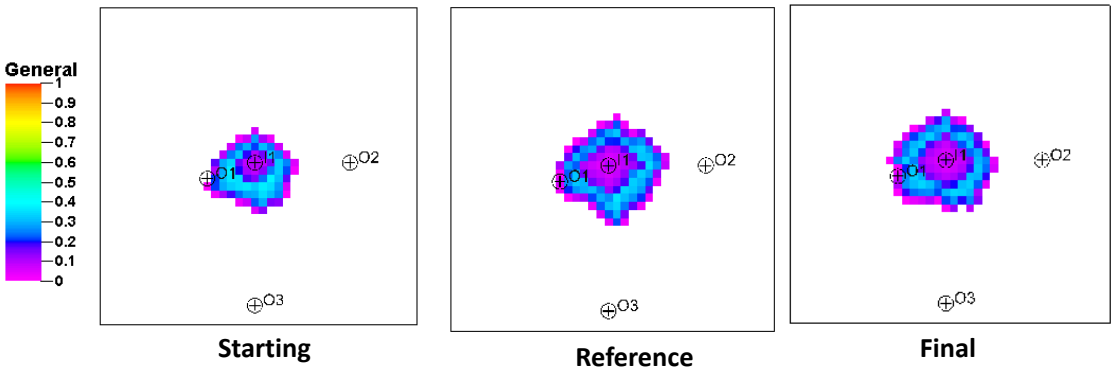


**Fig. 3.39 – Gas saturation difference between gas saturation at the end of the 3rd year (end of two year forecasting) and 1st year (end of history matching period) for starting, reference and final (after proposed approach) models.**

For better understanding of the improvement in the spatial distribution of the gas saturation difference at the end of the 3rd year and 1st year for the final model, a cross-plot of comparison of gas saturation difference (**Fig. 3.39**) for the reference and final model (after proposed approach) along with reference and starting model is illustrated in **Fig. 3.40**. It can be observed that the coefficient of correlation has improved significantly from 0.73 to 0.88 after the proposed approach.

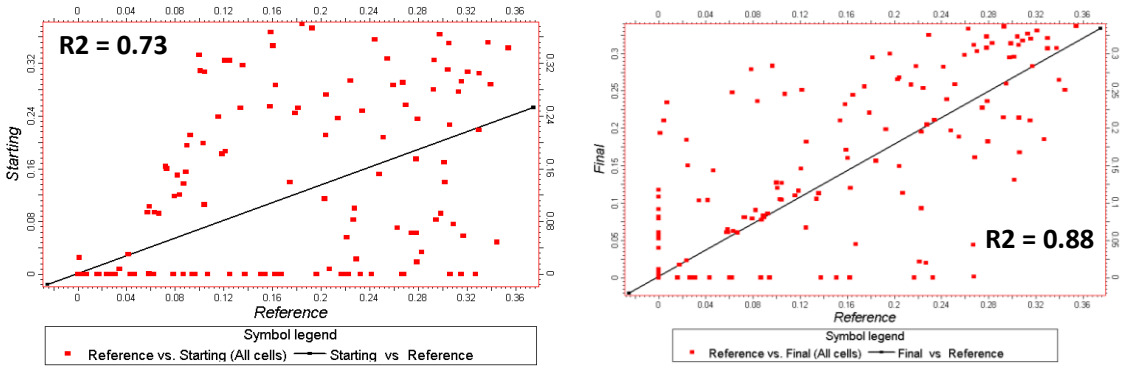


**Fig. 3.40 – Cross-plot comparison of gas saturation difference at the end of 3rd year and 1st year for the reference and final models (right), reference and starting models (left).**

The proposed approach described in **section 3.2** has been applied to 2-D synthetic cases for $CO_2$ sequestration using full physics compositional model.

### 3.4.2 3-D Example

The proposed workflow (**Fig. 3.1**) is now demonstrated on a 3-D simulation model. The historical pressure data for inversion has been generated using a 3-D synthetic model. This synthetic model was generated using sequential Gaussian simulation of the porosity well log data from an actual $CO_2$ injection well. This $CO_2$ injection well (Weaber horn) is located in the Illinois basin and is drilled through Mt. Simon sandstone formation which is considered to be a good candidate for $CO_2$ sequestration (Finley, 2005). Mt. Simon formation is overlain by three thick shale formations which will act as good seals during $CO_2$ sequestration. Permeability field was generated using a permeability-porosity correlation derived from the core data of Weaber horn well. This synthetic model is referred as the 'reference model' in this study. The principal features of the reference model are as follows,

1. Model dimension is 40000 feet x 40000 feet x 1319 feet.
2. Number of gridcells in X direction = 40, Number of gridcells in Y direction = 40, Number of layers = 55.
3. Grid cell dimension in X direction = Grid cell dimension in Y direction = 1000 ft.
4. The 3-D model consists of pore-volume multipliers at the boundary to simulate a large reservoir.
5. Permeability in X direction = Permeability in Y direction = 10 times the permeability in Z direction.
6. Top of the reservoir is @ 7011 feet and bottom of the reservoir is 8330 feet.
7. Equilibrated pressure is 1972 psi @ 7011 feet (top of reservoir).
8. Compositional model used in described in **section 3.4.1**.
9. Well is in the middle of the simulation model @ i =20, j = 20, perforated in 150 feet thick ~1 darcy zone near the bottom of the formation (Layer no. 49).

10. Injection rate for 500000 metric tonnes of $CO_2$ / year, which is approximately 23 mmscf/day.
11. Well efficiency factor is 0.92 (11 months of injection followed by 1 month of shut-in).
12. Three observation well O1, O2 and O3 are at different distances from injection well I1 as shown in **Fig. 3.41**. O1 is ~1 mile from I1, O2 is ~ 2 miles from I1 and O3 is ~ 3 miles from I1.
13. Three observation wells measuring bottom-hole pressure @ 8150 feet in the 49$^{th}$ layer.
14. Simulation time is 1 year and bottom-hole pressure observations are taken every day (@ 8150 feet).

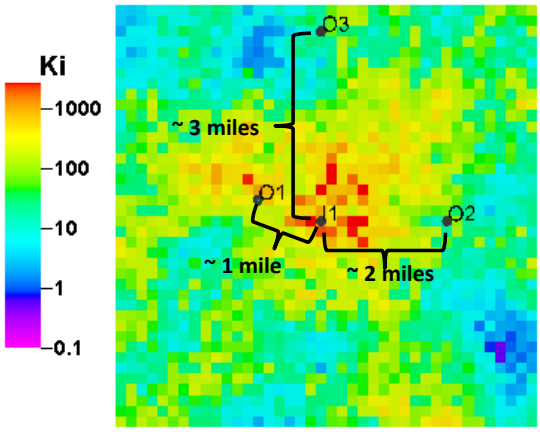


**Fig. 3.41 – Well locations and their relative distances are shown on the permeability map (md) of the 49$^{th}$ layer of the 3-D model.**

The variogram used for porosity population in the 3-D reference model is illustrated in **Fig. 3.42** along with the variogram inputs. The porosity field using sequential Gaussian simulation is shown in **Fig. 3.42**.

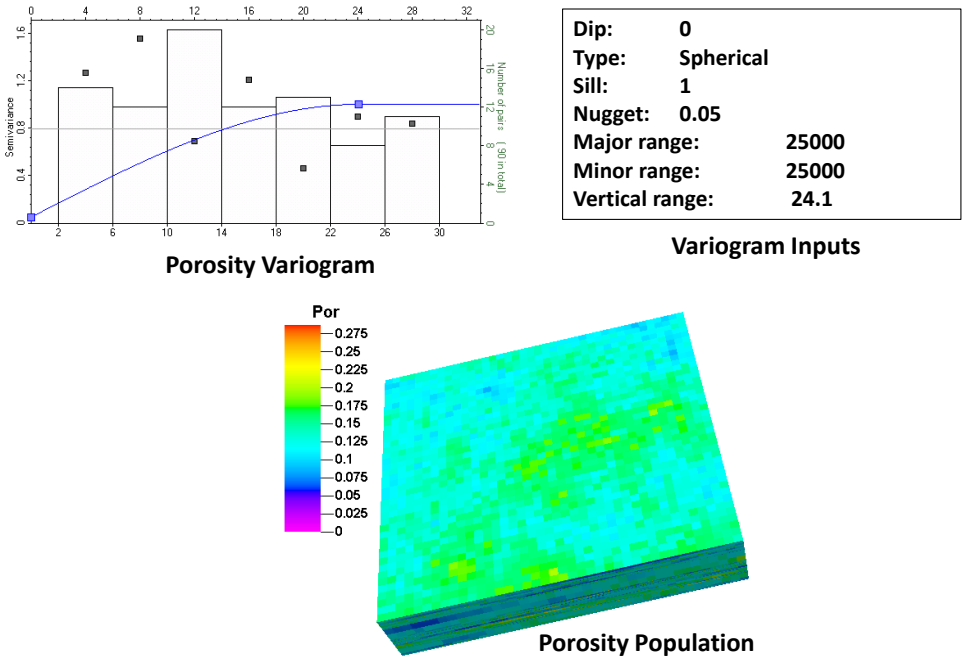


**Fig. 3.42 – Porosity variogram along with input parameters used for populating porosity in the reference model.**

The permeability in the reference model is generated using a permeability-porosity correlation based on the available core data and is shown in **Fig. 3.43**. The vertical section (X-Y) of permeability through injection well I1 is also illustrated in **Fig. 3.43**. The histogram of the populated permeability shows that most of the permeability lies between 10 md and 1000 md. Maximum permeability is limited to 2600 md based on the core data.

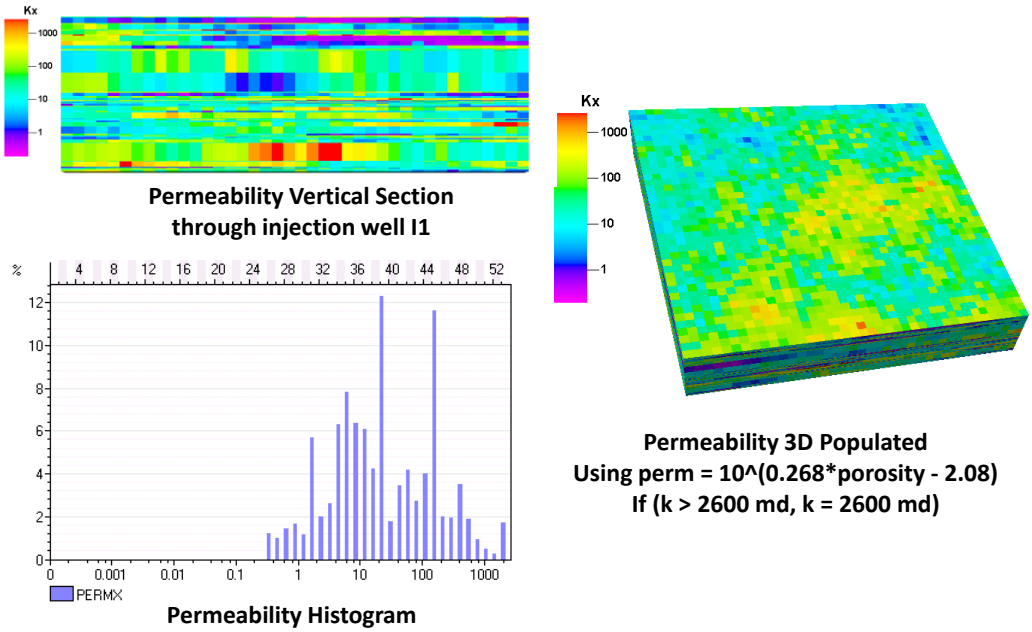


**Fig. 3.43 –Reference model permeability population for the 3-D model.**

Starting (initial) porosity field was generated using the same variogram but different random number for sequential Gaussian simulation. Care was taken that the there was a very little difference in total pore-volume between reference and starting field. The same porosity-permeability transform as in the reference model was used to generate the permeability field shown in **Fig. 3.44**.

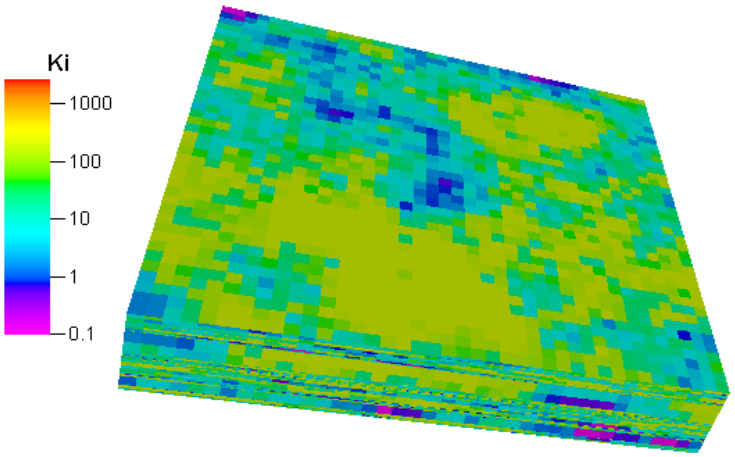


**Fig. 3.44 – Starting (initial) model permeability (md) for the 3-D model.**

Due to small improvement in bottom-hole pressure matches of all wells using pore-volume calibration as presented in **section 3.4.1.2.1.** , it will not be performed for the 3-D model.

### 3.4.2.1 Bottom-hole Pressure Inversion

Bottom-hole pressure (BHP) inversion is carried out using the method described in **section 3.2.2.** The improved pressure match for injector I1 is shown in **Fig. 3.45**. A considerable improvement in the pressure match is observed.

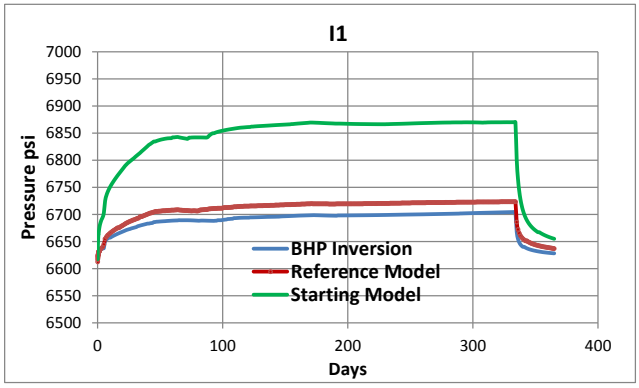


**Fig. 3.45 – Bottom-hole pressure match for well I1 after BHP inversion.**

A bottom-hole pressure match after BHP inversion for the observation wells is shown in **Fig. 3.46**. Significant improvement is seen for the observation wells O1 and O2 in spite of having measurements only in the 49$^{th}$ layer. The bottom-hole pressure match for well O3 has slightly worsened after BHP inversion, possibly due to the fact that it is farthest from the injection well I1.

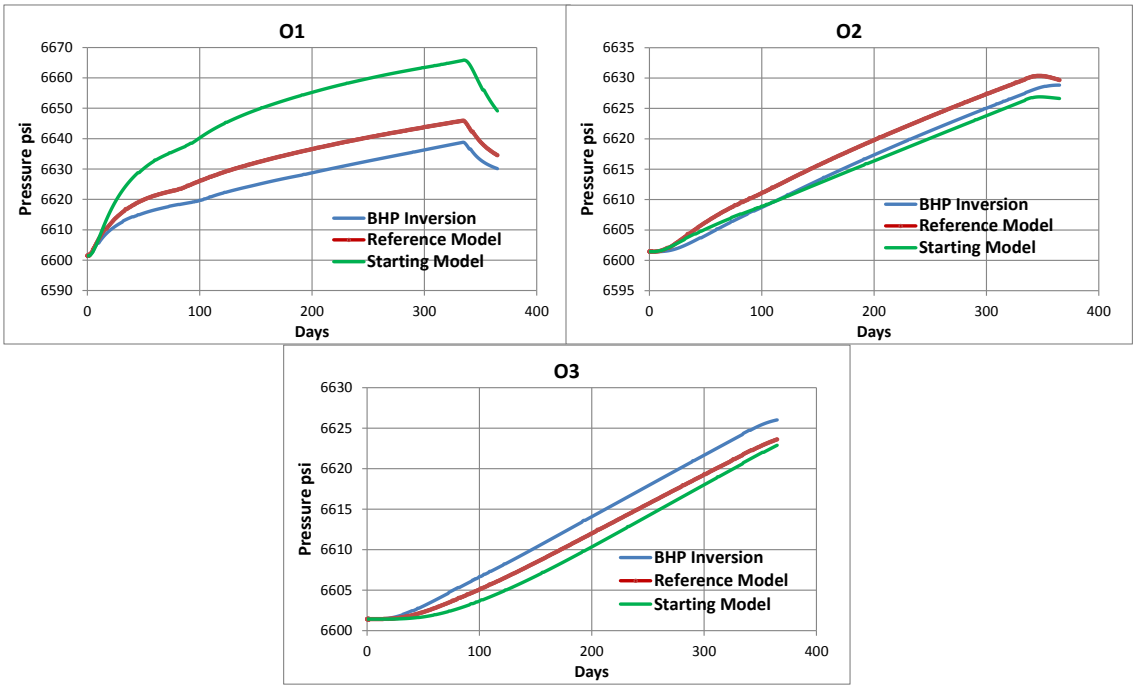


**Fig. 3.46 – Bottom-hole pressure match for observation wells O1, O2 and O3 after BHP inversion.**

The permeability field after BHP inversion is compared to the reference and starting (initial) permeability field for the layers 49$^{th}$, 47$^{th}$ and 45$^{th}$ in **Fig. 3.47**. Layers 44 to 49 were more sensitive to BHP sensitivities than other layers as the injection is taking place in the 49$^{th}$ layer and the $CO_2$ plume is rising due to buoyancy. Some improvements are observed in the BHP inverted permeability field compared to the starting (initial) permeability.

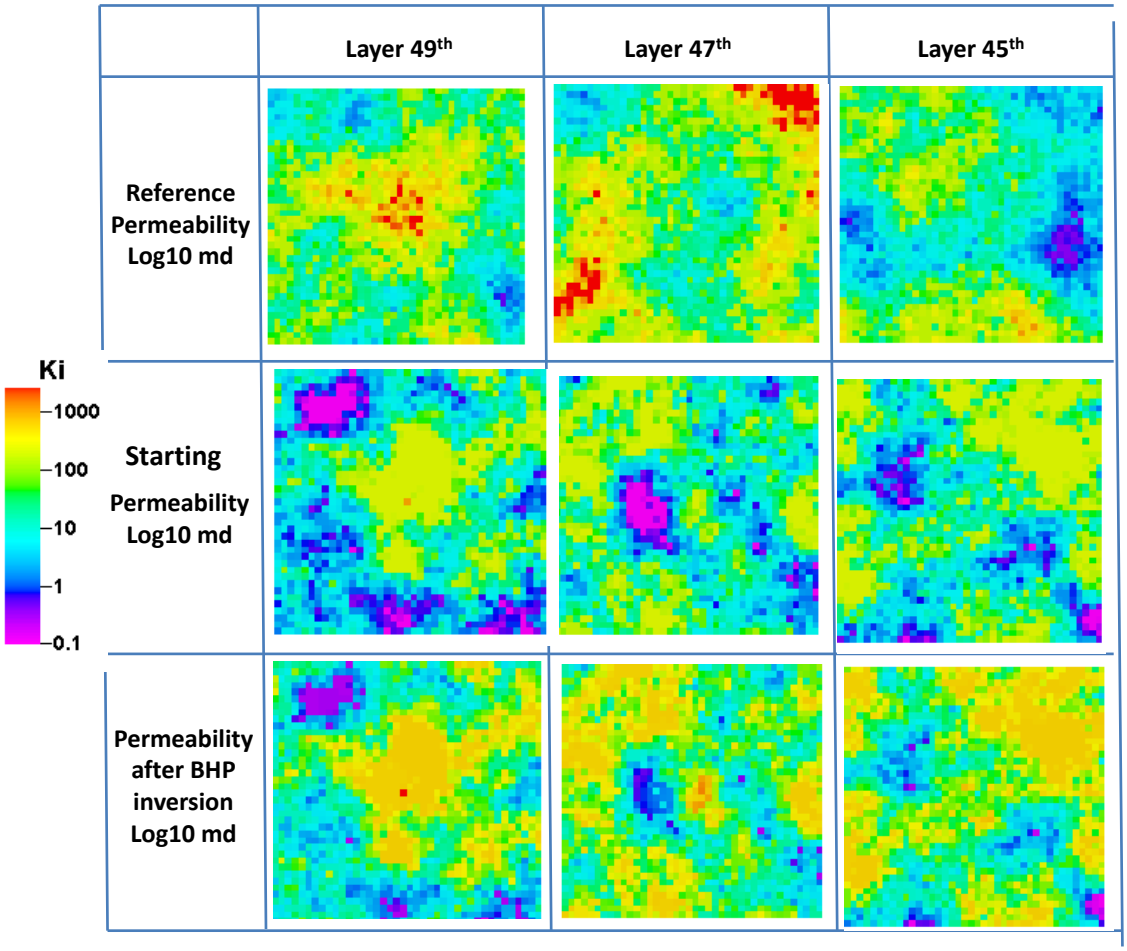


**Fig. 3.47 – Permeability field (md) after BHP inversion for layers 49, 47 and 45 compared to reference and starting (initial) permeability field.**

For further understanding, the changes in permeability made after BHP inversion are compared to the permeability changes required for layers 49$^{th}$, 47$^{th}$ and 45$^{th}$ in **Fig. 3.48**. Permeability changes required are derived by subtracting starting (initial) permeability field from reference permeability field.

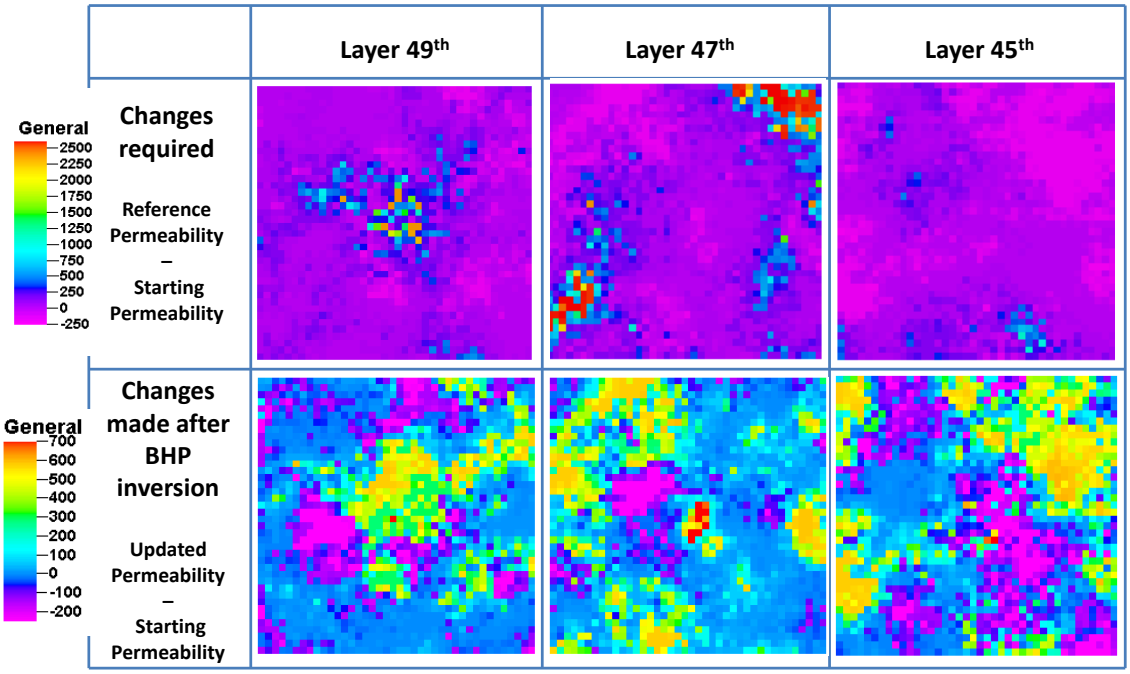


**Fig. 3.48 –Permeability changes required (md) are compared with changes made after BHP inversion for layers 49, 47 and 45.**

The changes made after BHP inversion are quite similar when compared to the changes required for 49$^{th}$ layer. But the results are not quite similar for 47$^{th}$ and 45$^{th}$ layers possibly due to the fact that pressure measurements are only taken for layer 49$^{th}$ and there is not enough pressure data to resolve the layers 47$^{th}$ and 45$^{th}$. With the limited pressure data, it is not expected to reproduce the permeability field in the 3-D.

### 3.4.2.2 Pressure Peak Arrival-time Inversion

After BHP inversion, pressure peak arrival time inversion for observations wells O1, O2 and O3 is carried out using compositional streamline tracing as described in **Appendix B.1**. The peak arrival time improvement after pressure arrival–time inversion is shown in **Fig. 3.49**. The peak arrival time after pressure peak arrival time inversion (X axis) is compared to reference model peak arrival time (Y axis). It can be observed that only observation well O3 has shown improvement regards to peak arrival time after BHP inversion.

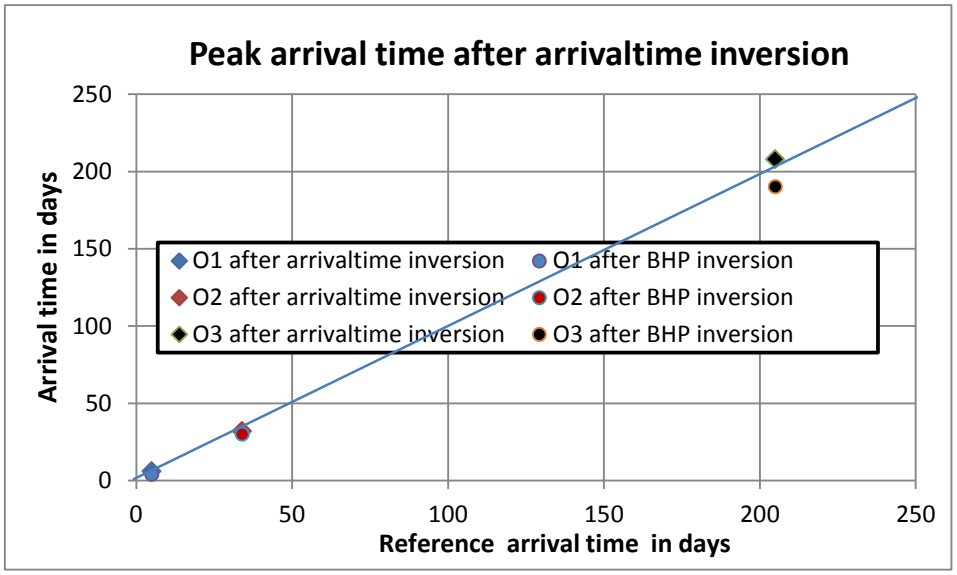


**Fig. 3.49 – Peak arrival time comparison between pressure peak arrival time inversion and BHP inversion.**

A little improvement is observed in pressure match for injector I1 after arrival time inversion is shown in **Fig. 3.50**.

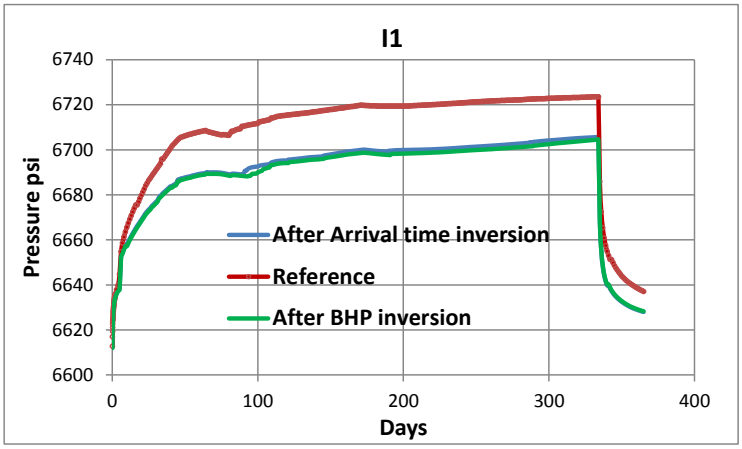


**Fig. 3.50 – Bottom-hole pressure match for well I1 after pressure peak arrival time inversion (blue) compared to bottom-hole pressure after BHP inversion (green).**

The bottom-hole pressures for observation wells O1, O2 and O3 after pressure peak arrival time inversion are shown in **Fig. 3.51**. No improvement in bottom-hole pressure match is observed for well O1 and O2. However, improvement is observed in bottom-hole pressure match for well O3 which is congruent to improvement in peak arrival time match fro well O3, illustrated in **Fig. 3.49**.

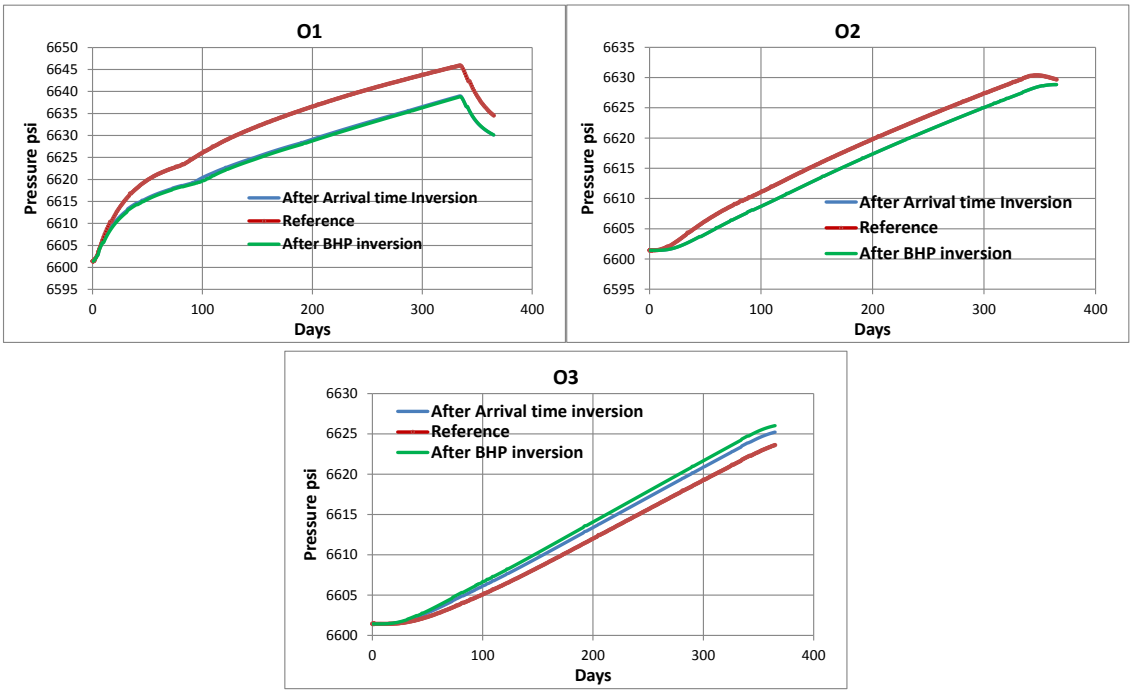


**Fig. 3.51 – Bottom-hole pressure match for observation wells O1, O2 and O3 after pressure peak arrival time inversion (blue) compared to bottom-hole pressure after BHP inversion (green).**

The permeability field after pressure peak arrival time inversion is compared to the reference permeability field and permeability field after BHP inversion for layers 49, 47 and 45 in **Fig. 3.52**. Improvement is seen in the area between well O3 and I1 over the permeability field derived after BHP inversion. This new improvement after pressure peak arrival time inversion corresponds to low permeability region around well O3 in the reference model. This permeability improvement around well O3 is consistent with the arrival time improvement for well O3 in **Fig. 3.49**.

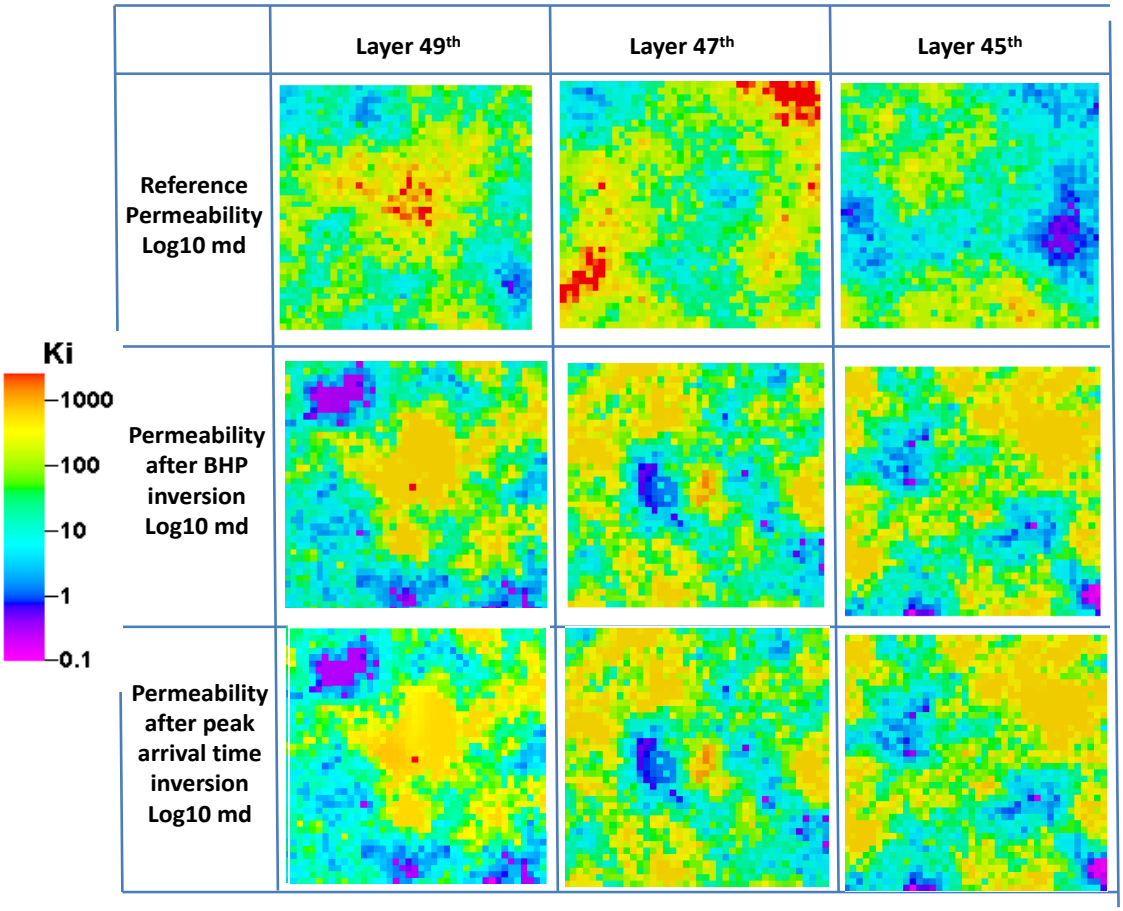


**Fig. 3.52 – Permeability field (md) after pressure peak arrival time inversion for layers 49, 47 and 45 compared to reference and permeability field after BHP inversion.**

The permeability changes made to the permeability after BHP inversion and after pressure peak arrival time inversion are illustrated for layer 49$^{th}$, 47$^{th}$ and 45$^{th}$ in **Fig. 3.52**. It can be observed that a lower permeability area around well O3 is generated during pressure peak arrival time inversion resulting in improvement in peak arrival time match for well O3 (after BHP inversion) as illustrated in **Fig. 3.53**. The lowering of permeability is only present in the 49$^{th}$ layer. There are no changes to permeability for 47$^{th}$ and 45$^{th}$ layers, after BHP inversion. This is due to the fact that pressure measurements are only taken for 49$^{th}$ layer and therefore peak arrival time inversion is only done using pressure trajectories (represented by streamlines) passing through

observation wells in the 49th layer. There is not enough pressure data to resolve remaining layers. More pressure measurements will help in resolving remaining layers.

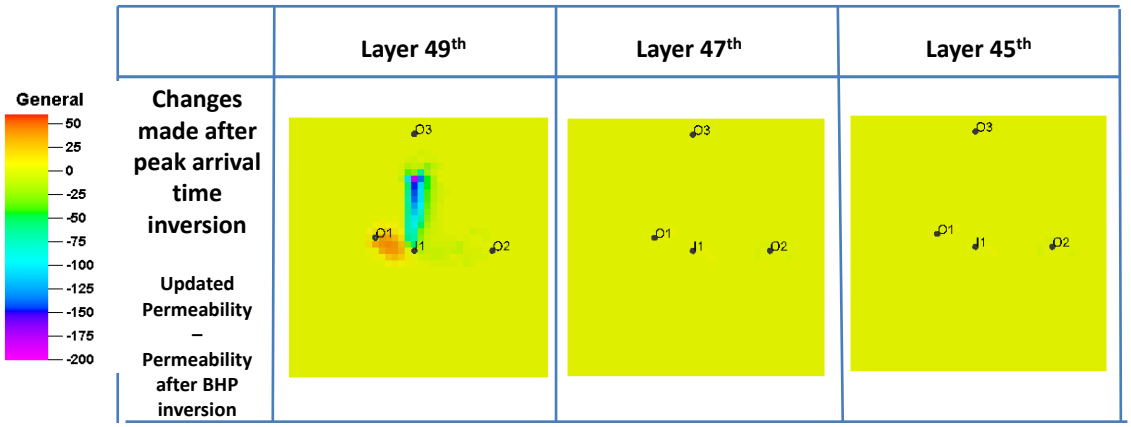


**Fig. 3.53 – Permeability changes (md) made after pressure peak arrival time inversion for layers 49, 47 and 45.**

### 3.4.2.3 Gradient Based Constant Permeability Multiplier Inversion

In the final stage of the proposed approach a gradient based optimization technique using perturbation sensitivities is used to modify global multiplier on permeability in X direction. The final multiplier obtained on permeability after arrival time inversion is 0.775. The bottom-hole pressure results using this multiplier for injector I1 is shown in **Fig. 3.54**. A very good match to the reference pressure is observed for the injector well I1. Also significant improvement in the bottom-hole pressure after arrival time inversion is observed in **Fig. 3.54**.

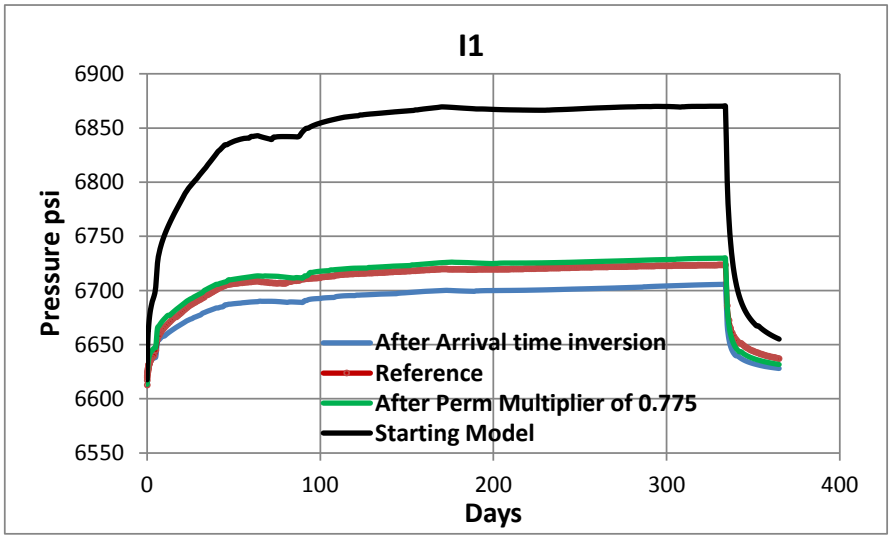


**Fig. 3.54 – Bottom-hole pressure match for well I1 after global permeability multiplier (green) compared to bottom-hole pressure after arrival time inversion (blue).**

Similarly a good bottom-hole pressure match after global permeability multiplier is observed for three observation wells O1, O2 and O3 in **Fig. 3.55**. There is considerable improvement in bottom-hole pressure compared to the result from starting (initial) model.

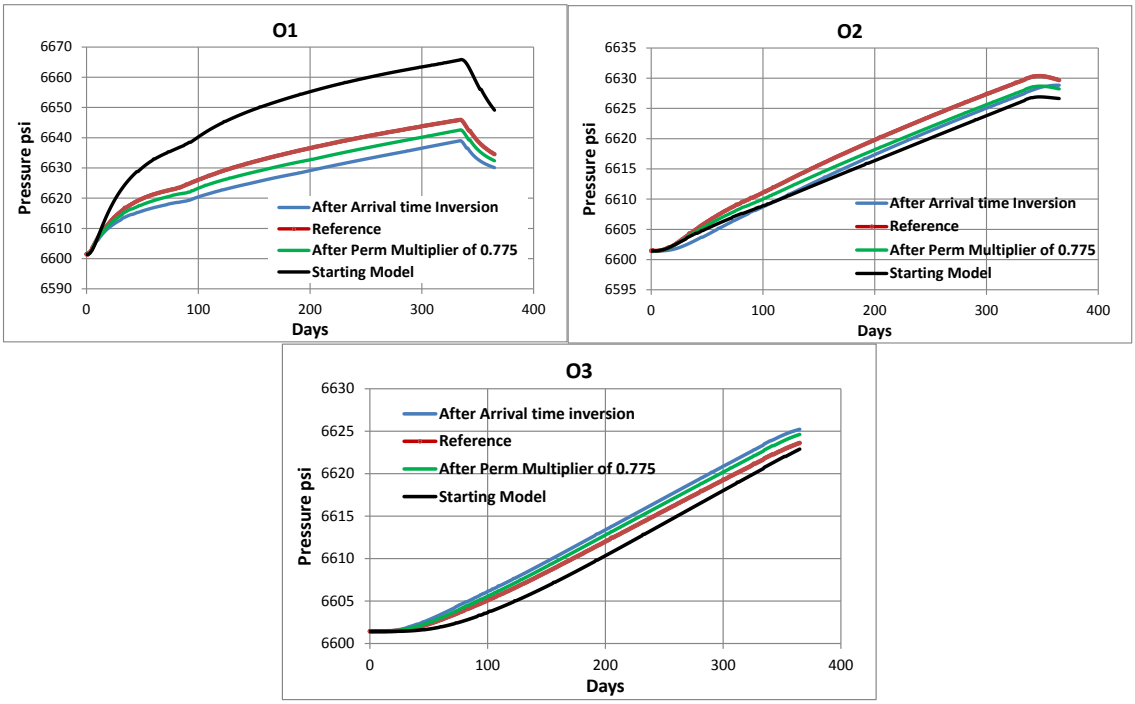


**Fig. 3.55 – Bottom-hole pressure match for observation wells O1, O2 and O3 after global permeability multiplier (green) compared to bottom-hole pressure after arrival time inversion (blue) and starting model (black).**

The permeability field after global permeability multiplier is compared to the reference permeability field and permeability after arrival time inversion for layer 49$^{th}$, 47$^{th}$ and 45$^{th}$ in **Fig. 3.56**. An overall lower shift in permeability to a lower side is observed over permeability field derived after the arrival time inversion. This lowering of the mean permeability is consistent with reference mean permeability.

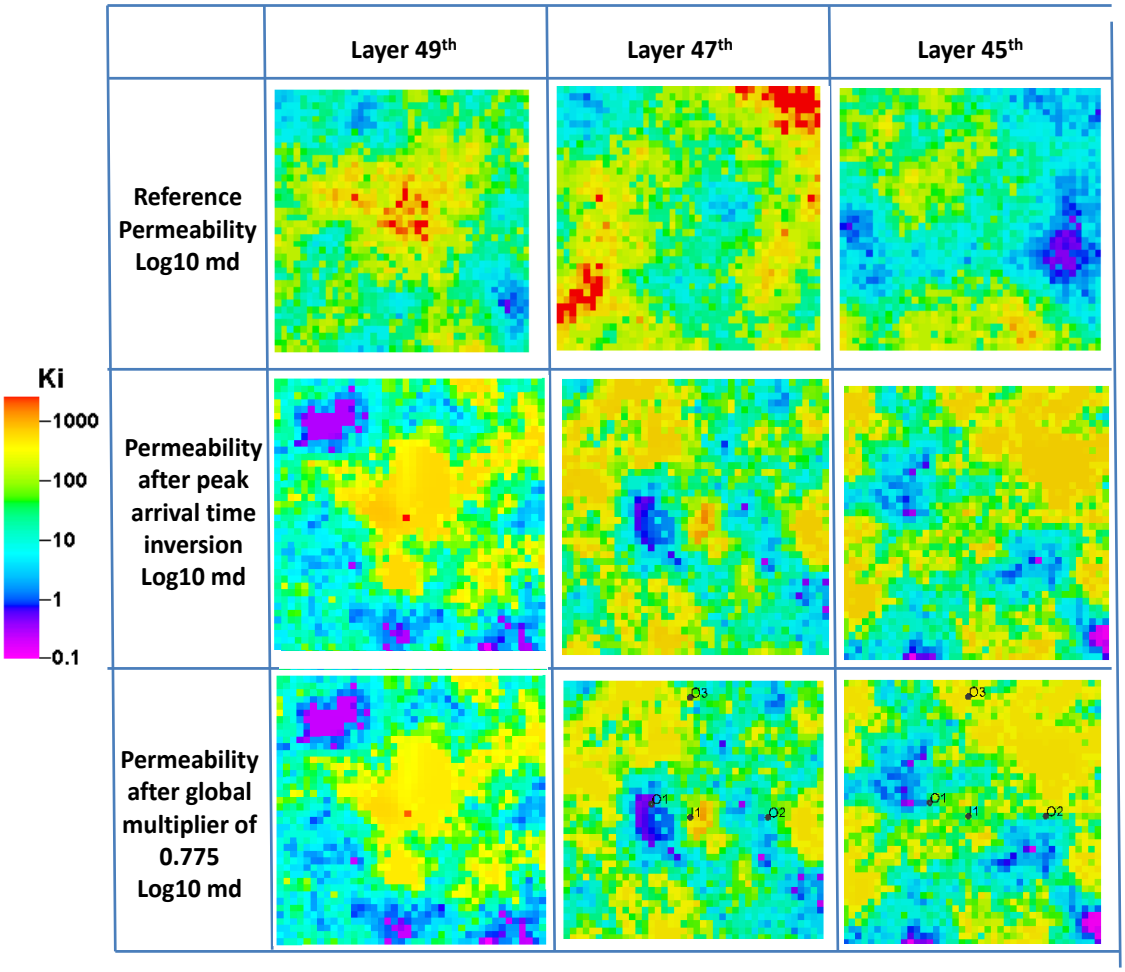


**Fig. 3.56 – Permeability field (md) after global permeability multiplier for layers 49, 47 and 45 is compared to reference and permeability field after arrival time inversion.**

The permeability field after global permeability multiplier is compared to the reference permeability field and starting permeability field for layer 49$^{th}$, 47$^{th}$ and 45$^{th}$ in **Fig. 3.57**.

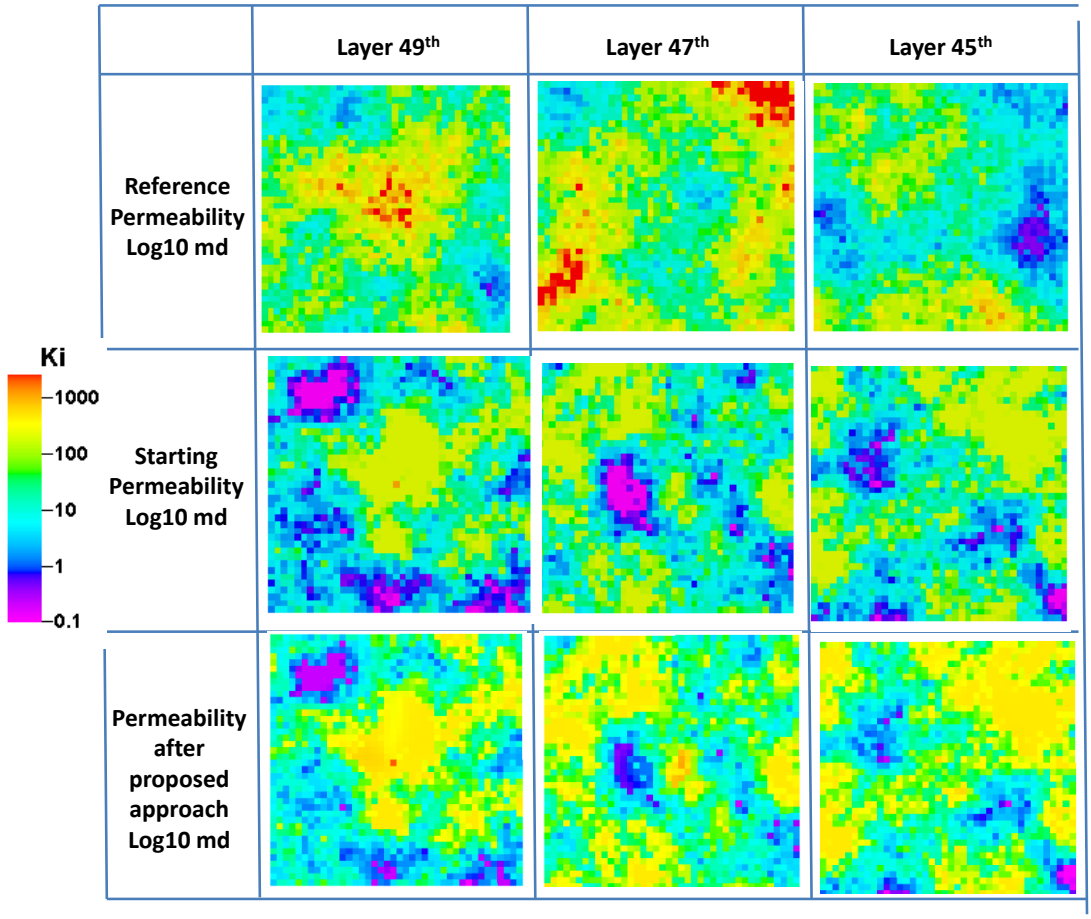


**Fig. 3.57 – Permeability field (md) after global permeability multiplier for layers 49, 47 and 45 is compared to reference and starting permeability field.**

For better understanding, the changes made after the proposed approach to the starting model are compared to the changes required in the starting model to match the reference model for layer 49$^{th}$, 47$^{th}$ and 45$^{th}$ in **Fig. 3.58.**

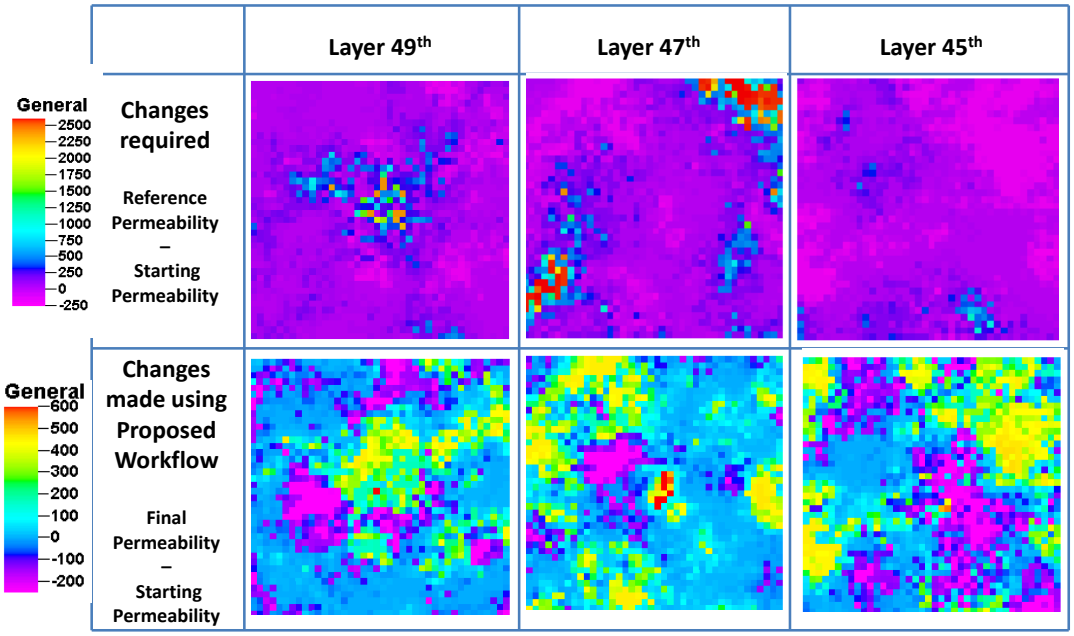


**Fig. 3.58 – Changes made after the proposed approach to the starting permeability field are compared to changes required for the layers 49, 47 and 45.**

It can be observed that the results for the final permeability field after proposed approach are not quite similar to the reference model. This is expected because of the fact that pressure measurements are only taken for injection layer ($49^{th}$) and there is not enough pressure data to resolve layers other layers. The 3-D inversion problem is highly non-unique and multiple permeability distributions will be able match the given pressure data. To address the non-uniqueness, the inversion is 'anchored' to the prior geological model using the 'norm' constraint discussed in **section 3.2.2**. Also, because of the diffusive nature of the pressure, the problem of bottom-hole pressure inversion is more suited to infer large scale continuity than small scale variation. For better resolving of permeability, extra dynamic information is needed. This extra information can be in form of time lapse seismic or more bottom-hole pressure data at different depths along the wells, above the injection layer. Time lapse seismic should be scheduled such that $CO_2$ plume has covered considerable volume in the reservoir to enable resolution of more spatial information.

### 3.4.2.4 Validation of History Matching

History matched model is validated by forecasting the bottom-hole pressure performance of the history matched model after proposed approach and comparing it with reference and starting (initial) model. The forecast period is for two years after 11 months of $CO_2$ injection at the rate of 25000 reservoir barrels per day, followed by 1 month of shut-in. The result for injection well I1 is illustrated in **Fig. 3.59**. On right a zoomed view is shown. Excellent agreement is observed for bottom-hole pressure for reference and history matched model in the forecast period after proposed approach.

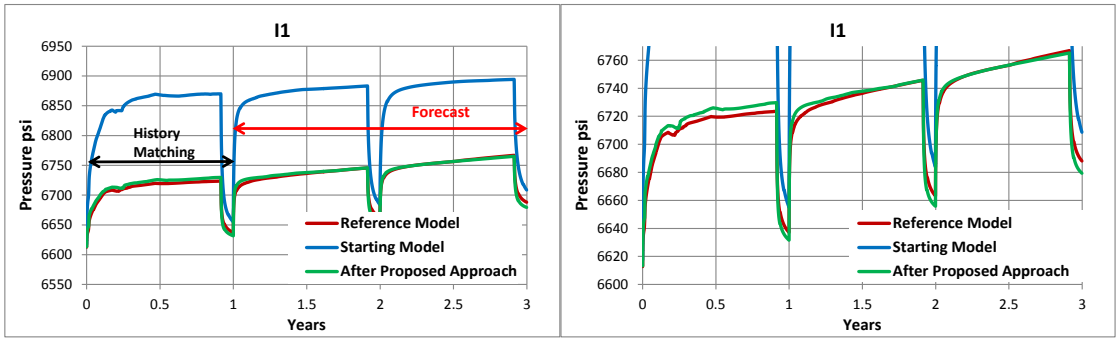


**Fig. 3.59 – Comparison of forecast of bottom-hole pressure for injection well I1 for history matched, reference and starting model. Zoomed view is shown on right. History matching is performed for 1 year followed by 2 years of forecasting.**

Similarly the results for observation wells O1, O2 and O3 are illustrated in **Fig. 3.60**. Barring well O3, a good agreement is observed for reference and history matched model in the forecast period after the proposed approach.

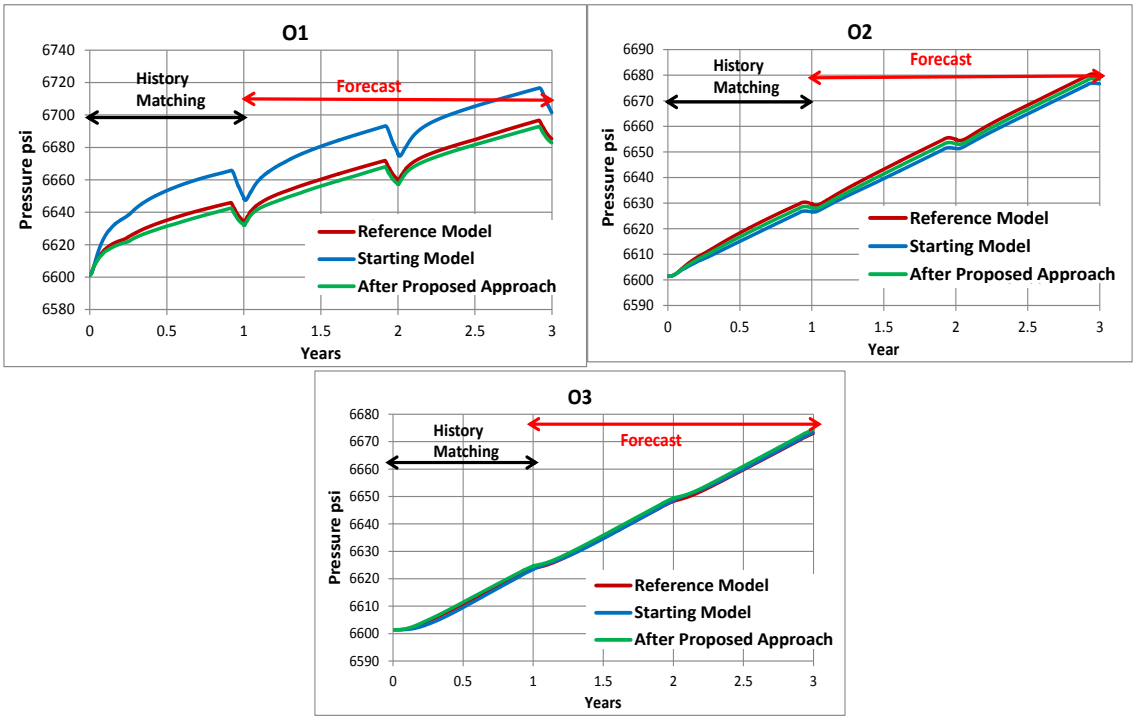


**Fig. 3.60 – Comparison of forecast of bottom-hole pressure for observation wells O1, O2 and O3 for history matched, reference and starting model. History matching is performed for 1 year followed by 2 years of forecasting.**

For better understanding of the improvement in bottom-hole pressure results, a cross-plot of gas saturation difference between 3$^{rd}$ year (end of forecasting) and 1$^{st}$ year (end of history matching) for the reference and final model (after proposed approach) along with reference and starting model is illustrated in **Fig. 3.61**. It can be observed that the coefficient of correlation has improved significantly from 0.715 to 0.78 after the proposed approach. This shows the value addition in $CO_2$ gas saturation estimation during forecasting in the simulation model using proposed approach for the bottom-hole pressure integration.

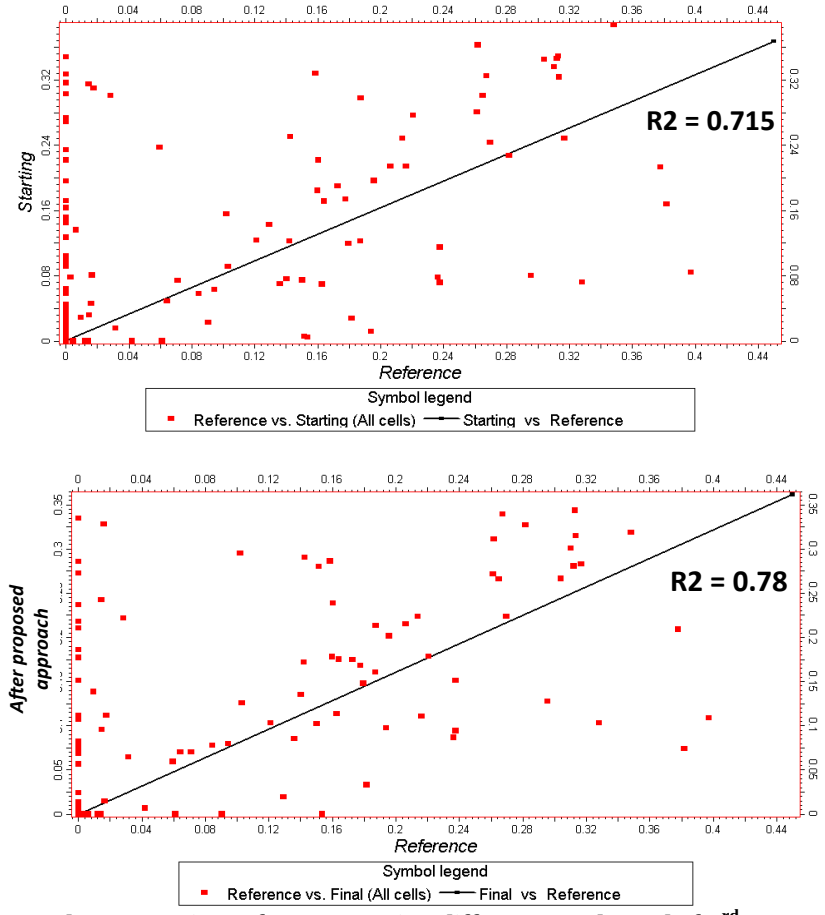


**Fig. 3.61 – Cross-plot comparison of gas saturation difference at the end of 3rd year and 1st year for the reference and final (after proposed) models (bottom), reference and starting models (top).**

### 3.4.2.5 Time-lapse Seismic History Matching

From the discussion in **section 3.4.2.3**, it was noted that for better resolution of permeability and prediction of gas saturation, extra dynamic information like time lapse seismic is needed. A demonstrative example of how time-lapse seismic can help will be illustrated in this section. In this work, the compositional streamlines are utilized (**Appendix B.1**) to determine the sensitivity of difference of time-lapse seismic attributes (Impendence or gas saturation derived from it) to changes in reservoir properties such as permeability (Rey et al., 2010). The sensitivities are then used in an

inverse modeling algorithm to calibrate the simulation model to time-lapse seismic data. The outcome is an improved description of permeability heterogeneity and spatial gas saturation distribution that is consistent with the 4-D seismic response. The details of the process along with the sensitivity derivation are discussed in Rey et al., (2010).

In this demonstration, time-lapse gas saturation will be used, although this inversion can be carried out easily for seismic impedance. It is assumed that gas saturation information is available at the end of $4^{th}$ and $12^{th}$ month. The objective in the time-lapse inversion is to minimize the difference between observed difference of gas saturation at the end of $4^{th}$ and $12^{th}$ month and simulated difference of gas saturation at the end of $4^{th}$ and $12^{th}$ month. Here difference in gas saturation is used because it captures the evolution of the gas saturation. This is much more non-unique problem than integrating single gas saturation surveys (Rey et al., 2010). Therefore, regularization terms are included to ensure spatial continuity and geologic realism (Yoon et al., 2001).

The permeability field after seismic inversion is compared to the reference and permeability field after the proposed approach in **Fig. 3.62**, for the layers $49^{th}$, $47^{th}$ and $45^{th}$. Most of the permeability change is in area around the injector.

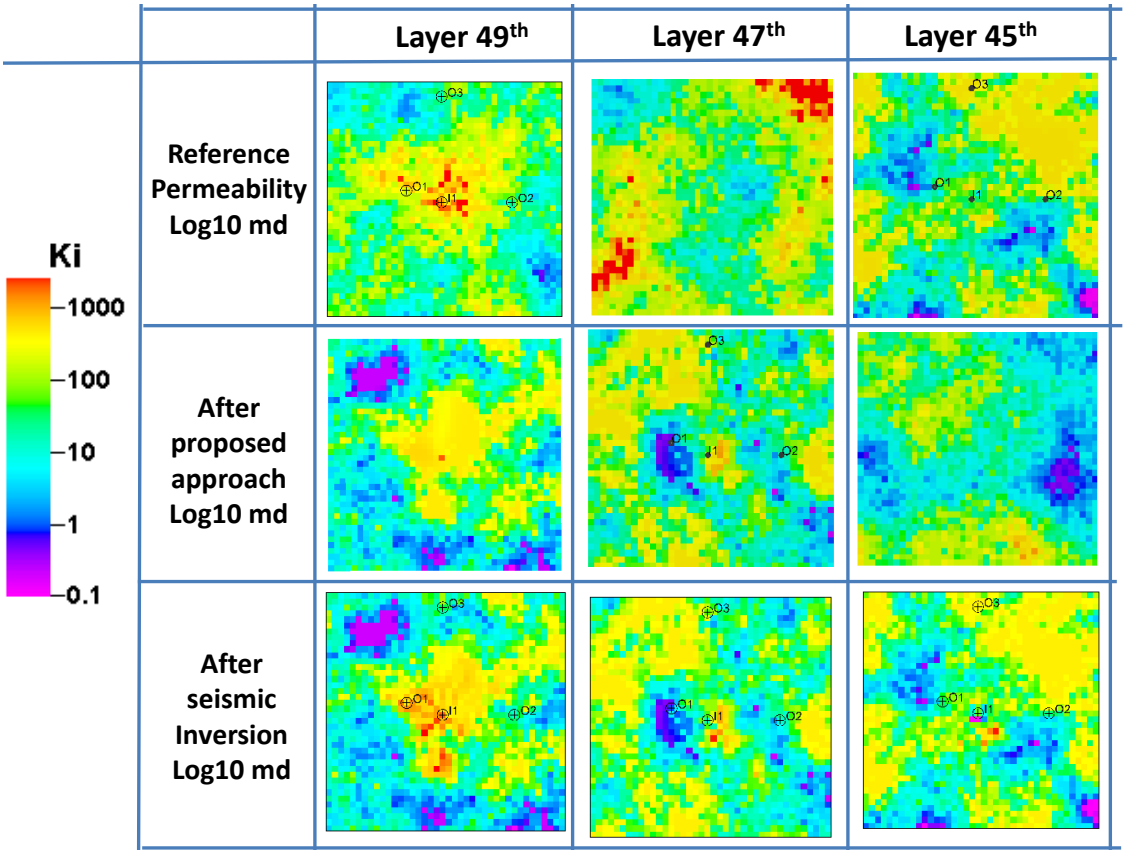


**Fig. 3.62 – Permeability field (md) after seismic inversion for layers 49, 47 and 45 is compared to reference and permeability field after proposed approach.**

For better understanding, changes made in the permeability after the seismic inversion are compared to the changes required in the permeability after proposed approach in **Fig. 3.63**. It can be observed that all the changes are in the area surrounding the injector well as the information provided by the gas saturation is in limited area around the injector well.

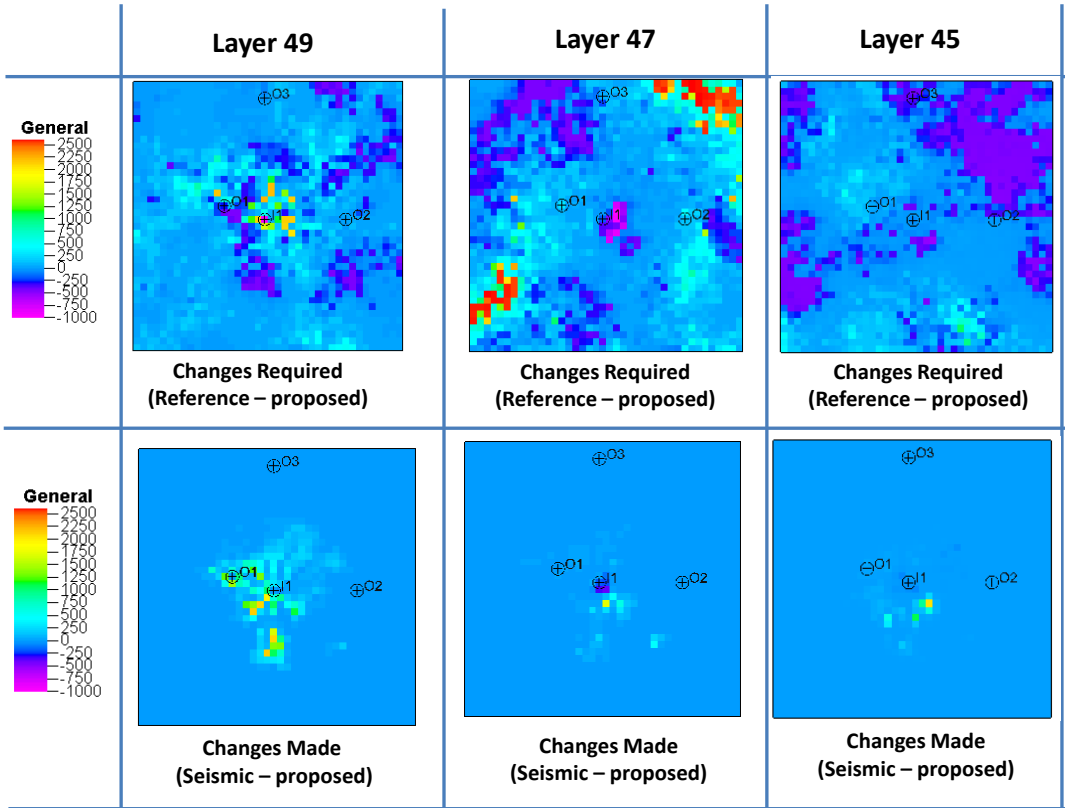


**Fig. 3.63 – Permeability (md) changes made after seismic inversion for layers 49, 47 and 45 is compared to the changes required in the permeability field after proposed approach.**

A similar forecast is run on the final seismic inverted model as in **section 3.4.2.4**. A cross-plot of gas saturation difference between 3$^{rd}$ year (end of forecasting) and 1$^{st}$ year (end of history matching) for the reference and seismic inverted model along with reference and bottom-hole pressure inverted model (after proposed approach) is illustrated in **Fig. 3.64**. It can be observed that the coefficient of correlation has improved significantly from 0.78 to 0.85 after the proposed approach. This shows the value addition in $CO_2$ gas saturation estimation during forecasting in the simulation model after time-lapse seismic data integration.

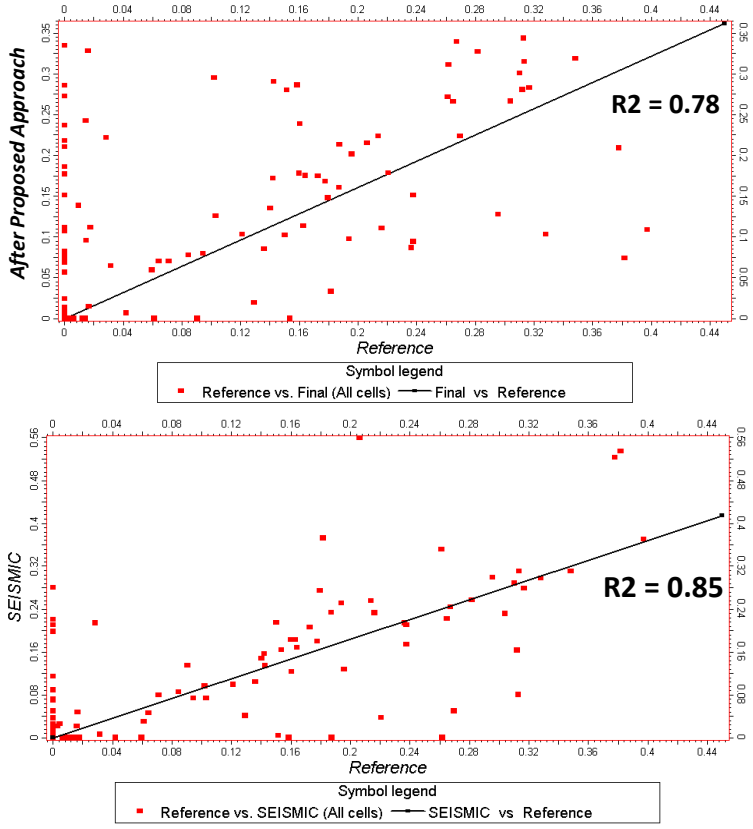


**Fig. 3.64 – Cross-plot comparison of gas saturation difference at the end of 3rd year and 1st year for the reference and after seismic inversion models (bottom), reference and after proposed approach models (top).**

Although the objective of the seismic inversion here is calibrate spatial gas saturation the inversion has helped in improving bottom-hole pressure match in injector I1 and observation well O1 as compared to proposed approach as illustrated in **Fig. 3.65**. There is no change in the pressure match for observation wells O2 and O3 as they are away for the region where changes were made.

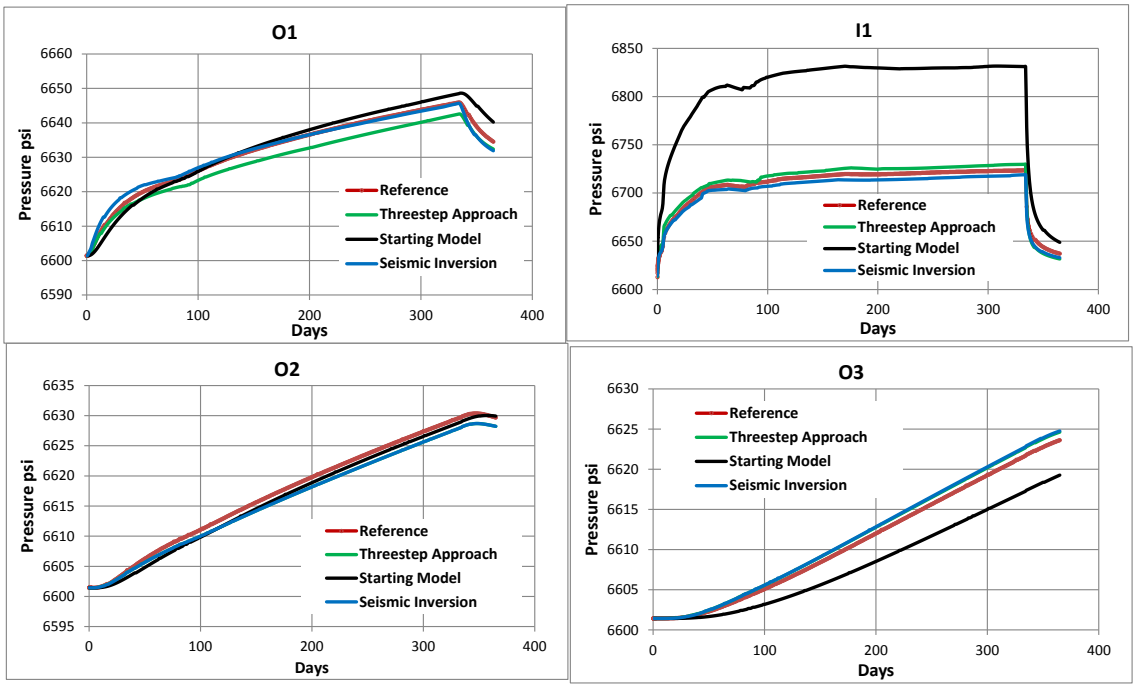


**Fig. 3.65 – Comparison of bottom-hole pressure for all wells after seismic inversion to the reference, starting and after proposed approach models.**

## 3.5 Summary and Conclusions

A novel proposed approach to update geological models using bottom-hole pressure data injection and observation wells during $CO_2$ sequestration has been proposed. In the proposed approach, the first step consists of volume calibration using information from pseudo-steady state flow regime of the injection well. This is followed by bottom-hole pressure inversion of zeroth-order frequency (mean) of the bottom-hole pressure at the injection well. This is followed by peak pressure arrival time inversion at the observation wells. As a last step, a gradient minimization technique is used to modify global multiplier of permeability (X direction).

The proposed approach has been demonstrated on a 2-D synthetic model with two cases. In the first case where the starting model is geo-statistically similar to the reference model, the approach has been successful in matching the bottom-hole pressure at the injection and observation wells. An improved correlation coefficient was obtained

for the gas saturation difference between end of forecast and end of history matching for the final model compared to the starting model.

For the second case where the starting model is geo-statistically dissimilar to the reference model, the approach has been successful in reproducing the large-scale features of the reference field. In addition excellent match was obtained for the bottom-hole pressures of all the wells and peak arrival time of observation wells for both cases. Finally, the forecasting capability of the inverted model after proposed approach compared reasonably well to the reference case for both cases. Also, an improved correlation coefficient was obtained for the gas saturation difference between end of forecast and end of history matching for the final model compared to the starting model.

The proposed approach was also applied to a 3-D model with injection in a high permeability layer with encouraging results. The final bottom-hole pressure results showed satisfactory match with the reference model. However, the 3-D problem is highly non-unique and there can be multiple permeability fields matching the data. Also, because of the diffusive nature of the pressure, the problem of bottom-hole pressure inversion is more suited to infer large scale continuity than small scale variations. In the proposed approach, the condition of 'proximity' to the prior (starting) model is imposed. The forecast results for the injection and observation wells were satisfactory and improved correlation coefficient was obtained for the gas saturation difference between end of forecast and end of history matching for the final model compared to the starting model. For better resolution of permeability, extra dynamic information is needed. This extra information can be in form of time lapse seismic or more bottom-hole pressure data at different well locations. A simple illustration of integrating seismic data (gas saturation surveys) to improve gas saturation forecast is discussed.

The proposed work only deals with the data integration of bottom-hole pressure data during $CO_2$ sequestration. Besides permeability, other uncertainties in bottom-hole pressure integration such as anisotropy and relative permeability need to be explored. The value addition of extra information in resolving permeability field can be studied. The extra information can be time lapse seismic or more bottom-hole pressure data at

different locations. Also, the pressure calibrated model can be used for the optimization of $CO_2$ sequestration (Flett et al., 2007) which deals with maximization of hydro-dynamically trapped $CO_2$. In addition, the optimization of location and number of injection wells to maximize $CO_2$ trapping and minimize costs can also be explored.

# CHAPTER IV

# OPTIMAL WATER FLOOD MANAGEMENT UNDER GEOLOGICAL UNCERTAINTY USING ACCELERATED PRODUCTION STRATEGY*

## 4.1 Summary

Waterflood optimization via rate control is receiving increased attention because of rapid developments in the smart well completions and i-field technology. The use of inflow control valves (ICV) allows us to optimize the production/injection rates of various segments along the wellbore, thereby maximizing sweep efficiency and delaying water breakthrough. A practical and efficient approach is proposed for computing optimal injection and production rates given multiple geologic models with application to smart wells. Specifically, the trade-off between maximizing oil recovery vs. maximizing NPV is examined using a penalized misfit function (norm term) for optimization. The waterflood sweep efficiency is maximized by equalizing the arrival times of the waterfront at the producing wells and the production acceleration is accomplished using a 'norm' constraint on the arrival times to accelerate injection/production rates. The 'optimal' strategy is decided based on a compromise between the two. Previous work primarily focused on sweep efficiency optimization and did not account for production acceleration. There are four important elements in the proposed approach that makes it particularly well-suited for large-scale field applications. First, streamlines are used to efficiently and analytically compute the sensitivity of the arrival times with respect to well rates. For finite-difference models, the streamlines are easily derived from the

* Part of this chapter is reprinted with permission from "Optimal Water Flood Management Under Geological Uncertainty Using Accelerated Production Strategy" by Taware, S., Sharma, S., Datta-Gupta, A. and Alhuthali, A. 2010. Paper SPE 133882-MS presented at the 2010 SPE Annual Technical Conference and Exhibition, 19-22 September 2010, Florence, Italy. 

velocity field. Second, geological uncertainty is accounted via a stochastic optimization framework that relies on a combination of the expect value and variance of a performance measure from multiple realizations for risk assessments. Third, analytical forms for gradients and Hessian of the objective functions are derived which make the proposed optimization computationally efficient for large field cases. Finally, optimization is performed under operational and facility constraints using a sequential quadratic programming approach. Multiple examples are presented to support the robustness and efficiency of the proposed optimization scheme. These include 2D synthetic examples for validation and a 3D benchmark field application.

## 4.2 Introduction

In this chapter, the previous work of Alhuthali et al., (2010) is extended. A novel approach is proposed that accounts for accelerated production strategy by redefining the objective function for optimization. Specifically, a penalized misfit function is proposed for optimization that not only equalizes the arrival time of the waterfront at the producers to maximize sweep, but also minimizes the magnitude of the arrival time to accelerate the production. Unlike the prior work of Alhuthali et al., (2010), the objective function now consists of two terms. The first term attempts to maximize the sweep efficiency. The second term, also known as the 'norm' term or 'regularization' term attempts to accelerate the production. By adjusting the weight on the norm term, one can examine the tradeoff between equalizing arrival time (maximizing sweep) and production acceleration (maximizing NPV). The optimal decision is a compromise between the two and can be arrived at by using a trade-off curve.

The organization of the chapter is as follows. First, the major steps of the proposed approach are outlined. Next, the underlying mathematical formulation is discussed. Finally, the robustness and application of the proposed approach is demonstrated using a 2D heterogeneous examples and a 3D synthetic field example. Incorporation of the geological uncertainty using the proposed approach is also illustrated using the same 3D synthetic field example.

### 4.3 Approach

The primary objective of the proposed approach is to obtain an optimal as well as accelerated production strategy for waterflooding based upon a trade-off between maximizing sweep efficiency and maximizing NPV. This work builds on the previous work of Alhuthali et al., (2010) whereby the sweep efficiency is maximized by equalizing arrival time of waterfront at producers via rate control. The approach is general and can be employed using both finite-difference and streamline models. In addition, the approach can be implemented on multiple realizations to account for geological uncertainty using a stochastic framework. The proposed optimization approach involves following steps:

- **Flow Simulation and streamline tracing**. The first step is to perform flow simulation for a time interval of interest for every geologic realization. If a finite-difference simulator is used, then streamlines are traced using the fluid fluxes derived from the flow simulation (Datta-Gupta and King, 2007).
- **Computation of the objective function, analytical sensitivities and Jacobian**. The second step is to compute the objective function for optimization. Unlike the previous work of Alhuthali et al., (2010), the objective function now consists of two terms. The first term is the travel time residual which quantifies the misfit between the desired arrival time and the computed arrival time at each producer for every geologic realization. By minimizing the arrival time residual, the sweep efficiency is maximized. In this chapter, it is proposed to augment the objective function with an additional penalty term that minimizes the ‘norm’ of the arrival time itself to accelerate fluid production. Using streamlines, analytical sensitivities are calculated, which are defined as the partial derivatives of arrival time with respect to well rates. The sensitivities are then used to compute the Jacobian which is defined as the gradient of the residuals.

- **Computation of analytical gradient and Hessian**. The next step is to compute the gradient and Hessian of the objective function using above computed residuals and the analytical Jacobian.
- **Minimization and optimal rate allocation**. The objective function is then minimized using Sequential Quadratic Programming (SQP) technique (Nocedal and Wright 2006) to generate required changes in rates subject to appropriate field constraints.

The above-mentioned steps are repeated until a pre-defined stopping criterion on the objective function or the rates is satisfied. Then optimization moves to the next time interval.

### 4.4 Mathematical Background

In this section, modifications are made to the objective function previously proposed by Alhuthali et al., (2010) to derive optimal injection/production rate allocations that attempt to maximize waterflood sweep efficiency as well as the NPV via production acceleration.

#### 4.4.1 Objective Function Formulation

The earlier work of Alhuthali et al., (2010) maximized sweep efficiency during waterflooding via rate control. This was accomplished by minimizing an objective function that ensured that the waterfront arrives nearly at the same time for all producers in a given group of injectors and producers within the field. For a single geologic realization *j*, the objective function was formulated as the square of the $l_2$-norm of the arrival time residuals as follows,

$$\mathbf{e}_j^T \mathbf{e}_j = \sum_{m=1}^{N_{group}} \sum_{i=1}^{N_{prod,m}} \left( t_{d,m}(\mathbf{q}) - t_{i,m}(\mathbf{q}) \right)^2 \quad \text{..... (4.1)}$$

The arrival time residuals are represented by the vector **e** in the **Eq. 4.1**. The variable $t_{i,m}$ represents the calculated arrival time at well *i*, belonging to group *m*. The desired arrival time, $t_{d,m}$ for the well group *m* is given by the arithmetic average of $t_{i,m}$ for each iteration during the optimization (Alhuthali et al., 2010). The vector **q** contains the control variables and has a dimension of *n*, the number of well rates to be optimized. **Eq. 4.1** focuses on maximizing the sweep efficiency, often at the expense of the NPV. This is because no credit is given to production acceleration or the time value of money. To account for production acceleration, the objective function in the **Eq. 4.1** is revised as follows,

$$p(\mathbf{q}) = \sum_{m=1}^{N_{group}} \sum_{i=1}^{Nprod,m} \left(t_{d,m}(\mathbf{q}) - t_{i,m}(\mathbf{q})\right)^2 + \eta \sum_{m=1}^{N_{group}} \sum_{i=1}^{Nprod,m} \left(t_{i,m}(\mathbf{q})\right)^2 \quad \text{(4.2)}$$

which can be expressed as follows,

$$p(\mathbf{q}) = \mathbf{e}_j^T \mathbf{e}_j + \eta\, \mathbf{t}_j^T \mathbf{t}_j \quad \text{(4.3)}$$

The variable $t_{i,m}$ represents the calculated arrival time at well *i*, belonging to group m. The desired arrival time, $t_{d,m}$ for the well group m is given by the arithmetic average of $t_{i,m}$ for each iteration during the optimization. The vector **q** contains the control variables. Addition of a 'norm' term ($\eta$) to the objective function ensures that the magnitude of the arrival time is also reduced along with their variance. This reduction in arrival time will lead to the acceleration of oil production and water injection and thus ensuring that the optimization doesn't reduce the production and injection rates of the wells too much to delay water breakthrough, particularly for the highly productive wells. By adjusting the weight, $\eta$ on the norm term, one will be able to decide on the trade-off between equalizing arrival time and accelerating production/injection. The optimal selection of the $\eta$ will be done using a tradeoff curve. The proposed approach will retain

the advantages of the Alhuthali et al., (2010) approach viz. the analytical computation of the gradient and hessian of the objective function using streamline-derived sensitivities.

### 4.4.2 Optimization Post-water Breakthrough

Optimization has been formulated in terms of arrival time of the waterfront at the producers. A natural question arises: what happens after water breakthrough? The optimization is carried out after water breakthrough at a well by incorporating the well water cut into the objective function so as to prevent allocating high production rates to wells with high water cut. To accomplish this, the arrival time definition to a well is modified to include the water cut at the well as follows,

$$t'_{i,m}(\mathbf{q}) = t_{i,m}(\mathbf{q}) * \left(1 - f_{w\,i,m}\right)^{\alpha} \quad \text{.....} \quad (4.4)$$

In the above expression, the arrival time, $t_{i,m,}$ at well *i* which belongs to group *m* has been altered to incorporate the well water cut, $f_{w\,i,m}$. If the water cut is zero, the modified arrival time is the same as the original arrival time. When the water cut at the well is greater than zero, the original arrival time will be rescaled based on the level of water cut. If the water cut is high, the original arrival time will be reduced significantly. The extent of reduction can be controlled by the exponent term, $\alpha$. As a consequence, the rate allocation to the well will be lowered in relation to the wells with less water cut.

### 4.4.3 Objective Function: Gradient and Hessian

The gradient of the objective function in the **Eq. 4.2** is given by the following expression,

$$\nabla_q p(\mathbf{q}) = 2\mathbf{J}^T\mathbf{e} + \eta\left(2\mathbf{S}^T\mathbf{t}\right) \quad \text{.....} \quad (4.5)$$

Also in **Eq. 4.5**, **t** is the arrival time vector given by following expression,

$$t_{i,m}(\mathbf{q}) = \frac{1}{N_{fsl,i}} \sum_{l=1}^{N_{fsl,i}} \tau_{l,i} \Big/ \left[ \frac{df_w}{dS_w} \right]_{S_w = S_{wf,l}} \quad \text{..... (4.6)}$$

In the above expression, $N_{fsl,i}$ represents the number of the 'fast' streamlines connected to the producer *i* belonging to the well group *m*. Typically the fastest 20% of all arriving streamlines at the producer are used. The variable τ represents the streamline time-of-flight. It is measured from injector (source) to producer (sink). The time of flight τ, which is computed using the total fluid velocities, is converted to waterfront arrival time by dividing by the frontal speed which is the breakthrough slope of the water-oil fractional flow curve $\frac{df_w}{dS_w}$ (Datta-Gupta and King, 2007). The Jacobian matrix, **J**, in **Eq. 4.5** is given by the following expression,

$$\mathbf{J} = \nabla_q \mathbf{e} \quad \text{..... (4.7)}$$

where **e** is the vector of arrival time residuals at all producing wells in all groups. A single element of **e** corresponding to producer *i* in group *m* is given by,

$$e_{i,m} = t_{d,m}(\mathbf{q}) - t_{i,m}(\mathbf{q}) \quad \text{..... (4.8)}$$

where desired arrival time $t_{d,m}$ for a group of producers is computed as the arithmetic average of the calculate arrival times at the producers within this group given as follows,

$$t_{d,m}(\mathbf{q}) = \frac{\sum_{i}^{N_{prod,m}} t_{i,m}(\mathbf{q})}{N_{prod,m}} \quad \text{..... (4.9)}$$

Every element in jacobian matrix $J$ is given by,

$$J_{ij} = \left[ \frac{1}{N_{Group}} \sum_{k=1}^{N_{Group}} S_{kj} \right] - S_{ij} \quad \text{..... (4.10)}$$

where $N_{Group}$ is number of wells in a group. Every element in sensitivity matrix $S$ is given by **Eq. 4.11** and **Eq. 4.12**.

$$S_{ij} = -\frac{t_{i,m}}{q_j} \quad \forall i = j$$

$$S_{ij} = 0 \quad \forall i \neq j \quad \text{..... (4.11)}$$

$j$ is a producer

In **Eq. 4.11**, it is assumed that $t_{i,m}$ is sensitive only to the production of producer $i$. The sensitivity of $t_{i,m}$ is considered to be negligible with respect to the rates of other producers. This seems to be a reasonable approximation for optimization purposes (Alhuthali et al., 2007). If the derivative is taken with respect to the rate of an injector, the sensitivity coefficient can be written as follows,

$$S_{ij} = -\frac{\sum_{l=1}^{N_{fsl,i,j}} \tau_{l,i,j} \Big/ \left[ \frac{df_w}{dS_w} \right]_{S_w = S_{wf,l}}}{q_j N_{fsl,i}} \quad if \quad N_{fsl,i,j} \neq 0$$

$$S_{ij} = 0 \quad if \quad N_{fsl,i,j} = 0 \quad \text{..... (4.12)}$$

$j$ is an injector

Unlike the **Eq. 4.11**, the injection rate can impact the arrival time at multiple producers and the sensitivity matrix will have off-diagonal terms. In the **Eq. 4.12**, the variable $N_{fsl,i,j}$ is the number of the 'fast' streamlines connecting producer $i$ to the injector $j$. This number represents only a fraction of $N_{fsl,i}$ the total number of the 'fast'

streamlines connected to the producer *i*. If the injector *j* is not connected to producer *i* through a 'fast' streamline i.e. ($N_{fsl,i,j}$=0), then the arrival time at producer *i* is not sensitive to a perturbation in the rate of injector *j*.

The analytical calculation of sensitivities leads to an analytical calculation of the Jacobian matrix. Consequently, this leads to an analytical calculation of the gradient and Hessian of objective function. It is important to emphasize that the computation of the Jacobian matrix requires a single flow simulation and thus leads to a substantial savings in computation time. The Hessian of the objective function in **Eq. 4.2** is given by the following expression,

$$\nabla_q^2 p(\mathbf{q}) = 2\mathbf{J}^T\mathbf{J} + \eta\left(2\mathbf{S}^T\mathbf{S}\right) \quad (4.13)$$

### 4.4.4 Minimization

In the proposed approach, the **Eq. 4.14** is minimized using the Sequential Quadratic Programming (SQP) algorithm for nonlinear constrained optimization (Nocedal and Wright 2006). The problem is formulated into a series of quadratic programming (QP) sub-problems which can be solved at each major iteration *k*. The QP sub-problem is mainly a quadratic approximation of the Lagrangian of the **Eq. 4.14** which is given in the following form,

$$L(\mathbf{q},\boldsymbol{\lambda}_L,\boldsymbol{\lambda}_K) = f\left(\mathbf{q}\right) + \boldsymbol{\lambda}_L^T\mathbf{h}(\mathbf{q}) + \boldsymbol{\lambda}_K^T\mathbf{g}(\mathbf{q}) \quad (4.14)$$

The vectors $\boldsymbol{\lambda}_L$ and $\boldsymbol{\lambda}_K$ refer to the Lagrange multipliers corresponding to the equality constraints and the Karush-Kuhn-Tucker multipliers corresponding to the inequality constraints. The further details on formulating the QP sub-problem can be found in the previous work (Alhuthali et al., 2008). In this application, the SQP algorithm (MATLAB®) has been used to obtain optimal rates for the nonlinear constrained optimization problem.

### 4.4.5 Accounting for Geological Uncertainty

To address geological uncertainty, the **Eq. 4.2** needs to be generalized to handle multiple realizations. This is accomplished in terms of an expected value of the misfit in the **Eq. 4.3** for multiple realizations penalized by its standard deviation given as follows,

$$f(\mathbf{q}) = E[p(\mathbf{q})] + r\sigma[p(\mathbf{q})] \quad (4.15)$$

**Eq 4.3** can be derived within the decision analysis framework (Simpson et al., 2000; Guyaguler and Horne, 2004; Bickel et al., 2006; Alhuthali et al., 2010). The variable *r* is the risk coefficient that weights the trade-off between the expected value and the standard deviation. A positive *r* means that the decision maker is risk averse, while a negative *r* means that the decision maker is risk prone.

While accounting for the geologic uncertainty using the **Eq. 4.15**, one needs to consider the expected value over multiple realizations (Alhuthali et al., 2008). For example for risk coefficient (*r*) = 0, the gradient of the objective function in the **Eq. 4.15** is given by the following expression,

$$\nabla_q f(\mathbf{q}) = 2E[\mathbf{J}^T\mathbf{e}] + \eta\left(2E[\mathbf{S}^T\mathbf{t}]\right) \quad (4.16)$$

Similarly the Hessian of the objective function in the **Eq. 4.15** is given by the following expression,

$$\nabla_q^2 f(\mathbf{q}) = 2E[\mathbf{J}^T\mathbf{J}] + \eta\left(2E[\mathbf{S}^T\mathbf{S}]\right) \quad (4.17)$$

### 4.4.6 Software Implementation

The entire workflow of streamline based rate optimization has been implemented using software, DESTINY, which is called by MATLAB® software. DESTINY is developed as part of a joint industry project at the Texas A&M University. Streamlines can be traced using the fluxes generated by a variety of commercial finite-difference simulator.

For streamline simulators, the streamlines are already readily available and this step is not needed. Thus, the proposed workflow can be implemented in both finite difference and streamline simulators. The use of commercial simulators allows availing of complex well management capabilities, horizontal/multilateral wells and other complicated well trajectories along with advanced three-phase flow physics. The entire workflow is illustrated in **Fig. 4.1**. MATLAB® software reads the MS-Excel based input and then runs the commercial simulator for the desired time. Then it runs DESTINY for tracing streamlines, followed by software called as TOFSENS which calculates the analytical sensitivities described in **section** 4.4.4. MATLAB® software uses the analytical sensitivities to calculate optimized rates using Sequential Quadratic Programming (SQP).

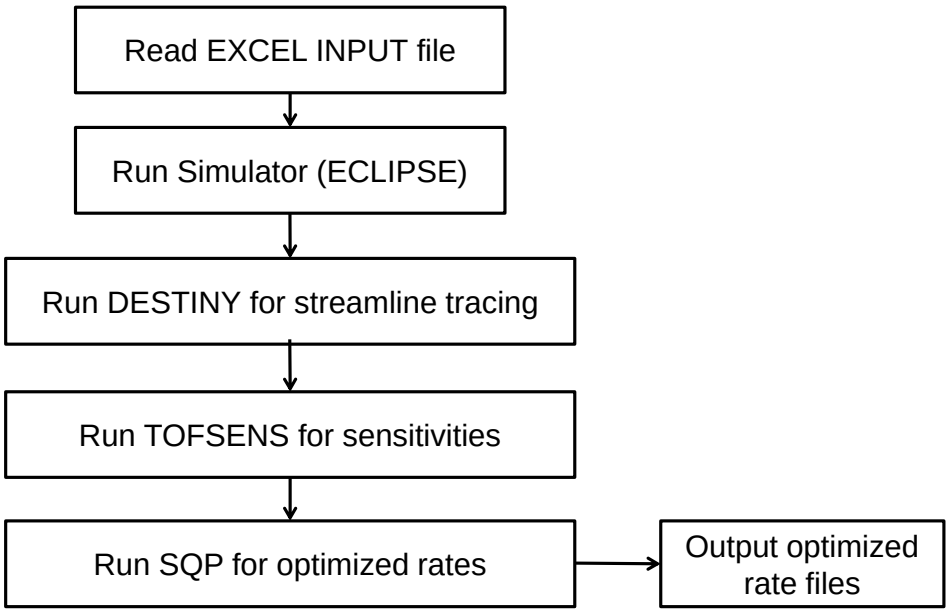


**Fig. 4.1 – Illustration of the workflow showing overall steps in streamline based rate optimization.**

## 4.5 Applications and Discussion

In this section, 2D heterogeneous examples are used to illustrate the proposed approach. Next, the practical feasibility of the approach is demonstrated using a 3D synthetic field example, the benchmark Brugge field case (Peters et al., 2009) using single as well as multiple realizations. ICVs (Inflow Control Valves) and hierarchical field as well as well level constraints have been used with the proposed penalized objective function to show the benefits of the accelerated production strategy while trying to optimize sweep efficiency.

### 4.5.1 Illustration of the Approach: 2D Heterogeneous Example

In this section, the proposed approach of using the norm term is illustrated using waterflooding in the 2D heterogeneous examples as shown in **Fig. 4.2** and **Fig. 4.5**. First using **Fig. 4.2**, it is demonstrated that given a starting condition norm term (**Eq. 4.2**) in the proposed modification, helps in picking a particular arrival time equalization solution among several non-unique solutions that also minimizes arrival time ($\tau$) which results in acceleration of rates subject to constraints. Then the proposed accelerated production strategy using the norm term is compared with two other methods using **Fig. 4.5:-** the prior work that relies on sweep efficiency maximization (Alhuthali et al., 2010) and Net Present Value (NPV) optimization (Brouwer and Jansen 2004). The trade-off between maximizing NPV and maximizing sweep efficiency is also illustrated and then a method to decide on the optimal compromise via a trade-off curve is proposed. The implications on the injection efficiency which is a measure to reallocate fluid amongst injectors (Datta-Gupta and King, 2007) are also examined.

#### 4.5.1.1 Working of the Norm Term in the Accelerated Production Strategy

A synthetic 2D field (**Fig. 4.2**, 50x50 grid) with four producers and an injector (inverted 5 spot) is used for the illustration.

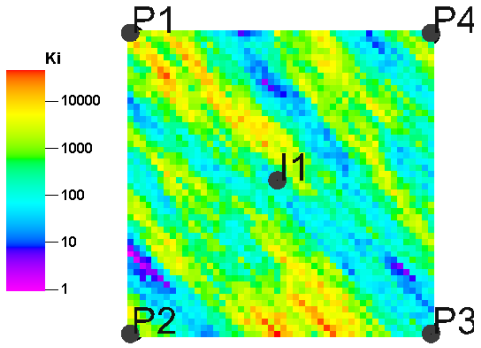


**Fig. 4.2 - Synthetic 2D permeability field (md) with inverted 5-spot water injection.**

To illustrate the working of the norm term in the proposed method, two cases are run whose results are shown in **Fig. 4.3.** The cases are: η (norm term weight) = 0 (**Fig. 4.3, top**) and η = 2 (**Fig. 4.3, bottom**). Constraints used in the optimization are as follows:

Injection rate <= 800 rb /day, Production rate for each well <= 300 rb/day,

Voidage balance condition. Optimization time step = 0.5 year.

Producer starting rates = 200 RB/day each. Injector starting rate = 800 RB /day

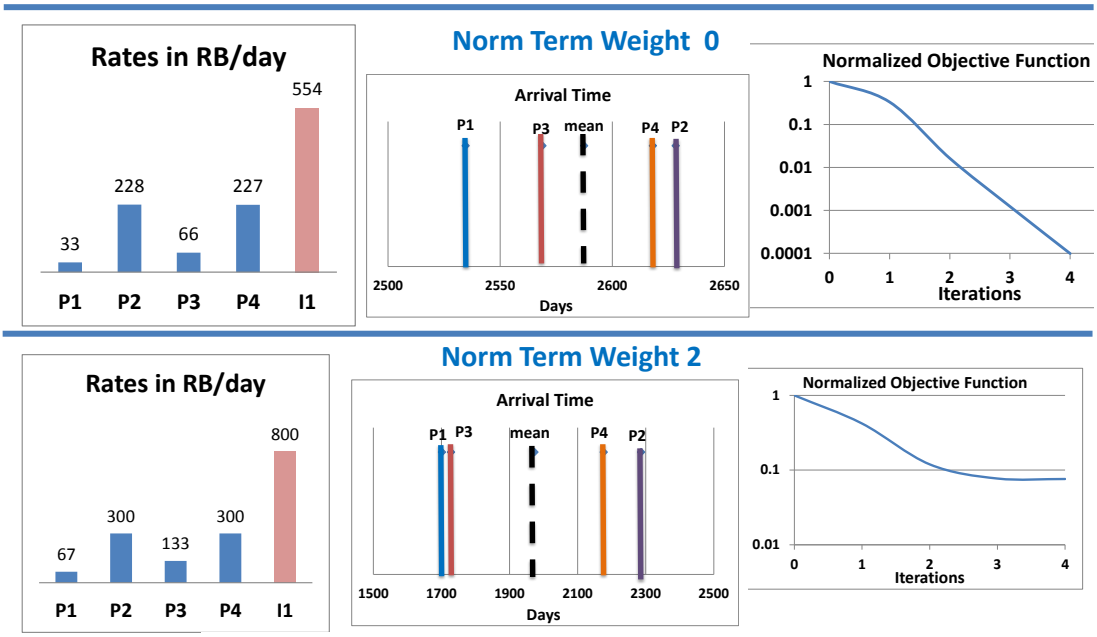


**Fig. 4.3 – Rates for two cases with norm term weight 0 and 2.**

It can be observed that for the case of norm term weight = 0 (**Fig. 4.3, top**), the optimized rates are shown on the left. Arrival time for four producers is shown in the middle and the objective function plot is shown on the right. Similarly for the case of norm term weight = 2 (**Fig. 4.3, bottom**), the optimized rates are shown on the left. Arrival time for four producers is shown in the middle.

Comparing both cases it can be observed that for the case of norm term weight = 2, the optimized injection rate hits the constraint along with sum of production rates due to voidage balance condition. But the objective function has not reached the tolerance limit (0.0001) compared to the case with norm term weight = 0, illustrating that arrival time misfit has not been minimized. This shows that if constraints are hit, sweep efficiency is not maximized.

To further illustrate the working of the norm term, the contour plots of the proposed augmented arrival time optimization objective function with norm term weight = 2 (right) and norm term weight = 0 (left) are plotted in **Fig. 4.4**. Contour plots are plotted by keeping P1 and P3 at converged rates of 33 RB/day and 66 RB/day

respectively for norm term weight = 0 and varying P2 and P4 in a specific range at voidage balance so that the minima is visible. It can be observed that for case of norm term weight = 0 (**Fig. 4.4, left**), the optimized rates are shown in the bottom. Similarly for case of norm term weight = 2 (**Fig. 4.4, right**), the optimized rates are shown in the bottom. For norm term weight = 0, minima are observed and solution is stuck in it (plotted by red circle). For norm term weight = 2, solution is plotted as red circle. It has hit the constraints. There is a different minimum beyond the constraints (black lines) which also minimizes arrival time, after using the norm term weight = 2. Thus, norm term helps in picking a particular non-unique arrival time equalization solution which also minimizes arrival time resulting in rate acceleration subject to the constraints. The issue of existence of multiple local minima in the solution space during rate optimization is discussed in detail in **Appendix C.2.a**.

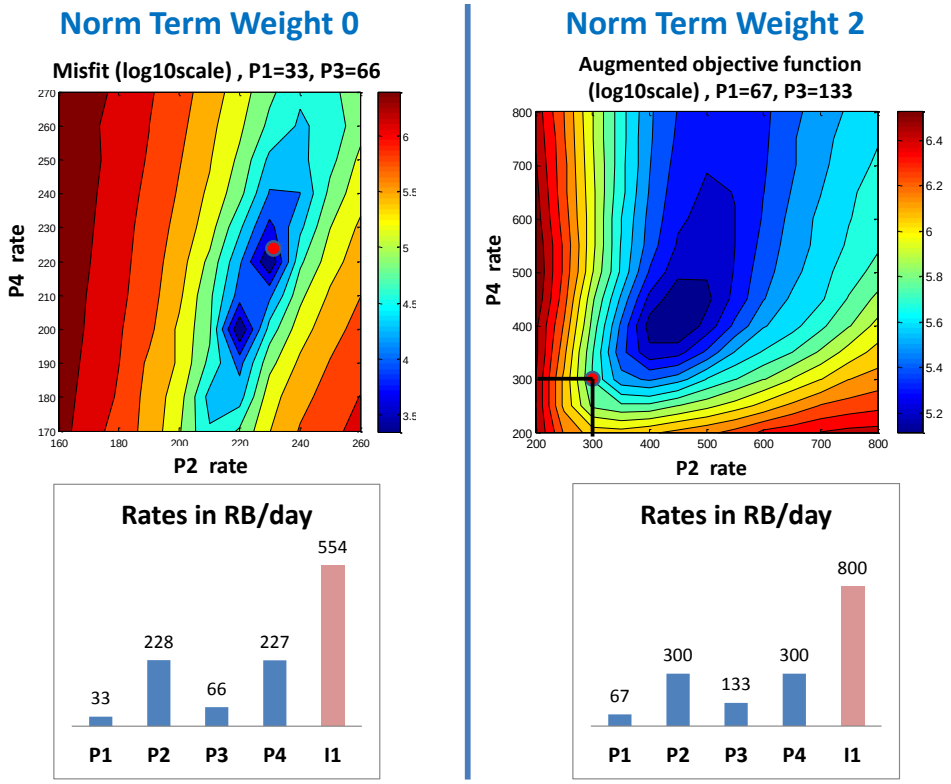


**Fig. 4.4 - Contour plots for two cases with norm term weight 0 and 2.**

In addition, different starting rates result in different converged rates due to existence of multiple local minima. This issue is discussed in detail in **Appendix C.2.b**. Two cases are shown – **case 1** where all producers have starting rates of 200 RB/day (**Fig 4.4**) and **case 2** where P1 and P3 have starting rates of 150 RB/day while P2 and P4 have starting rates of 250 RB/day. Norm term weight of 2 is used on the case 2 to illustrate the working on the norm term in **Appendix C.3** under case 2. Comparing cases 1 and 2 in **Appendix C.3**, it can be observed that for norm term weight = 0, different starting rates have resulted in solution getting stuck in different minima with different converged rates for both cases. But for norm term weight = 2, a similar minima is observed beyond the constraints for both cases. Rates achieved after convergence are also similar for both cases for norm term weight = 2. In conclusion, given a starting condition, norm term is helping to pick up a particular arrival time equalization solution which minimizes arrival time and thus accelerating rates subject to the constraints.

Other issue discussed is that why instead of using norm term, the rates cannot be simply scaled up to hit the first constraint and preserve the minimum value of the objective function. The reason for this is that there is a nonlinear relationship between time of flight (arrival time of waterfront) and rates, for compressible water-oil case with dissolved gas. The relationship is shown to become more linear for incompressible water-oil. This issue is discussed in detail in **Appendix C.1.a**. So even if the rates are scaled to hit the constraint the minimum value of the objective function is not preserved, it increases because decrease in travel time is offset by the increase in difference between arrival time and desired arrival time due to non-linearity between time of flight and rates. This is discussed in detail in **Appendix C.1.b**.

Additionally, for voidage balance case while optimizing both injector (injector rate is not fixed) and producer, norm term helps in accelerating production and reduces penalty on high productive wells. As there is less freedom due to voidage balance constraint acceleration is achieved by sacrificing injection efficiency. This issue has been discussed in detail in **Appendix C.4.a**. On the other hand, for non-voidage balance

case, norm term helps in preventing slowing down of wells and improves injection efficiency. This issue has been discussed in **Appendix C.4.b**.

#### 4.5.1.2 Comparison of Accelerated Production Strategy with NPV Optimization

In this section the proposed method is compared with NPV (Net Present Value) optimization. NPV optimization solution was obtained using perturbation sensitivities.

The example case is a 2D waterflood (50x50 grid) as shown in **Fig. 4.5**. A high permeability channel connects the injector, I1 to the producer, P1 and thus, will lead to preferential fluid movement and reduced sweep efficiency. This gives an ample opportunity for improving sweep efficiency through rate control and to examine the efficacy of the proposed accelerated production strategy as compared to NPV optimization. The blackoil simulation used compressible oil with dissolved and free gas and water.

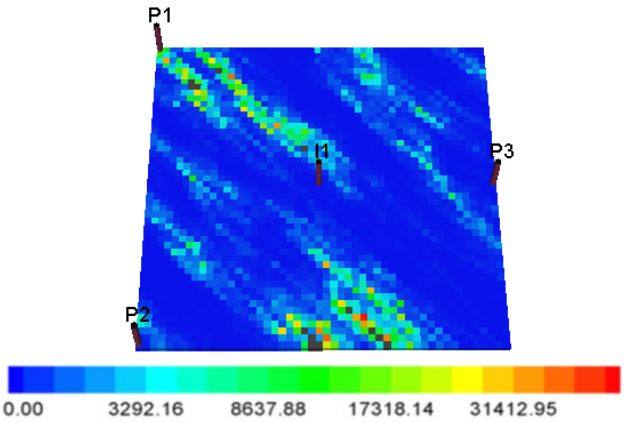


**Fig. 4.5 - Well configuration for 2D heterogeneous permeability (md) example.**

The total production time period is set to be 5000 days and the optimization is carried out with five time intervals, each interval being 1000 days. The constraints imposed on the optimization are as follows,

- Inequality constraints: Total field production rate ≤ 800 RB/D
- Equality constraints: Injection rate equal to total production rate (voidage balance)
- Starting total injection and production rate = 800 RB/day.
- Starting production well rate = 266.66 RB/day.
- Maximum allowable production rate per well = 300 RB/D
- If producing well water cut exceeds 90%, the well rate is set to 10 RB/D

Additional parameters used for NPV optimization are as follows,

- Oil price = $50/bbl.
- Water production and injection cost = $5/bbl.
- Discount rate = 10% p.a.

**Fig. 4.6** shows the water saturation distribution at three different times for various optimization cases. The first column corresponds to the NPV optimization. The second column (norm term weight = 0) corresponds to the sweep efficiency optimization without accelerated production. This case is identical to the earlier method proposed by Alhuthali et al., (2010). The third and the fourth columns correspond to varying degrees of production acceleration using norm term weights.

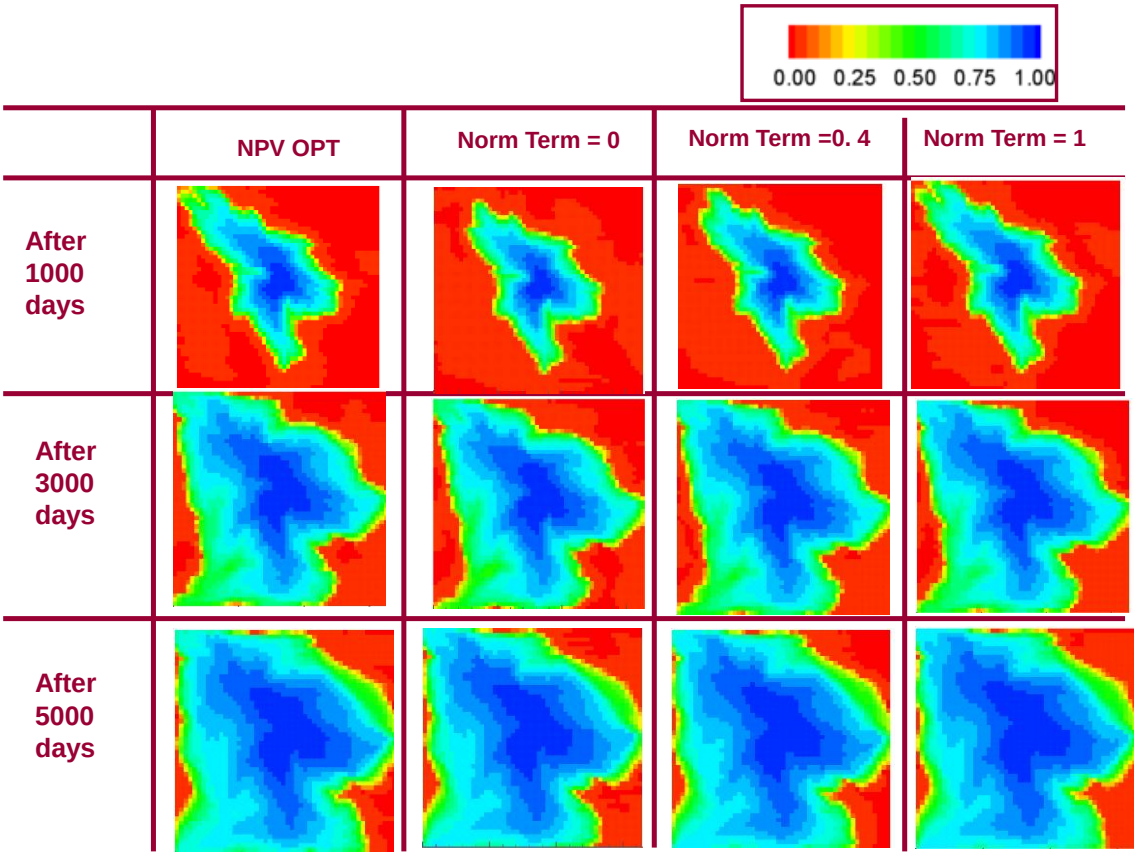


**Fig. 4.6 - Water saturation maps for NPV optimization and arrival-time optimization with different norm term weights (1000, 3000 and 5000 days).**

**Fig. 4.7** shows the rate allocation to the producers at various times steps for these four different optimization scenarios. When the goal is solely to maximize the sweep efficiency (norm term weight = 0), a very low production rate is allocated to producer P1 from the very beginning to prevent early water breakthrough and to equalize the arrival time at all producers. This is in spite of the fact that P1 is located in a high permeability region and can potentially produce at a much higher rate, at least at early times. As the norm term is increased, the well P1 is allocated more production and as can be seen from **Fig. 4.6**, this is because with inclusion of the norm term, the goal is not only to increase the sweep efficiency but also to achieve that increased sweep as fast as possible. Thus, a

similarity between rates for NPV optimization and the arrival time optimization is observed with high norm term weight.

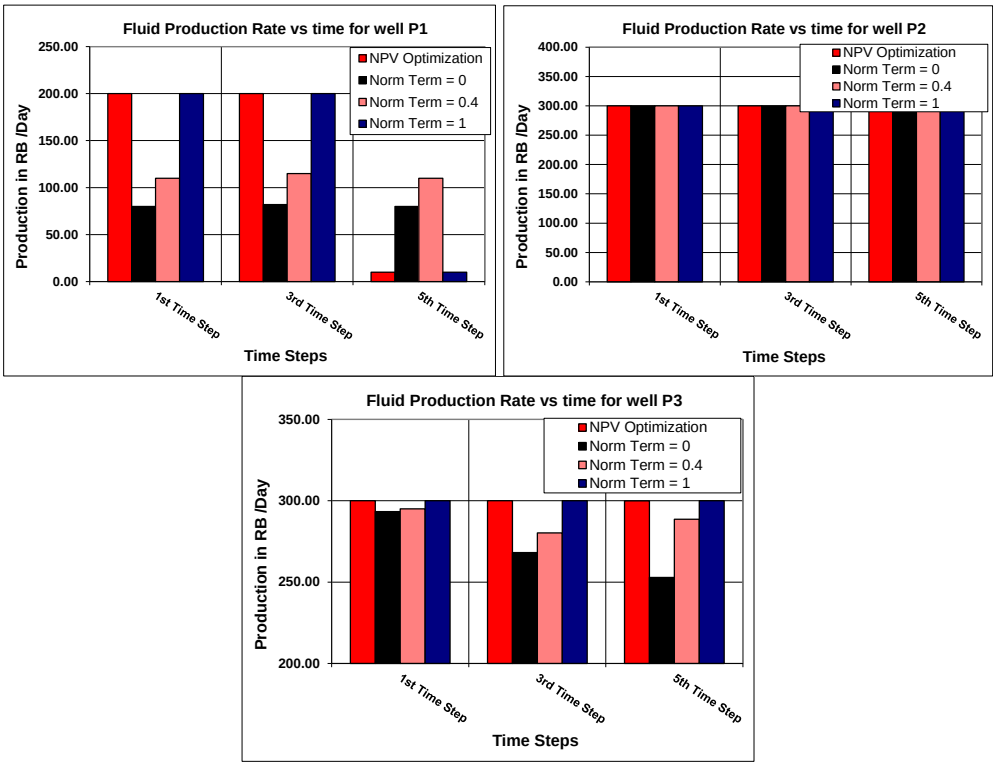


**Fig. 4.7 - Production rates for wells P1, P2 and P3 for NPV optimization and arrival time optimization with different Norm Term weights (1000 (1st timestep), 3000 (3rd timestep) and 5000 (5th timestep) days).**

**Fig. 4.8** shows plots of cumulative oil production and cumulative water injection for the field. It can be observed that the higher cumulative oil production is closely correlated to higher cumulative injection, as expected. As the norm term weight is increased, the injection rate rapidly reaches its limit and the production rates are also increased accordingly. The case with the highest norm term weight of 1 has cumulative injection and production profiles that are similar to that of NPV optimization.

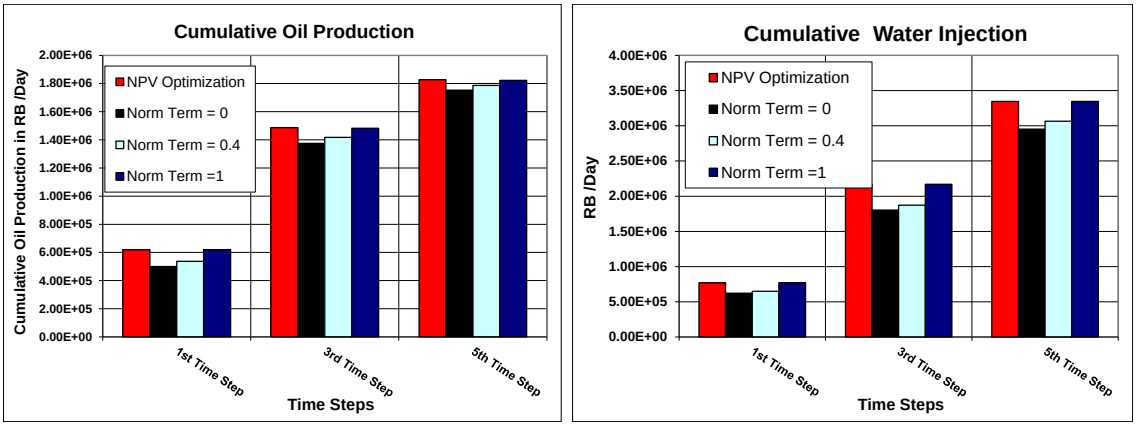


**Fig. 4.8 - Cumulative oil production and cumulative water injection for NPV optimization and arrival time optimization with different norm term weights (1000 (1st timestep), 3000 (3rd timestep) and 5000 (5th timestep) days).**

This can also be seen in **Fig. 4.9** which shows the NPV for various norm term weights and for the case with optimized NPV. For the highest norm term weight of 1, the NPV is the same as that obtained by NPV optimization. For the 2D synthetic example, the NPV optimization was carried out by computing the rate sensitivities using numerical perturbation.

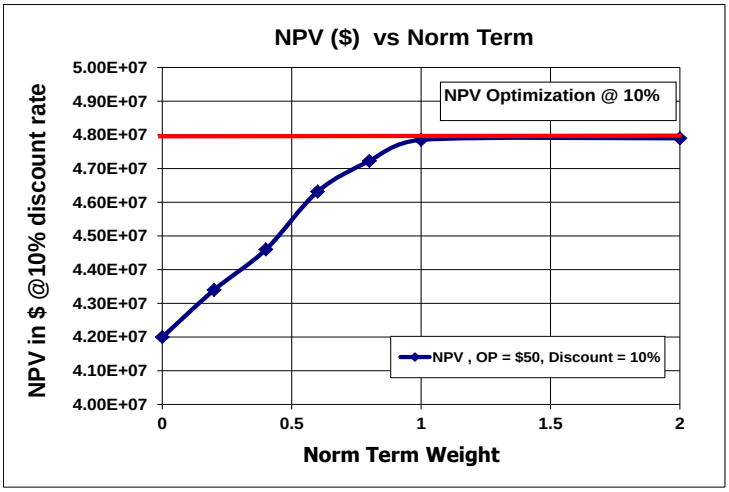


**Fig. 4.9 - NPV performance vs norm term compared with NPV perturbation sensitivities.**

**Fig. 4.10** shows the water cut performance for various norm term weights and also, for the NPV optimization. It can be observed that as the production is being accelerated due to higher norm terms for wells P1 and P3, the water breakthrough also occurs earlier. For NPV optimization, the water breakthrough occurs the earliest and the rise of water cut is also the steepest. The benefits of arrival time optimization only (norm term weight = 0) in terms of delaying water breakthrough and reducing the water production is apparent from these results. As the norm term weight is increased, both injection and production rates are progressively increased leading to earlier breakthrough and increased water production as in the case of NPV optimization. For producer P2 the watercut profile is same for all the cases and is similar to NPV optimization, this is due to the fact that same production rate is allocated to the P2 (i.e. 300 RB/day) for all the cases as the producer lies in low permeability region.

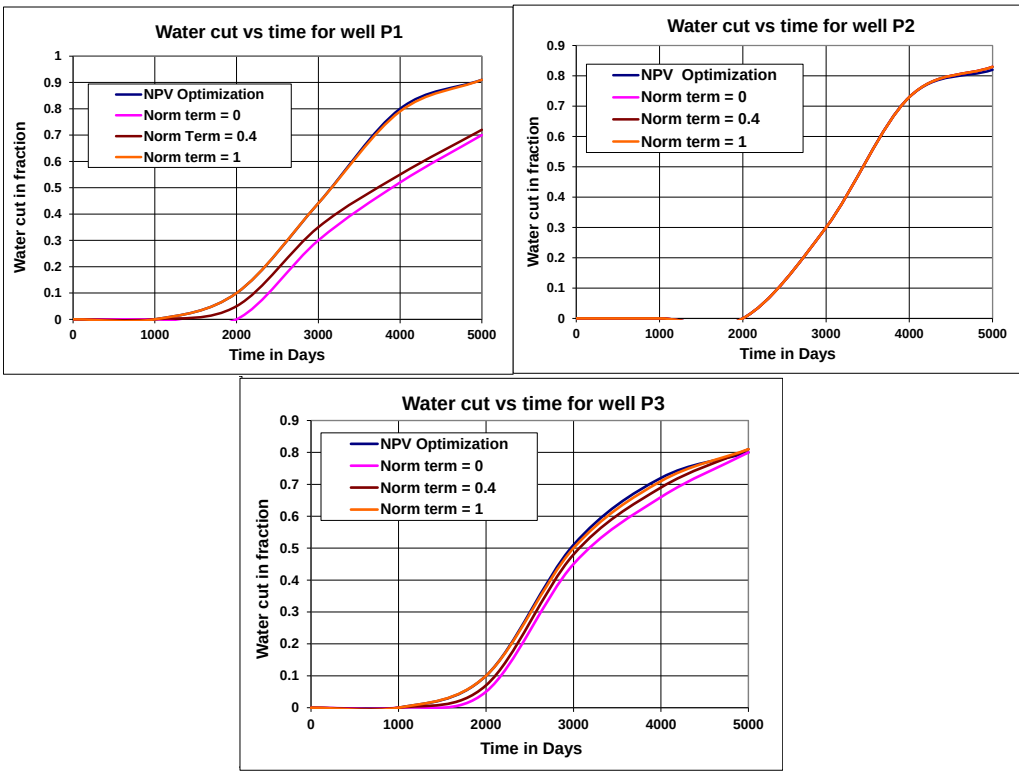


**Fig. 4.10 – Water-cut for wells P1, P2 and P3 for NPV optimization and arrival time optimization with different norm term weights.**

For the 2D five-spot case, the injection efficiency has been plotted in **Fig. 4.11** for various norm term weights as well as for the NPV optimization. It can be observed that as the production accelerated (that is, norm term weight is increased), the injection efficiency of the water flood reduces because of increased water production. These results clearly show the tradeoff between accelerating production and increasing injection efficiency.

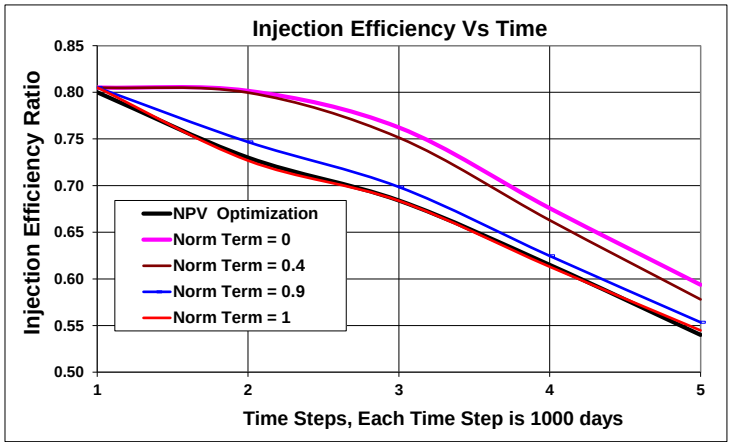


**Fig. 4.11- Injection efficiency for various norm term weights compared with NPV optimization.**

A natural question then arises: how to select the optimal norm term weight? This has been illustrated in **Fig. 4.12** where the cumulative NPV (normalized to unity) has been plotted against the norm term. This gives a well defined minimum curvature radius point as shown by the circle. Beyond minimum curvature radius point for higher norm term there is little incremental benefit in NPV. Because of the trade-off between NPV and sweep efficiency or injection efficiency, this point can be considered to be the best compromise between the two. Thus, the optimal norm term weight for this case is found out to be around 1.

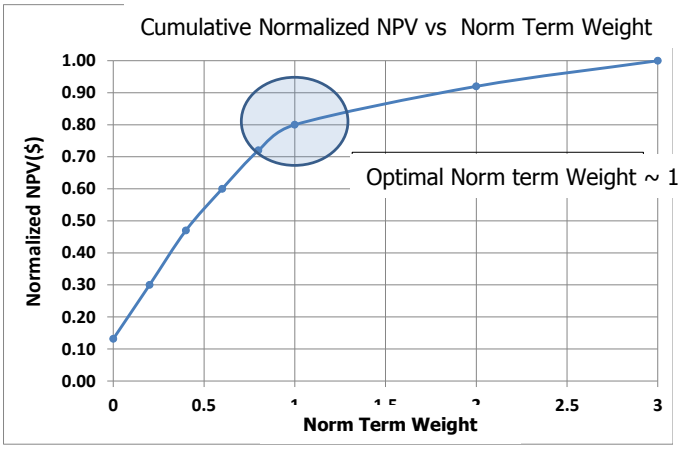


**Fig. 4.12 - Cumulative normalized NPV vs the norm term weight for selection of optimal norm term weight.**

### 4.5.2 3D Synthetic Field Example: The Benchmark Brugge Field Case.

#### 4.5.2.1 Introduction

In this section a 3D synthetic field case, the Brugge field is used to illustrate the practical feasibility of the proposed accelerated production approach. The Brugge field is a synthetic benchmark case that was set up as part of an SPE Applied Technology Workshop (ATW) to evaluate various closed loop control strategies for production optimization. The details for this case can be found in Peters et al., (2009). Here the proposed accelerated arrival time optimization approach is applied to the Brugge field for a period of 20 years after 10 years of prior production.

A series of model realizations were generated based on the reservoir properties and well log attributes extracted from a high-resolution geologic model consisting of 20 million grid cells. The Brugge field properties (permeability, porosity) are based on a North Sea Brent-type field. The structure of the Brugge field consists of an E-W elongated half-dome with a large boundary fault at its north edge, and one internal fault with a modest throw at an angle of around 20 degrees to the north boundary fault. The simulation model consists of 60000 gridblocks with 9 layers. It has 20 vertical producers

completed mainly in the top 8 layers and 10 peripheral injectors completed in all 9 layers. The locations of the injection and production wells are shown in **Fig. 4.13**.

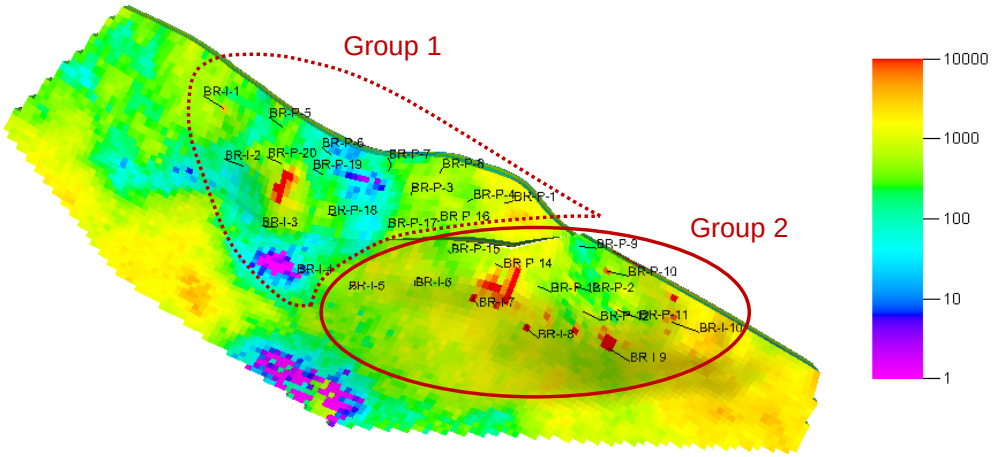


**Fig. 4.13 - Brugge field and wells locations. Permeability is plotted in log10 scale.**

The first 10 years of the production history of the field was provided for history matching purposes (Peters et al., 2009). The production history was based on a 'true model' response with added noise. The closed loop control approach consisted of two steps: (i) model updating via production data integration using the field production history for the first 10 years and (ii) production optimization, whereby rates are allocated over the next 20 years.

In this study, the focus is on the production optimization part for the Brugge field using the proposed accelerated production strategy. The details of the history matching have been discussed in a previous publication (Alhuthali et al., 2010). The comparison of the results is done with previously proposed sweep efficiency optimization based on equalization of arrival times. The optimization is carried out under following two scenarios:

- Production optimization for 20 years using a single history matched model

- Production optimization for 20 years using ten history matched realizations and application of the optimized rates on a blind realization.

For optimization purposes, the wells are divided into two groups based on the location of the internal fault as shown in **Fig. 4.13**. Group 1 includes the following production wells: BR-P-1, 3, 4, 5, 6, 7, 8, 16, 17, 18, 19, 20 and the following injection wells: BR-I-1, 2, 3, 4, 5, and 6. Group 2 has the following production wells: BR-P-2, 9, 10, 11, 12, 13, 14, and 15, and the following injection wells: BR-I-7, 8, 9, and 10. This grouping is used for calculating analytical sensitivities of the waterfront arrival times with respect to production / injection rates. Most of the wells in the Brugge field are equipped with three inflow control valves (ICVs) and the optimization is implemented by controlling the rates of the ICVs. Some additional constraints imposed during optimization are as follows:

- Maximum production rate per producer: 3000 RB/Day.
- Maximum injection rate per injector: 4000 RB/Day.
- Maximum allowable flowing injection bottom-hole pressure: 2626 Psia.
- Minimum allowable flowing production bottom-hole pressure: 740 Psia.
- Maximum field production rate: 60000 RB/Day. (Not described in Peters et al., (2009), but based on 20 producers).
- Maximum field injection rate: 40000 RB/Day. (Not described in Peters et al., (2009), but based on 10 injectors).
- Water cut limit for producer: 90%. After that, well is shutdown.
- The optimized rates are reported at ½ year intervals.

Also, there are operational limitations and facility constraints at different levels of production hierarchy. The facility constraints are related to field production/injection handling capacities. These different levels of production hierarchies have been illustrated in **Fig. 4.14**.

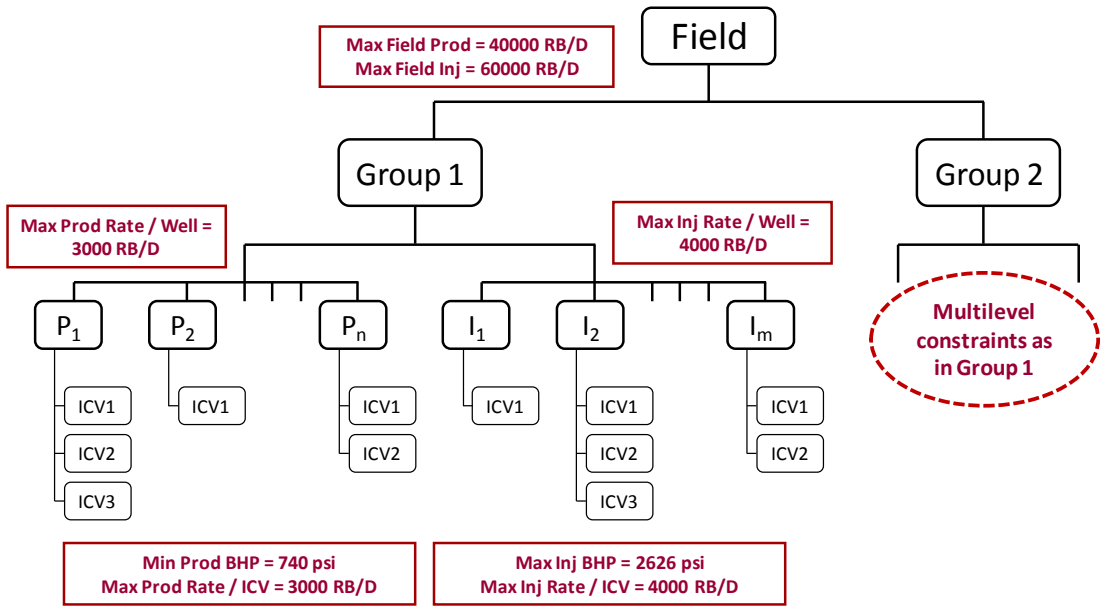


**Fig. 4.14 - Hierarchical diagram showing operational limitations and facility constraints at all levels of the production hierarchy.**

For the Brugge field, the total number of production ICVs is 53 and the total number of injection ICVs is 30. Comprehensive constraint matrices were set up for the field-scale optimization under specified operational and facility constraints using the SQP algorithm. Also, these matrices were updated dynamically to ensure that the above-mentioned constraints are satisfied at each hierarchical level. This ensured that the sweep efficiency optimization with and without accelerated production strategy always honored all the constraints at all levels of the production hierarchy. The oil price and costs of production and injection for calculation of NPV are assumed to be as follows (Peters et al., 2009).

- Oil Price = \$50/bbl. Cost of Water Production = Cost of Water Injection = \$5/bbl. Discount Rate = 10% p.a.
- Total production period for optimization = 20 years.

### 4.5.2.2 Flood Optimization Using Single Geologic Model

In this section, the proposed optimization is limited to a single geologic model. Thus, the uncertainty in the geologic model is not considered during optimization. The impact of geological uncertainty will be discussed in **section 4.5.2.4.**

The optimization results are compared with a base case that involves reactive control. Reactive control means that all the producing wells are produced at their maximum capacity subject to constraints (same for injectors) and shut down as the producers reach 90% water cut. The NPV for different norm terms is shown in **Fig. 4.15**. The NPV has been shown for 5 years, 10 years and 20 years of optimization. Recall that the case with a norm term weight of zero corresponds to sweep efficiency optimization only, without accounting for the acceleration effects. Although the sweep efficiency optimization performs better than the base case with reactive control, the benefits of production acceleration in improving the NPV is quite obvious from these results. As expected, it is observed that as the norm term weight increases, accelerated production is obtained along with higher NPV.

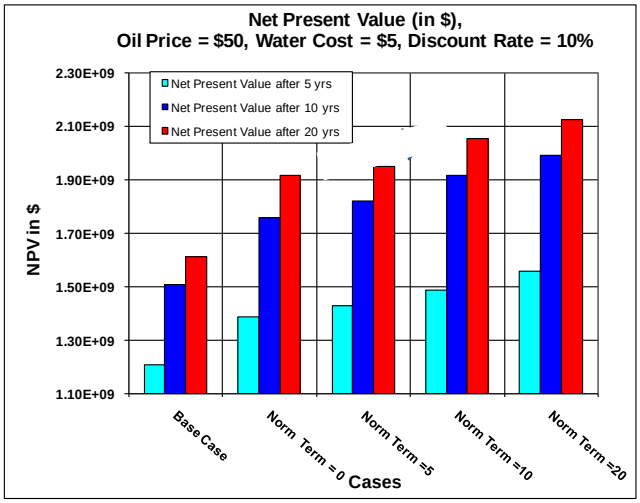


**Fig. 4.15 - NPV comparison for the Brugge field for different values of the norm term weights with the base case after 5, 10 and 20 years of optimization.**

**Fig. 4.16** shows the cumulative oil production and cumulative water injection for the base case and various norm terms for acceleration. It can be observed that for a norm term weight of zero (sweep efficiency optimization only) the cumulative oil production is more for same amount of cumulative water injection than any other case. Thus, the sweep efficiency optimization is more efficient at utilizing the injected water than accelerated production strategies. However, as the norm term weight is increased, the injectors tend to inject at their limit to accelerate the flood front. As a result of the increased injected volume, the cumulative oil production is also increased.

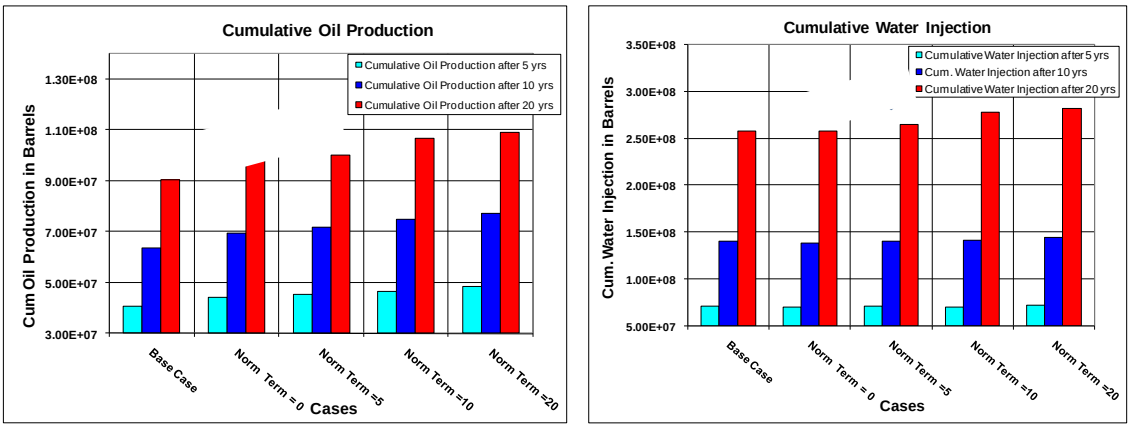


**Fig. 4.16 - Cumulative oil production and cumulative water injection after 5, 10 and 20 years of optimization.**

**Fig. 4.17(a)** shows the injection efficiency for various norm term weights. It can be observed that the injection efficiency of the waterflood decreases as the norm term weight is increased. Thus, production acceleration takes place at the expense of the injection efficiency. As discussed before for the 2D example, the trade-off curve can be used for selecting the optimal level of production acceleration. The trade-off curve to choose an optimal norm term weight for the Brugge field case is shown in **Fig. 4.17(b)**. The optimal norm term weight is found to be around 4 in this case.

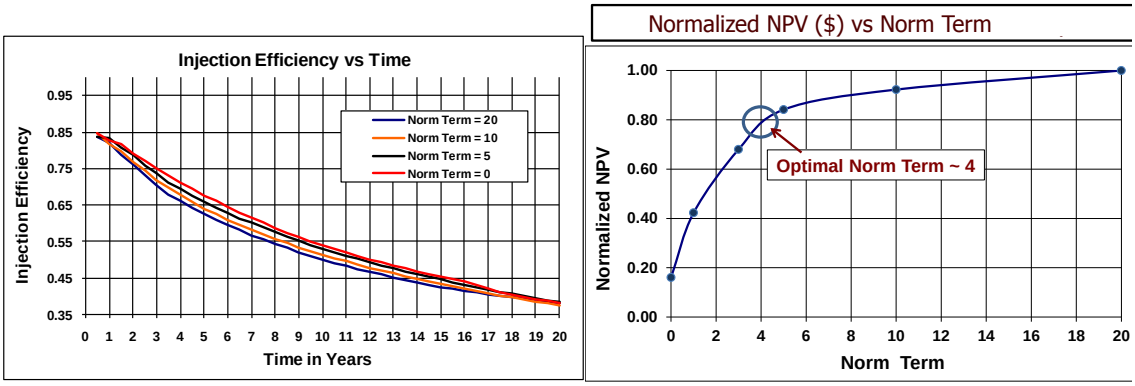


**Fig. 4.17 - (a) Injection efficiency for various norm term weights (b) Selection of optimal norm term weight using trade-off curve analysis.**

**Fig. 4.18** shows permeability for layers 3 and 8 of a single realization of Brugge field. Finally, **Fig. 4.19** shows the oil saturation differences for the base case, sweep efficiency optimization (norm term weight = 0) and accelerated production strategy (norm term weight = 10), for these two selected layers (3 and 8). In second row the difference between initial oil saturation and saturation after 20 years for base case is shown. In the third row difference between base case oil saturation and sweep efficiency optimization (norm term weight = 0) oil saturation after 20 years is shown. Finally, in the fourth row difference between sweep efficiency optimization (norm term weight = 0) oil saturation and accelerated production strategy (norm term weight = 10) oil saturation after 20 years is shown. As expected, both cases of optimization show improved sweep, compared to the base case. Because of increased cumulative water injection, the accelerated strategy leads to additional gain in swept volumes. Again tradeoff curve discussed earlier can be used to select optimal tradeoff between production acceleration and sweep efficiency maximization.

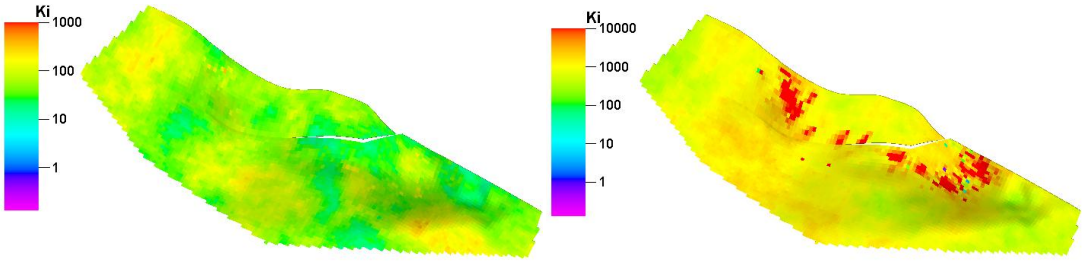


**Fig. 4.18 - Permeability for layer 3 and layer 8 of a single realization of Brugge field.**

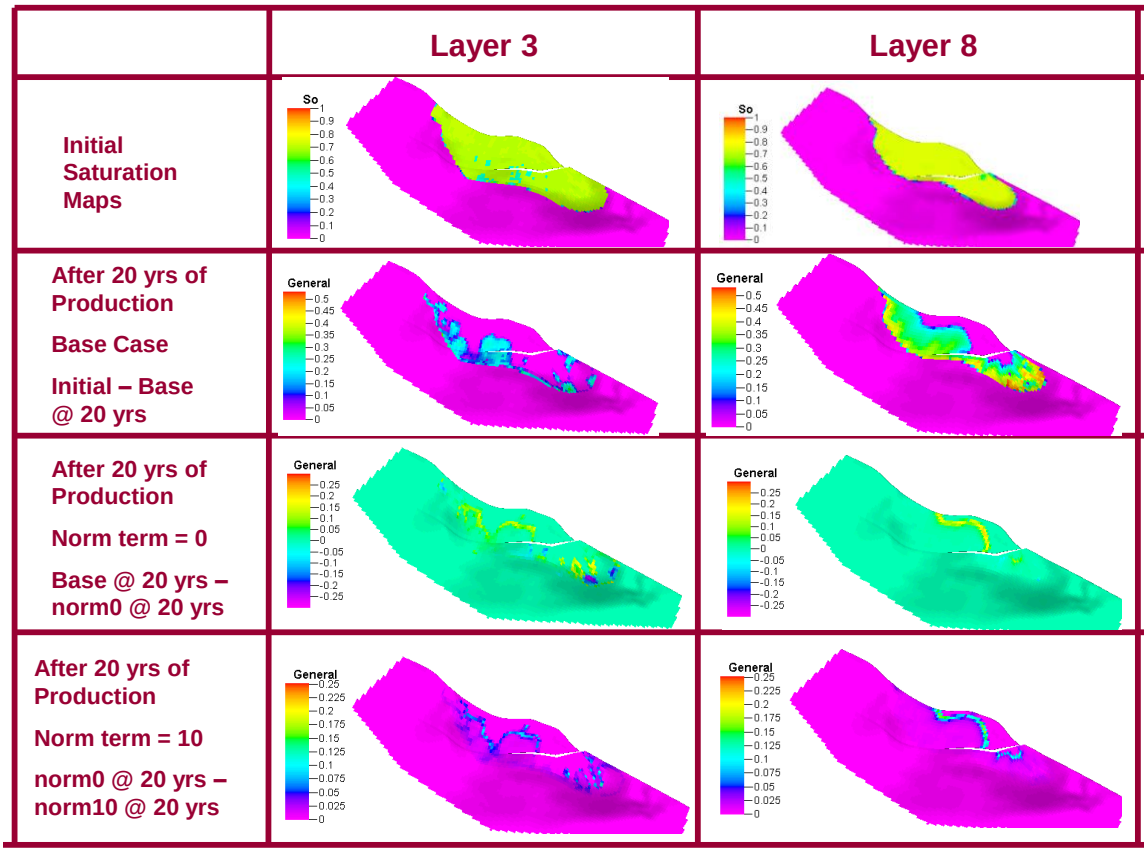


**Fig. 4.19 - Oil saturation difference maps for Layer 3 and 8 for base case, norm term weight = 0 and norm term weight = 10.**

#### 4.5.2.3 Flood Optimization Using Multiple Models: Accounting for Geological Uncertainty

In this section geological uncertainty is incorporated into the optimization using multiple geologic realizations. Ten realizations of the Brugge field are used for rate optimization (Peters et al., 2009). The optimization was carried out using the expected value formulation as discussed before (**Eq. 4.16**) under risk neutral conditions ($r = 0$). To examine the robustness of the optimization with respect to geological uncertainty, the optimized rates obtained from these ten realizations are applied to a blind realization which was not included in the optimization process. For comparison purposes, the optimal rates obtained from the single realization optimization (discussed in **section 4.5.2.2**) are applied to the same blind realization.

To illustrate the variability amongst the geologic realizations, **Fig. 4.20** illustrates the permeability distribution in the top layer for each of the 10 realizations used during optimization.

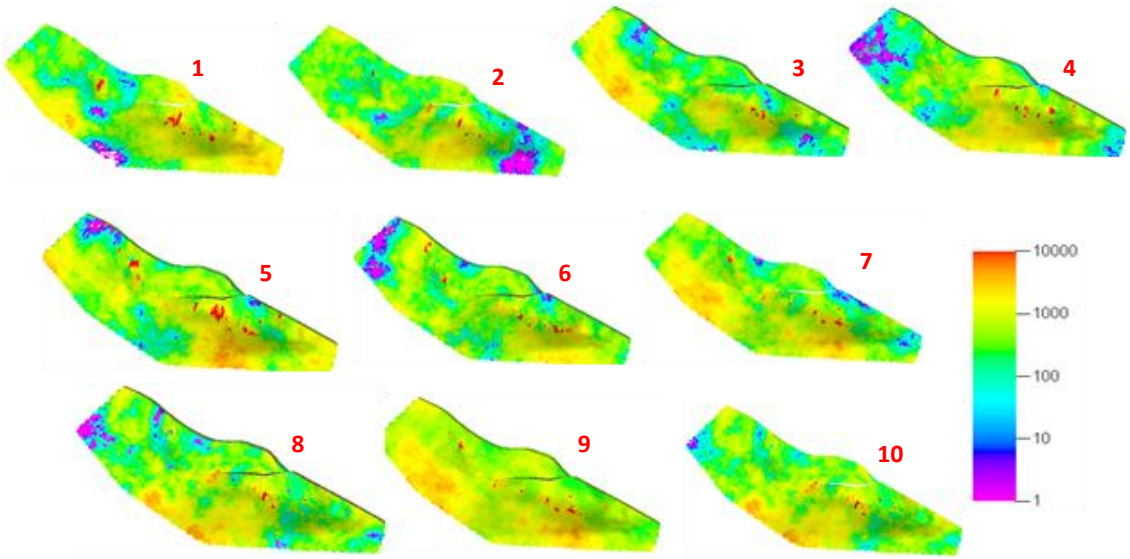


**Fig. 4.20 - Permeability for layer 1 of 10 realizations used in stochastic optimization.**

Again, for comparison purposes, the top layer permeability for the blind realization used to test the optimization methods is shown in **Fig. 4.21.**

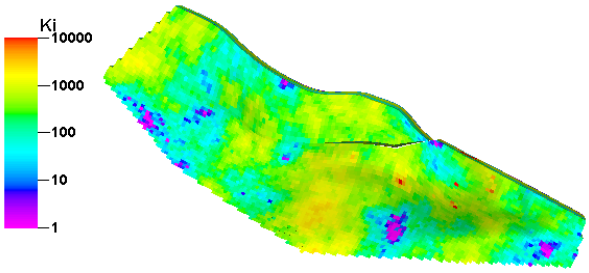


**Fig. 4.21 - Permeability for layer 1 of blind realization used in stochastic optimization.**

**Fig. 4.22** shows the performance of the blind realization in terms of cumulative oil production and cumulative water injection. The results have been shown for two cases. The first case uses the rates derived from optimization of a single realization (realization no. 1 in **Fig. 4.20**) that have been applied to the blind realization. Thus, there is no consideration of the geological uncertainty for this case. The second case accounted for geological uncertainty by carrying out the optimization simultaneously over ten realizations and these optimal rates are then applied to the blind realization.

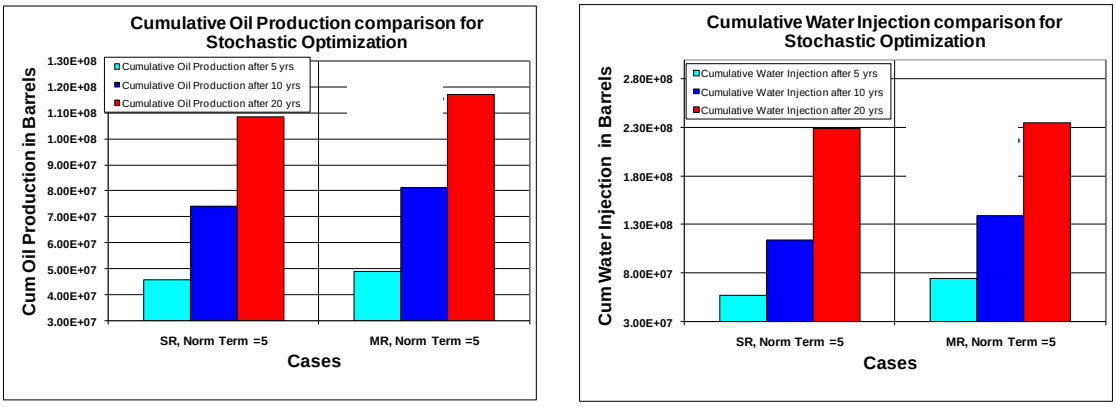


**Fig. 4.22 - Cumulative oil production and cumulative water injection after 5,10 and 20 years for single realization (SR) and multiple realization (MR) optimization for norm term weight = 5.**

For single as well as multiple realization optimizations, a norm term weight of 5 is used. It can be observed that the use of multiple realizations has resulted in almost 9% incremental oil recovery as compared to the single realization after 20 years, for the blind realization with only 0.5% incremental water injection. Similarly, an 8% increase in NPV is seen for the multi-realization optimization **(Fig. 4.23).** This clearly seems to demonstrate the benefits of accounting for geological uncertainty during optimization in terms of robustness of the optimality conditions.

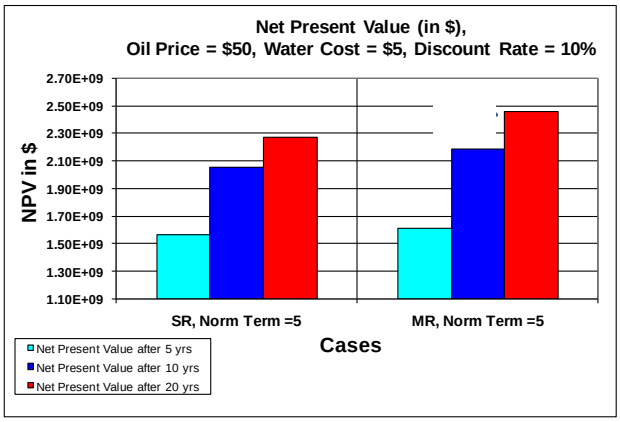


**Fig. 4.23 – NPV ($) after 5, 10 and 20 years for single realization (SR) and multiple realization (MR) optimization for norm term weight = 5.**

Permeability for layers 3 and 8 used in the stochastic optimization is illustrated in **Fig. 4.24**.

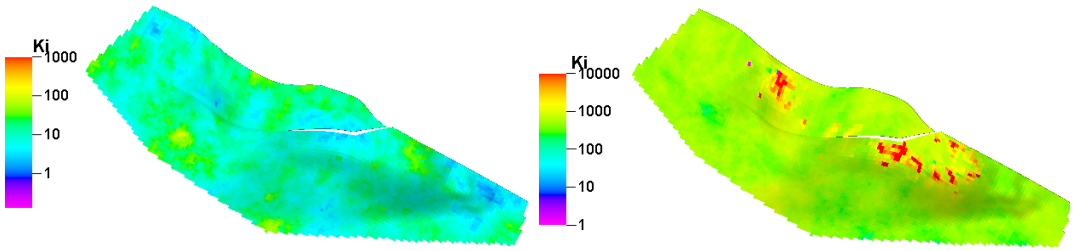


**Fig. 4.24 - Permeability for layer 3 and layer 8 of blind realization used in stochastic optimization.**

Finally, **Fig. 4.25** shows the oil saturation distribution for these two selected layers (3 and 8). Again, there is comparison of the difference in oil saturation distribution for the blind realization after 20 years using the rates derived from the single realization and multiple realization optimizations. In second row the difference between initial oil saturation (blind realization) and saturation after 20 years (blind realization) using single realization optimization is shown. In third row difference between oil saturation after 20 years (blind realization) using single realization optimization and multiple realization optimization is shown. The improved sweep from the multiple realization case again reflects the benefits of accounting for geological uncertainty and is consistent with the increased cumulative production as shown in **Fig. 4.22**.

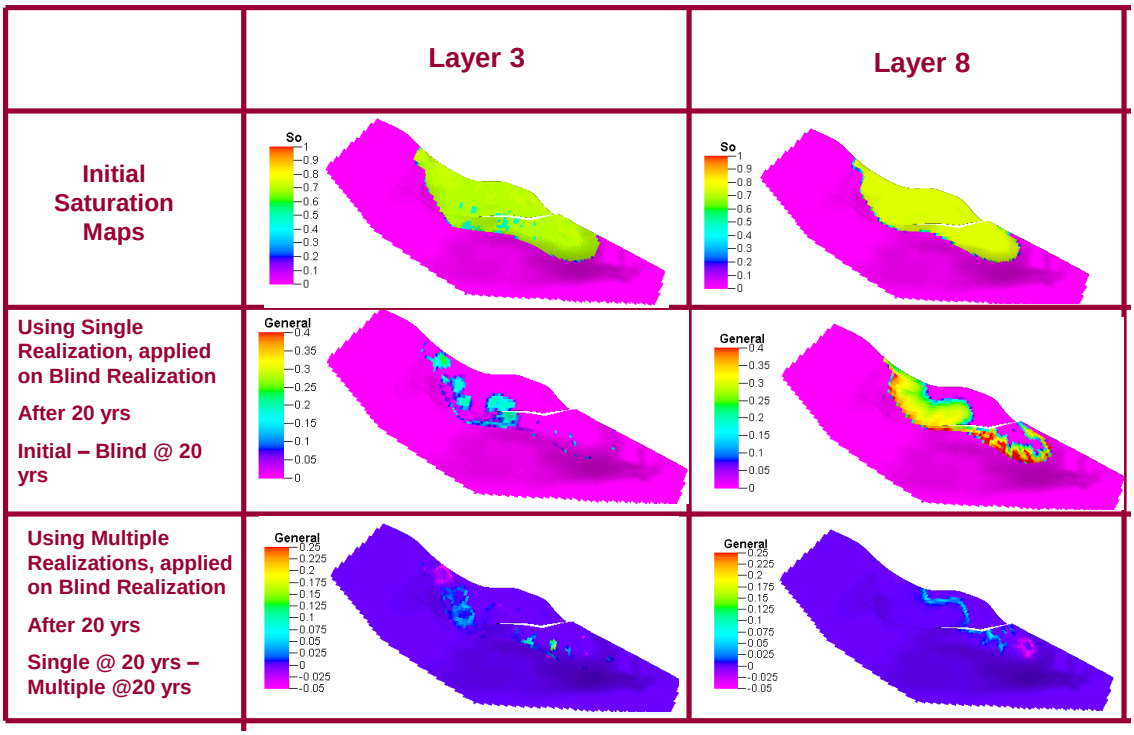


**Fig. 4.25 - Oil saturation difference maps for layer 3 and 8 for single realization and multiple realization optimization for norm term weight = 5.**

### 4.6 Summary and Conclusions

In this chapter the trade-off between sweep efficiency and Net Present Value (NPV) in the field-scale rate optimization is explored and a practical and efficient way of optimal rate allocation based on a compromise between the two is proposed. Because of the economic as well as regulatory constraints, field-scale optimization is typically not based solely on NPV or maximizing recovery. The previous work mainly focused on maximizing recovery or sweep efficiency and did not account for production acceleration. Previous work has been built upon to account for both NPV as well as maximizing sweep efficiency through a trade-off analysis. Some specific conclusions from this study are as follows:

- An augmented objective function (norm term) for field-scale rate optimization is proposed that accounts for maximizing sweep efficiency as well as production acceleration.
- Given a starting condition, norm term helps in picking a particular arrival time equalization solution among several non-unique solutions that also minimizes arrival time which results in acceleration of rates subject to constraints.
- It has been illustrated that during production optimization, there is a tradeoff between maximizing sweep efficiency and maximizing NPV. Optimum tradeoff can be selected based on the 'trade-off curve' between the cumulative NPV and the weight on the norm term.
- For voidage balance case while optimizing both injector (injector rate is not fixed) and producer, norm term helps in accelerating rates and reduces penalty on high productive wells while sacrificing injection efficiency. On the other hand, for non-voidage balance case, norm term prevents slowing down of wells and improves injection efficiency.
- Different starting rates of wells during optimization result in different converged rates. This is due to the existence of multiple local minima.
- Streamlines derived from a finite-difference simulator have been utilized to analytically compute the gradient and Hessian of the objective function using a

single flow simulation per optimization iteration. This makes the proposed approach particularly well-suited for field-scale rate optimization using high resolution geological models having large number of wells.

- The robustness and practical feasibility of the proposed approach to capture hierarchy of rate and pressure constraints in realistic production scenarios have been demonstrated using a 3D synthetic benchmark field example with smart wells and inflow control valves. Stochastic optimization was also implemented to take geological uncertainty into consideration. The value of using multiple realizations in improving the robustness of the optimization in terms of oil recovery and enhancing NPV has been clearly illustrated using the 3D example.

# CHAPTER V

# WELL PLACEMENT UNDER UNCERTAINTY USING STREAMLINE BASED QUALITY MAPS*

## 5.1 Summary

The placement of infill producers and injectors is an important aspect in the overall development strategy of any field and is particularly challenging for mature fields with high levels of water-cut. Previous screening approaches based upon static reservoir quality maps have limited applicability as these do not account for the drainage and swept volumes from existing wells. In contrast, direct application of formal optimization methods such as evolutionary algorithms and adjoint-based methods to high resolution geologic models may better represent reservoir dynamics but can be complex to implement or computationally prohibitive.

A novel method is proposed for well placement optimization that relies on streamlines which represents the flow paths in the reservoir and the time of flight which represents the travel time of fluids along streamlines. Specifically, the streamline time of flight from the injectors provides swept volumes for injectors whereas streamline time of flight from producers gives drainage volumes for producers. These quantities can be effectively combined to a 'total time of flight' to locate the potential regions of poorly swept and drained oil in the reservoir. The proposed approach utilizes a dynamic measure based on the total streamline time of flight combined with static parameters to identify potential locations for infill drilling. Areas having high value of the dynamic

---

* Part of this chapter is reprinted with permission from "Well Placement Optimization in a Mature Carbonate Waterflood using Streamline-based Quality Maps" by Taware, S., Park, H., Datta-Gupta, A., Bhattacharya, S., Tomar, A., Kumar, M. and Rao, H. 2012. Paper SPE 155055-MS presented at the 2012 SPE Oil and Gas India Conference and Exhibition, 28-30 March 2012, Mumbai, India. 

measure (‘Sweet-spots’) are both poorly drained and poorly swept, making them attractive for drilling infill wells.

The power and utility of the proposed method is illustrated on a mature offshore carbonate field in western India. The simulation model was history matched using a hierarchical history matching approach that follows a sequence of calibrations from global to local parameters in coarsened and fine scales. Using the proposed method on the history matched model a dynamic measure map is obtained highlighting areas suitable for drilling infill wells. Finally, the performance of infill wells located using the dynamic measure map is compared with wells located using traditional well placement techniques, for example, oil pore-volume map from the simulation model. The proposed method consistently outperforms the traditional approaches. Subsequent field infill drilling in the field has validated the approach. In addition the proposed approach is also illustrated on a heavy oil field under strong aquifer drive.

The organization of this chapter is as follows. First, the problem of optimal well placement is briefly introduced. Then the major steps of the proposed method are outlined. After that rationale for dynamic measure is discussed. Following this proposed approach is demonstrated on 2D synthetic case along with a method to incorporate geological uncertainty. This is followed by showcasing the advantage of two-step approach of using ‘Sweet-Spots’ from dynamic measure map as starting points for a formal optimization algorithm (SPSA) for optimal well placement. This is followed by demonstration of power and utility of the proposed method on a mature offshore carbonate field and sector model of a heavy oil field by using ‘Sweet-Spots’ directly as optimal well locations.

## 5.2 Introduction

Placement of the infill producers and injectors is an important aspect of the overall development strategy of any field. Well placement optimization becomes particularly important in mature fields where new infill wells have to be drilled based on an improved understanding of the reservoir description and performance. There could be a large number of possible candidate locations for new infill wells. To search through and

evaluate all the possible locations is not practically feasible, particularly for high resolution geologic models consisting of multimillion cells. In addition, geologic uncertainty is accounted using multiple plausible realizations while deciding on optimal well placement locations. For large-scale field applications, a practical method is needed to mitigate the computational burden associated with the large number of search locations to minimize the number of simulation runs.

Previous applications of well placement optimization have utilized derivative-free optimization methods such as genetic algorithm or simulated annealing which are typically computationally expensive and thus, may not be well-suited for large-scale field applications (Centilmen et al., 1999). More efficient gradient based optimization algorithms that compute the gradient by solving adjoint equations have also been used. However, the adjoint methods are difficult to implement and typically require access to the simulator source code. The gradient-based methods can require a large number of iterations to converge and are very sensitive to the starting point for the optimization. Because of these difficulties, large-scale field applications of well placement optimization have been relatively few and far between. Many of the field applications have used upscaled models which tend to homogenize the reservoir and are unable to properly characterize the bypassed oil location which is closely tied to the well placement optimization problem. In this chapter, a novel streamline-based method is utilized to identify the potential locations of bypassed oil through detection of stagnant regions in the reservoir based on the streamline time of flight. This approach leads to a significant reduction in the search space for the optimization, making it practical for large-scale field applications. Dynamic measure is defined based on a combination of streamline attributes and reservoir properties and demonstrate its application for well placement optimization in an offshore carbonate reservoir.

### 5.3 Proposed Streamline-based Methodology

Streamlines define flow paths of different phases in the reservoir. They have spatial information of where which phases (oil, water and gas) are present and how they are moving in the reservoir. Also, the time of flight along a streamline is related to the transport time of fluids along the streamlines (Datta-Gupta and King, 2007). So, by using streamlines one can infer if the individual phases or total fluids are moving fast or slow in the reservoir. Streamlines inherently take structure of the reservoir, geometry of well patterns, existing drainage and swept areas and reservoir drive mechanism into consideration. In addition both streamlines and the time of flight can be computed very efficiently based on the velocity field at a given time. If needed, this velocity field can be derived from a finite difference simulator honoring full physics of multi-phase fluid flow, complex well management and trajectories.

A novel method is proposed for well placement optimization that relies on streamlines and associated time of flight to locate the potential regions for bypassed oil. The proposed method is practical for large field cases with multi-million grid cells, large number of wells and for multiple geological realizations to incorporate uncertainty. The proposed approach utilizes a dynamic measure based on the *total streamline time of flight* to identify 'Sweet-spots' for infill drilling and can be used with both streamline and finite-difference simulators. Ability to work with finite difference simulators ensures that all the aspects of active reservoir management, complex well trajectories along with complete physics of three phase flow are taken into consideration. A brief outline of the steps in the proposed method is as follows. (Please refer to **Fig. 5.1** and **Fig. 5.2** which illustrate the entire workflow).

- **Trace streamlines and compute total time of flight based on the velocity field of a finite-difference simulator**. To start with, fluxes required for tracing streamlines are read from the 'restart file' of the simulator corresponding to start of planning period (**Fig. 5.1)**. The total fluid fluxes are utilized to trace streamlines which represent the flow paths in the reservoir. Along the streamlines, two sets of time of flights are computed. The *time of flight from the injector* (TOFI) is the time required for a neutral particle to travel along the streamline starting from an injector. Contours of time of flight from the injector represent the reservoir swept volumes associated with the injector at various times. Similarly, the *time of flight from the producers* (TOFP) is computed in which the starting point of the streamlines is producers. Contours of time of flight from the producer represent the reservoir drainage volumes associated with the producers at various times. Both TOFI and TOFP are mapped onto the underlying grid cells using an arithmetic average of the time of flights of the streamlines within a given cell. The total time of flight (TOFT) is summation of time of flights from injectors and time of flight from producers, mapped to grid-cells (**Fig. 5.1)**. Texas A&M software DESTINY (Jimenez et al., 2010) has been used to perform this task for a variety of commercial or proprietary simulators. Based on total time of flight poorly drained and swept regions are identified. High values of the total time of flight highlight poorly drained and poorly swept areas.

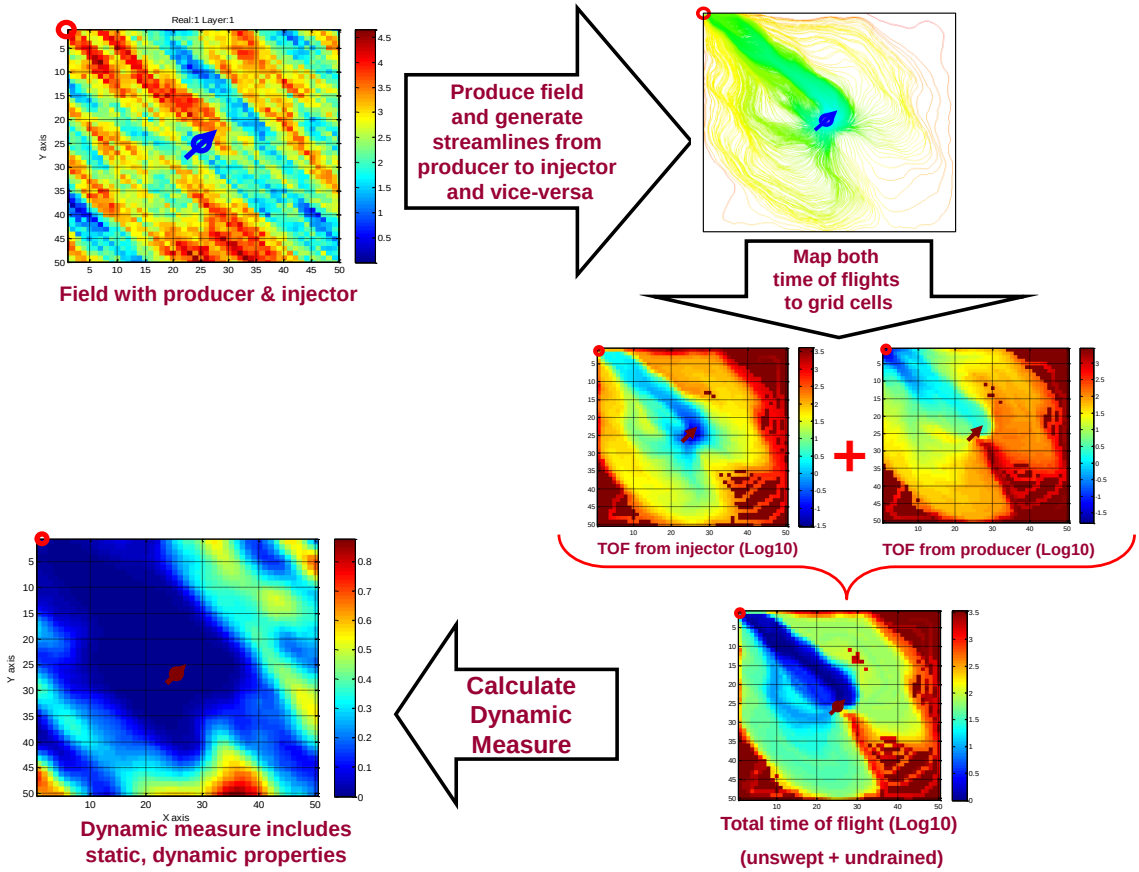


**Fig. 5.1 – Illustration of workflow for generating dynamic measure map based on total time of flight.**

- **Calculate a dynamic measure based on total time of flight and static and dynamic properties**. Next the total time of flight (TOFT) is combined with other static and dynamic properties to define a dynamic measure. Static properties used are permeability and pore-volume. Pore-volume takes structure and net to gross ratio (NTG) into consideration. Dynamic properties being used are oil saturation and oil relative permeability to account for the amount of remaining oil and its mobility. Static and dynamic properties are read from the simulation output files corresponding to the start of the planning period (**Fig. 5.2)**. Instead of absolute values of these properties relative values are being used. This is because the absolute values can vary by orders of magnitude not only between properties but

also within a property. Relative values give more importance to relationship between different regions in the model for a particular property. For relative values, normalized rank of grid block values for each property is calculated. Every grid block is given an ascending rank based on the value for a property. The grid block with lowest value is given rank 1 and so on. The ranks are then normalized to be between 0 and 1. The proposed dynamic measure is a product of rank normalized values of these properties for each grid block. Detail discussion about dynamic measure is given later in this section.

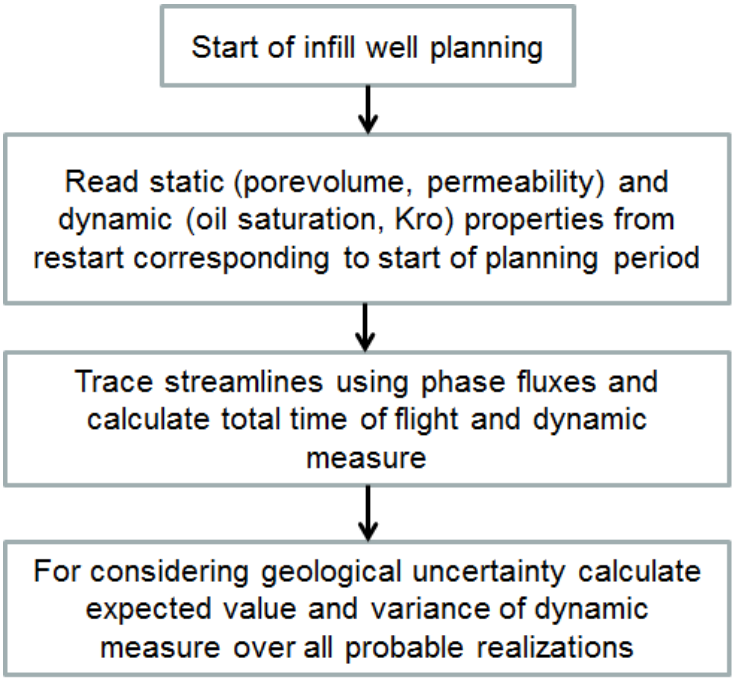


**Fig. 5.2 – Illustration of the workflow showing overall steps in generating streamline based quality maps.**

- **Perform well placement optimization by either of two methods:**
  a. Directly use ‘Sweet-spots’ as potential well placement locations. The ‘Sweet-spots’ are regions with high dynamic measure values. This approach is useful for large and mature field cases where it can be computationally prohibitive to do a formal optimization. The dynamic measure map can also be easily reconciled with available geological, geophysical and facilities data helping in prudent decision making. The demonstrative field examples are shown in **section 5.4**.
  b. Use ‘Sweet-spots’ as starting point during application of a formal optimization technique such as adjoint-based methods. This will help in reducing the number of simulations required for formal optimization problems to converge as the starting points are expected to be close to the solution. This approach will be demonstrated in detail using Simultaneous Perturbation Stochastic Approximation (SPSA) in **section 5.4.3**.

- **Multiple geologic realizations to account for geologic uncertainty**. Dynamic measure is calculated for multiple realizations and the risk analysis is performed using the maps of mean and variance of the dynamic measure over multiple realizations. Various types of geological uncertainties like structure, permeability, pore-volume, contacts and reservoir drive mechanisms can be taken into consideration while optimizing the well placement location. A demonstrative example is shown in **section 5.4.2**.

The main advantage of the proposed method is its computational efficiency as the optimum areas for infill drilling can be found rather quickly. This not only makes our approach suitable for large-scale field applications but also allows for uncertainty assessment through examination of multiple geologic realizations. The uncertainty assessment is of particular importance in well placement because typically geologic uncertainty can be an overriding factor in the decision to drill or not to drill. Also

dynamic measure being a grid property can be easily reconciled with available geological and geophysical data during decision making. In addition use of 'Sweet-spots' as starting points for formal optimization algorithm will reduce the number of iterations and lower the chance of getting stuck in local minima.

### 5.3.1 Dynamic Measure: Background and Rationale

The proposed dynamic measure has been derived mainly heuristically and the rationale behind this measure is discussed here. The dynamic measure (*DM*) is a combination of static properties such as permeability (*k*), *porevolume* (including Net to Gross, NTG) and dynamic properties, specifically oil saturation ($S_o$), rock type or region dependent oil relative permeability (*kro)* and the streamline total time of flight (*TOFT*). All these properties are rank normalized as described earlier. The dynamic measure is computed as the following product,

$$Dynamic\ Measure(DM) = (TOFT_{RN} \cdot So_{RN} \cdot porevolume_{RN} \cdot k_{RN} \cdot kro_{RN}) \quad \text{…..... (5.1)}$$

Subscript ***RN*** denotes rank normalization of the property. Rank normalization of property is done for each grid cell. To provide a rationale for the dynamic measure, let us look at the oil volumetric flux $q_o$ for a grid cell given by,

$$q_o = PI \cdot \frac{kro(S_O)}{\mu_o(\overline{P}) \cdot B_o(\overline{P})} \cdot (\overline{P} - P_{wf}) \quad \text{……..(5.2)}$$

Where

$$PI = \frac{k \cdot (\Delta z) \cdot (NTG)}{7.08 \cdot 10^{-3} \cdot \left[ \ln\left(\frac{r_o}{r_w}\right) + S \right]} \quad \text{……(5.3)}$$

Where, $kro(S_o)$ is the relative oil permeability which is the function of oil saturation. Also, $\mu_o(\bar{P})$ is oil viscosity and $B_o(\bar{P})$ is oil formation volume factor, both are function of average reservoir pressure. Because one is interested in relative oil productivity for a given drawdown, parameters common to the grid blocks such as $\mu_o(\bar{P})$ and $B_o(\bar{P})$ can be factored out (Kharghoria et al., 2003). Also, $q_o$ represents volumetric oil flux and contains no information about the total oil volume associated with it. Hence, $\phi \cdot S_O$ is added to incorporate the oil volume (Kharghoria et al., 2003). Therefore, the dynamic measure can be heuristically represented as,

$$DM \cong \Delta z \cdot NTG \cdot \phi \cdot S_O \cdot k \cdot k_{ro}(S_O) \quad \text{.....(5.4)}$$

The oil bearing capacity $\Delta z \cdot NTG \cdot \phi \cdot S_O$ can be represented by $porevolume \cdot S_O$. Adding total time of flight (*TOFT*) to these terms will highlight the areas that are poorly drained and swept. Hence, the dynamic measure is computed as follows,

$$Dynamic\ Measure\ (DM) = Porevolume \cdot S_O \cdot k \cdot k_{ro}(S_O) \cdot TOFT \quad \text{.....(5.5)}$$

Using rank normalization for the reason discussed above,

$$Dynamic\ Measure\ (DM) = (TOFT_{RN} \cdot So_{RN} \cdot Porevolume_{RN} \cdot k_{RN} \cdot kro_{RN}) \quad \text{.....(5.6)}$$

### 5.3.2 Software Implementation

The entire workflow has been implemented in software, DESTINY, developed as part of a joint industry project at the Texas A&M University. Streamlines can be traced using the fluxes generated by a variety of commercial finite-difference simulator. For streamline simulators, the streamlines are readily available and this step is not needed.

Thus, the proposed workflow can be implemented in both finite difference and streamline simulators. The use of commercial simulators allows availing of complex well management capabilities, horizontal/multilateral wells and other complicated well trajectories along with advanced three-phase flow physics. The workflow in DESTINY is illustrated in **Fig. 5.1**. First, static properties such as pore-volume, permeabilities are read from the simulator output file. Next, dynamic properties, for example, oil saturation, oil relative permeability and phase fluxes are read from the simulator 'restart file' corresponding to the start of planning period. Using the total fluid fluxes, streamlines are traced starting from the injectors and the TOFI is calculated. Similarly, the TOFP is computed by tracing streamlines from the producers. The total time of flight is calculated by summing TOFI and TOFP at each grid cell. The calculation of time of flight based dynamic measure is illustrated in **Fig. 5.2** using a 2D heterogeneous permeability field. At the time of interest, the streamline time of flight is calculated starting from producers and injectors and the time of flights are mapped to the grid cells. If there are multiple streamlines passing through a cell, then the time of flight is averaged and that value is assigned to that grid cell. For total time of flight, both time of flights (from producers and from injectors) are added. After mapping total time of flight to grid cells, dynamic measure is calculated as shown in **Fig. 5.5.** For considering geologic uncertainty expected value and variance of dynamic measure is calculated over multiple realizations. This will be illustrated in **section 5.5.2**.

### 5.4 Synthetic Applications

The proposed approach is illustrated using a 2D synthetic example. A comparison of dynamic measure map with a robust cumulative oil map is also shown. A method to consider geological uncertainty is also illustrated. In addition use of sweets-spots as starting point using a formal optimization method namely SPSA is also demonstrated. Also the proposed approach is illustrated using a high resolution simulation model of a mature carbonate field under waterflood and a sector model of heavy oil field under strong aquifer.

### 5.4.1 2D Synthetic Example

In this example, the use of the dynamic measure in aiding infill well placement is illustrated using a 2D example having one producer and injector. The permeability field is shown in the log10 scale in **Fig. 5.3** along with remaining oil volume after one year of production and injection in **Fig. 5.4.** The 2D field was produced for one year on voidage balance of 400 RB / day. The objective here is to find an optimum well location for a second producer which maximizes cumulative field oil production for the next 5 years.

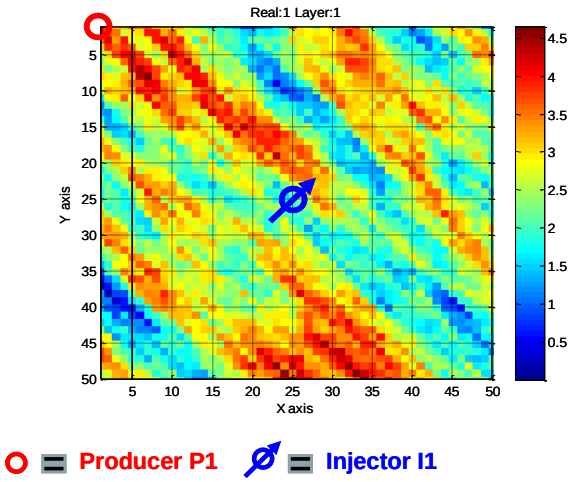


**Fig. 5.3 – Permeability field (log10) for synthetic 2D case.**

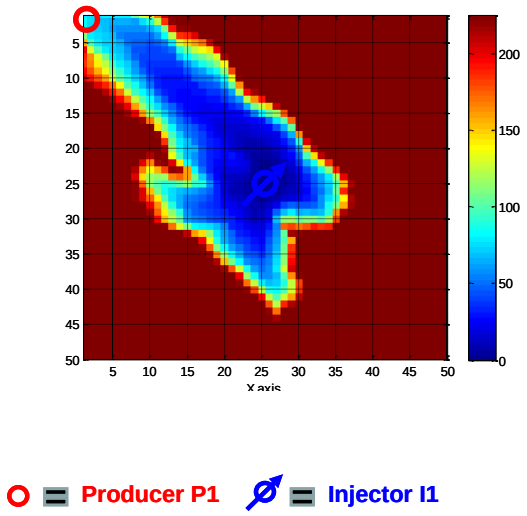


**Fig. 5.4 – Remaining oil porevolume (RB) after one year of production and injection for synthetic 2D case.**

**Fig. 5.5** shows time of flight from producer and from injector in log10 scale. Large time of flight from producer highlights areas which are not being drained while large time of flight from injector highlights areas which are not being swept.

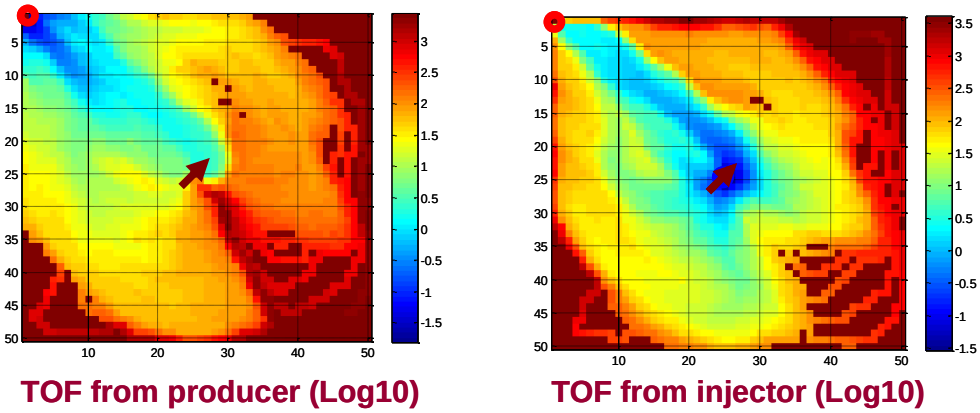


**Fig. 5.5 – Time of flight from producer (left) and time of flight from injector (right) for synthetic 2D case.**

Total time of flight (TOFT) highlights areas which are both difficult to drain and sweep. TOFT map for this 2D case is shown in **Fig. 5.6** in the log10 scale.

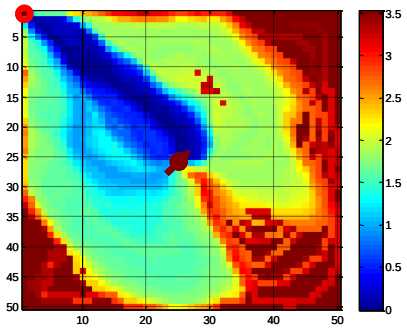


**Fig. 5.6 – Total time of flight for synthetic case.**

Dynamic measure is calculated using this TOFT as discussed before. Dynamic measure for this 2D example is shown in **Fig. 5.7**. For comparison purposes, a field cumulative oil map **(Fig. 5.7)** is generated by placing a producer in turn in each available grid cell and producing the model for next five years. The production conditions are of voidage balance of 400 RB/ day. The cumulative oil map is a representation of the value addition of an additional producer to field cumulative oil. It can be seen that 'high' regions in the dynamic measure map coincide with 'high' regions in the cumulative oil map. This validates the proposed approach to infill well placement. It must be pointed out that for this synthetic example, 2498 flow simulations are needed, one per available grid cell, to generate the cumulative oil map. The dynamic measure calculations require no additional simulations, other than generation of streamlines and computing the time of flight. Finally, the high value regions in dynamic measure map can be used as starting points in a formal optimization algorithm. The advantage of this is illustrated in **section 5.4.3**.

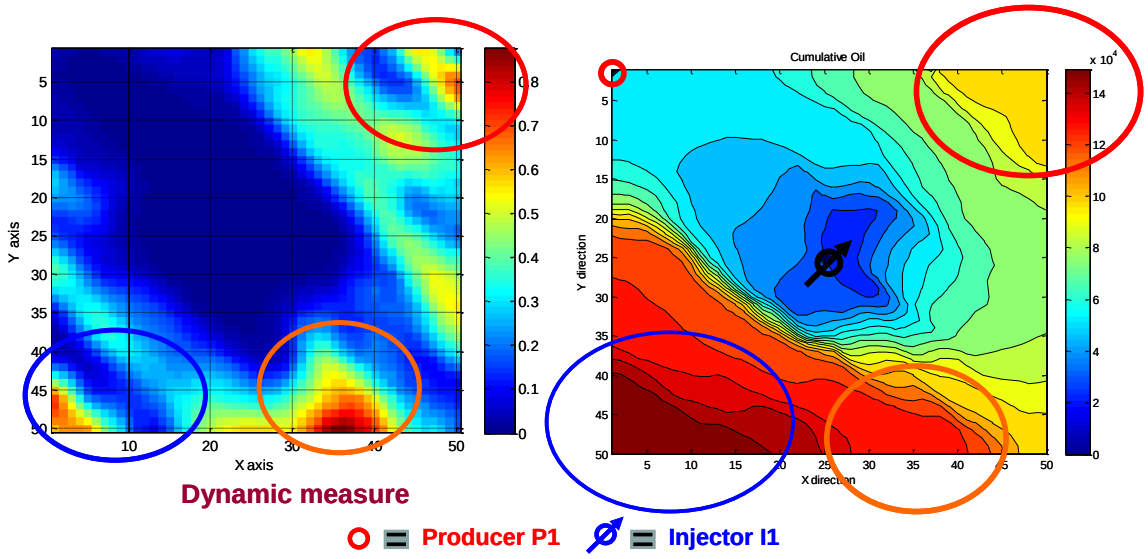


**Fig. 5.7 – Dynamic measure map (left) and robust cumulative oil map (right) for synthetic 2D case.**

The proposed dynamic measure was also compared with a previously proposed measure $q_o$ map (Kharghoria et al., 2003) that is based solely on oil productivity without explicitly considering the poorly drained and swept regions. **Fig. 5.8** shows $q_o$ map for this 2D example in the top right corner. **Fig. 5.8** also shows the dynamic measure map for the same case in top left corner. In bottom part of **Fig. 5.8** a field cumulative oil map is shown. This robust cumulative oil map is generated by placing a producer, one at a time, in each remaining grid cells and producing the model for next five years. It can be seen that the dynamic measure map shows much better correspondence with the robust cumulative oil map.

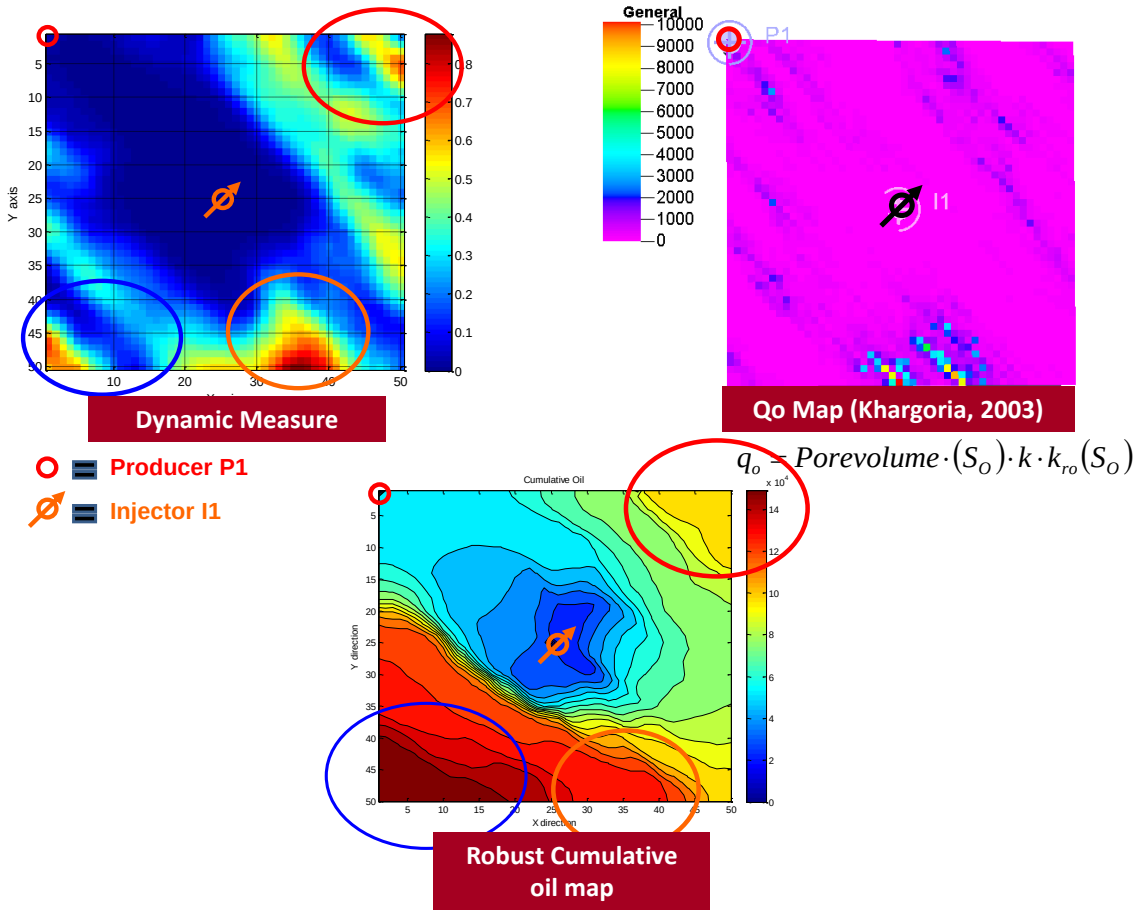


**Fig. 5.8 – Comparison of $q_o$ map (top right) and dynamic measure map (top left) with robust cumulative oil map shown in the bottom.**

For further understanding of better correspondence of dynamic measure map with the robust cumulative oil map, compared to the $q_o$ map, a comparison of rank correlation plot is shown in **Fig. 5.9**. A rank correlation plot is a cross-plot between ascending ranks of grid-cells in two maps, based on their respective property values. In **Fig. 5.9**, on the top, a rank correlation plot between $q_o$ map and robust cumulative oil map is plotted showing correlation coefficient of 0.29. While on the bottom a rank correlation plot between dynamic measure map and robust cumulative oil map is plotted. This has significantly higher correlation coefficient of 0.56 than rank correlation cross-

plot for $q_o$ map. This illustrates better correspondence of dynamic measure map with the robust cumulative oil map compared to the $q_o$ map.

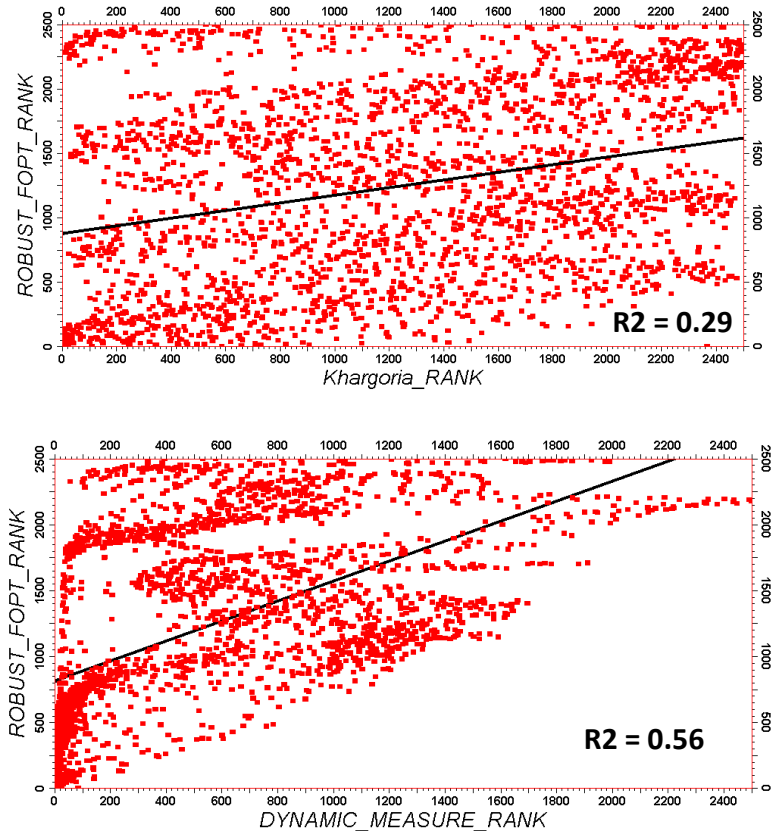


**Fig. 5.9 – Comparison of rank correlation plot for $q_o$ map (top) and dynamic measure map (bottom) with robust cumulative oil map.**

### 5.4.2 Geologic Uncertainty Using Multiple Realizations

It is important to incorporate geologic uncertainty in well placement decision. Geologic uncertainties can consist of structure (faults, tops, pore volumes etc), contacts, permeability, saturations etc. Uncertainties can be incorporated in the proposed dynamic measure using multiple realizations. The approach is illustrated using four different

permeability realizations of the 2D example (‘true’ permeability) in Fig. 5.5. Other types of uncertainties such as pore-volume, structure etc. can also be incorporated. The permeability for these four realizations is shown in **Fig. 5.10** along with permeability for ‘true’ case. Remaining oil for four realizations is shown in **Fig. 5.11** along with true case, after producing for 1 year on voidage balance of 400 RB/day. It can be seen that there is considerable uncertainty in remaining oil distribution for the four different realizations.

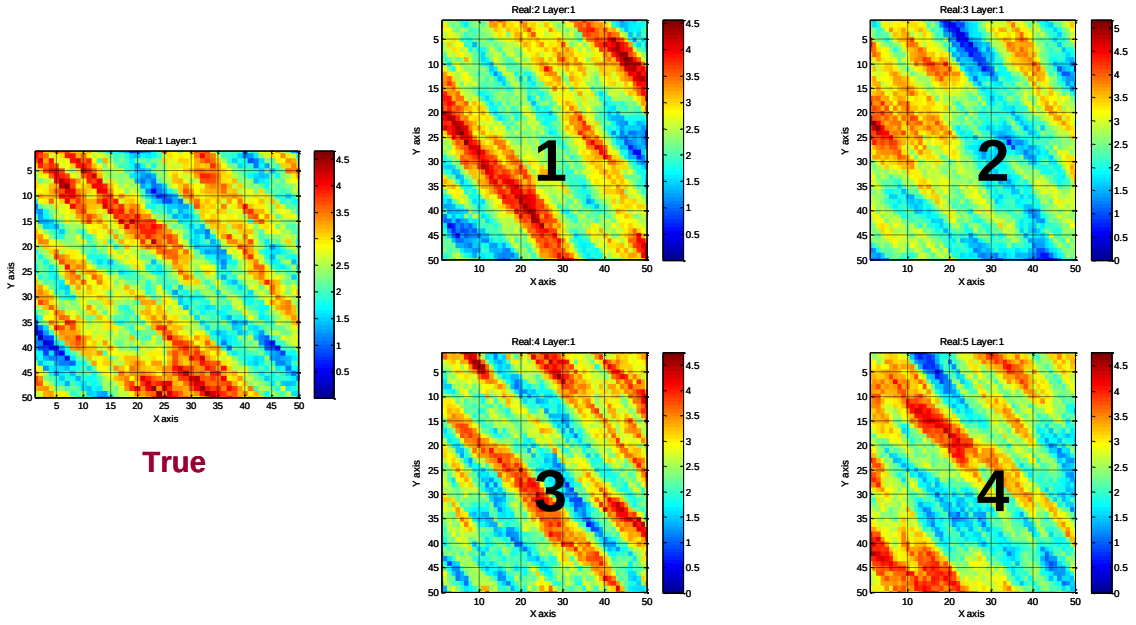


**Fig. 5.10 – Four permeability realizations used for generating dynamic measure map under geologic uncertainty along with true case.**

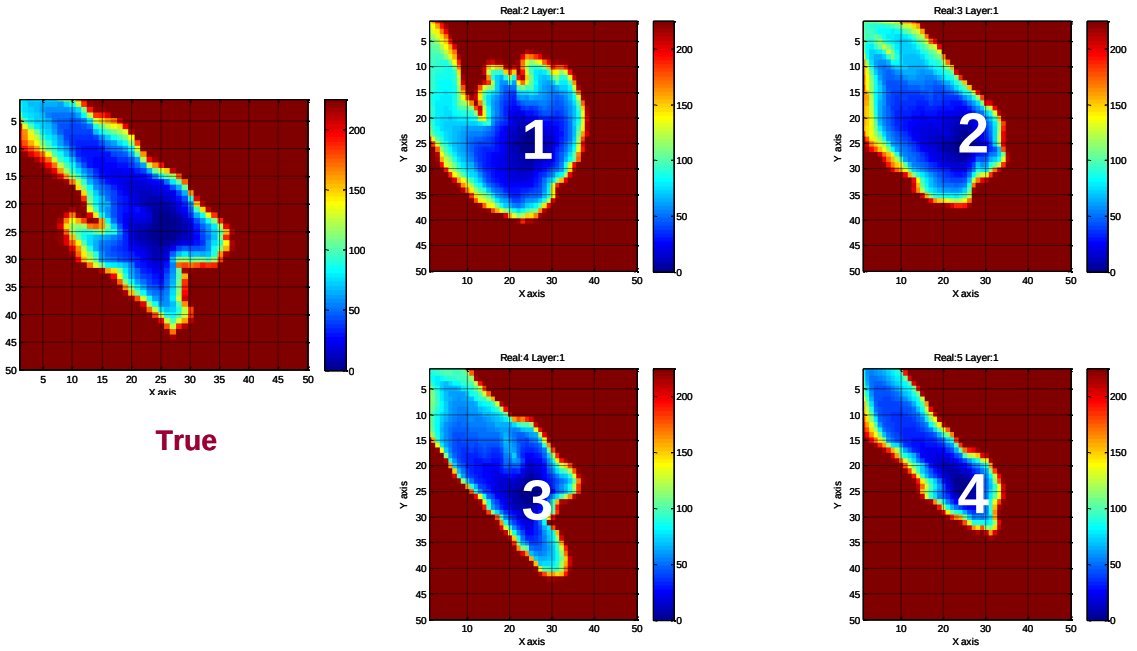


**Fig. 5.11 - Remaining oil porevolume (RB) is shown for four realizations along with true case after producing the true case for one year.**

Dynamic measure is shown for true case as well as four realizations in **Fig. 5.12**. The results from the multiple realizations can be analyzed as follows.

- *Expected value map of dynamic measure over all realizations:* Here an expected value (mean) of the dynamic measure is taken over all realizations.
- *Variance map of dynamic measure over all realizations:* Here, a variance of the dynamic measure is computed over all realizations. Variance quantifies the degree of confidence in the dynamic measure. Lower the variance of an area, higher is the confidence in dynamic measure for that area.

Areas with high ‘expected’ value of the dynamic measure and low value of variance of the dynamic measure are the more probable regions for drilling next infill well based on available information.

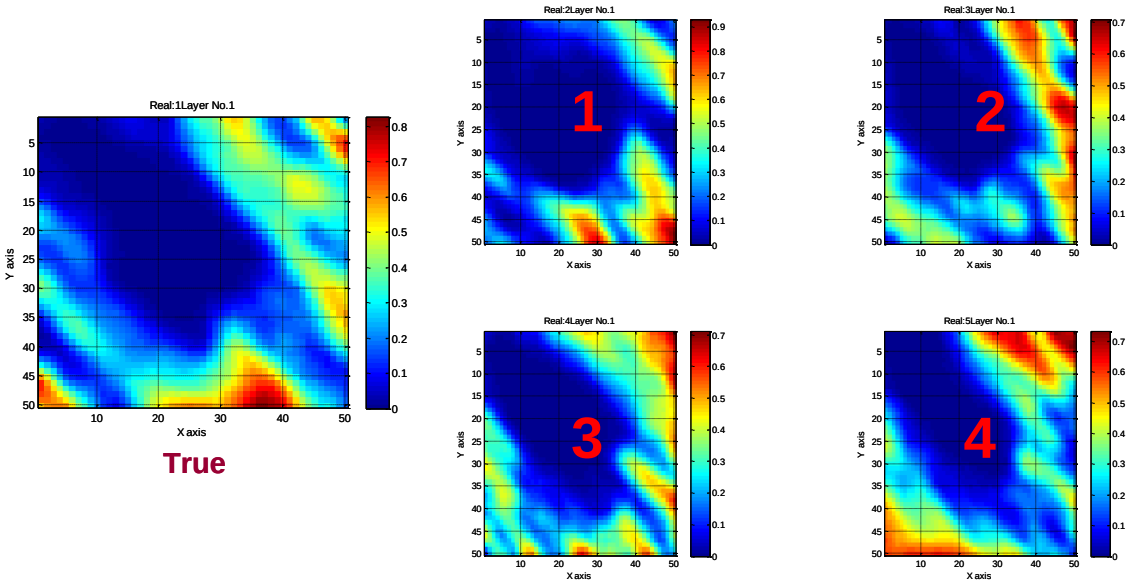


**Fig. 5.12 – Dynamic measure map is shown for four realizations along with true case after producing the true case for one year.**

The expected value map is compared with the field cumulative oil map for the 'true' case in **Fig. 5.13.** It can be seen that 'high' regions in the expected value map coincide with the 'high' regions in the cumulative oil map for true case.

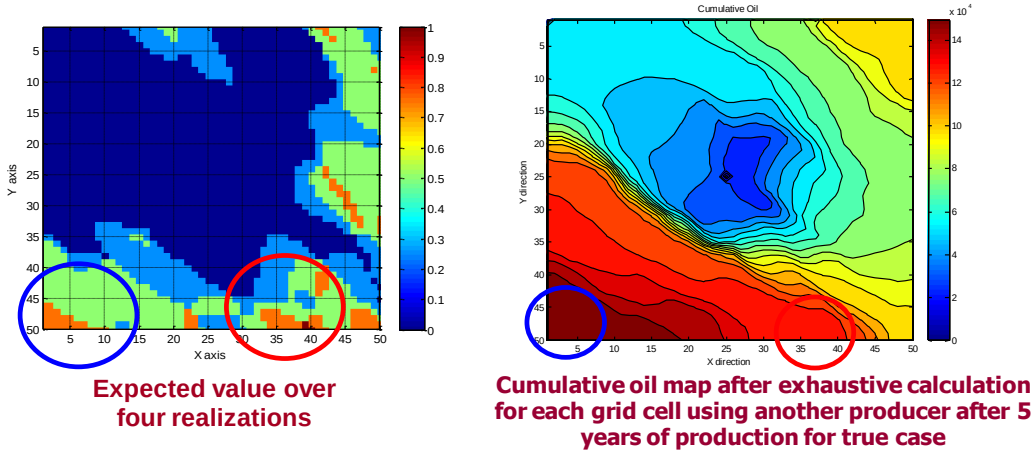


**Fig. 5.13 – Comparison of expected value map of dynamic measure over four realizations to a robust field cumulative oil map for true case.**

Uncertainly in decision making for drilling next wells can be evaluated by using this expected value map in conjunction with the variance map as shown in **Fig. 5.14**.

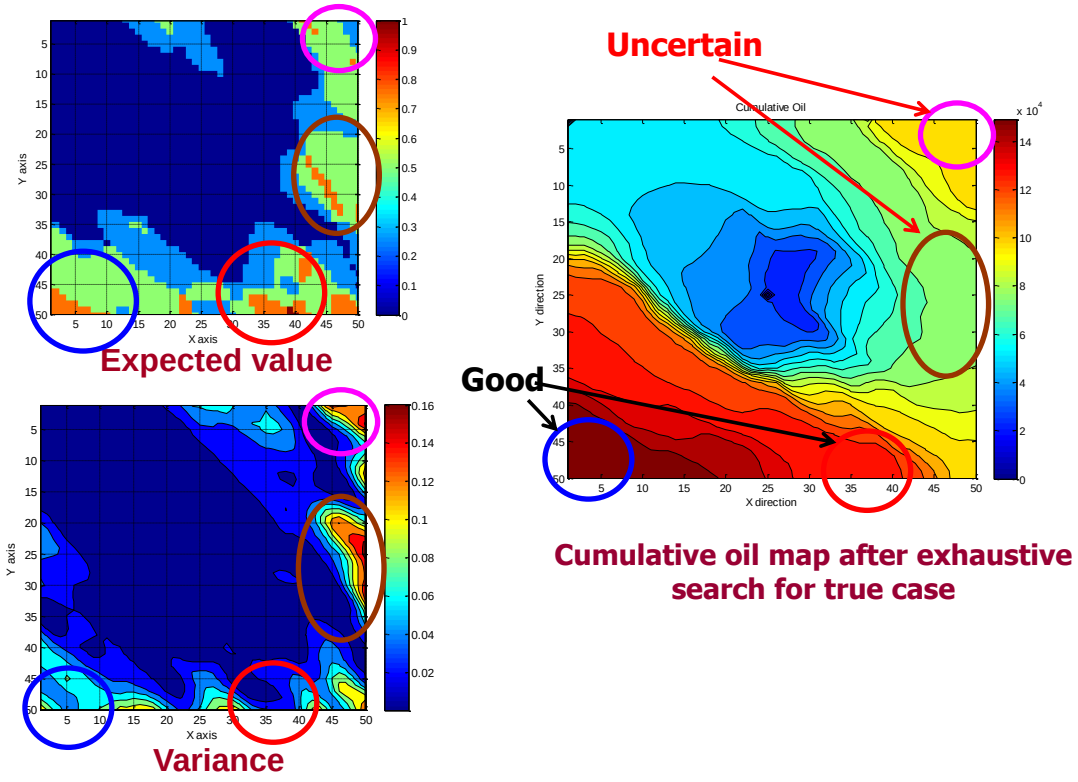


**Fig. 5.14 – A comparison of variance map along with expected value map of dynamic measure over four realizations to a robust field cumulative oil map for true case.**

### 5.4.3 Sweet-spots as Starting Points in Formal Optimization Method

In this section the use of 'Sweet-spots' (high value dynamic measure regions) as starting points in a formal optimization method is illustrated. The main advantage of this method will be its computational efficiency as the optimum location will be reached in a relatively few iterations (simulations) because of the reduced search space. The formal optimization algorithm used for illustration is the Simultaneous Perturbation Stochastic Approximation (SPSA). SPSA is an algorithmic method for optimizing systems with multiple unknown parameters. The SPSA algorithm has shown promise in the past because it is well-suited for discrete variables and requires only two function evaluations (simulations) per iteration of the optimization, regardless of the dimension of the

optimization problem. Briefly, in this approach, a random direction is selected for all the parameters from a Bernoulli distribution and only two function evaluations are carried out for all the parameters in the selected directions simultaneously. From these, an estimate of the descent direction is made and a step is taken in this direction. The computational efficiency of the method stems from the fact that only two simulations are needed for each iteration. The speed is further improved by reducing the number of simulations required using ‘Sweet-spots’.

#### 5.4.3.1 SPSA Theory and Algorithm Description

Simultaneous Perturbation Stochastic Approximation (SPSA) uses only objective function measurements similar to methods such as simulated annealing or genetic algorithms. This contrasts with algorithms requiring direct measurements of the gradient of the objective function (which are often difficult to obtain is case of well placement) Further, SPSA is especially efficient in high-dimensional problems in terms of providing a good solution for a relatively small number of measurements of the objective function.

The essential feature of SPSA, which provides its power and relative ease of use in difficult multivariate optimization problems, is the gradient approximation that requires only two objective function measurements per iteration regardless of the dimension of the optimization problem. These two measurements are made by simultaneously varying in a "proper" random fashion all of the variables in the problem (the "simultaneous perturbation"). This contrasts with the classical ("finite-difference") method where the variables are varied one at a time. If the number of terms being optimized is $p$, then the finite-difference method takes $2p$ measurements of the objective function at each iteration (to calculate one gradient approximation) while SPSA takes only two measurements.

The essential features of SPSA which makes it useful for discrete optimization problems like well placement are as follows,

1. SPSA is useful where sensitivity calculation is difficult such as in problems like well placement optimization.
2. SPSA only requires two objective function measurements per iteration regardless of the problem dimension. This is useful for field cases with large number of variables (discrete and continuous) to optimize.
3. SPSA can be easily adapted to any reservoir simulator without need to access the source code.

SPSA has been used previously for optimal well placement (Bangerth et al., 2005). The objective in this section is to illustrate that by using 'Sweet-spots' from dynamic measure map as starting points, a better solution and faster convergence is obtained and not to develop a novel well placement optimization algorithm (Yeten et al., 2003, Bangerth et al., 2005, Zandvliet et al., 2008, Sarma et al., 2008).

Basic SPSA algorithm (Spall, 1992) is described in **Appendix D.1** which relies on stochastic approximation of gradient. For more details about local convergence proof of SPSA please refer to a publication by Spall, (1992). Modifications are required in basic SPSA algorithm for well placement optimization as it is an integer optimization problem. These modifications are described in **Appendix D.2.**

#### 5.4.3.2 SPSA Algorithm for Well Placement Optimization

The use of SPSA algorithm for well placement is illustrated in the workflow diagram in **Fig. 5.15.** The mathematical description of algorithm is presented in **Appendix D.3**. This algorithm is a based on well placement algorithm presented by Bangerth et.al, (2005).

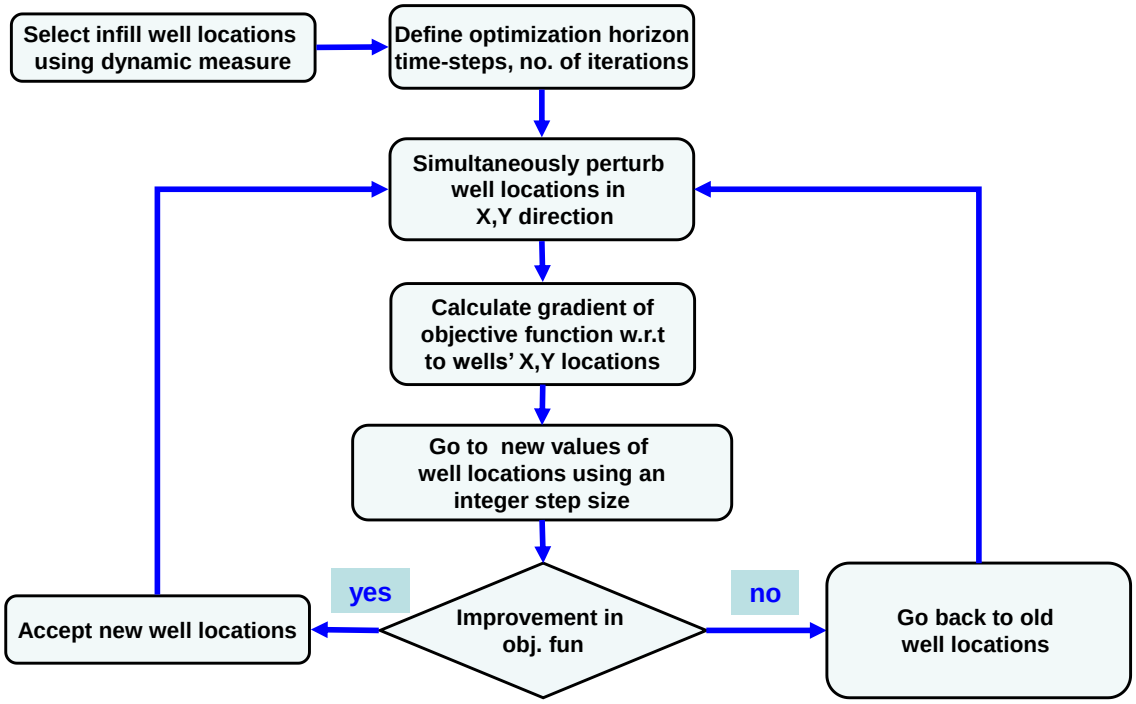


**Fig. 5.15 - Schematic of workflow for well-placement using SPSA.**

### 5.4.3.3 Well Placement Using SPSA and Sweet-spots

Well placement using 'Sweet-spots' from dynamic measure map as starting points is illustrated using a 2D permeability field which is shown in **Fig. 5.3** having one producer and injector. This field is produced at a voidage balance of 400 RB /day for 1 year. These production conditions are same as used in **section 5.5.1**. The optimization algorithm used is SPSA which has been described in **section 5.5.3.2**.

The objective is to place a new producer (P2) to maximize cumulative oil for next 5 years under the following production constraints,

1. Producer P1 = Producer P2 = 200 RB /day
2. Injector I1 = 400 RB /day
3. Total production rate = Total injection rate (Voidage balance)

The faster convergence using 'Sweet-spots' from the dynamic measure map as starting points (**Fig. 5.16)** is demonstrated for well placement optimization. There are 6 starting locations for well P2. Three of them are in the high value regions (Sweet-spots)

of dynamic measure map (red, blue, green) and remaining three are arbitrarily chosen with one (black) present in opposite corner from producer P1.

**Fig. 5.17** shows the final locations for well P2 using six starting locations after well placement optimization using SPSA algorithm under previously described production constraints. The field cumulative oil after next 5 years after drilling new producer P2 for these six starting locations is illustrated in **Fig. 5.17**. It can be observed that the green well has converged faster than the neighboring brown well. This is expected as the green well is starting at a better location as shown in the robust map in **Fig. 5.17**. It can also be observed that the red well converges fastest to the best solution compared to other starting locations. It can be concluded that by selecting starting locations using 'Sweet-spots' in a dynamic measure map, faster convergence is achieved. Also it can be observed that it is difficult for a gradient based optimization algorithm to find global maximum if its starting point is near local maxima, as there is a possibility of getting stuck in local maxima.

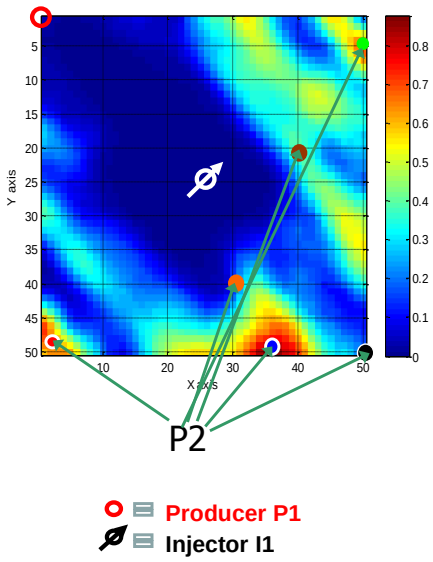


**Fig. 5.16 - Starting points for new wells for synthetic 2D case on the dynamic measure map.**

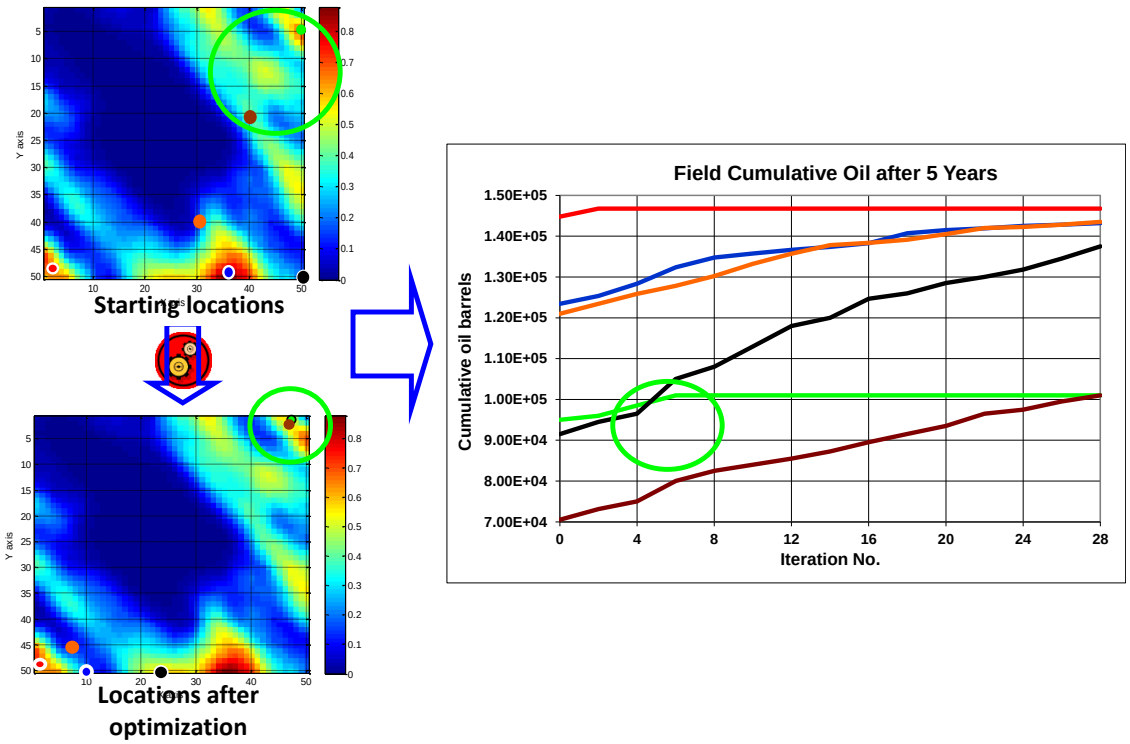


**Fig. 5.17 - Final locations for well P2 after wellplacement optimization along with field cumulative oil performance for all the demonstration wells.**

## 5.5 Field Applications

The utility of the proposed method is demonstrated on a mature offshore carbonate field (**section 5.5.1**) and a sector model of a heavy oil field (**section 5.5.2**) by using 'Sweet-Spots' directly as optimal well locations

### 5.5.1 Mature Carbonate Field in Offshore India

The offshore field is a highly heterogeneous carbonate reservoir located in the western coast of India in the vicinity of the giant Mumbai High field. It is the second largest field of the western offshore basin off the west coast of the Indian peninsula and started commercial production in 1985. The development history of the field is shown in **Fig. 5.18**. The development includes 3 phases during 1984-2002 and additional development

during 2002-2003 (Mitra et al., 2008). Many platforms including lots of wells were developed during those periods. For example 161 wells in 14 platforms were commissioned in the field during the first 3 phases.

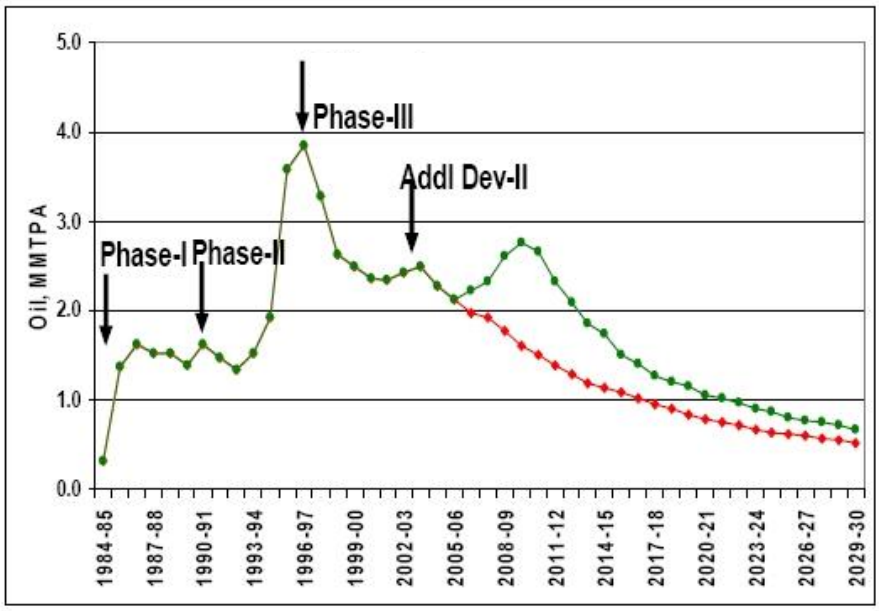


**Fig. 5.18 - The development history of an offshore field, India (Mitra et al., 2008).**

The field has been producing over 20 years and is currently producing with a substantial water-cut. The redevelopment plan was drawn in 2006 to improve oil recovery factor of main reservoir (i.e. Bassein). A major redevelopment effort is ongoing to sustain and improve production from these fields through selective infill drilling, optimization of well trajectories and state-of-the-art reservoir management practices.

The simulation model consists of approximately 1 million grid cells with 24 layers. It contains lots of faults in the field of which some are following I direction and some lie across J direction as shown in **Fig. 5.19**.

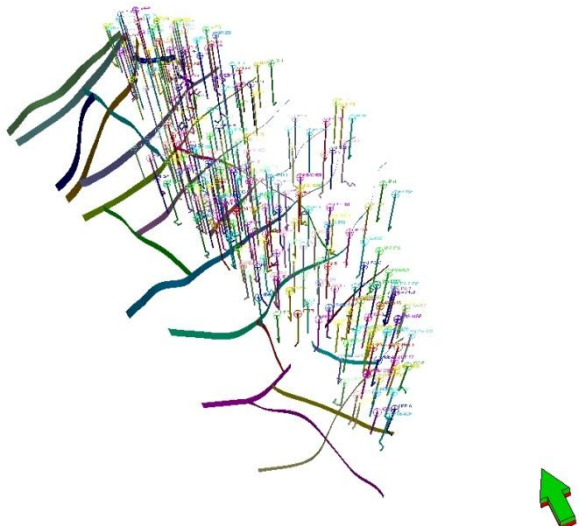

**Fig. 5.19 - Faults in offshore field, India.**

Average permeability for this field is about 73 md. Permeability fields and initial oil saturations are shown in **Fig. 5.20** and **Fig. 5.21** respectively. It is observed that high saturation oil zones, layer 5$^{th}$ through 13$^{th}$, are embedded in high permeability zones around the field.

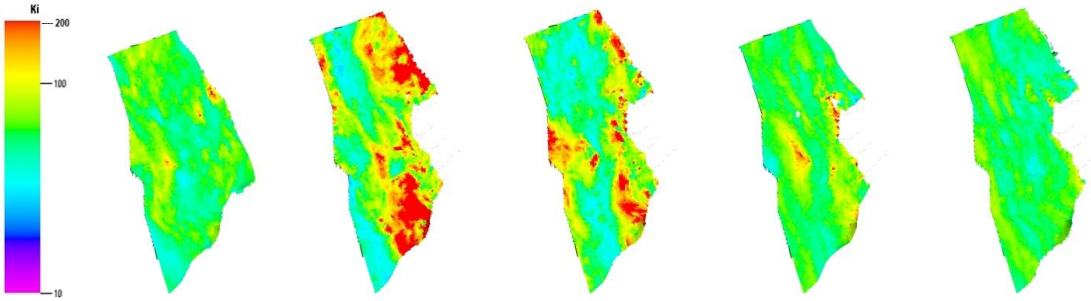


**Fig. 5.20 - Permeability field by layer (1st , 5th, 11th, 13th, 21st layer from left to right).**

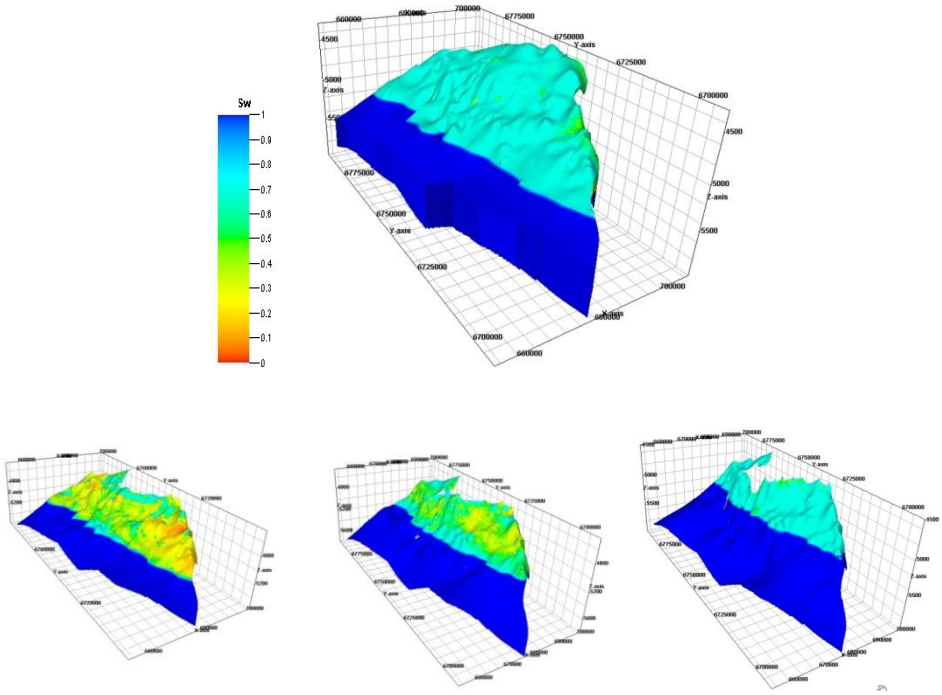


**Fig. 5.21 - Initial oil saturation field (top) and by layer (5th, 13th, 24st layer from left to right).**

### 5.5.1.1 History Matching

The simulation model was history matched using a hierarchical history matching approach associated with multi-scale inversion that follows a sequence of calibrations from global to local parameters in coarsened and fine scales (Park, 2012). The history matching workflow for this field is illustrated in **Fig. 5.22.**

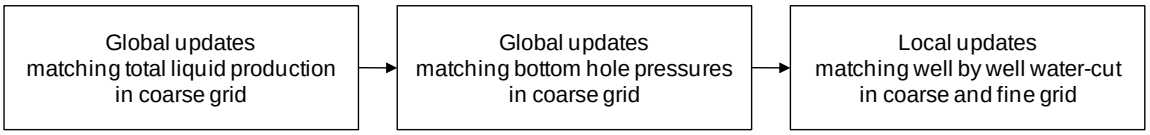


**Fig. 5.22 - Strategy and workflow for history matching of the offshore field, India.**

The objective of this history matching study was defined as matching well by well water-cut and bottom-hole pressure. Because the initial reservoir model had large number of grid cells, it required long simulation run time. Therefore, grid coarsening was used for calibrating global parameters. Global parameter calibration process included sensitivity analysis, cluster analysis and updating of parameters by Genetic Algorithm. In the first stage, the field wide reservoir energy (pressure) and regional production are matched by adjusting pore volume multipliers. It was followed by matching of the bottom-hole pressures in the coarse grid. In this stage, regional energy (pressure) and platform wise production were matched by calibrating regional permeability multipliers. Aquifer size and strengths were also used as additional history matching variables. The final stage involved local parameter (grid block permeability) updating to match well by well water-cut using streamline-assisted generalized travel time inversion method (GTTI) (He et al.,2002). Multiscale calibration which decomposes parameter estimation problem by scales was used at this step. The GTTI history matching approach has been applied and performed successfully in real field cases (Cheng et al. 2004; Hohl et al. 2006; Qassab et al. 2003; Rey et al. 2009). The initial (starting) and updated (history matched) permeability for layers 5, 10, 15 and 20 are shown in **Fig. 5.23**.

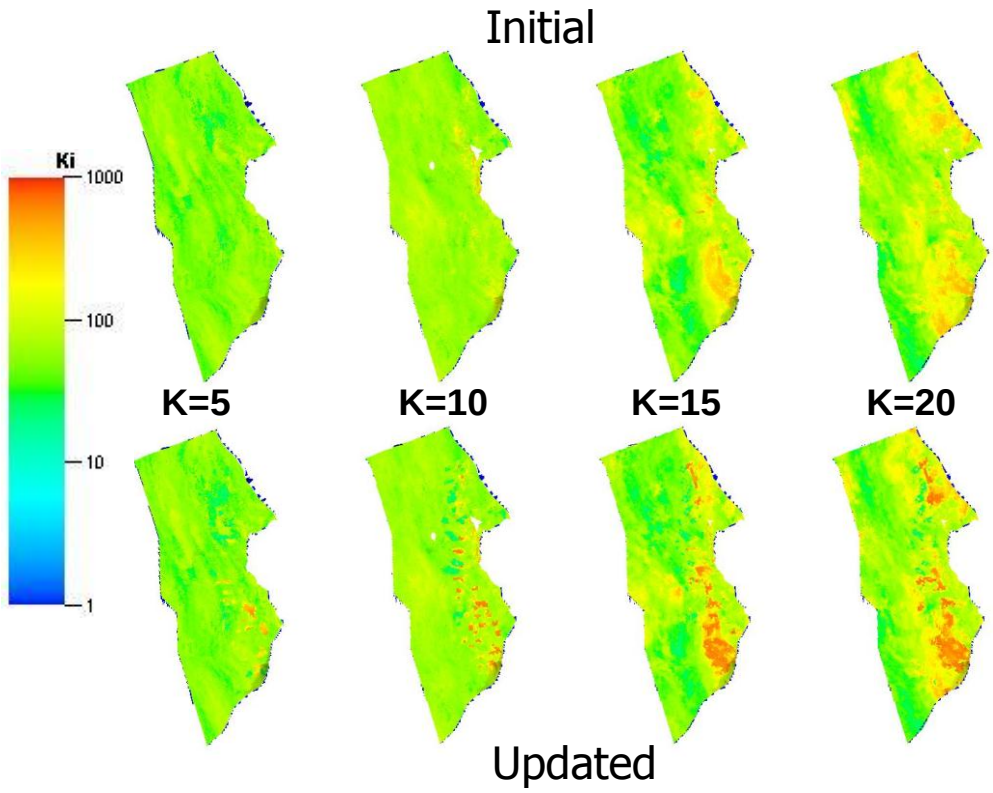


**Fig. 5.23 – Initial (starting) and updated (history matched) permeability for layer 5, 10, 15 and 20 for field case.**

### 5.5.1.2 Well Placement

Proposed method is utilized on the history matched model to obtain a dynamic measure map highlighting areas suitable for drilling infill wells. Comparison is done between production results from well locations using dynamic measure map and traditional well placement techniques (oil pore-volume map). Streamlines with time of flight from producer in log10 scale are shown in **Fig. 5.24**. High time of flight from producer highlights regions which are difficult to drain. Streamlines with time of flight from injector in log10 scale are shown in **Fig. 5.25.** High time of flight from producer

highlights regions which are difficult to drain. Total time of flight (i.e. summation of time of flight from producer and time of flight from injector) is plotted as a grid property as shown in **Fig. 5.26** for the field. The regions with high total time of flight highlight regions which are difficult to drain and sweep. These regions are of interest for drilling next well.

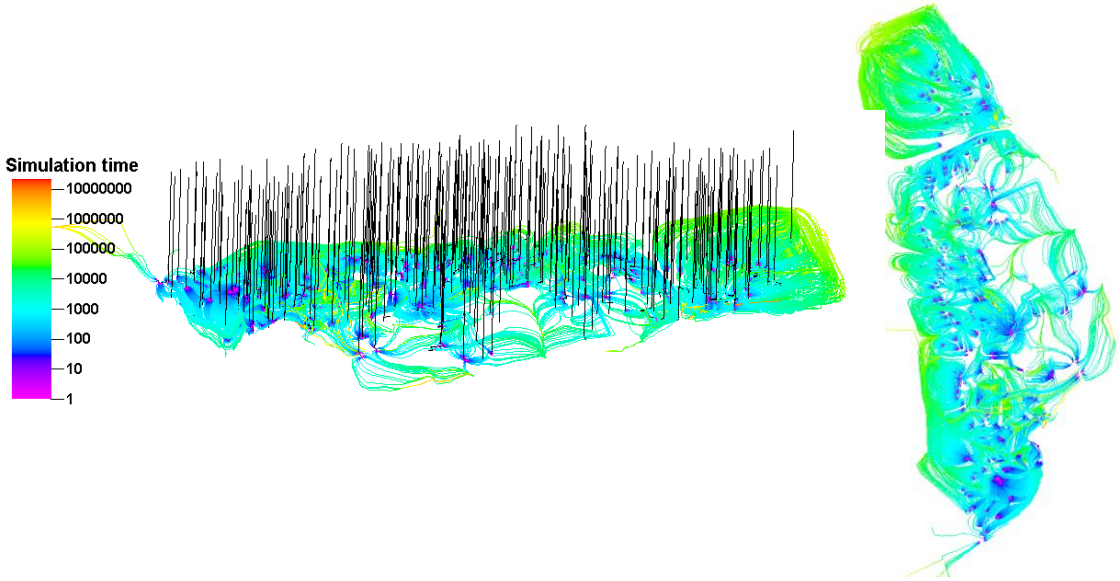


**Fig. 5.24 – Streamlines showing time of flight from producer to injector in log10 scale. High time of flight from producer highlights areas difficult to drain.**

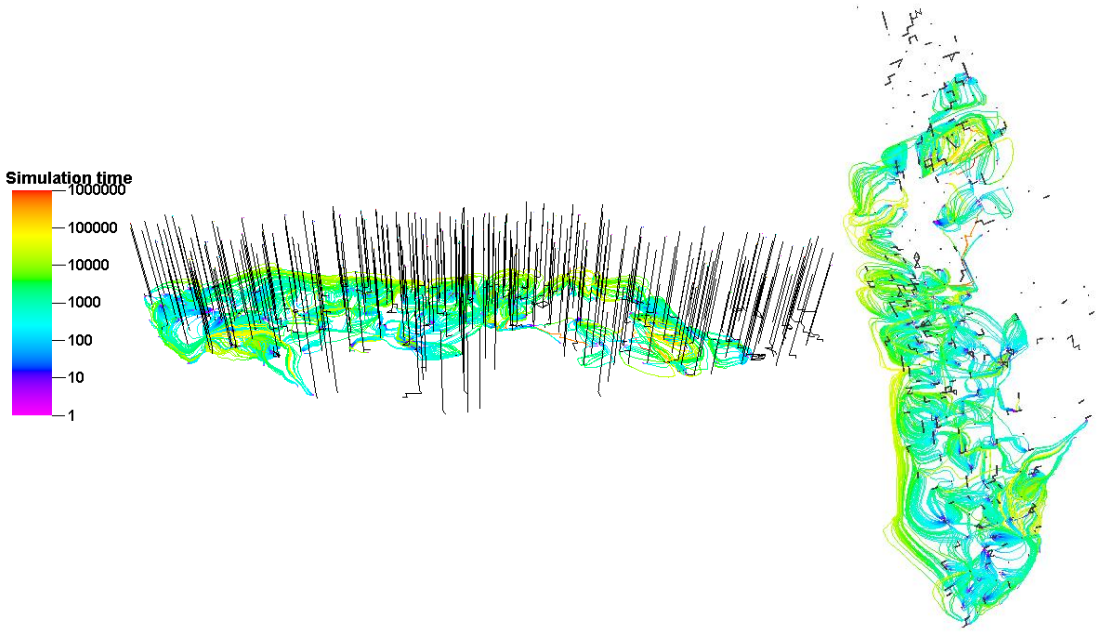


**Fig. 5.25 – Streamlines showing time of flight from injector to producer in log10 scale. High time of flight from injector highlights areas difficult to sweep.**


**Fig. 5.26 – Total time of flight (time of flight from producer + time of flight from injector) highlighting poorly drained and swept regions shown in log10 scale.**

Dynamic measure map (values greater than 0.3) is shown in **Fig. 5.27**. It can be seen that north region of the field is prominently highlighted. This region is of interest for drilling next wells. Dynamic measure map (values greater than 0.4) for layers 5 and 6 is shown in **Fig. 5.28**.

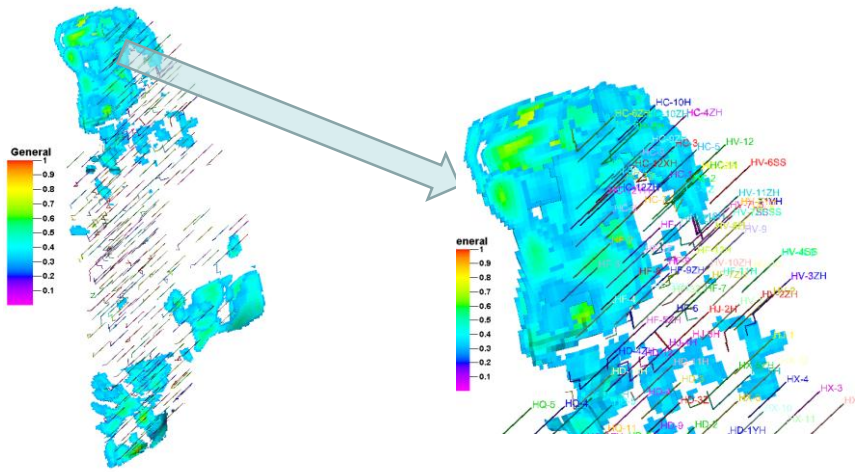


**Fig. 5.27 – Dynamic measure map for values greater than 0.3 with zoomed up view of north area on right.**

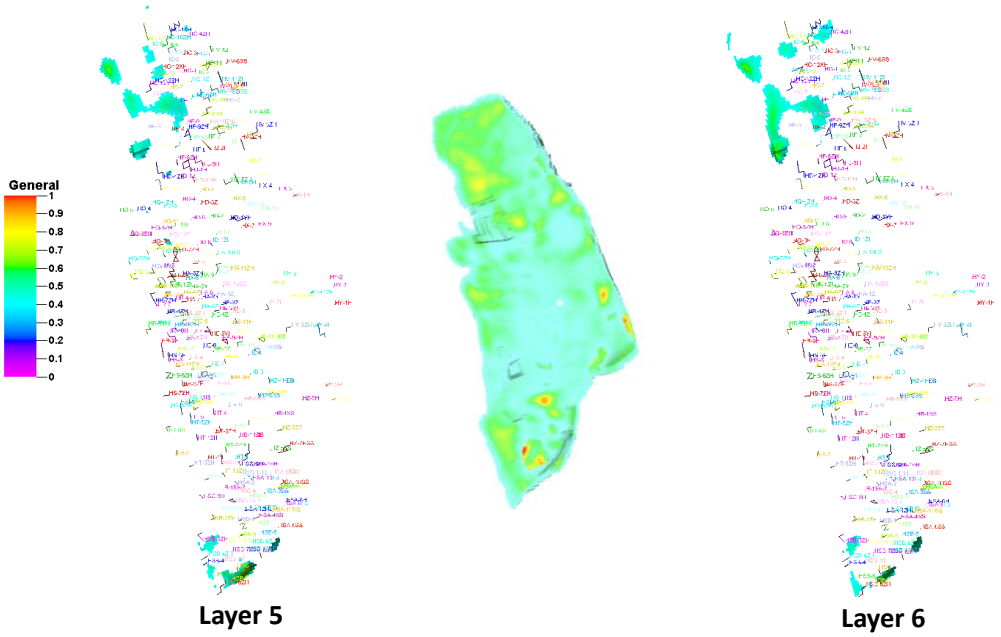


**Fig. 5.28 – Dynamic measure map for values greater than 0.4 for layer 5 and 6 of the field case.**

The dynamic measure map is compared with oil pore-volume map in **Fig. 5.29.** Wells TOF1 and TOF2 are drilled in high regions of dynamic measure map while well OIL1 and OIL2 are drilled in high regions of oil porevolume map. Four scenarios listed below are run individually,

1. Using dynamic measure map, producer (TOF1) is drilled @ i->94, j->53, k->5-10
2. Using dynamic measure map, producer (TOF2) is drilled @ i->86, j->23, k->5-10
3. Using oil pore-volume map, producer (OIL1) is drilled @ i->48, j->172, k->5-10
4. Using oil pore-volume map, producer (OIL2) is drilled @ i->55, j->188, k->5-10

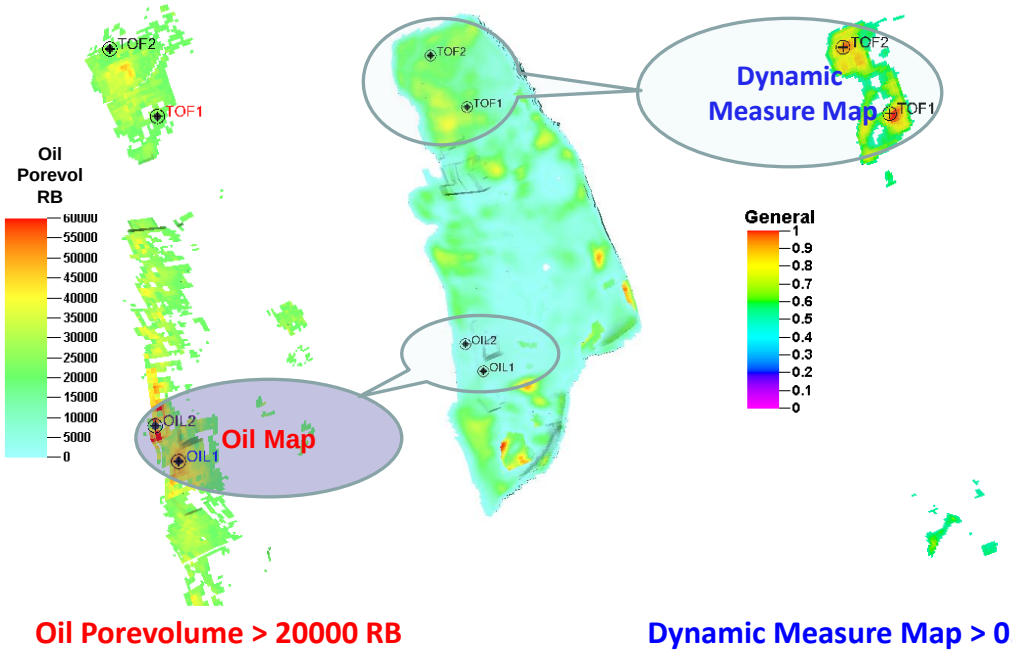


**Fig. 5.29 - Dynamic measure map (values > 0.5, shown right) and oil porevolume map (values > 20000 RB, shown left) for a field case at start of optimization. Illustration wells TOF1, TOF2 (based on dynamic measure map) and OIL1, OIL2 (based on oil porevolume map) are also shown on both maps.**

Simulations are run for following production constraints which are described as follows,

1. Base history matched simulation is run until March 2011. Dynamic measure map is generated for this timestep.
2. Simulation is run from April 2011 to April 2016 – Prediction stage.
3. Well production is on reservoir control of 10000 RB/day and BHP limit of 500 psi.

Well cumulative oil is plotted for all the four scenarios in **Fig. 5.30.** Wells TOF1 and TOF2 show considerable higher cumulative well oil production than OIL1 and OIL2. This highlights the importance of taking drainage and sweep patterns of existing wells into consideration while deciding future infill well locations.

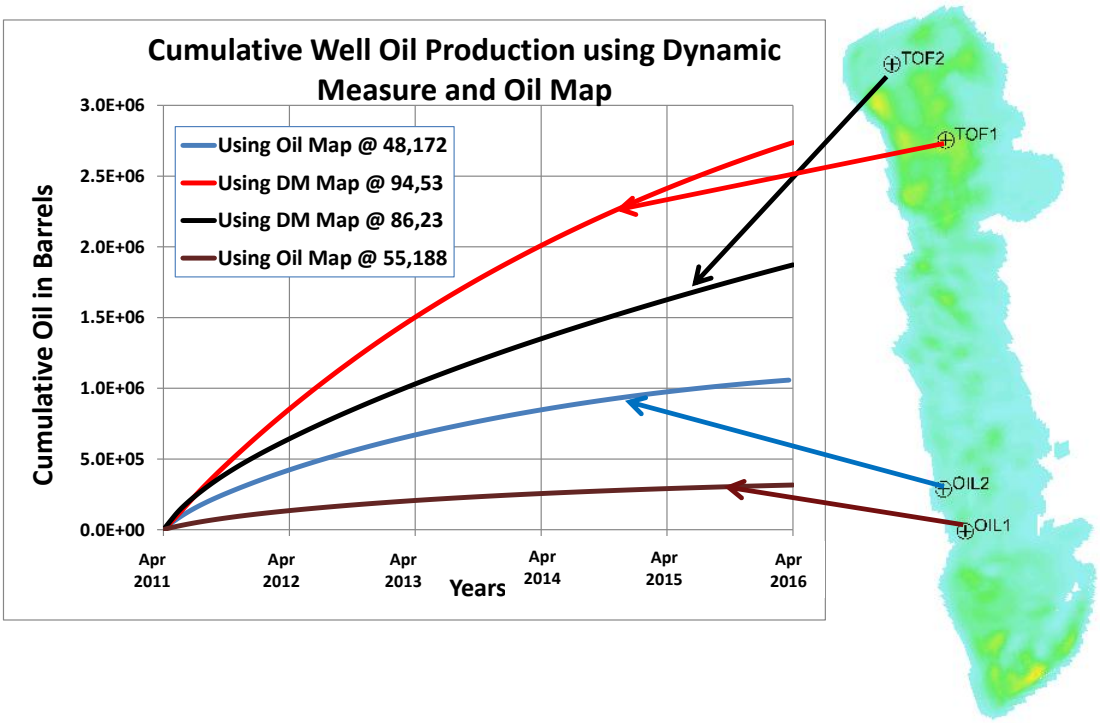


**Fig. 5.30 - Well cumulative oil for the four illustrative wells during prediction for next five years.**

The operator drilled three infill wells after March 2011. A notable amount of clean oil is being produced from these wells. After plotting these wells on dynamic measure map they were found out to be in high dynamic measure region as shown in **Fig. 5.31**. This encouraging result verifies the proposed method.

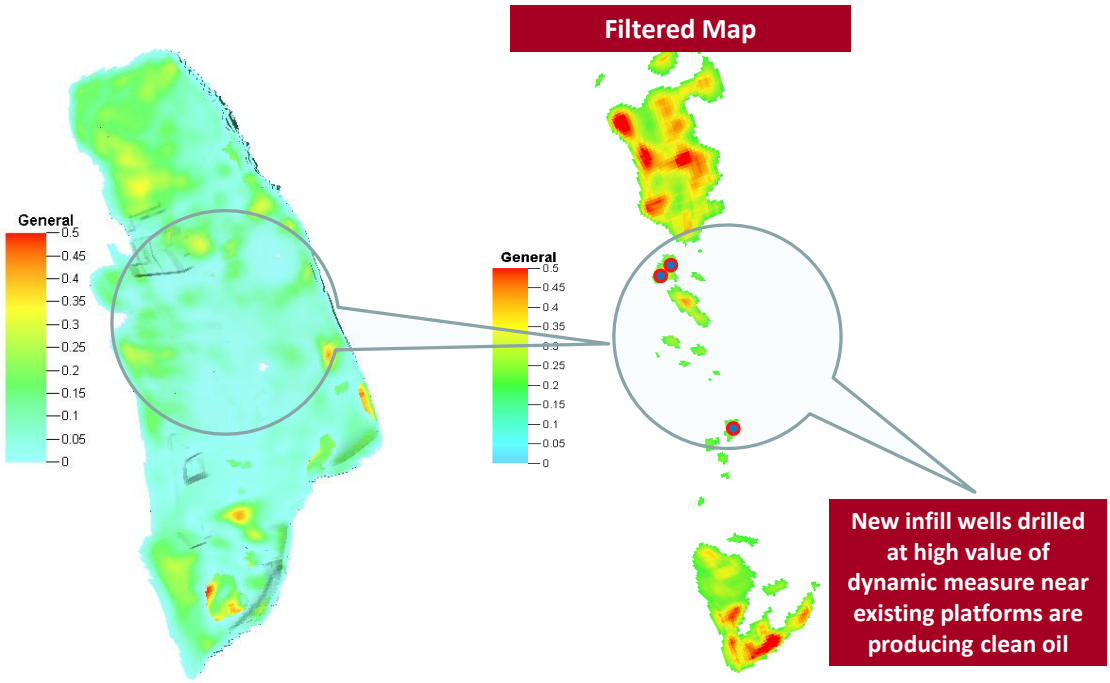


**Fig. 5.31 – Actual field results after drilling infill wells.**

### 5.5.2 Heavy Oil Sector Model

The utility of the proposed method is illustrated on a sector simulation model of a heavy oilfield under a strong aquifer drive. This field only has producers.

#### 5.5.2.1 History Matching

A history matching exercise was carried out before generating dynamic measure map for infill well placement. The results and methodology of history matching are not discussed here. History matched permeability and porosity are shown in **Fig. 5.32.** The producers are also shown in **Fig. 5.32.**

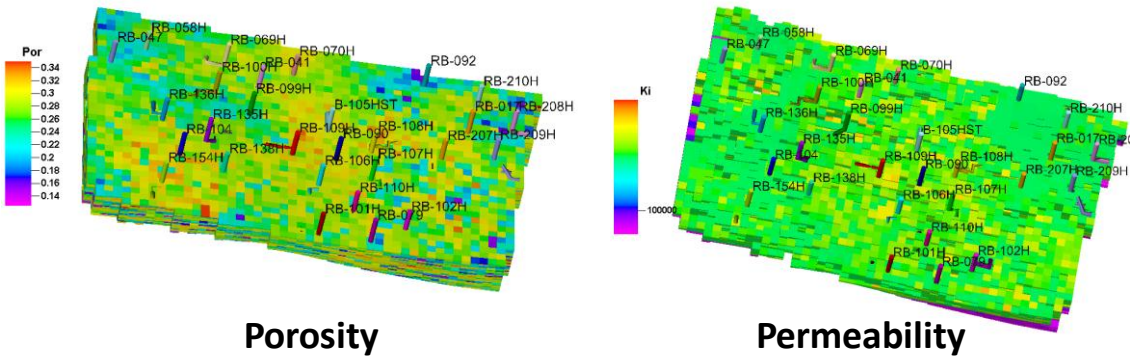


**Fig. 5.32 – History matched porosity (left) and permeability (right) in simulation sector model of the heavy oil field.**

The streamlines in side and top view are shown in **Fig. 5.33** for the sector model. It can be seen that in the history matched model there is lot of pressure support to the reservoir from underlying aquifer. Also there is considerable connectivity in the model which was observed in the well tests data.

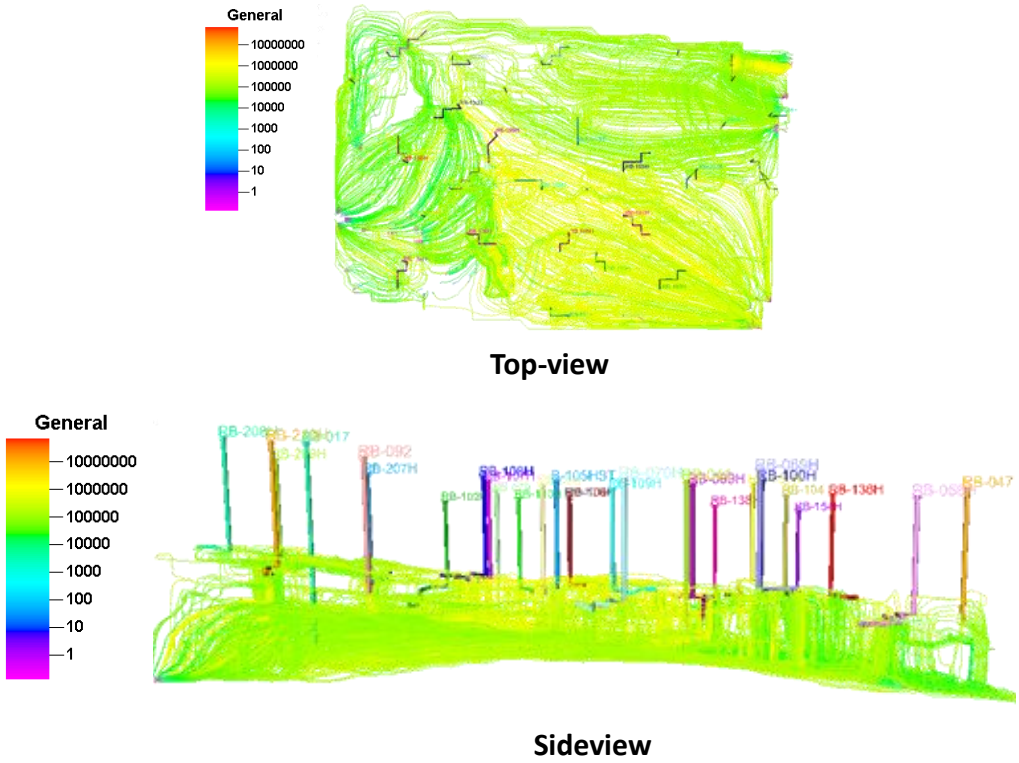


**Fig. 5.33– Streamlines showing time of flight in log10 scale from aquifer in history matched model, shown in top-view (top) and sideview (bottom) at the end of historical production data.**

### 5.5.2.2 Well Placement

The time of flight (here only time of flight from producers to aquifer is considered) maps are shown in **Fig. 5.34**. The regions showing high time of flight from producers are the regions difficult to drain by the producers.

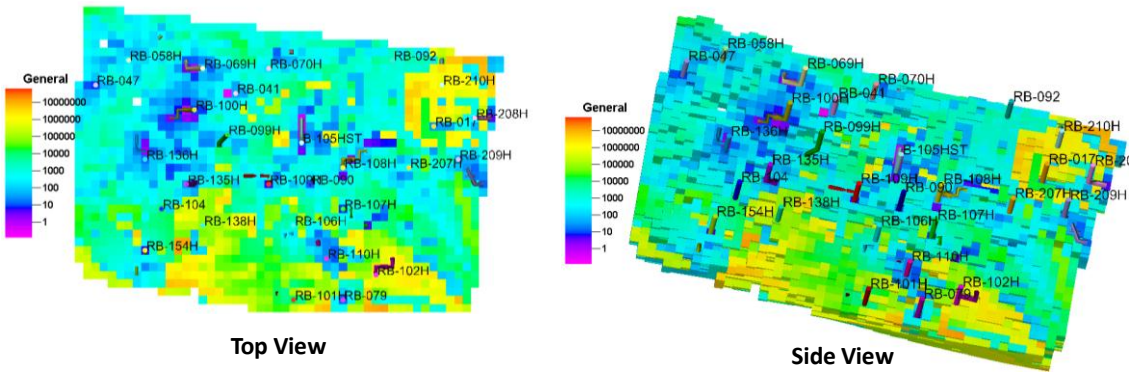


**Fig. 5.34 - Time of flight from producers in log10 scale in the history matched model mapped to the grid at the end of historical production data.**

The dynamic measure map at different filter levels is shown in **Fig. 5.35**. The high value areas of dynamic measure in the reservoir (**Fig. 5.35)** highlight high probable areas for drilling next well as these areas are difficult to drain by producers and sweep by aquifer.

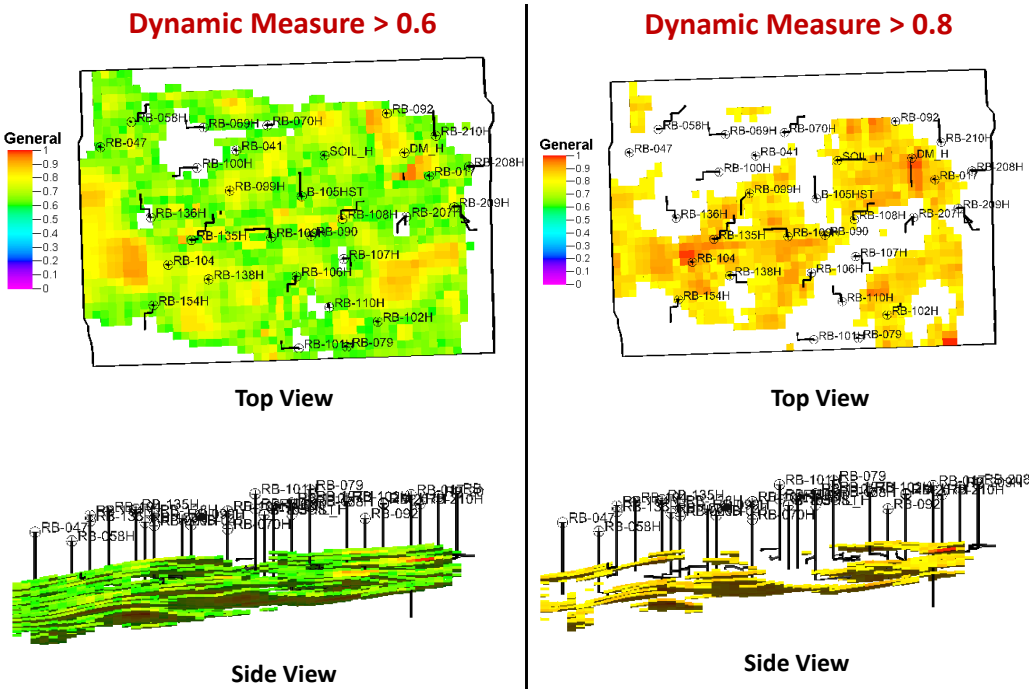


**Fig. 5.35 – Dynamic measure with value filter of 0.6 (left) and 0.8 filter (right) at the end of historical production data.**

The dynamic measure map (filtered for values > 0.8) is compared with the remaining oil porevolume map (filtered for values > 20000 reservoir barrels) as shown in **Fig. 5.36.** It can be seen from **Fig. 5.36** that oil porevolume map doesn't offer any judgmental information on where to drill the next infill well. For comparison between dynamic measure map and oil porevolume map, two horizontal wells are drilled in the high value regions of both maps shown in **Fig. 5.36**. The trajectories of both horizontal wells are described in **Fig. 5.36**. Both wells (SOIL_H and DM_H) are produced at 20000 reservoir barrels per day for period of five years.

| Oil Porevolume | | | |
|---|---|---|---|
| X | Y | Z1 | Z2 |
| 31 | 12 | 1 | 6 |
| 32 | 12 | 6 | 6 |
| 33 | 12 | 6 | 6 |
| 34 | 12 | 6 | 6 |
| 35 | 12 | 6 | 6 |

| Dynamic Measure Map | | | |
|---|---|---|---|
| X | Y | Z1 | Z2 |
| 40 | 12 | 1 | 6 |
| 40 | 13 | 6 | 6 |
| 40 | 14 | 6 | 6 |
| 40 | 15 | 6 | 6 |
| 40 | 16 | 6 | 6 |

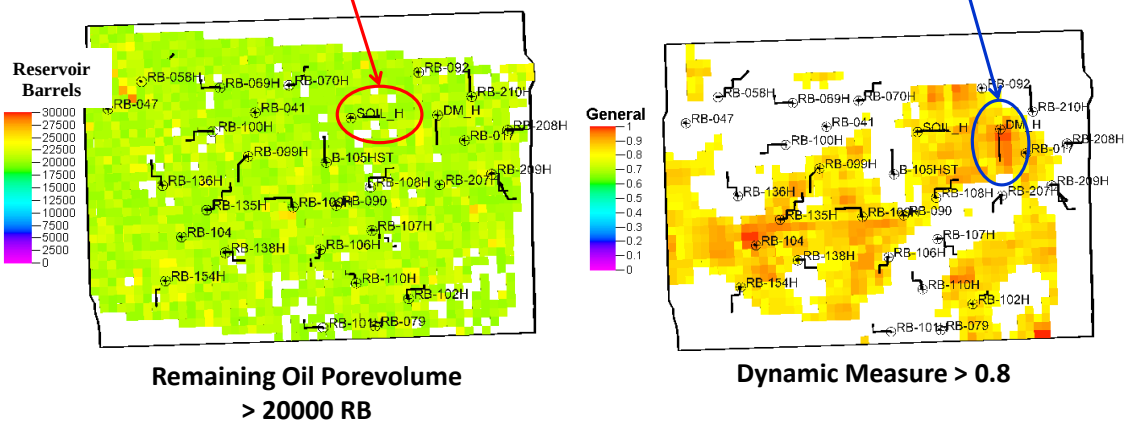


**Remaining Oil Porevolume > 20000 RB**

**Dynamic Measure > 0.8**

**Fig. 5.36 – Trajectory for comparative well based on remaining oil pore-volume map (left) and dynamic measure map (right).**

The comparative performance of two drilled wells (**Fig. 5.36**) for cumulative oil production is shown in **Fig. 5.37**. It can be seen that well drilled using dynamic measure map has produced 42% more oil than well using oil pore volume map at the end of five years. This shows the importance of taking existing drainage areas into consideration for drilling next well. The utility of the proposed method has been demonstrated for a sector model of a heavy oilfield under a strong aquifer. It should be noted that it is computationally inexpensive to generate dynamic measure map.

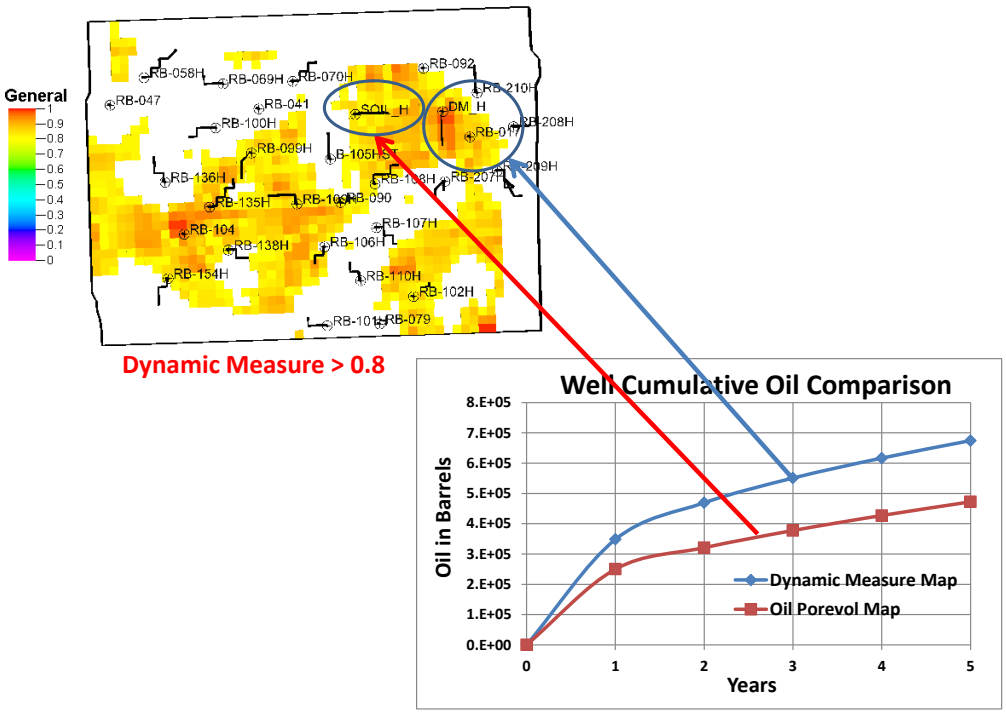


**Fig. 5.37 – Cumulative well oil production comparison for two comparative wells is shown in the graph (bottom right). Locations of the two comparative wells are shown in top left corner in dynamic measure map.**

## 5.6 Summary and Conclusions

A practical novel method has been proposed for well placement optimization that relies on streamlines and total time of flight to locate the potential regions of poorly swept and drained oil. The proposed new approach utilizes a dynamic measure based on the total streamline time of flight combined with static and dynamic parameters to identify "Sweet Spots" for infill drilling.

The main advantage of the proposed method is its computational efficiency in calculating dynamic measure map. This has made the approach suitable for large-scale field application while enabling uncertainty assessment through examination of multiple geologic realizations. The dynamic measure map can also be easily reconciled with available geological, geophysical and facilities data helping in prudent decision making.

The proposed approach was tested on a 2D synthetic case, which was compared against a robust solution. The proposed approach has a better rank correlation coefficient with the robust solution, compared to previous method based solely on oil productivity. In addition it is advantageous to use ‘Sweet-spots’ as starting points in the formal optimization algorithm viz. SPSA which was demonstrated for the case of optimal well placement. Using ‘Sweet-spots’ as starting points resulted in faster convergence (less number of iterations), compared to ad-hoc selection of starting points.

The complete workflow was also demonstrated on a multi-million cell reservoir model of a mature carbonate field with notable success. The infill locations based on dynamic measure map have shown good success and dynamic measure map will be used in future development planning of the field.

In addition the workflow was also demonstrated on a sector model of a heavy oil field with notable success. Following conclusions can be deduced from the study,

- Total time of flight reflects poorly swept and drained regions and it can be used for inferring next well location.
- It is computationally efficient to generate the dynamic measure maps based on total time of flight. This makes the proposed method practical for multi-million grid cell simulation models.
- Geological uncertainty can be taken into consideration using expected value and variance of dynamic measure over multiple realizations.
- Use of ‘Sweet-spots’ as starting points in a formal well placement optimization method like SPSA leads to faster convergence i.e. less number of iterations.
- Application of dynamic measure map to a large mature carbonate field case has been shown with notable success. Subsequent field results have verified the approach. In addition the workflow was also demonstrated on a sector model of a heavy oil field with notable success.

# CHAPTER VI

# CONCLUSIONS AND

# FUTURE RESEARCH RECOMMENDATIONS

Reservoir management is a critical aspect in astute management of petroleum reservoirs. Considerable development has been done in the different aspects of reservoir management. Three important aspects of reservoir management have been specifically discussed in this dissertation. These are history matching, production optimization and infill well placement. Incremental innovation has been done in history matching to make the streamline based generalized travel time applicable to a multimillion cell carbonate field with hundreds of wells and decades of production history. The proposed modification during inversion uses grid coarsening during simulation. A novel workflow has also been proposed for integration of bottom-hole pressure in the simulation model during $CO_2$ sequestration. Incremental innovation has also been done in the discipline of production optimization using streamlines. The previous streamline-based rate optimization approach which focused on equalizing arrival time of the waterfront to producers for a group of injectors has been modified to account for accelerated production in addition to maximizing sweep efficiency. A practical novel method has been proposed for well placement optimization that relies on streamlines and total time of flight to locate the potential regions of poorly swept and drained oil.

In **chapter II,** a pragmatic application of streamline based generalized travel time inversion is presented using flux reconstruction for large simulation models using grid coarsening to reduce simulation time. The proposed approach has been demonstrated on a synthetic field. Generalized travel time inversion using grid coarsening on the coarsened model was compared with non-coarsened model. The results were quite comparable although coarsened inversion using the proposed method might take more iteration than non-coarsened inversion but considerably less simulation time than non-coarsened models.

The proposed approach was successfully applied on a multimillion cell carbonate field with hundreds of wells and decades of production history. Streamlines traced by reconstructing fluxes from the grid coarsened simulation model of this field give comparable results when compared to a non-coarsened simulation model. Remarkable improvement is seen in the history match of production responses like liquid rate, oil rate and water-cut at the field, platform and well level. It should be noted that there were minimum changes done in the model during inversion. Expected improved connectivity between platforms was seen in the inverted model which was not present in the initial model. This improved connectivity was verified by matched production history of one of the wells.

Future research in this area can be conducted, on using the coarsened fluxes obtained during coarsened simulation directly for streamline tracing leading to better streamline tracing than the proposed approach. Also a dual scale approach can be easily be implemented whereby inversion is carried out using the proposed approach till a considerable reduction in well by well watercut mismatch is obtained and then for further reduction in mismatch original workflow can be applied with non-coarsened model. This will lead to considerable savings in computational time for large simulation models with long runtimes.

In **chapter III**, a novel approach to update geological models using bottom-hole pressure data at injection and observation wells during $CO_2$ sequestration has been proposed. In the proposed approach, the first step consists of volume calibration using information from pseudo-steady state flow regime of the injection well. This is followed by bottom-hole pressure inversion of zeroth-order frequency (mean) of the bottom-hole pressure at the injection well. This is followed by peak pressure arrival time inversion at the observation wells. As a last step, a gradient minimization technique is used to modify global multiplier of permeability (X direction).

The proposed approach has been demonstrated on a 2-D synthetic model with two cases. In the first case where the starting model is geo-statistically similar to the reference model, the approach has been successful in matching the bottom-hole pressure

at the injection and observation wells. An improved correlation coefficient was obtained for the gas saturation difference between end of forecast and end of history matching for the final model compared to the starting model.

For the second case where the starting model is geo-statistically dissimilar to the reference model, the approach has been successful in reproducing the large-scale features of the reference field. In addition excellent match was obtained for the bottom-hole pressures of all the wells and peak arrival time of observation wells for both cases. Finally, the forecasting capability of the inverted model after proposed approach compared reasonably well to the reference case for both cases. Also, an improved correlation coefficient was obtained for the gas saturation difference between end of forecast and end of history matching for the final model compared to the starting model.

The proposed approach was also applied to a 3-D model with injection in a high permeability layer with encouraging results. The final bottom-hole pressure results showed satisfactory match with the reference model. However, the 3-D problem is highly non-unique and there can be multiple permeability fields matching the data. Also, because of the diffusive nature of the pressure, the problem of bottom-hole pressure inversion is more suited to infer large scale continuity than small scale variations. In the proposed approach, the condition of 'proximity' to the prior (starting) model is imposed. The forecast results for the injection and observation wells were satisfactory and improved correlation coefficient was obtained for the gas saturation difference between end of forecast and end of history matching for the final model compared to the starting model. For better resolution of permeability, extra dynamic information is needed. This extra information can be in form of time lapse seismic or more bottom-hole pressure data at different well locations. A simple illustration of integrating seismic data (gas saturation surveys) to improve gas saturation forecast is illustrated.

The proposed work only deals with the data integration of bottom-hole pressure data during $CO_2$ sequestration. Besides permeability, other uncertainties in bottom-hole pressure integration such as anisotropy and relative permeability need to be explored. The value addition of extra information in resolving permeability field can be studied.

The extra information can be time lapse seismic or more bottom-hole pressure data at different locations. Also, the pressure calibrated model can be used for the optimization of $CO_2$ sequestration (Flett et al., 2007) which deals with maximization of hydro-dynamically trapped $CO_2$. In addition, the optimization of location and number of injection wells to maximize $CO_2$ trapping and minimize costs can also be explored.

In **chapter IV**, the trade-off between sweep efficiency and Net Present Value (NPV) in the field-scale rate optimization is explored and a practical and efficient way of optimal rate allocation based on a compromise between the two is proposed. Because of the economic as well as regulatory constraints, field-scale optimization is typically not based solely on NPV or maximizing recovery. The previous work mainly focused on maximizing recovery or sweep efficiency and did not account for production acceleration. Previous work has been built upon to account for both NPV as well as maximizing sweep efficiency through a trade-off analysis. Some specific conclusions from this study are as follows,

- An augmented objective function (norm term) for field-scale rate optimization is proposed that accounts for maximizing sweep efficiency as well as production acceleration.
- Given a starting condition, norm term helps in picking a particular arrival time equalization solution among several non-unique solutions that also minimizes arrival time which results in acceleration of rates subject to constraints.
- It has been illustrated that during production optimization, there is a tradeoff between maximizing sweep efficiency and maximizing NPV. Optimum tradeoff can be selected based on the 'trade-off curve' between the cumulative NPV and the weight on the norm term.
- For voidage balance case while optimizing both injector (injector rate is not fixed) and producer, norm term helps in accelerating rates and reduces penalty on high productive wells while sacrificing injection efficiency. On the other hand, for non-voidage balance case, norm term prevents slowing down of wells and improves injection efficiency.

- Different starting rates of wells during optimization result in different converged rates. This is due to the existence of multiple local minima.
- Streamlines derived from a finite-difference simulator have been utilized to analytically compute the gradient and Hessian of the objective function using a single flow simulation per optimization iteration. This makes the proposed approach particularly well-suited for field-scale rate optimization using high resolution geological models having large number of wells.
- The robustness and practical feasibility of the proposed approach to capture hierarchy of rate and pressure constraints in realistic production scenarios have been demonstrated using a 3D synthetic benchmark field example with smart wells and inflow control valves. Stochastic optimization was also implemented to take geological uncertainty into consideration. The value of using multiple realizations in improving the robustness of the optimization in terms of oil recovery and enhancing NPV has been clearly illustrated using the 3D example.

The future research can be conducted in this area on enhanced oil recovery (EOR) applications of the streamline based rate optimization with norm term. In addition research can also be conducted in finding optimal starting points for rate optimization as starting points influence the rate optimization process.

In **chapter V,** a novel approach for well placement utilizing a dynamic measure based on the total streamline time of flight combined with static and dynamic parameters to identify “Sweet Spots” for infill drilling has been proposed. The main advantage of the proposed method is its computational efficiency in calculating dynamic measure map. This has made the approach suitable for large-scale field application while enabling uncertainty assessment through examination of multiple geologic realizations. The dynamic measure map can also be easily reconciled with available geological, geophysical and facilities data helping in prudent decision making. The proposed approach was tested on a 2D synthetic case, which was compared against a robust solution. The proposed approach has a better rank correlation coefficient with the robust solution, compared to previous method based solely on oil productivity. In addition it is

advantageous to use ‘Sweet-spots’ as starting points in the formal optimization algorithm viz. SPSA which was demonstrated for the case of optimal well placement. Using ‘Sweet-spots’ as starting points resulted in faster convergence (less number of iterations), compared to ad-hoc selection of starting points.

The complete workflow was also demonstrated on a multi-million cell reservoir model of a mature carbonate field with notable success. The infill locations based on dynamic measure map have been verified by subsequent drilling and dynamic measure map will be used in future development planning of the field. In addition the workflow was also demonstrated on a sector model of a heavy oil field with notable success.

The following conclusions can be deduced from the work,

- Total time of flight reflects poorly swept and drained regions and it can be used for inferring next well location.
- It is computationally efficient to generate the dynamic measure maps based on total time of flight. This makes the proposed method practical for multi-million grid cell simulation models.
- Geological uncertainty can be taken into consideration using expected value and variance of dynamic measure over multiple realizations.
- Use of ‘Sweet-spots’ as starting points in a formal well placement optimization method like SPSA leads to faster convergence (less number of iterations).
- Application of dynamic measure map to a large mature carbonate field case has been shown with notable success. Subsequent field results have verified the approach. In addition the workflow was also demonstrated on a sector model of a heavy oil field with notable success.

This research can be further explored in the aspect of well trajectory optimization. The trajectory can be parameterized by using few parameters (Onwunalu et al., 2010). Again a two-step approach can be used whereby starting points for the optimization can be selected using dynamic measure map. In addition utility of the

proposed approach to different recovery processes like steam-injection, gas injection and $CO_2$ sequestration can be investigated. The application to non-conventional recovery processes like shale gas and oil using hydraulic fracturing can also be explored.

# NOMENCLATURE

## Chapter II

| | |
|---|---|
| *DX* | Gridcell length along X direction, L, feet |
| *DY* | Gridcell length along Y direction, L, feet |
| *DZ* | Gridcell length along Z direction, L, feet |
| *PV* | Pore volume of gridcell, $L^3$, Barrel |
| *Depth* | Depth of center of a gridcell from a datum, L, feet |
| *FLOOILI* | Oil flux in X direction, $L^3/t$, Reservoir Barrel/day |
| *FLOOILJ* | Oil flux in Y direction, $L^3/t$, Reservoir Barrel/day |
| *FLOOILK* | Oil flux in Z direction, $L^3/t$, Reservoir Barrel/day |
| *FLOWATI* | Water flux in X direction, $L^3/t$, Reservoir Barrel/day |
| *FLOWATJ* | Water flux in Y direction, $L^3/t$, Reservoir Barrel/day |
| *FLOWATK* | Water flux in Z direction, $L^3/t$, Reservoir Barrel/day |
| *Kx* | Permeability along X direction, $L^2$, mD |
| *Ky* | Permeability along Y direction, $L^2$, mD |
| *Kz* | Permeability along Z direction, $L^2$, mD |
| *Permx* | Permeability along X direction, $L^2$, mD |
| *Permy* | Permeability along Y direction, $L^2$, mD |
| *Permz* | Permeability along Z direction, $L^2$, mD |
| *TransX* | Transmissibility along X direction, $L^3$, cP-rb/day/psi |
| *TransY* | Transmissibility along Y direction, $L^3$, cP-rb/day/psi |
| *TransZ* | Transmissibility along Z direction, $L^3$, cP-rb/day/psi |

## Chapter III

| | |
|---|---|
| $A_k$ | Real functions that relate to the amplitude of the wave |
| B | Fluid Formation Volume Factor, dimensionless, fraction |
| C | Phase compressibility, $Lt^2/m$, 1/psi |

| | |
|---|---|
| $c_t$ | Total compressibility, $Lt^2/m$, 1/psi |
| $K$ | Absolute Permeability, $L^2$, mD |
| $L$ | Second order spatial difference operator |
| m | Reservoir model parameter |
| $M$ | Stacked Sensitivity Matrix |
| $P$ | Pressure, $m/Lt^2$, psi |
| $q$ | Fluid production rate, $L^3/t$, Barrel/Day [m3/d] |
| $t_{max}$ | peak arrival time of pressure, t, day(s) |
| $V_p$ | Connected pore-volume, $L^3$, Reservoir Barrels |
| $\alpha$ | Diffusivity coefficient, $L^2/t$, md-psi/cp |
| $\tau$ | Diffusive time of flight / time of flight, t, day(s) |
| $\zeta$ | Distance along the pressure front trajectory, L, feet |
| $\psi$ | Pressure front trajectory |
| $\phi$ | Porosity, dimensionless, fraction |
| $\sigma$ | Phase of the propagating pressure front, radians |
| $\hat{P}$ | Fourier transform of pressure |
| $\rho$ | Density, $m/L^3$, $lbm/ft^3$ [$kg/m^3$] |
| $\lambda$ | Mobility, $tL^3/m$, mD/cp |
| $\mu$ | Viscosity, m/Lt, cp [Pa.s] |
| ω | Frequency, 1/t, Hertz. |

**Chapter IV**

| | |
|---|---|
| e | Arrival time residual vector, day(s) |
| $e_{i,m}$ | arrival time residual at well *i* (producer) which belong to group *m*, day(s) |
| $f_w$ | Water cut, dimensionless, fraction |
| f**(q)** | Scalar objective function, $t^2$, sq day(s) |
| **g(q)** | Inequality constraints, $L^3/t$, Barrel/Day [$m^3/d$] |
| **h(q)** | Equality constraints, $L^3/t$, Barrel/Day [$m^3/d$] |
| *i* and *j* | Well index, dimensionless |

| | |
|---|---|
| $j$ | Geological realization index, dimensionless |
| $k$ | Iteration index, dimensionless |
| $N_{sl,I}$ | Number of streamline connecter to well $i$ (producer) |
| $N_{fsl,i}$ | Number of fast streamlines connected to well $i$ (producer) |
| $N_{fsl,i,j}$ | Number of fast streamlines between well $i$ (producer) and well $j$ (injector) |
| $m$ | Group index, dimensionless |
| $N_{prod,m}$ | Number of production well(s) in group $m$ |
| $N_{group}$ | Number of group(s) , dimensionless |
| **q** | Total fluid rate vector, Barrel/Day [$m^3$/d] |
| $r$ | Risk coefficient, dimensionless |
| $S_{ij}$ | Sensitivities coefficient, $t^2/L^3$, sq Day/Barrel [$s^2/m^3$] |
| **t** | Arrival time vector, t, day(s) |
| SQP | Sequential Quadratic Programming |
| $t_{i,m}$ | Arrival time at producer $i$ which belongs to group $m$, day(s) |
| $t_{d,m}$ | Desired arrival time for group $m$, day(s) |
| $\alpha$ | Exponent term, dimensionless |
| $\eta$ | 'Norm' penalty term, dimensionless |
| $\sigma$ | Standard deviation |
| $\lambda_K$ | Karush-Kuhn-Tucker multipliers for inequality constraints |
| $\lambda_L$ | Lagrange multipliers for equality constraints |

**Chapter V**

| | |
|---|---|
| $a$ | Step size, dimensionless |
| $B_o$ | Oil formation volume factor, dimensionless, fraction |
| $DM$ | Dynamic measure, dimensionless, fraction |
| $g$ | Gradient of the objective function, dimensionless. |
| $k$ | Iterate number, dimensionless |
| $K$ | Permeability, $L^2$, mD |

| | |
|---|---|
| *Kro* | Oil relative permeability, dimensionless, fraction |
| *NTG* | Net to Gross ratio, dimensionless, fraction |
| *O* | Objective function |
| $\overline{P}$ | Average pressure, m/Lt$^2$, psi |
| *p* | Parameter vector to be optimized |
| *Perm* | Permeability, L$^2$, mD |
| *Porevol* | Pore-volume, L$^3$, Reservoir Barrels |
| $P_{wf}$ | Bottomhole flowing pressure, m/Lt$^2$, psi |
| *q* | Fluid production rate, L$^3$/t, Barrel/Day [m3/d] |
| $\phi$ | Porosity, dimensionless, (fraction) |
| $\mu$ | Viscosity, m/Lt, cp [Pa.s] |
| $q_o$ | Oil production rate, L$^3$/t, Barrel/Day [m3/d] |
| *S* | Mechanical skin, dimensionless |
| *So* | Oil saturation, dimensionless, fraction |
| *Soil* | Oil saturation, dimensionless, fraction |
| *TOFI* | Time of flight measured from injector, t, day(s) |
| *TOFP* | Time of flight measured from producer, t, day(s) |
| *TOFT* | Total time of flight, t, day(s) |
| τ | Time of flight, t, day(s) |
| z | Thickness, L, feet |

# REFERENCES

Alhuthali, A.H., Datta-Gupta, A., Yuen, B., and Fontanilla, J.P. 2008. Optimal Rate Control under Geologic Uncertainty. Paper SPE 113628 presented at the SPE/DOE Symposium on Improved Oil Recovery, Tulsa, Oklahoma, USA. DOI: 10.2118/113628-MS.

Alhuthali, A.H., Datta-Gupta, A., Yuen, B., and Fontanilla, J.P. 2010. Field Applications of Waterflood Optimization via Optimal Rate Control with Smart Wells. *SPE Reservoir Evaluation & Engineering* **13** (3): 406–422. DOI: 10.2118/118948-PA.

Alhuthali, A.H., Oyerinde, D., and Datta-Gupta, A. 2007. Optimal Waterflood Management Using Rate Control. *SPE Reservoir Evaluation & Engineering* **10** (5): 539–551. DOI: 10.2118/102478-PA.

Arsac, J. 1966. *Fourier Transforms and the Theory of Distributions*, Prentice-Hall, Upper Saddle River, New Jersey, USA.

Artus, V., Durlofsky, L.J., Onwunalu, J., and Aziz, K. 2006. Optimization of Nonconventional Wells under Uncertainty Using Statistical Proxies. *Computational Geosciences* **10** (4): 389-404.

Bangerth, W., Klie, H., Matossian, V., Parashar, M., and Wheeler, M.F. 2005. An Autonomic Reservoir Framework for the Stochastic Optimization of Well Placement. *Cluster Computing* **8** (4): 255-69.

Benson, S. 2006. Monitoring Carbon Dioxide Sequestration in Deep Geological Formations for Inventory Verification and Carbon Credits. Paper SPE 102833

presented at Annual technical Conference and Exhibition, San Antonio, Texas, USA. DOI: 10.2118/102833-MS.

Bhark, E., Jafarpour, B., and Datta-Gupta, A. 2010. A New Adaptively Scaled Production Data Integration Approach Using the Discrete Cosine Parameterization. Paper SPE 129183 presented at SPE Improved Oil Recovery Symposium, Tulsa, Oklahoma, USA. DOI: 10.2118/129183-MS.

Bhowmik, S., Srinivasan, S., and Bryant, S. 2011. Inferring Migration of $CO_2$ Plume Using Injection Data and a Probabilistic History Matching Approach, *Energy Procedia* **4:** 3841-3848. DOI: 10.1016/j.egypro.2011.02.320.

Bittencourt, A. and Horne, R. 1997. Reservoir Development and Design Optimization. Paper SPE 38895 presented at the SPE Annual Technical Conference and Exhibition, San Antonio, Texas, USA. DOI: 10.2118/38895-MS.

Bouzarkouna, Z., Ding, Y., and Auger, A. 2011. Well Placement Optimization with the Covariance Matrix Adaptation Evolution Strategy and Meta-models. *Computational Geosciences* **16** (1): 75–92.

Brouwer, D.R. and Jansen, J.D. 2004. Dynamic Optimization of Water Flooding with Smart Wells Using Optimal Control Theory. *SPE Journal* **9** (4): 391–402. DOI: 10.2118/78278-PA.

Brun, B., Gosselin, O., and Barker, J.W. 2004. Use of Prior Information in Gradient-Based History Matching. *SPE Journal* **9** (1): 67–78. DOI: 10.2118/ 66353-PA.

Calderon, C.E., and Mohaghegh, S.D. 2010. Characterization and Simulation of ECBM: History Matching of Forecasting $CO_2$ Sequestration in Marshal County, West

Virginia. Paper SPE 139034 presented at SPE Eastern Regional Meeting, Morgantown, West Virginia, USA. DOI: 10.2118/139034-MS.

Centilmen, A., Ertekin, T., and Grader, A. 1999. Applications of Neural Networks in Multiwell Field Development. Paper SPE 56433 presented at the SPE Annual Technical Conference and Exhibition, Houston, Texas, USA. DOI: 10.2118/56433-MS.

Chadwick, R.A., Arts, R., and Eiken, O. 2005. 4D Seismic Quantification of a Growing $CO_2$ Plume at Sleipner, North Sea. *6th Petroleum Geology Conference* **6**: 1385–1399.

Chadwick, R.A. 2010. Quantitative Analysis of Time-Lapse Seismic Monitoring Data at the Sleipner $CO_2$ Storage Operation. *The Leading Edge* **29** (2): 170-177.

Cheng, H., Khargoria, A., He, Z., and Datta-Gupta, A. 2006. Fast History Matching of Finite Difference Models Using Streamline Derived Sensitivities. *SPE Reservoir Evaluation and Engineering* **8** (5): 426-436. DOI: 10.2118/89447-PA.

Cheng, H., Datta-Gupta, A., and He, Zhong. 2005. A Comparison of Travel Time and Amplitude Inversion for Production Data Integration into Geologic Models: Sensitivity, Non-linearity and Practical Implications. *SPE Journal* **10** (1): 75-90. DOI: 10.2118/84570-PA.

Cheng, H., Wen, X. H., and Milliken, W.J. 2004. Field Experiences with Assisted and Automatic History Matching Using Streamline Models. Paper SPE 89857 presented at the SPE Annual Technical Conference and Exhibition, Houston, Texas, USA. DOI: 10.2118/89857-MS.

da Cruz, P.S., Horne, R.N., and Deutsch, C.V. 2004. The Quality Map: A Tool for Reservoir Uncertainty Quantification and Decision Making. *SPE Reservoir Evaluation & Engineering* **7** (1): 6–14. DOI: 10.2118/87642-PA.

Datta-Gupta, A., Yoon, S., Barman, I., and Vasco, D.W. 1998. Streamline-Based Production Data Integration. *Journal of Petroleum Technology* **50** (12): 72-76.

Datta-Gupta, A., Yoon, S.S., Pope, G.A., and Vasco, D.W. 2002. Inverse Modeling of Partitioning Inter-well Tracer Tests: A Streamline Approach. *Water Resources Research* **38** (6), 1079. DOI: 10.1029/2001/WR000597.

Datta-Gupta, A., and King, M.J. 2007. *Streamline Simulation: Theory and Practice*. Textbook Series, Society of Petroleum Engineers, Richardson, Texas, USA.

Delépine, N., Clochard, V., Labat, K., and Ricarte, P. 2011. Post-stack Stratigraphic Inversion Workflow Applied to Carbon Dioxide Storage: Application to the Saline Aquifer of Sleipner Field. *Geophysical Prospecting* **59:** 132–144. DOI: 10.1111/j.1365-2478.2010.00905.

*DESTINY User Guide 2011*, MCERI Research Group, Texas A&M University.

Devegowda, D., Arroyo-Negrete, E., Datta-Gupta, A., and Douma, S. 2007. Efficient and Robust Reservoir Model Updating Using Ensemble Kalman Filter with Sensitivity-Based Covariance Localization. Paper SPE 106144 presented at the SPE Reservoir Simulation Symposium, The Woodlands, Texas, USA. DOI: 10.2118/106144-MS.

Durlofsky, L.J., Behrens, R.A., Jones, R.C., and Bernath, A. 1996. Scale Up of Heterogeneous Three Dimensional Reservoir Descriptions. *SPE Journal* **1** (3): 313-326. DOI: 10.2118/30709-PA.

*ECLIPSE©, Version 2010.2*. 2010. Houston, Texas, USA. Schlumberger Information Solutions.

Emerick, A., Silva, E., Messer, B., Almeida, L., Szwarcman, D., Pacheco, M.A., and Vellasco, M. 2009. Well Placement Optimization Using a Genetic Algorithm with Nonlinear Constraints. Paper SPE 118808 presented at the SPE Reservoir Simulation Symposium, Woodlands, Texas, USA. DOI: 10.2118/118808-MS.

Fatemi, E., Enguist, B., and Osher, S. 1995. Numerical Solution of the High Frequency Asymptotic Expansion of the Scalar Wave Equation. *Journal of Computational Physics* **120**: 145-155.

Finley, R. 2005. *An Assessment of Geological Carbon Sequestration Options in the Illinois Basin*, *Illinois State Geological Survey Final Report*. US DOE Contract: DE-FC26-03NT41994, Champaign, Illinois, USA.

Flett M., Gurton R., and Weir G. 2007. Heterogeneous Saline Formations for Carbon Dioxide Disposal: Impact of Varying Heterogeneity on Containment and Trapping. *Journal of Petroleum Science and Engineering* **57**: 106–118.

Fowler, M. L., and Young, M. A. 1996. Some Practical Aspects of Reservoir Management. Paper SPE 37333 presented at SPE Eastern Regional Meeting, Columbus, Ohio, USA. DOI: 10.2118/37333-MS.

Gavalas, G.R., Shah, P.C., and Seinfeld, J.H. 1976. Reservoir History Matching by Bayesian Estimation. *SPE Journal* **16** (6): 337-350.

Guerra, N. Y., and Narayanasamy, R. 2006. Well Location Selection from Multiple Realizations of a Geomodel Using Productivity Potential Maps: A Heuristic Technique. SPE paper 102903 presented at the 1st International Oil Conference and Exhibition, Cancun, Mexico. DOI: 10.2118/102903-MS.

Guyaguler, B. 2002. Optimization of Well Placement and Assessment of Uncertainty. Ph.D Thesis.

Guyaguler, B., and Horne, R. 2004. Uncertainty Assessment of Well Placement Optimization. *SPE Reservoir Evaluation & Engineering* **7** (1): 24-32. DOI: 10.2118/87663-PA.

Ha-Duong, M., and Keith, D. W. 2003. Carbon Storage: The Economic Efficiency of Storing $CO_2$ in Leaky Reservoirs. *Clean Technology in Environmental Pollution* **5:** 181–189.

He, Z., Yoon, S., and Datta-Gupta, A. 2002. Streamline-Based Production Data Integration with Gravity and Changing Field Conditions. *SPE Journal* **7** (4): 423-436. DOI: 10.2118/81208-PA.

Hohl, D., Jimenez, E., and Datta-Gupta, A. 2006. Field Experiences with History Matching an Offshore Turbiditic Reservoir Using Inverse Modeling. Paper SPE 101983 presented at the SPE Annual Technical Conference and Exhibition, San Antonio, Texas, USA. DOI: 10.2118/101983-MS.

Jimenez, E., Datta-Gupta, A., and King, M. J. 2010. Full Field Streamline Tracing in Complex Faulted Systems with Non-neighbor Connections. *SPE Journal* **15** (1): 7-17. DOI: 10.2118/113425-PA.

Jimenez, E., Sabir, K., Datta-Gupta, A., and King, Michael J. Spatial Error and Convergence in Streamline Simulation. 2007. *SPE Reservoir Evaluation & Engineering* **10** (3): 221-232. DOI: 10.2118/92873-PA.

Jong, U-K, Datta-Gupta, A., Jimenez, E., and Hohl, D. 2010. A Dual-Scale Approach to History Matching High Resolution Geologic Models. *Journal of Petroleum Science and Engineering* **71** (3): 147-159.

Kulkarni, K.N., Datta-Gupta, A., and Vasco, D.W. 2001. A Streamline Approach for Integrating Transient Pressure Data into High Resolution Reservoir Models. *SPE Journal* **6** (3): 273–282. DOI: 10.2118/74135-PA.

Kharghoria, A., Cakici, M., Narayanasamy, R., Kalita, R., Sinha, S., and Jalali, Y. 2003. Productivity-Based Method for Selection of Reservoir Drilling Target and Steering Strategy. Paper SPE 85431 presented at the SPE/IADC Middle East Drilling Technology Conference and Exhibition, Abu Dhabi, United Arab Emirates. DOI: 10.2118/85431-MS.

Kim, J.U., Datta-Gupta, A., Brouwer, R., and Haynes, B. 2009. Calibration of High Resolution Reservoir Models Using Transient Pressure Data. Paper SPE 124834 presented at SPE Annual Technical Conference and Exhibition, New Orleans, Louisiana, USA. DOI: 10.2118/124834-MS.

King, M., Burn, K., Wang, P., Muralidharan, V., Alvardo, F., Ma, X., and Datta-Gupta, A. 2005. Optimal Coarsening of 3D Reservoir Models for Flow Simulation. Paper SPE 95759 presented at the SPE Annual Technical Conference and Exhibition, Dallas, Texas. DOI: 10.2118/95759-MS.

Kline, M., and Kay, I.W. 1965. *Electromagnetic Theory and Geometrical Optics*. John Wiley and Sons, New York City, New York, USA.

Kravtsov, Y.A., and Orlov, Y.I. 1990. *Geometrical Optics of Inhomogeneous Media*. Springer-Verlag, New York City, New York, USA.

Krogstad, S., Hauge, V., and Gulbransen, A. 2009. Adjoint Multi-Scale Mixed Finite Elements. Paper SPE 119112 presented at SPE Reservoir Simulation Symposium, Woodlands, Texas, USA. DOI: 10.2118/119112-MS.

Kumar, A. 2008. Time-Lapse Seismic Modeling and Production Data Assimilation for Enhanced Oil Recovery and Carbon Dioxide Sequestration. Ph.D Thesis.

Lee, W.J. 1982. *Well Testing*. SPE Textbook Series. Richardson, Texas, USA.

Leonenko, Y. 2008. Reservoir Engineering to Accelerate the Dissolution of $CO_2$ Stored in Aquifers. *Environmental Science & Technology* **42.8**: 2742.

Liu, N., and Oliver, D.S. 2005. Critical Evaluation of the Ensemble Kalman Filter on History Matching of Geologic Facies. *SPE Reservoir Engineering and Evaluation* **8** (6): 470-477. DOI: 10.2118/92867-PA.

Liu, N., and Jalali, Y. 2006. Closing the Loop between Reservoir Modeling and Well Placement and Positioning. Paper SPE 98198 presented at the Intelligent Energy Conference and Exhibition, Amsterdam, Netherlands. DOI: 10.2118/98198-MS.

Mahani, H., Ashjari, M., and Firoozabadi, B. 2007. Reservoir Flow Simulation Using Combined Vorticity-Based Gridding and Multi-Scale Upscaling. Paper SPE 110306 presented at the Asia Pacific Oil and Gas Conference and Exhibition, Jakarta, Indonesia. DOI: 10.2118/110306-MS.

Mamonov, A., Couet, B., Bailey, W., Prange, M., Djikpesse, H., and Druskin, V. 2007. Optimal Gridding: A Fast Proxy for Large Reservoir Simulations. Paper SPE 111378 presented at SPE/EAGE Reservoir Characterization and Simulation Conference, Abu Dhabi, UAE. DOI: 10.2118/111378-MS.

Mantilla, C.A., Srinivasan, S., Cross, E.A., and Bryant, S.L. 2009. Inexpensive Assessment of Plume Migration during $CO_2$ Sequestration. SPE 126693. SPE International Conference on $CO_2$ Capture, Storage, and Utilization, San Diego, California, USA. DOI: 10.2118/126693-MS.

*MATLAB® Documentation*, 1994-2012, The MathWorks, Inc.

Mishra, S., Kelley, M., Zeller, E., Gupta, N., Bhattacharya, I., and Hammond, M. 2011. Analyzing Pressure Falloff Data from $CO_2$ Injection Projects – The Mountaineer Experience. Presented at Tenth Annual Conference on Carbon Capture & Sequestration, Pittsburgh, Pennsylvania, USA.

Mitra, N.K., and Kumar, A. 2008. Managing Mature Indian Offshore Fields - A Case History. Paper SPE 117950 presented at the Abu Dhabi International Petroleum Exhibition and Conference, Abu Dhabi, UAE. DOI: 10.2118/117950-MS.

Moore, C., and Doherty, J. 2005. The Cost of Uniqueness in Groundwater Model Calibration. *Advances in Water Resources* **29** (4): 605-623. DOI: 10.1016/j.advwatres.2005.07.003.

Naevdal G., Brouwer D. R., and Jansen J. D. 2006. Waterflooding Using Closed-Loop Control. *Computational Geosciences* **10**: 37–60. DOI: 10.1007/s10596-005-9010-6.

Nakajima, L., and Schiozer, D. 2003. Horizontal Well Placement Optimization Using Quality Map Definition. Paper Canadian Petroleum Society 2003-053 presented at the Canadian International Petroleum Conference, Calgary, Alberta, Canada.

Nocedal, J., and Wright, S.J. 2006. *Numerical Optimization*, 2nd edition. Springer Science. New York, USA.

Nooner, S.L., Eiken, O., Hermanrud, C., Sasagawa, G.S., Stenvold, T., and Zumberge, M.A. 2007. Constraints on the In-situ Density of $CO_2$ with in the Utsira Formation from Time-Lapse Seafloor Gravity Measurements. *Journal of Greenhouse Gas Control* **1**: 198–214.

Oliver, D.S., Reynolds, A.C., and Liu, N. 2008. *Inverse Theory for Petroleum Reservoir Characterization and History Matching*. Cambridge University Press, New York, USA.

Onwunalu, J., and Durlofsky, L.J. 2010. Application of a Particle Swarm Optimization Algorithm for Determining Optimum Well Location and Type. *Computational Geosciences* **14** (1): 183–198.

Oruganti, Y. D., and Bryant, S.L. 2009. Pressure Buildup during $CO_2$ Storage in Partially Confined Aquifers. *Energy Procedia* **1** (1): 3315-3322. DOI: 10.1016/j.egypro.2009.02.118.

Oyerinde, A., Datta-Gupta, A., and Milliken, W. 2009. Experiences with Streamline-Based Three Phase History Matching. *SPE Reservoir Engineering and Evaluation* **12** (4): 528-541. DOI: 10.2118/109964-PA.

Ozdogan, U., Sahni, A., Yeten, B., Guyaguler, B., and Chen, W. 2005. Efficient Assessment and Optimization of a Deepwater Asset Development Using Fixed Pattern Approach. Paper SPE 95792 presented at the SPE Annual Technical Conference and Exhibition, Dallas, Texas, USA. DOI: 10.2118/95792-MS.

Ozdogan, U., and Horne, R. 2006. Optimization of Well Placement under Time-dependent Uncertainty. *SPE Reservoir Evaluation & Engineering* **9** (2): 135-45. DOI: 10.2118/90091-PA.

Park, H., 2012. A Hierarchical Multi-Scale Approach to History Matching and Optimization for Reservoir Management in Mature Fields. Ph.D Thesis.

Peters, E., Arts, R.J., Brouwer, G. K., and Geel, C.R. 2009. Results of the Brugge Benchmark Study for Flooding Optimization and History Matching. Paper SPE 119094 presented at the SPE Reservoir Simulation Symposium, The Woodlands, Texas, USA. DOI: 10.2118/119094-MS.

Qassab, H., Pavlas, M.K., and Afaleg, N. 2003. Streamline-Based Production Data Integration under Realistic Field Conditions: Experience in a Giant Middle-Eastern Reservoir. Paper SPE 84079 presented at the SPE Annual Technical Conference and Exhibition, Denver, Colorado, USA. DOI: 10.2118/84079-MS.

Quenes, A., Bhagavan, S., Bunge, P., and Travis, B. 1994. Application of Simulated Annealing and Other Global Optimization Methods to Reservoir Description: Myth and Realities. Paper SPE 28415 presented at the SPE Annual Technical Conference and Exhibition, New Orleans, Louisiana, USA. DOI: 10.2118/28415-MS.

Rey, A., Ballin, P.R., and Vitalis, C.F. 2009. Assisted History Matching in an Offshore Turbidite Reservoir with Active Reservoir Management. Paper SPE 124950 presented at the SPE Annual Technical Conference and Exhibition, New Orleans, Louisiana, USA. DOI: 10.2118/124950-MS.

Rey, A., Taware, S.V., and Datta-Gupta, A. 2010. Use of Time-Lapse Seismic Data for Heterogeneity Characterization during $CO_2$ Sequestration in Saline Aquifers. Paper SPE 139519 presented at SPE International Conference on $CO_2$ Capture, Storage, and Utilization, New Orleans, Louisiana, USA. DOI: 10.2118/139519-MS.

Gasda, S.E, Bachu, S., and Celia, M.A. 2004. Spatial Characterization of the Location of Potentially Leaky Wells Penetrating a Deep Saline Aquifer in a Mature Sedimentary Basin. *Environment Geology* **46** (6-7)**:** 707–720. DOI: 10.1007/s00254-004-1073-5.

Sarma, P., Durlofsky, L. J., and Aziz, K. 2005. Efficient Closed-Loop Production Optimization under Uncertainty. Paper SPE 94241 presented at the Europec/EAGE Annual Conference, Madrid, Spain. DOI: 10.2118/94241-MS.

Sarma, P., and Chen, W.H. 2008. Efficient Well Placement Optimization with Gradient-Based Algorithms and Adjoint Models. Paper SPE 112257 presented at the SPE Intelligent Energy Conference and Exhibition, Amsterdam, Netherlands. DOI: 10.2118/1122570-MS.

Spall, J.C. 1992. Multivariate Stochastic Approximation Using a Simultaneous Perturbation Gradient Approximation. *IEEE Transactions on Automatic Control* **37** (3): 332-341.

Spall, J.C. 2002. Adaptive Stochastic Approximation by the Simultaneous Perturbation Method. *IEEE Transactions on Automatic Control* **45** (10): 1839-1853.

Spycher, N., and Pruess, K. 2003. $CO_2$-$H_2O$ Mixtures in the Geological Sequestration of $CO_2$. II. Partitioning in Chloride Brines at 12-100 C and up to 600 bar. *Geochimica et Cosmochimica Acta* **69** (13): 3309-3320.

Stenerud, V.R., Kippe, V., Datta-Gupta, A., and Lie, K.A. 2008. Adaptive Multi-Scale Streamline Simulation and Inversion for High Resolution Geomodels. *SPE Journal* **13** (10): 99-111. DOI: 10.2118/106228-PA.

Sudaryanto, B., and Yortsos. Y.C. 2001. Optimization of Displacements in Porous Media Using Rate Control. Paper SPE 71509 presented at the SPE Annual Technical Conference and Exhibition, New Orleans, Louisiana, USA. DOI: 10.2118/71509-MS.

Tavakkolian, M., Jalali, F., and Amadi, M.A. 2004. Production Optimization Using Genetic Algorithm Approach. Paper SPE 88901 presented at the Annual SPE

International Technical Conference Exhibition, Abuja, Nigeria. DOI: 10.2118/88901-MS.

Van Essen, G. M., Zandvliet, M. J., Van Den Hof, P. M., Bosgra, O. H., and Jansen, J. D. 2006. Robust Waterflooding Optimization of Multiple Geological Scenarios. Paper SPE 102913 presented at the Annual Technical Conference and Exhibition, San Antonio, Texas, USA. DOI: 10.2118/102913-MS.

Vasco, D.W., and Datta-Gupta, A. 1999. Asymptotic Solutions for Solute Transport. *Water Resources Research* **35** (1): 1-16. DOI: 10.1029/98WR02742.

Vasco, D.W., Yoon, S., and Datta-Gupta, A. 1999. Integrating Dynamic Data into High Resolution Reservoir Models Using Streamline-Based Analytic Sensitivity Coefficients. *SPE Journal* **4** (4): 389-399. DOI: 10.2118/49002-PA.

Vasco, D.W., Keer, H., and Karasaki, K. 2000. Estimation of Reservoir Properties Using Transient Pressure Data: An Asymptotic Approach. *Water Resources Research* **36** (12): 3447-3465. DOI: 10.1029/2000WR900179.

Vasco, D.W., and Datta-Gupta, A. 2001. Asymptotics, Saturation Fronts and High Resolution Reservoir Characterization. *Transport in Porous Media* **42**(3): 315-350. DOI: 10.1023/A:1006788413831.

Vasco, D.W., and Finsterle, S. 2004. Numerical Trajectory Calculations for the Efficient Inversion of Transient Flow and Tracer Observations. *Water Resources Research* **40**: W01507. DOI: 10.1029/2003WR002362.

Vasco, D.W., and Karasaki, K. 2006. Interpretation and Inversion of Low Frequency Head Observations. *Water Resources Research* **42**: W05408. DOI: 10.1029/2005WR004445.

Vlemmix, S., Joosten, G.J., Brouwer, D.R., and Jansen, J.D. 2009. Adjoint-Based Well Trajectory Optimization in a Thin Oil Rim. Paper SPE 121891 presented at SPE EUROPEC/EAGE Annual Conference and Exhibition, Amsterdam, Netherlands. DOI: 10.2118/121891-MS.

Wang, C., Li, G., and Reynolds, A. C. 2007. Production Optimization in Closed-Loop Reservoir Management. Paper SPE 109805 presented at the SPE Annual Technical Conference and Exhibition, Anaheim, California, USA. DOI: 10.2118/109805-MS.

Wilson, M., and Monea, M. 2004. *IEA GHG Weyburn $CO_2$ Monitoring & Storage Project, Summary Report 2000–2004*. Petroleum Technology Research Centre, Regina, Canada.

Wright, I., Mathieson, A., and Ringrose, P. 2009. An Overview of Active Large-Scale $CO_2$ Storage Projects. Paper SPE 127096 presented at SPE International Conference on $CO_2$ Capture, Storage and Utilization, San Diego, California, USA. DOI: 10.2118/127096-MS.

Wu, Z., and Datta-Gupta, A. 2002. Rapid History Matching Using a Generalized Travel Time Inversion Method. *SPE Journal* **7** (2): 113-122. DOI: 10.2118/78359-PA.

Yeh, W. 1986. Review of Parameter Estimation Procedures in Groundwater Hydrology: The Inverse Problem. *Water Resources Research* **22** (2): 95–108. DOI: 10.1029/WR022i002p00095.

Yeten, B., Durlofsky, L., and Aziz, K. 2003. Optimization of Nonconventional Well Type, Location and Trajectory. *SPE Journal* **8** (3): 200-10. DOI: 10.2118/86880-PA.

Yin, J., Park, H., Datta-Gupta, A., King, M., and Choudhary, M. 2010. A Hierarchical Streamline Assisted History Matching Approach with Global and Local Parameter Updates. Paper SPE 132642 presented at SPE Western Regional Meeting, Anaheim, California, USA. DOI: 10.2118/132642-MS.

Yoon, S. S., Malallah, A., Datta-Gupta, A., Vasco, D. W., and Behrens, R. A. 2001. A Multi-Scale Approach to Production Data Integration Using Streamline Models. *SPE Journal* **6** (2): 182-192. DOI: 10.2118/71313-PA.

Zandvliet, M.J., Handels, M., van Essen, G.M., Brouwer, D.R., and Jansen, J.D. 2008. Adjoint-Based Well Placement Optimization under Production Constraints. *SPE Journal* **3** (4): 392–399. DOI: 10.2118/105797-PA.

# APPENDIX A

## A.1 Grid Coarsening Scheme

Static properties such as permeability, pore-volume, transmissibility etc. are upscaled during coarsening as shown in **Fig A.1**. Within each coarse block the properties are simply upscaled from non-coarsened (*n*) to coarsened (*c*) in a single amalgamation (*I1*, *I2*) x (*J1*, *J2*) x (*K1*, *K2*). *I1* and *I2* are I index of start and end non-coarsened grid cells of amalgamation and so on. Details are taken from the manual of the commercial simulator (ECLIPSE, 2010) which was deployed. The non-coarsened indexes are shown in the schematic **Fig A.1** below.


**Fig. A.1 - Schematic of non-coarsened grid showing I, J and K indexes for each grid cell.**

Pore volume of the coarse cells is simply the sum of the individual pore volumes of the fine cells described as follows,

$$PV_c = \sum_n PV_n \quad \text{..... (A.1)}$$

$PV_n$ is pore volume of non-coarsened cells to be amalgamated. $PV_c$ is assigned to the representative cell. Depth of coarse cells is derived as follows,

$$Depth_c = \frac{\sum_n PV_n Depth_n}{PV_n} \quad \text{(A.2)}$$

$Depth_n$ is depth of non-coarsened cells to be amalgamated. $Depth_c$ is assigned to the representative cell. Dimensions *DX*, *DY* and *DZ* of fine cells are then aggregated as follows,

$$DX_n = \frac{\sum_n DX_n}{(J2-J1+1)(K2-K1+1)}, DY_n = \frac{\sum_n DY_n}{(I2-I1+1)(K2-K1+1)}, \; DZ_n = \frac{\sum_n DZ_n}{(J2-J1+1)(I2-I1+1)} \quad \text{(A.3)}$$

$DX_n$ , $DY_n$ and $DZ_n$ are dimensions of the non-coarsened grid cells to be amalgamated. $DX_c$, $DY_c$ and $DZ_c$ are assigned to the representative cell. *Permx*, *Permy* and *Permz* of fine cells are coarsened as follows,

$$Kx_c = \frac{\sum_n PV_n Kx_n}{PV_c}, Ky_c = \frac{\sum_n PV_n Ky_n}{PV_c}, Kz_c = \frac{\sum_n PV_n Kz_n}{PV_c} \quad \text{(A.4)}$$

with $Kx_n$ , $Ky_n$ and $Kz_n$ as permeabilities of the non-coarsened grid cells to be amalgamated and $Kx_c$, $Ky_c$ and $Kz_c$ as values to be assigned to the representative cell. Transmissibilities *Tranx* of fine cells are coarsened as follows,

$$TransX_c = \sum_J \sum_K \left[ \frac{1}{\sum_I \left( \frac{1}{TransX_n} \right)} \right], TransY_c = \sum_I \sum_K \left[ \frac{1}{\sum_J \left( \frac{1}{TransY_n} \right)} \right], TransZ_c = \sum_J \sum_I \left[ \frac{1}{\sum_K \left( \frac{1}{TransZ_n} \right)} \right] \quad \text{(A.5)}$$

In the above equations, $TransX_n$, $TransY_n$ and $TransZ_n$ are transmissibilities of the non-coarsened grid cells to be amalgamated and $TransX_c$, $TransY_c$ and $TransZ_c$ are assigned to the representative cell. Here the summations in J and K direction of *TransX* are over the X-direction faces of I-indexed fine cells within an amalgamation. Summation of the term $\sum_I \left( \frac{1}{TransX_n} \right)$ is over all I-indexed fine cells within an amalgamation. This is done similarly for Y and Z direction.

## A.2 Flux Reconstruction at Non-Coarsened Scale from Coarsened Scale in Y Direction

The schematic for flux reconstruction, i.e., conversion of coarsened flux in amalgamation to non-coarsened fluxes in Y direction is shown in **Fig. A.2**.

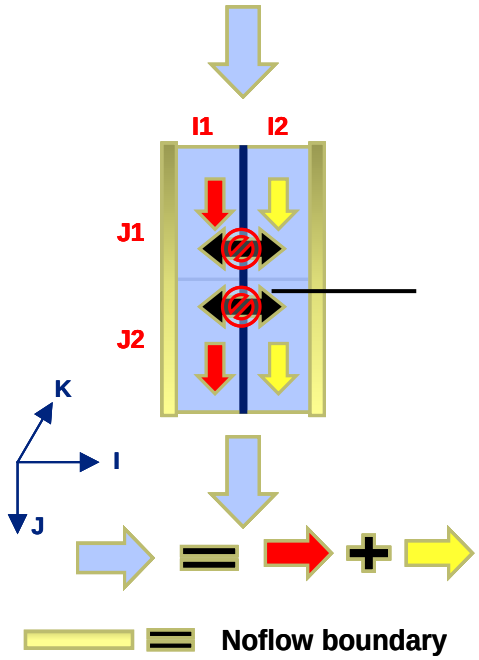


**Fig. A.2 - Schematic of non-coarsened flux reconstruction (red and yellow) using coarsened flux (light blue) for 2x2 coarsening in Y direction.**

Taking harmonic average of *TransY* along Y direction for a particular I index *I1* and particular K index *K1*, at non-coarsened scale (*n*),

$$TransY_{K1,I1} = \frac{J2 - J1 + 1}{\sum_{J}\left(\frac{1}{TransY_n}\right)} \quad \text{.....(A.6)}$$

This harmonic average transmissibility $TransY_{K1,J1}$ along the Y direction is used to redistribute phase fluxes in Y direction in the non-coarsened grid. Y direction Phase

Fluxes for non-coarsened cells along a particular I index *I1* and K index *K1* are calculated as follows,

$$FLOOILJ_{K1,I1} = \frac{TransY_{K1,I1}}{\sum_K \sum_I TransY_{K,I}} \bullet FLOOILJ_C \quad \text{..... (A.7)}$$

$$FLOWATJ_{K1,I1} == \frac{TransY_{K1,I1}}{\sum_K \sum_I TransY_{K,I}} \bullet FLOWATJ_C \quad \text{..... (A.8)}$$

$$FLOGASJ_{K1,I1} == \frac{TransY_{K1,I1}}{\sum_K \sum_I TransY_{K,I}} \bullet FLOGASJ_C \quad \text{.....(A.9)}$$

Similarly for other cells with $n^{th}$ K Index and $n^{th}$ I Index are calculated as follows,

$$FLOOILJ_{Kn,In} = \frac{TransY_{Kn,In}}{\sum_K \sum_I TransY_{K,I}} \bullet FLOOILJ_C \quad \text{.....(A.10)}$$

$$FLOWATJ_{Kn,In} = \frac{TransY_{Kn,In}}{\sum_K \sum_I TransY_{K,I}} \bullet FLOWATJ_C \quad \text{.....(A.11)}$$

$$FLOGASJ_{Kn,In} = \frac{TransY_{Kn,In}}{\sum_K \sum_I TransY_{K,I}} \bullet FLOGASJ_C \quad \text{..... (A.12)}$$

## A.3 Flux Reconstruction at Non-Coarsened Scale from Coarsened Scale in Z Direction

The schematic for flux reconstruction i.e. conversion of coarsened flux in amalgamation to non-coarsened fluxes in Z direction is shown in **Fig.A.3**.

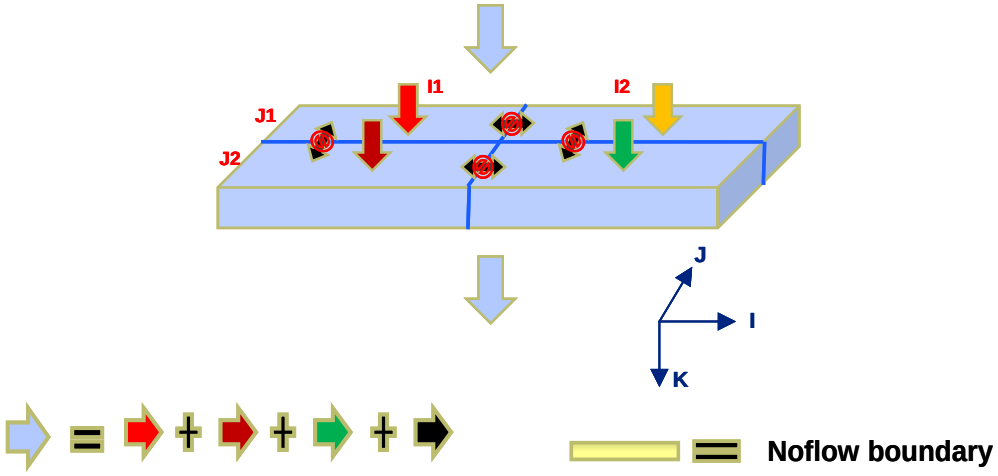


**Fig. A.3 - Schematic of non-coarsened flux reconstruction (red, yellow, brown and green) using coarsened flux (light blue) for 2x2 coarsening in Z direction.**

Taking harmonic average of *TransZ* along Z direction for a particular I index *I1* and particular J index *J1*, at non-coarsened scale (n),

$$TransZ_{I1,J1} = \frac{K2 - K1 + 1}{\sum_{K}\left(\frac{1}{TransZ_n}\right)} \quad \text{.....(A.13)}$$

This harmonic average transmissibility $TransZ_{I1,J1}$ along the Z direction is used to redistribute phase fluxes in Z direction in the non-coarsened grid. Z direction Phase Fluxes for non-coarsened cells along a particular I index *I1* and J index *J1* are calculated as follows,

$$FLOOILK_{I1,J1} = \frac{TransZ_{I1,J1}}{\sum_{I}\sum_{J} TransZ_{I,J}} \bullet FLOOILK_C \quad \text{.....(A.14)}$$

$$FLOWATK_{I1,J1} = \frac{TransZ_{I1,J1}}{\sum_{I}\sum_{J} TransZ_{I,J}} \bullet FLOWATK_C \quad \text{.....(A.15)}$$

$$FLOGASK_{I1,J1} = \frac{TransZ_{I1,J1}}{\sum_{I}\sum_{J} TransZ_{I,J}} \bullet FLOGASK_C \quad \text{.....(A.16)}$$

Similarly for other cells with nth J Index and n[th] I Index are calculated as follows,

$$FLOOILK_{In,Jn} = \frac{TransZ_{In,Jn}}{\sum_{I}\sum_{J} TransZ_{I,J}} \bullet FLOOILK_{C} \quad \text{..... (A.17)}$$

$$FLOWATK_{In,Jn} = \frac{TransZ_{In,Jn}}{\sum_{I}\sum_{J} TransZ_{I,J}} \bullet FLOWATK_{C} \quad \text{..... (A.18)}$$

$$FLOGASK_{In,Jn} = \frac{TransZ_{In,Jn}}{\sum_{I}\sum_{J} TransZ_{I,J}} \bullet FLOGASK_{C} \quad \text{..... (A.19)}$$

# APPENDIX B

## B.1 Compositional Streamline Tracing

Streamline trajectories form the underlying basis for the sensitivity calculations described in **section 3.2.2**. The $CO_2$ saturation sensitivities are defined as 1-D integrals along streamlines. In this appendix, the tracing of streamlines in compositional modeling of $CO_2$ sequestration is briefly described. The streamline tracing is carried out using the approach proposed by Jimenez et al., (2010) for corner-point cells using iso-parametric transformation from the physical coordinate (*x,y,z*) to the unit cube coordinates $(\alpha,\beta,\gamma)$. This approach has two important elements: first the volumetric flux, rather than velocity, is interpolated within the grid-cell; second, the Jacobian of transformation $J(\alpha,\beta,\gamma)$ to the unit cube, instead cell volume, is used to relate volumetric flux and velocity.

Jimenez et al., (2007; 2010) used a psuedo time of flight, $T$ for simplifying streamline tracing method so that time of flight can be calculated by rigorously accounting for the spatially varying Jacobian within the corner point cell. The pseudo time of flight is defined as follows:

$$dT = \frac{1}{\phi}\frac{d\tau}{J(\alpha,\beta,\gamma)} = \frac{d\alpha}{dQ_1(\alpha)} = \frac{d\beta}{dQ_2(\beta)} = \frac{d\gamma}{dQ_3(\gamma)} \quad \text{.....(B.1)}$$

The streamline trajectories are obtained by integrating the above equation in all three directions. For example, the integral in the α direction is given as follows:

$$\int_0^{T_E} dT = \int_{\alpha_0}^{\alpha}\left(\frac{d\alpha}{dQ_1(\alpha)}\right) = \int_{\alpha_0}^{\alpha}\left(\frac{d\alpha}{\alpha_1 + c_1\alpha}\right) \quad \text{.....(B.2)}$$

Solving the above integral:

$$T_E = \frac{1}{c_1}\ln\left(\frac{a_1 + c_1\alpha}{a_1 + c_1\alpha_0}\right) \quad \text{.....(B.3)}$$

Identical constructions will arise for the β and γ directions. The actual pseudo time of flight *T* is given by the minimum over allowable edges Jimenez et al., (2007).

$$\Delta T = Min \;\; Positive \left(\Delta T_E, \Delta T_W, \Delta T_F, \Delta T_B, \Delta T_T, \Delta T_B\right)$$

Once the pseudo time of flight *T* is known, the exit coordinate of the particle can be easily calculated. For example, by rearranging **Eq. B.3**, we get the $\alpha$ coordinate of the exit point,

$$\alpha_e = \alpha_0 + \left(\alpha_1 + \alpha_0 c_1\right)\left(\frac{e^{c_1 T} - 1}{c_1}\right) \quad \text{.....(B.4)}$$

Knowing the unit space coordinates $(\alpha, \beta, \gamma)$, a tri-linear interpolation is used to transform the unit coordinates into the physical space (Datta-Gupta and King, 2007). The last step is to convert pseudo time of flight *T* to the actual time of flight τ. This is given by the following integral (Jimenez, 2007),

$$\tau = \phi \int_0^T J\left(\alpha(T), \beta(T), \gamma(T)\right) dT \quad \text{.....(B.5)}$$

As mentioned before, a compositional simulator is used for modeling $CO_2$ sequestration. Compositional simulators typically provide the flux of individual components in different phases. The flow rate of component '*c*' embedded in the phase *p* into cell '*i*' from the neighboring cell '*n*' i.e. $Q^c_{Pni}$ is given as follows (ECLIPSE 300 Technical Description)

$$Q^c_{Pni} = T_{ni}\left(M^c_p\right) dP_{Pni} \quad \text{.....(B.6)}$$

Where $T_{ni}$ is the transmissibility between the cells, $dP_{Pni}$ is the potential difference and $M^c_p$ is the generalized mobility of component *c* in the phase *p* given as

$$M_p^c = x_p^c k_{rp}(S_p)\frac{b_p^m}{\mu_p} \quad \text{.....(B.7)}$$

where the fluid mobility $M_p^c$ is evaluated in the upstream cell for each phase separately. The above identities are derived for tracking component *c* in phase *p*. So for tracking a particular component, the component flux in all the phases is summed up. For phase tracking, the fluxes of all the components are summed up for that particular phase. The streamlines for peak arrival time inversion are traced based on total fluxes (sum of all phase fluxes) leading to continuous trajectories.

# APPENDIX C

## C.1 Instead of using norm term, why the rates cannot be simply scaled up to hit the first constraint and preserve the minimum value of the objective function?

a) The optimization problem is not linear. There is no linear relationship between time of flight (arrival time of waterfront) and rates for compressible water-oil case but relationship becomes more linear for incompressible water-oil case (Fig-C.1).

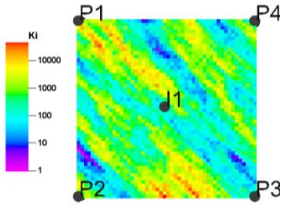


It can be seen that if all the rates (producers and injector) are halved equally average time of flight at four producers is not exactly doubled. This shows there no strict linear relationship between time of flight and rates. This is effect to compressibility of oil – water along with presence of gas

| Average Time of flight in days compressible oil water | | | | |
|---|---|---|---|---|
| | **P1** | **P2** | **P3** | **P4** |
| **Inj =800, all prod = 200** | 889.05 | 3922.67 | 1571.42 | 3269.30 |
| **Inj =400, all prod = 100** | 1895.38 | 8446.58 | 3028.05 | 6222.71 |
| **Factor** | **2.132** | **2.153** | **1.927** | **1.903** |

If simple PVT properties are used (i.e incompressible oil-water and no gas) the relationship between time of flight and rates becomes more linear than above case

| Average Time of flight in days incompressible oil water | | | | |
|---|---|---|---|---|
| | **P1** | **P2** | **P3** | **P4** |
| **Inj =800, all prod = 200** | 844.60 | 3726.54 | 1492.85 | 3105.84 |
| **Inj =400, all prod = 100** | 1710.23 | 7463.56 | 2975.45 | 6160.60 |
| **Factor** | **2.025** | **2.003** | **1.993** | **1.984** |

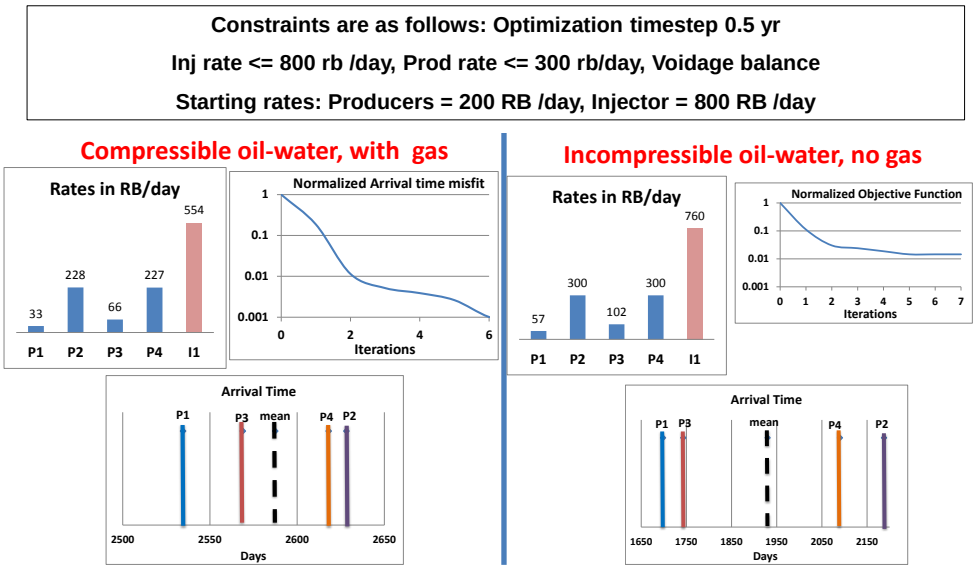


Different degrees of linearity between arrival time and rates give different optimized rates. In case of compressible oil-water with gas no producer hits constraint although objective function was reduced, while in incompressible case two producers hit constraint with objective function converging above 0.01

**Fig - C.1: Relationship between time of flight and rate**

b) If converged rates in case of compressible oil-water with gas (fig-C.2) are shifted up to hit first constraint, does objective function value stays same? No, it increases and sweep efficiency is not maximized (Fig – C.2).

Converged rates of all producers along with injector in the case of compressible oil-water with gas shown in previous answer, are shifted to hit first constraint. The first constraint hit is by well P2 of 300 RB /day. It can be seen that there is an increase in the objective function because decrease in travel time is offset by the increase in difference between arrival time and desired arrival time. These rates cannot be simply scaled up due to no strict linear relationship between arrival time and rates for compressible oil-water with gas case.

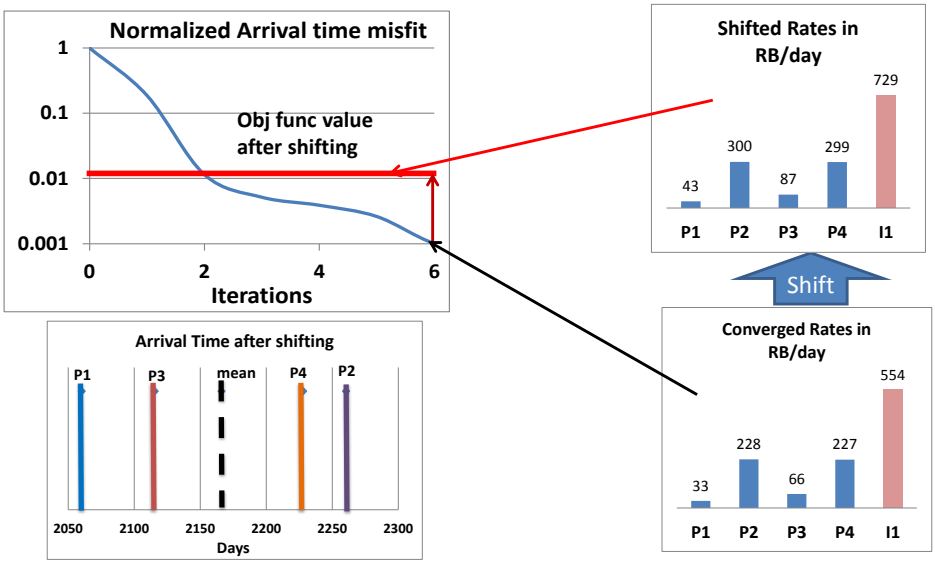


**Fig – C.2: Objective function shifts up when rates are shifted equally to hit first constraint.**

**C.2 Are the solutions for rate optimization unique? - No**

a) There is a clear existence of multiple local minima in the solution space during rate optimization. Arrival time misfit is calculated for different rates of well P1, P2, P3 and P4. Contour plots are plotted by keeping P1 and P3 constant.

A synthetic 2D field (**Fig. C.3**) with four producers and an injector (inverted 5 spot) is used for illustration. Compressible oil with dissolved and free gas and water are used as fluids for blackoil simulation.

Process of calculating arrival time misfit using exhaustive search is described as below,

1) Vary rates of P1, P2, P3 and P4 through arrays ranging from 10 RB/day to 300 RB/day in increment of 10 RB/day.
2) Injector I1 is given rate equal to summation of all producer rates.
3) For each set of rates calculate arrival time misfit.
4) Plot the contour plots by keeping rate of P1 and P3 constant. This is due to the fact that there is less variation in their rates found in multiple minimum solutions.

The case run for calculating arrival time misfit using exhaustive search is described below in **Fig. C.3**, as below,

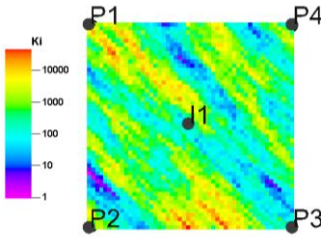


**Constraints are as follows:**
Inj rate <= 800 rb /day, Prod rate <= 300 rb/day, Voidage balance. Optimization time step = 0.5 year
Exhaustive search was carried out for finding different local minimas in the arrival time misfit objective function

**Fig. C.3 - Case run for exhaustive search of local minima**

Some of the local minima observed are plotted below (**Fig. C.4**) by keeping the rates of producers P1 and P3 constant. Many more local minima exist which are not illustrated here.

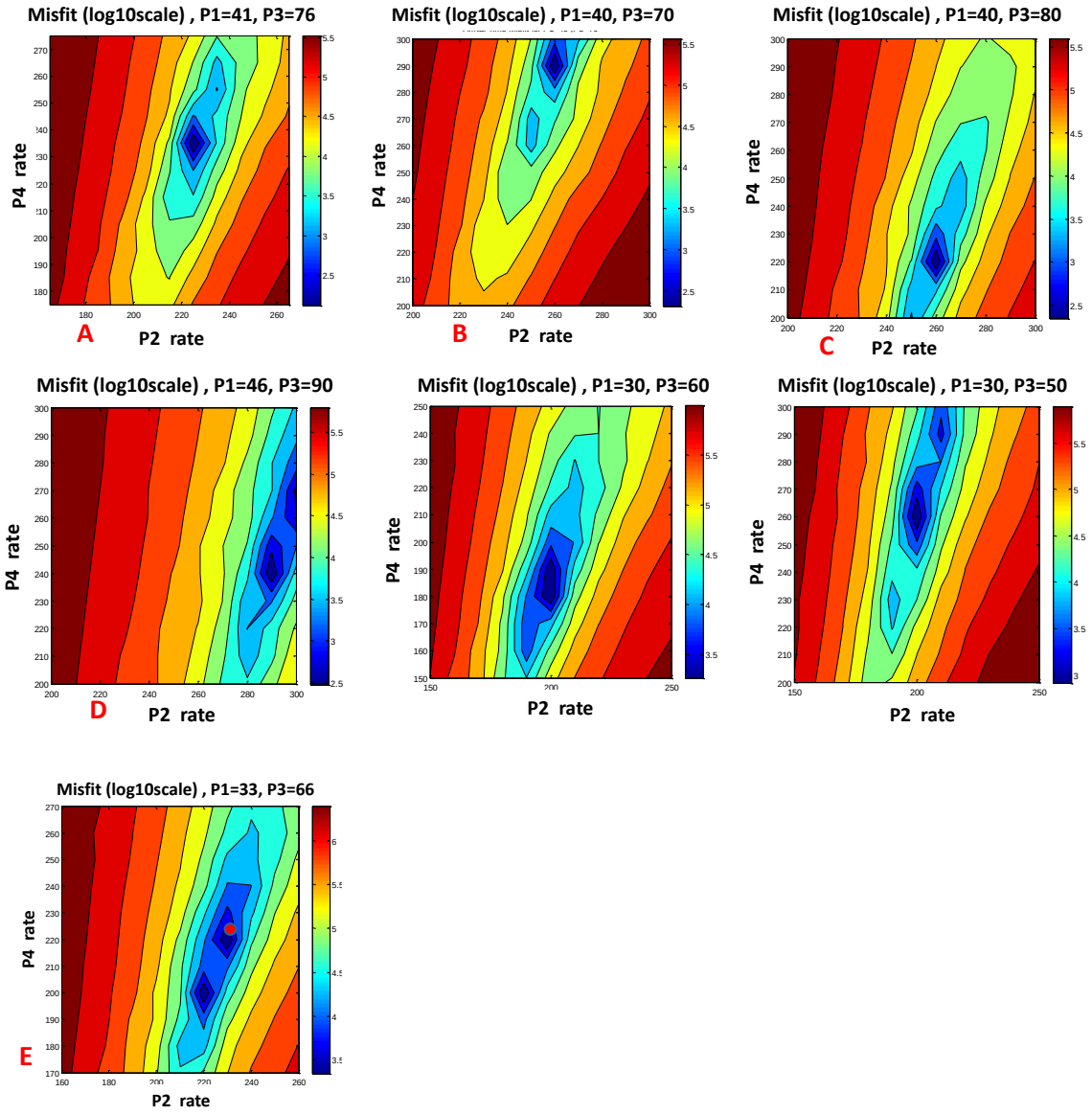


**Fig. C.4 - Some local minima found during exhaustive search.**

b) Different starting rates give different converged rates, verifying existence of local minima (Fig. C.5).

The point is illustrated using two cases which are discussed below,

1) Starting rates of 200 RB/day for each producer and injector is injecting at 800 RB/day.
2) Starting rates of 150 RB/day for P1 and P3, 250 RB/day for P2 and P4. Injector is injecting at 800 RB/day.

It can be observed in **Fig. C.5** that after using different starting rates, optimized rates are converging to different rates. This verifies the existence of multiple local minima. The minima for each case is shown in the contour plot calculated by varying rates for P2 and P4 and keeping rate for P1 and P3 at converged rate. Local minima with trapped solution (red circle) is also observed.

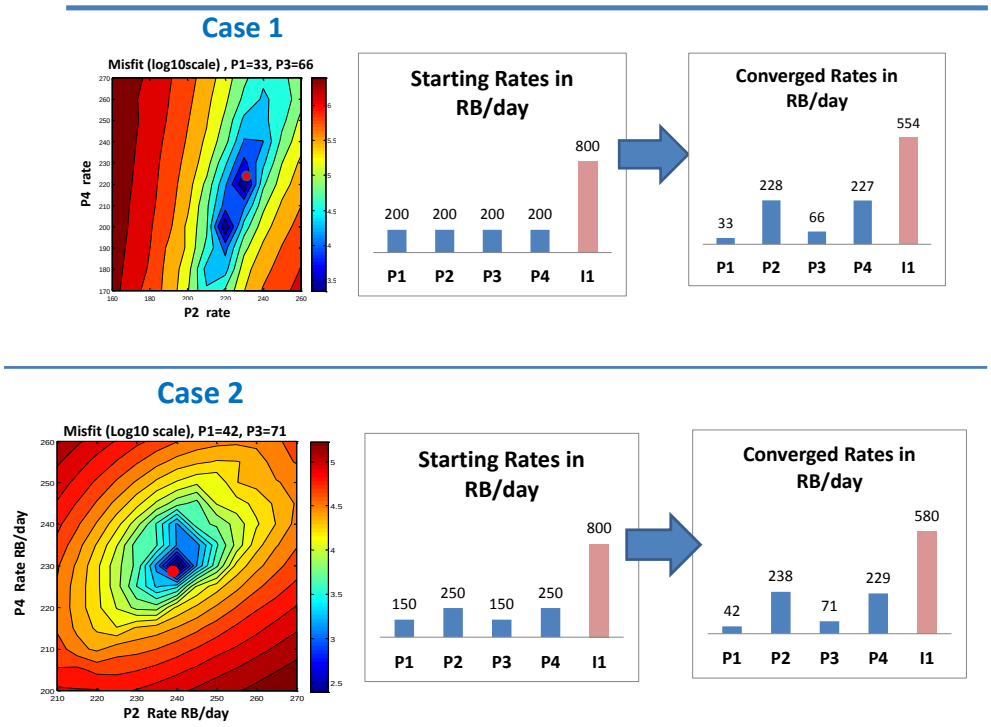


**Fig. C.5 - Different starting points give different converged rates verifying existence of local minima**

**C.3 What does the norm term do?**

Given a starting condition, norm term helps in picking a particular arrival time equalization solution among several non-unique solutions that also minimizes arrival time ($\tau$) which results in acceleration of rates subject to constraints.

There are number of non-unique converged solutions for arrival time equalization method proposed earlier by Alhuthali et al., (2008). This has been demonstrated in **section** C.2.

The modified arrival time equalization equation consists of an augmented norm term to minimize the 'norm' of the arrival time to accelerate fluid production given as follows,

$$p(\mathbf{q}) = \sum_{m=1}^{N_{group}} \sum_{i=1}^{Nprod,m} \left(t_{d,m}(\mathbf{q}) - t_{i,m}(\mathbf{q})\right)^2 + \eta \sum_{m=1}^{N_{group}} \sum_{i=1}^{Nprod,m} \left(t_{i,m}(\mathbf{q})\right)^2$$

In presence of multiple non-unique solutions, norm term helps in picking a particular arrival time equalization solution which also minimizes arrival time resulting in acceleration of rates. This minimization of arrival time is controlled by $\eta$ which is the weight on the norm term.

The variable $t_{i,m}$ represents the calculated arrival time at well i, belonging to group m. The desired arrival time, $t_{d,m}$ for the well group m is given by the arithmetic average of $t_{i,m}$ for each iteration during the optimization. The vector **q** contains the control variables. Addition of a 'norm' term to the objective function ensures that the magnitude of the arrival time is also reduced along with their variance. This reduction in arrival time will lead to the acceleration of oil production and water injection and thus ensuring that the optimization doesn't reduce the production and injection rates of the wells too much to delay water breakthrough, particularly for the highly productive wells. By adjusting the weight, $\eta$ on the norm term, one will be able to decide on the trade-off between equalizing arrival time and accelerating production/injection.

To illustrate the working of norm term, two cases are run which are shown in **Fig. C.6** and **Fig. C.7**. In first case the starting rates are same as first case in **C.2.b** while second case has same starting rates as second case in **C.2.b**. Field is the same quarter spot discussed before in point **C.1**.

*Case 1: Starting Rates are 200 RB/day for producers, voidage balance*
Constraints used in optimization are as follows,
Injection rate <= 800 RB /day, Production rate for each well <= 300 RB/day,
Voidage balance condition. Optimization time step = 0.5 year.

The cases are run for η (norm term weight) = 0 (**Fig. C.6, left**) and η = 2 (**Fig. C.6, right**). The contour plots of the proposed augmented arrival time optimization objective function with norm term weight = 2 (right) and norm term weight = 0 (left) are plotted in **Fig. C.6**. Contour plots are plotted by keeping P1 and P3 at converged rates of 33 RB/day and 66 RB/day respectively for norm term weight = 0 and varying P2 and P4 in a specific range at voidage balance so that the minima is visible. It can be observed that for case of norm term weight = 0 (**Fig. C.6, left**), the optimized rates are shown in the bottom. Similarly for case of norm term weight = 2 (**Fig. C.6, right**), the optimized rates are shown in the bottom. For norm term weight = 0, minima are observed and solution is stuck in it (plotted by red circle). For norm term weight = 2, solution is plotted as red circle. It has hit the constraints. There is a different minima beyond the constraints (black lines) which also minimizes arrival time, after using the norm term weight = 2. Thus, norm term helps in picking a particular non-unique arrival time equalization solution which also minimizes arrival time resulting in rate acceleration subject to the constraints.

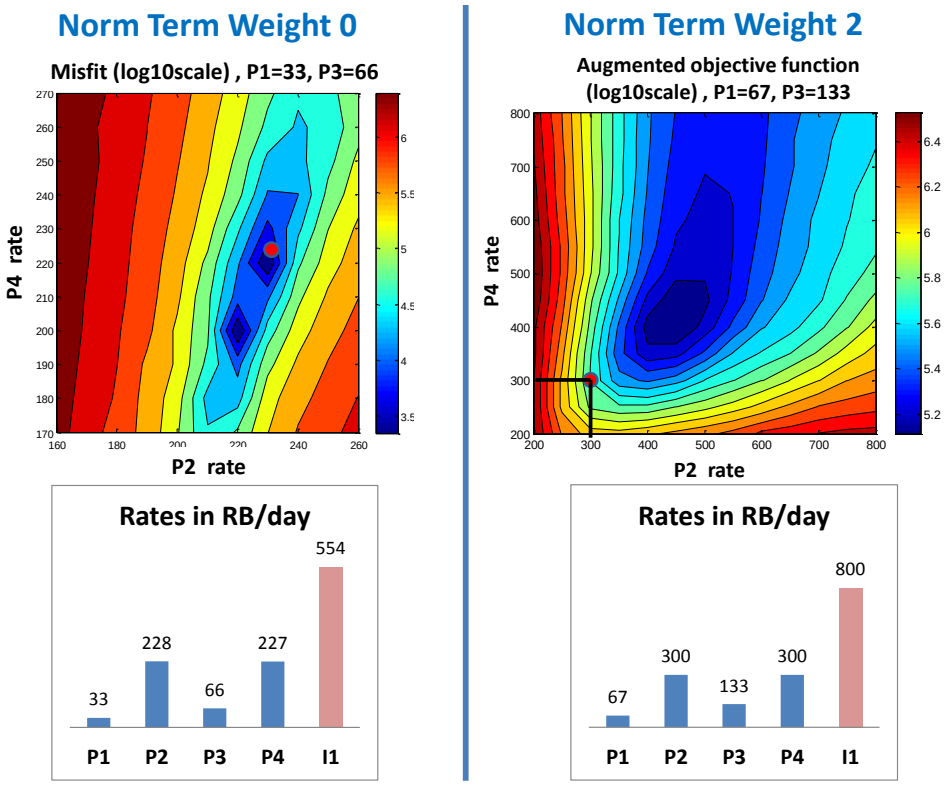


**Fig. C-6 - Two cases with Norm term weight 0 and 2. Starting rates are 200 RB/day for each producer and 800 RB/day for the injector.**

*Case 2: Starting Rates are different for producers, voidage balance*

Constraints used in optimization are as follows,

Injection rate <= 800 RB /day, Production rate for each well <= 300 RB/day,

Voidage balance condition. Optimization time step = 0.5 year.

Starting rates are 150 RB/day for P1 and P3 and 250 RB/day for P2 and P4 with 800 RB/day for the injector (voidage balance).

The cases are run for η (norm term weight) = 0 (**Fig. C.7, left**) and η = 2 (**Fig. C.7, right**).

The contour plots of the proposed augmented arrival time optimization objective function with norm term weight = 2 (right) and norm term weight = 0 (left) are plotted in **Fig. C.7**. Contour plots are plotted by keeping P1 and P3 at converged rates 42 RB/day

and 71 RB/day respectively for norm term weight = 0 and varying P2 and P4 in a specific range at voidage balance so that the minima is visible. It can be observed that for case of norm term weight = 0 (**Fig. C.7, left**), the optimized rates are shown in the bottom. Similarly for case of norm term weight = 2 (**Fig. C.7, right**), the optimized rates are shown in the bottom. For norm term weight = 0, minima are observed and solution is stuck in it (plotted by red circle). For norm term weight = 2, solution is plotted as red circle. It has hit the constraints. There is a different minima beyond the constraints (black lines) which also minimizes arrival time, after using the norm term weight = 2. Thus, norm term helps in picking a particular non-unique arrival time equalization solution which also minimizes arrival time resulting in rate acceleration subject to the constraints.

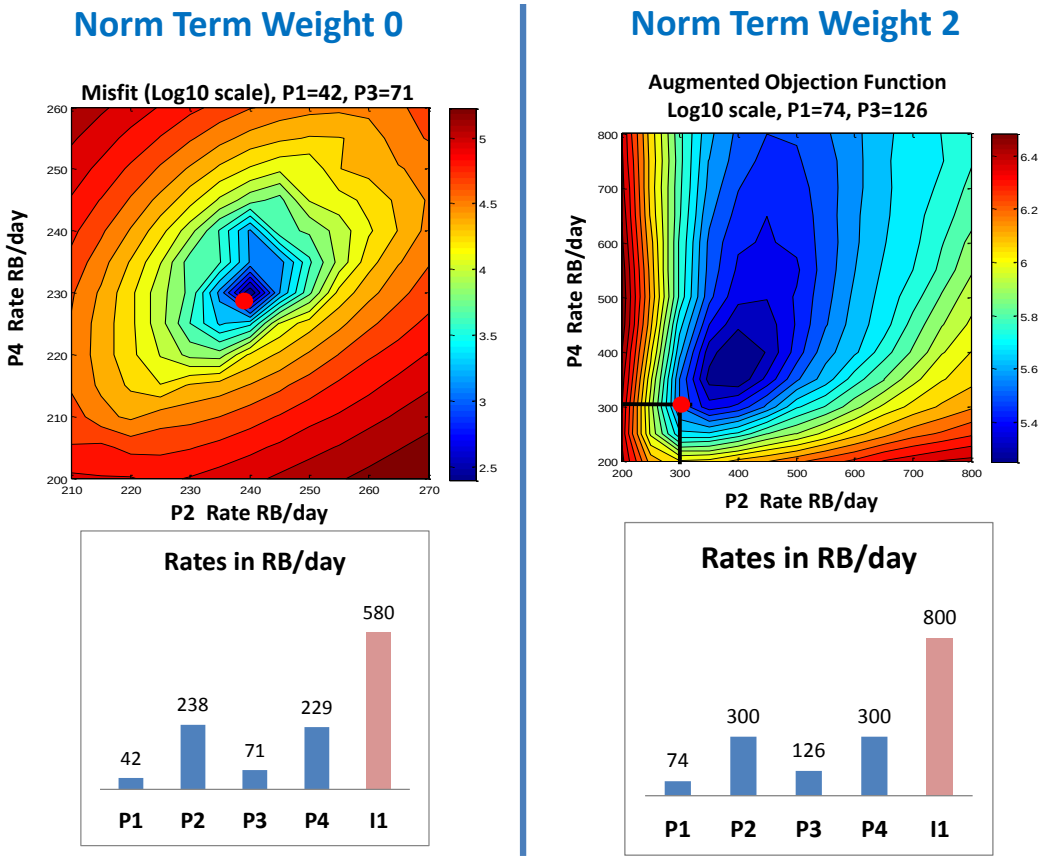


**Fig. C-7 - Two cases with Norm term weight 0 and 2. Starting rates are 150 RB/day for P1 and P3 and 250 RB/day for P2 and P4 with 800 RB/day for the injector.**

Comparing cases 1 and 2 it can be observed that for norm term weight = 0, different starting rates have resulted in solution getting stuck in different minima with different converged rates. But for norm term weight = 2, a similar minima is observed beyond the constraints for both cases. Rates achieved after convergence are also similar for both cases for norm term weight = 2

In conclusion, given a starting condition, norm term is helping to pick up a particular arrival time equalization solution which minimizes arrival time and thus accelerating rates subject to the constraints.

**C.4 How does norm term work in voidage and non-voidage balance cases**

While optimizing both injector (injector rate is not fixed) and producer, norm term helps in accelerating rates and reduces penalty on high productive wells. This is illustrated using two cases. One with voidage balance (total injection = total production) and another without voidage balance.

a) Voidage balance with Qinj <= 800, for Norm term weight ($\eta$) = 0 and $\eta$ =2. This case shows that norm term helps in accelerating rates by sacrificing injection efficiency

To illustrate the point of norm term helping in the accelerating rates by sacrificing injection efficiency, two cases are run.
The cases are: $\eta$ (norm term weight) = 0 (blue) and $\eta$ = 2 (red). Field is the same quarter spot discussed before in **Appendix C.1**. Optimization is carried out at voidage balance while optimizing both injectors and producers.

Constraints used in the optimization are as follows:
Injection rate <= 800 RB /day, Production rate for each well <= 300 RB/day,
Voidage balance condition. Optimization is run for 5 years.
Optimization time step = 0.5 year.
Producer starting rates = 200 RB/day each. Injector starting rate = 800 RB /day

The production rates for each year for each producer for both cases are shown in **Fig. C.8**. Injection rate for each year for injector is shown in **Fig. C.9**.

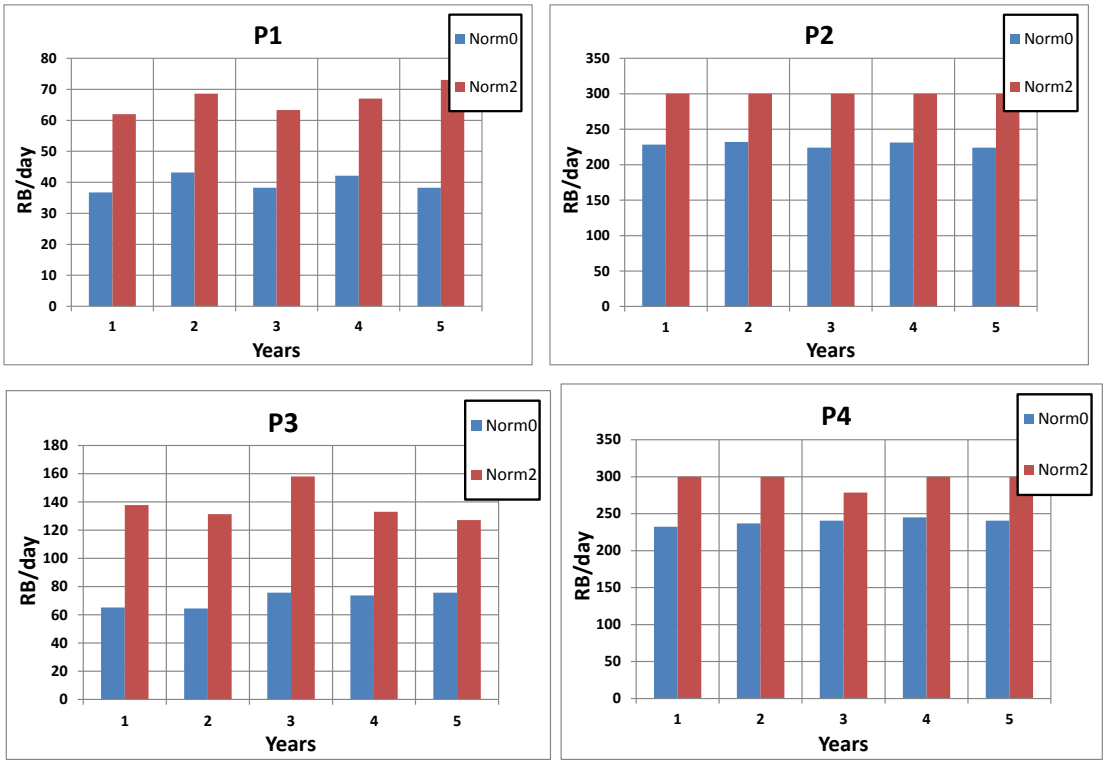


**Fig. C.8 - Production rates for each producer at each year for η (norm term) = 0 and η=2**

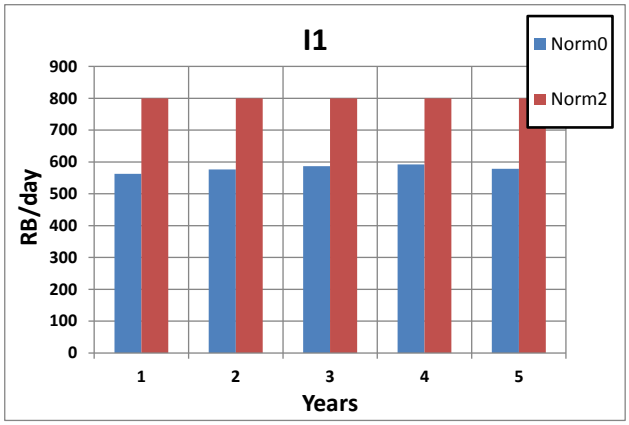


**Fig. C.9 - Injection rate at each year for η (norm term weight) = 0 and η=2**

Higher norm term has helped in accelerating production / injection. Corresponding increase in net present value is plotted in **Fig. C.10**.

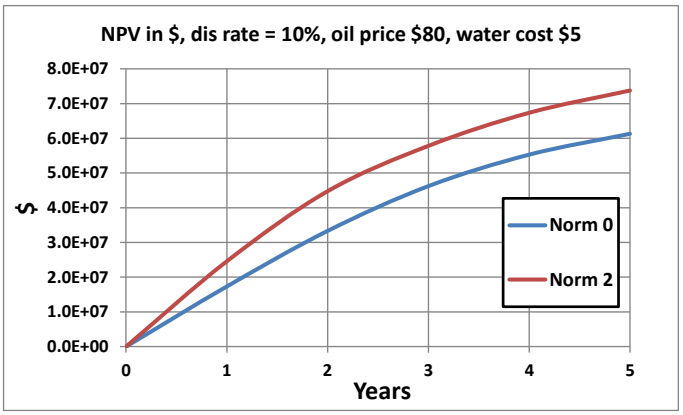


**Fig. C.10 – Net present value (NPV) in $ for η (norm term weight) = 0 and η=2**

As shown in **Fig. C.11**, this acceleration has been achieved by sacrificing injection efficiency.

Injection efficiency is given as follows,

$$Injection\ \ Efficiency\ \ = \frac{Cumulative\ \ oil\ \ produced\ in\ RB/day}{Cumulative\ \ water\ \ injected\ \ in\ RB/day}$$

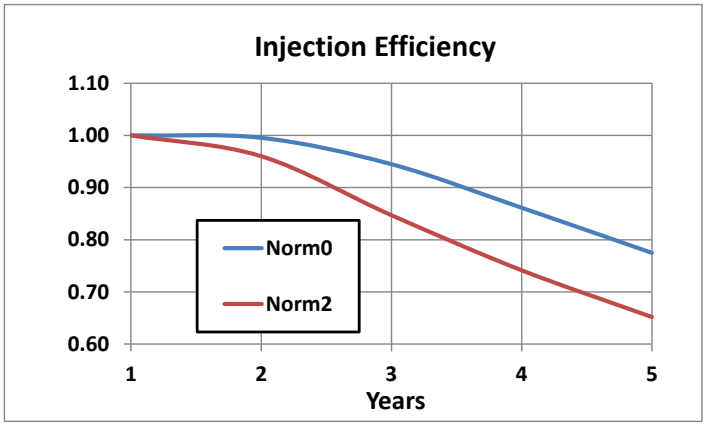


**Fig. C.11 - Injection efficiency for η (norm term weight) = 0 and η=2**

**Fig. C.11** clearly illustrates the tradeoff between equalizing arrival time (maximizing sweep) and production acceleration. In conclusion, for the voidage balance case while optimizing both injector (injector rate is not fixed) and producer, norm term helps in accelerating production and reduces penalty on high productive wells.

*b) Non voidage balance with Qinj <= 800, Norm term (η) = 0 and η =2. This case shows that norm term prevents slowing down of producers and improves injection efficiency*

To illustrate the point that norm term helps in slowing down of producers and improves injection efficiency, two cases are run.

The cases are: η (norm term weight) = 0 and η = 2. Field is the same quarter spot discussed before in **section** C.1. Optimization is carried out at no voidage balance while optimizing both injectors and producers.

Constraints used in the optimization are as follows:

Injection rate <= 800 RB /day, Production rate for each well <= 300 RB/day,

No Voidage balance condition. Optimization is run for 5 years.

Optimization time step = 0.5 year.

Producer starting rates = 200 RB/day each. Injector starting rate = 800 RB /day

The production rates for each year for each producer for both cases are shown in **Fig. C.12**. Injection rate at each year for injector is shown in **Fig. C.13,** along with injection / production ratio at each year.

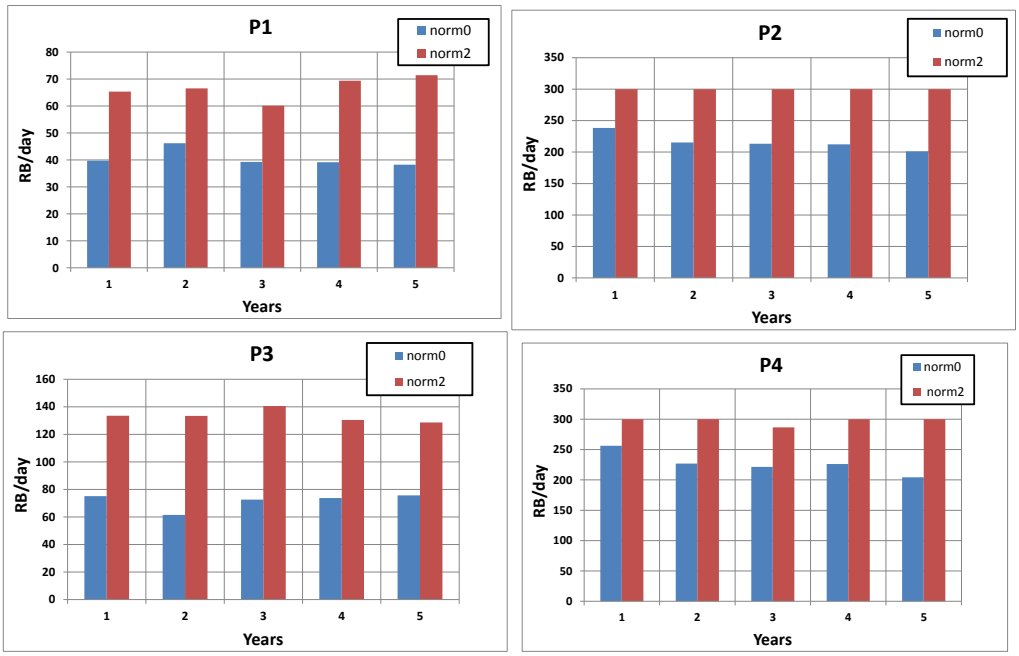


**Fig. C.12 - Production rates for each producer at each year for η (norm term weight) = 0 and η=2**

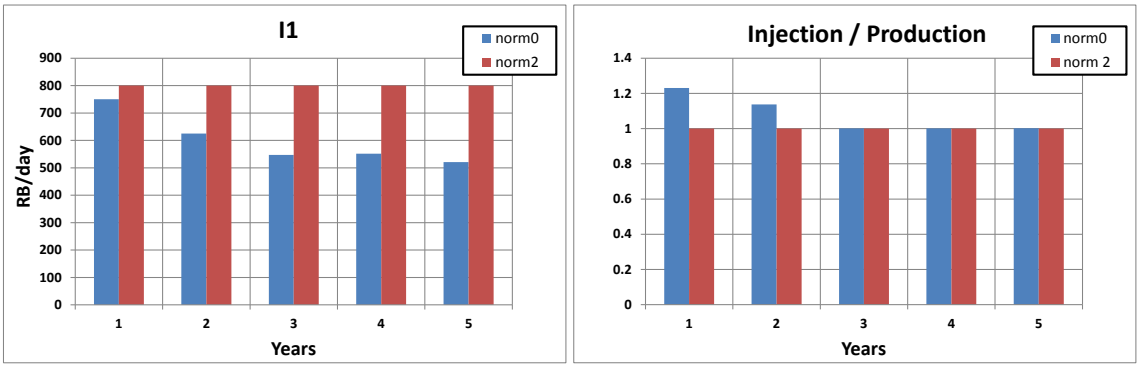


**Fig. C.13 - Injection rate at each year for η (norm term weight) = 0 and η=2 (left) along with injection / production ratio at each year for η (norm term weight) = 0 and η=2 (right).**

For norm term weight (η) = 0 (for no voidage balance) injection tends to be greater than production (**Fig C.13**) because optimization is equalizing the arrival time rather than minimizing it. This leads to lower injection efficiency for η=0 than η=2 as shown in **Fig C.14**. Higher norm term weight helps in minimizing the arrival time along with equalizing it. This leads to higher injection efficiency than η =0.

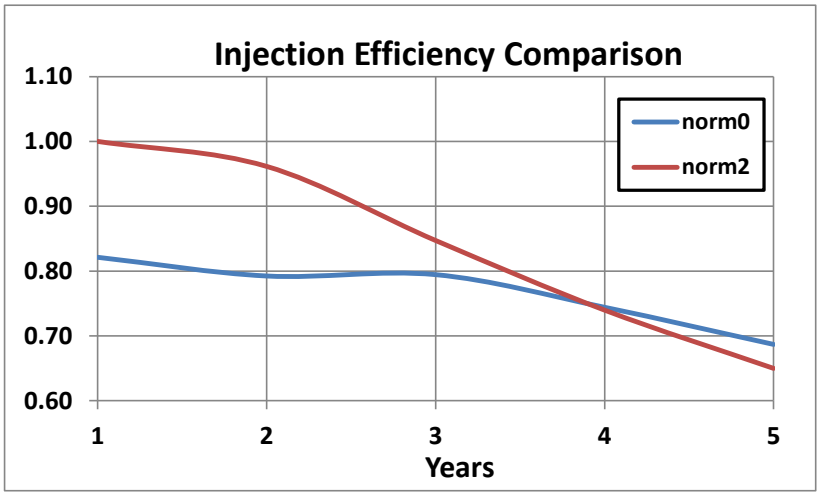


**Fig. C.14 - Injection efficiency for η (norm term weight) = 0 and η=2**

In conclusion, for non-voidage balance case, norm term prevents slowing down of producers and improving injection efficiency.

# APPENDIX D

## D.1 Basic SPSA (Simultaneous Perturbation Stochastic) Algorithm

The objective in the SPSA (Simultaneous Perturbation Stochastic Approximation) is to minimize (or maximize) a particular objective function *O(p)* by approximating its gradient $\nabla O(p_k)$ at iterate *k* stochastically using $\hat{g}_k(p_k)$. This process is done iteratively where *k* is a particular iteration. *p* is the parameter vector consisting of parameters (integers or real) to be optimized.

Value of parameter vector *p*, at next iteration *k+1* is given by

$$p_{k+1} = p_k - a_k \hat{g}_k(p_k) \quad \text{.....(D.1)}$$

Where $a_k$ is the step size at iterate *k*.

This is similar to the steepest descent algorithm where gradient is actually calculated.

The stochastic gradient $\hat{g}_k(p_k)$ which is calculated using minimum two function evaluations is derived as follows:

Let number of parameters in the parameter vector *p* be *n*. Generate *n* random variables from a Bernoulli distribution between -1 and 1. Let these random variables at iterate *k* be denoted by $k_n$.private empire

The stochastic gradient approximation $\hat{g}_k(p_k)$ of the objective function *O(p)* is given by

$$\hat{g}_k(p_k) = \frac{O(p_k + c_k k_n) - O(p_k - c_k k_n)}{2c_k} \quad \text{.....(D.2)}$$

Spall (1998, 2002) described guidelines for selecting $a_k$ and $c_k$, illustrated as follows

$$a_k = \frac{a}{(A+k+1)^{\alpha}} \quad \text{.....(D.3)}$$

$$c_k = \frac{c}{(k+1)^{\gamma}} \quad \text{.....(D.4)}$$

Where *a, c A,* $\alpha$ and $\gamma$ are positive real numbers given as

$$0 < \alpha \leq 1,\ \alpha - \gamma > 0.5\ , \alpha > 2\gamma$$

For details refer to publication by Spall (1998, 2002). Although the choice of *a*, *c*, *A*, $\alpha$ and $\gamma$ is case dependent and requires some trial and error. $\alpha$ =1 and $\gamma$ = 1/6 seems to be the most effective values, Spall (2002) recommended smaller values of $\alpha = 0.602$ and $\gamma = 0.101$ which he argued leads to faster convergence.

**D.2 Modifications to the Basic SPSA Algorithm for Well Placement (Bangerth et al., 2005)**

For well placement optimization only the discrete set of integers (*i* and *j* indexes of the grid cells) have to be considered for *p*. Certain modifications are required in the basic SPSD. The modifications are as follows:

a) $a_k g_k$ and $c_k$ need to be integers at each iterate to always ensure that all the evaluation points *p* are on an integer lattice (Bangerth et al., 2005). This is achieved by rounding off $a_k g_k$ and $c_k$ to the nearest integer.
b) All the evaluations points *p* (i and j indexes of the gridcells) have to stay within a specified grid boundary i.e. they shouldn't be outside the simulation grid. The evaluation point *p* is checked at each iterate. If new *p* is estimated beyond grid boundary then algorithm exits and uses the jump factor described in **section D.3.**

## D.3 Well Placement Optimization using SPSA Gradient Update

The implementation of SPSA algorithm for well placement optimization using gradient update is described as follows:

1) Let $k$ be the iterate number. Set $k$ =1, $\alpha_g = 0.602$, $\gamma_g = 0.101$.

2) While $k < k_{max}$ or convergence has not been reached following loop is executed.

   a. Choose a random direction $\Delta k_g$; $\Delta k_g \in (2 \cdot \text{Round}(\text{random}(P)) - 1)$
   where P = 2·(Number of wells) .. [for changing i and j location of well/s]

   b. Compute $c_g = \frac{c1}{(k+1)^{\gamma_g}}$ , $c_g$ is rounded off to nearest integer.

   $\alpha_g = \frac{\alpha 1}{(A1+k+1)^{\alpha_g}}$, where guidelines for selecting a1, A1 and c1 are given in Spall (1998). The values used here are, a1 = 0.001, c1 = 0.01 and A1 = 1.

   c. Evaluate objective function

   $$f^+ = f\left(p_{g,k} + c_g \Delta k_g\right), \quad f^- = f\left(p_{g,k} - c_g \Delta k_g\right)$$

   such that $c_g \Delta k_g \in \left(\frac{Nx}{JF}, \frac{Ny}{JF}\right)$

   where $p_{g,k}$ = vector containing current i,j position of the well/s at $k^{th}$ iterate.
   Nx = No. of gridcells in X direction, Ny = No. of gridcells in Y direction

JF = jump factor. Jump factor is used to increase the perturbation of i and j location of the wells if the solution is not improving.

d. Calculate approximate gradient

$$\bar{g}_k = \frac{\left(f^+ - f^-\right)}{2c_g}$$

e. Set $p_{g,k+1} = p_{g,k} - a_g \bar{g}_k \Delta k$ (Subject to grid boundary and $a_g \bar{g}_k$ is rounded off to the nearest integer).

f. Check convergence criteria. If convergence criteria is met change jump factor JF, subject to max JF, else, set k= k+1 and return to the start of loop.

# VITA


| | |
|---|---|
| Name | Satyajit Vijay Taware |
| Address | c/o Dr. Akhil Datta-Gupta<br>3116 TAMU, RICH-702<br>Dept. of Petroleum Engineering<br>Texas A&M University, College Station<br>Texas – 77843<br>United States of America. |
| Email Address | satyajit.taware@gmail.com |
| Education | Ph.D, Petroleum Engineering, Texas A&M University, USA, 2012.<br>M.E., Petroleum Engineering, Pune University, Pune, India, 2006.<br>B.E., Production Engineering, Pune University, Pune, India, 2004. |